Magnetoelectric coupling in cobalt-based tellurium (VI) oxides with complex spin structures

Stanislav Podchezertsev

Normandie Université

THÈSE

Pour obtenir le diplôme de doctorat

Spécialité CHIMIE

Préparée au sein de l'Université de Caen Normandie

Magnetoelectric coupling in cobalt-based tellurium (VI) oxides with complex spin structures

Présentée et soutenue par
Stanislav PODCHEZERTSEV

Thèse soutenue publiquement le 17/12/2020 devant le jury composé de		
Mme ISABELLE MIREBEAU	Directeur de recherche au CEA, CEA Saclay	Membre du jury
M. ALAIN PAUTRAT	Directeur de recherche au CNRS, ENSICAEN	Membre du jury
M. JUAN RODRIGUEZ CARJAVAL	Senior scientist, Institut Max Von Laue-Langevin/Grenoble	Membre du jury
Mme EMMANUELLE SUARD	Senior scientist, Institut Max Von Laue-Langevin/Grenoble	Membre du jury
M. NICOLAS BARRIER	Maître de conférences HDR, Université Caen Normandie	Directeur de thèse
Mme VIRGINIE SIMONET	Directeur de recherche au CNRS, Institut Néel	Président du jury

Thèse dirigée par NICOLAS BARRIER, Laboratoire de cristallographie et sciences des materiaux (Caen)

UNIVERSITÉ CAEN NORMANDIE

ED 591 PSIME

RISMA

Acknowledgements

First of all, I would like to thank my supervisors Nicolas Barrier, Emmanuelle Suard and Juan Rodriguez-Carvajal for their guidance during my PhD. I have no words to describe how grateful I am for all the support, care and patience they provided during the past three years. I was really lucky to have such a wonderful team of professionals to work with.

I would like thank CRISMAT laboratory staff who helped me during my visits to Caen. In particular, Sophie Dufourd, Silvie Collin and Laurence Herve for their help with sample preparations, Stephanie Gascoin for the XRD and EDS analysis, Alain Pautrat and Fabien Veillon for the bulk measurements and results interpretation.

The most part of my work was carried out using neutron scattering techniques, hereby I want to express my deepest gratitude towards the ILL staff, Ludovic Gendrin, Oscar Fabelo Rosa, Lucile Mangin-Thro, Bachir Ouladdiaf, Andrew Wildes, Thomas Hansen, Clemens Ritter, Vivian Nassif, Ines Puente Orench, Sofien Djellit, Robert Cubitt and Bjorn Fåk, as well as Françoise Damay from the LLB who provided assistance during neutron scattering experiments, data treatment and discussions.

Needless to say that a personal entourage plays a crucial role in everyday life. And here I want to mention the ILL PhD community who has become a place of comfort, mutual support and appreciation. There is also a group of PhD students at the CRISMAT lab who always provided warm greetings in Cean. I have special thanks to my friends and colleagues who participated in the discussion of my work: Alexander Sukhanov, Artem Korshunov, Irina Safiulina, Marta Crisanti and Antoin Hoez. As a PhD student I had a possibility to meet a lot of bright and enthusiastic young men and women from all over the world, every single one of whom has influenced me in a unique manner. But definitely the vast majority of them has become a great example and a source of inspiration for my professional and personal life.

Throughout my entire life, family and friends have been providing support unconditionally. Yekaterinburg, Saint Petersburg, Moscow, Berlin, Hamburg and Grenoble - thank you all.

And finally, I would like to thank Anna Stoianova for her care and love.

Contents

Introduction

Throughout the history of the humankind one can highlight different stages of society development by simply naming the hallmark material of that time period. For prehistoric society the predominant material was stone. Later when people tamed fire and learned mining, stone as the main tool component was substituted by copper-tin alloys and humanity entered the Bronze age. With the further technological improvements around 1000 BC civilization reached the point when it became possible to process iron which is widely used in all possible aspects of life ever since. Being present from the simplest hand tools up to the most complicated pieces of machinery the iron however had to step aside after semiconductor properties were discovered [1] and first p-n junction was invented [2, 3]. Nevertheless it took a while for semiconductor technology to spread out yet there are no doubts that nowadays we are living in the Silicon age - the most common semiconductor material. Although modern technology, entirely based on semiconductor devices, is extremely efficient it has some fundamental limitations related mainly to the size of a single transistor [4]. At this point it is becoming obvious that future technical breakthrough is ought to happen due to new substances exploiting other physical mechanisms. One of the most promising classes of materials to boost up technology in general and computational power in particular are magnetic multiferroics - materials exhibiting mutual coupling between intrinsic magnetic and electronic subsystems [5].

The history of magnetoelectricity is rich and by now is covering three centuries. It all started in 1865 with Maxwell's equations which showed that magnetic interactions and motions of electric charges are of the same nature [6]. At the very end of 19th century in 1894 Pierre Curie using symmetry considerations predicted the possibility of coupling between electronic and magnetic degrees of freedom in insulating crystals [7]. Yet the first real observation of magnetoelectric effect happened only in 1960 with the discovery of Cr_2O_3 [8] based on prediction made an year earlier by Dzyaloshinskii [9] followed by comprehensive investigation of boracites within which $Ni_3B_7O_{13}I$ was the most famous one for manifesting the strongest multiferroic properties [10]. One has to admit that despite the discovery of several multiferroic phases both found in Nature and obtained artificially [11] the general progress in the field was not that significant due to the lack of theoretical understanding of the phenomenon. Massive expansion of knowledge on correlated electronic systems like high-T_c superconductor cuprates [12] and manganites exhibiting colossal magnetoresistance [13] together with the elaboration of general quantum theory of ferroelectric effect [14, 15] had an important role for the scope of a future progress in the topic. Rethinking over the original idea of ferroelectric perovskites solid solutions containing magnetic ions [16] Nicola Spaldin provided an unpromising forecast on possibilities of coexistence of ferromagnetism and ferroelectricity [17]. But long anticipation at the end concluded with two influential works, each has become a pivotal point for an entire field of magnetoelectric materials. First was the discovery of a room temperature multiferroicity in $BiFeO_3$ thin films which inspired an intensive research on this compound with

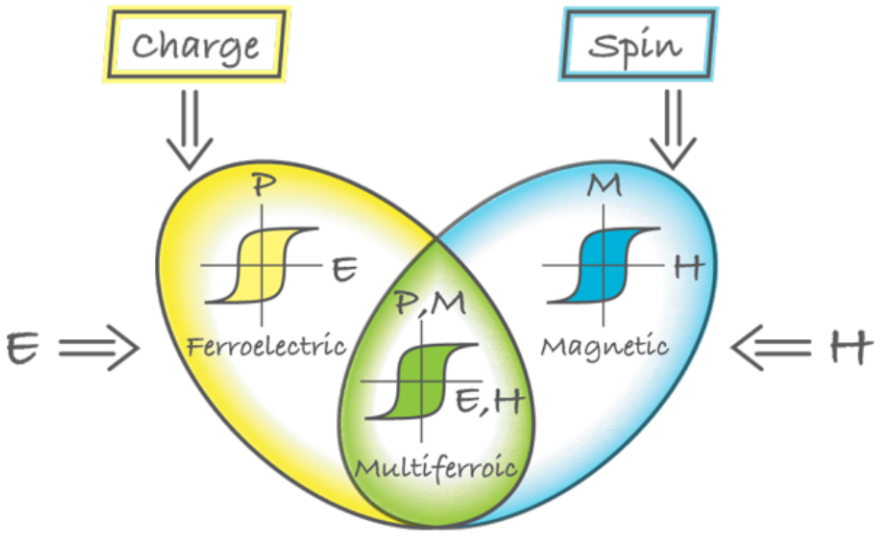

Figure 1: Magnetic multiferroics combine both spin and charge ordering. Ferroelectric and ferromagnetic materials demonstrate a hysteretic response of polarization and magnetization to an electric and magnetic field respectively. In the ideal case an interplay between electronic and magnetic degrees of freedom in multiferroics allows to have a magnetic response to an electric field and an electronic response to a magnetic field [5]

potential applications [18]. The second was observation of a new type of multiferroicity in $TbMnO_3$ [19]. In comparison to all previously known compounds where ferroelectricity and magnetism were linked indirectly, in case of $TbMnO_3$ magnetic ordering was the driving force for electric polarisation to occur, thus the coupling between two essential subsystems is intrinsically strong. In short time two other compounds exhibiting the same type of multiferroic behaviour were synthesized: $HoMnO_3$ [20] and $TbMn_2O_5$ [21] which stimulated enormous interest to the discipline leading to the discovery of a large numbers of novel materials and deeper understanding of microscopic mechanisms responsible for multiferroicity far beyond simple phenomenological model.

Certainly the major concern towards magnetic multiferroics is driven by fundamental interest towards the field. On one hand even the most well developed theoretical models are incapable of providing exhaustive explanation of all experimental observations, on the other hand properties demonstrated by known materials are incompatible with efficient device performance: low transition temperatures or weak magnetoelectric coupling makes production and exploitation technologically unfavorable. Nonetheless some composite materials find their applications in prototype devices such as sensors and actuators [22]. Also thin-film heterostructures of alternating ferroelectric and ferromagnetic layers may be used as transistors, tunneling junctions or magnetic sensors [23]. Moreover two co-dependent orders make such materials attractive for data storing. Simply combining electric polarization with magnetization opens brand-new horizons for building four-state memory elements [24]. Multiferroics could also improve energy consumption and increase speed of data-storage devices since manipulating a magnetic bit with low-voltage pulses produces less heat waste and increases the build-up time in comparison with electric currents generated by magnetic fields.

On top of that research on multiferroics is having a huge impact over fields of knowledge which are indirectly related or not even relevant for multiferroic materials themeselves

from the first glance. First of all one has to mention significant technological advance in characterization methods inspired by challenging tasks. To probe the behaviour of ferroelectric and magnetic regions significant progress was made in the field of non-linear laser spectroscopy [25, 26]; x-ray diffraction became able to resolve ionic shifts at femtometer scales [27]; electromagnons - a special type of excitations appearing in multiferroics - became available to detect with some improvements in terahertz spectroscopy [28]. High-energy physics has profited from discoveries made in the multiferroic area. For instance europium barium titanate has all required magnetic and electric properties for detecting a permanent electric dipole moment of the electron [29]. It was also shown that ferroelectric transition in h-$RMnO_3$ compounds and phase transitions in the early universe obey the same rules, which make the first a perfect playground for testing cosmological models [30, 31].

Hereby, a search and study of novel multiferroic compounds is of great importance either for expending the fundamental understanding of Nature and possible technical applications. So during this research work, cobalt based tellurium (VI) oxides with complex magnetic structures were studied. Among these compounds, significant attention was paid to the $Co_{5-x}Zn_xTeO_8$ spinel series for their potential magnetic multiferroic properties. During these 3 years, an extensive work was carried out on syntheses, the crystal structures refinements, and the characterisation of their magnetic and dielectric properties, combining several techniques: classical magnetic bulk characterization (SQUID, PPMS) and various neutron scattering experiments. This manuscript presents three chapters. Chapter 1 provides a general information on the magnetoelectric effect and multiferroic materials as well as the motivation to a current research. Chapter 2 is dedicated to the different experimental techniques that were used for the study on the spinel series of $Co_{5-x}Zn_xTeO_8$. In chapter 3 all the experimental results and their discussion are given. The last part corresponds to the general conclusion and perspectives.

Chapter 1

General information on magnetoelectric effect and multiferroic materials and motivation to the current research

In this chapter the major aspects of magnetoelectric effect will be given. The basic principles of time-space symmetry conservation and related ferroic orders are discussed. Coexistence of spin and charge ordering is considered first in terms of a phenomenological model based on Landau theory and then microscopic origins of emergence of the electric polarization are reviewed. Since the current project is dedicated to magnetoelectric compounds of spin origin, special attention is given to multiferroics type-II. Later in this chapter a motivation for the research of the $Co_{5-x}Zn_xTeO_8$ spinel series is given.

1.1 Ferroic orders, order parameters and their symmetry properties

As it was originally proposed by Schmid in 1994 multiferroics is a class of materials combining at least two primary ferroic orders [32]. Initially, the list of ferroics contained three types of order: ferroelectric, ferromagnetic and ferroelastic. All of them are described by the spontaneous emergence of a corresponding property called order parameter that is uniform within domains, geometrically restrained regions of media, that can be switched back and forth hysteretically by an appropriate external field. In case of ferroelectric ordering, the order parameter is an electric switchable polarization under electric field, for ferromagnets it is magnetization and magnetic field, and ferroelastic materials are characterised by spontaneous deformation under applied stress. However, this list got expanded with the discovery of so-called ferrotoroic order represented by toroidal moment generated by vortices of magnetic moments [33]. Similarly to examples mentioned above, toroidal moment could be also controlled by in-field manipulations. These four states make up a full list of currently discovered primary ferroic orders however they might be extended with some more complicated scenarios involving orbital orderings, other types of vortices and chiralities [34]. It is also necessary to mention that this classification includes also antiferroic orders like antiferroelectricity and antiferromagnetism in which associated moments are cancelling each other in an ordered state.

Space-time symmetry is a key point for primary ferroic orders characterization. All

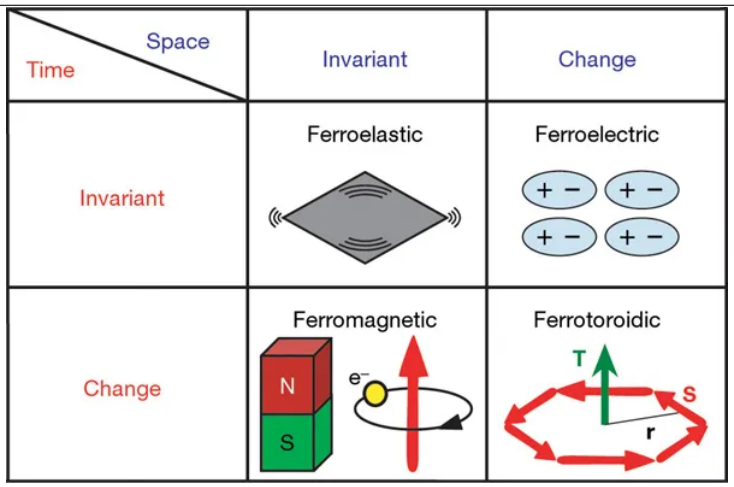

Figure 1.1: All four known ferroic states under the parity operations of space and time [33]

four states possess different transformation properties under the parity operators of time reversal and spatial inversion. For instance, ferroelectricity associated with spontaneous polarization $\mathbf{P}$, which is given by $\sum_i Q_i \mathbf{r}_i$ where Q_i stands for charge at the position r_i. Obviously with electric dipole emergence the space-inversion is violated whereas time-reversal symmetry is preserved. Magnetic moment $\mathbf{M}$, in turn, shows an opposite feature. Being an axial vector, this quantity can be represented as a current loop, thus is proportional to $(dQ\mathbf{r}/dt) \times \mathbf{r}$ where t is time. So magnetic moment $\mathbf{M}$ breaks time-reversal symmetry but remains invariant under the space inversion [35]. Emerging toroidal moment $\mathbf{T} \sim \mathbf{M} \times \mathbf{r}$ violates both space-inversion and time-reversal symmetries [36] whereas ferroelastic order does not break any [37].

Since polarization $\mathbf{P}$ and magnetic moment $\mathbf{M}$ have different symmetry properties, ferroelectric and ferromagnetic orders are independent in general. However these two order parameters might be conjugated through magnetoelectric coupling: a mutual co-dependence of electronic and magnetic subsystems of a material. So, in this case, multiferroics combining spin and charge ordering are space-time asymmetric.

1.2 Phenomenological model of magnetoelectric coupling

Landau's theory of phase transitions is a perfect tool to describe magnetoelectric coupling in matter in terms of order parameters. One can put down the free energy of a given system in terms of temperature T, applied electric field $\mathbf{E}$ and magnetic field $\mathbf{H}$ in the following form:

$$F(E,H,T) = F_0 + P_i E_i + \mu_0 M_i H_i + \frac{1}{2}\epsilon_0 \epsilon_{ij}(T) E_i E_j + \frac{1}{2}\mu_0 \mu_{ij}(T) H_i H_j + \alpha_{ij}(T) E_i H_j + \frac{\beta_{ijk}(T)}{2} E_i H_j H_k + \frac{\gamma_{ijk}(T)}{2} H_i E_j E_k + \pi_{ijkl}(T) E_i H_j \sigma_{kl} + \ldots \quad (1.1)$$

Here i, j, k and l are x, y and z components of vectors and tensors defined in the equation. The Einstein's rule of sum over repeated indices is assumed. The first term of equation 1.1 expresses the electric response of the system to an applied electric field, where ϵ_0 is the permittivity of free space and $\epsilon_{ij}(T)$ is the relative permittivity of the material. By analogy to the first term, the second term is the magnetic response to the magnetic field,

where μ_0 and $\mu_{ij}(T)$ are permeability of free space and relative permeability respectively. The third term describes the linear magnetoelectric effect via $\alpha_{ij}(T)$ coupling coefficient, whereas $\beta_{ijk}(T)$, $\gamma_{ijk}(T)$, and $\pi_{ijkl}(T)$ terms represent higher-order magnetoelectric effects [32, 38].

The magnetoelectric term couples indirectly both subsystems and can be represented in terms of magnetic-field-induced polarization $P_i(H_j)$ and electric-field-induced magnetization $M_i(E_j)$. Differentiating the free energy F with respect to H_i and then forcing $H_i = 0$ will give:

$$\mu_0 M_i = \alpha_{ij} E_j + \frac{\gamma_{ijk}(T)}{2} E_i E_j + ... \tag{1.2}$$

Carrying out the same calculation for E_i one will end up with:

$$P_i = \alpha_{ij} H_j + \frac{\beta_{ijk}(T)}{2} H_i H_j + ... \tag{1.3}$$

Proceeding further with the analysis of equation 1.1 one can estimate α_{ij} to achieve a non-negligible effect. For that high-order terms should be disregarded and the sum of the first three terms should have a positive value. Thus α_{ij} is bounded by geometric mean of both magnetic and electric susceptibility tensors [39]:

$$\alpha_{ij} \leq \epsilon_0 \epsilon_{ij} \mu_0 \mu_{ij} \tag{1.4}$$

Upon such a condition it is obvious that to carry a strong magnetoelectric coupling the material should possess both large ϵ_{ij} and μ_{ij}.

However the vast majority of known materials have poor linear magnetoelectric effect due to small values of one or both response functions. Yet this limitation could be overcome via higher order terms in equation 1.1 involving β_{ijk} and γ_{ijk}. For example it is known that for non-centrosymmetric piezoelectric paramagnet $NiSO_4 \cdot 6\,H_2O$ the indirect coupling $\beta_{ijk}(T) E_i H_j H_k$ term outperforms the linear coupling at low temperatures [40]. Dimensionality reduction could also result from β_{ijk} coupling, which was observed for magnetically ordered $BaMnF_4$ [41]. It was also shown that in some particular cases the γ_{ijk} term could also come into play and become a major driving force for magnetoelectric coupling, like it was observed for yttrium iron garnet [42].

The last term in equation 1.1 is also worth mentioning. The piezomagnetoelectric tensor π_{ijkl} describes a stress-induced (σ_{kl}) magnetoelectric effect [43]. This, or similar terms, might prevail in the free energy equation for composite multiferroic materials like thin-films and multilayers [18, 44, 45].

Symmetry is also playing an important role in this phenomenological approach. In general, magnetoelectric coefficients adopt the symmetry of the material [46, 47]. For instance, α_{ij} can have non-zero values only for non-centrosymmetric crystals. At this point an exhaustive understanding of magnetoelectric properties of a certain material could be achieved when the magnetic point group is known. Nonetheless nowadays it is known that some specific types of long-range spin arrangements can break the space-inversion symmetry which allows magnetic and electronic subsystems to couple. The last will be discussed in section 1.3.2.

1.3 Microscopic origins of electric polarization

In the previous section a phenomenological approach to the coupling between spin and charge orderings was given. But no profound insight on this phenomenon could be achieved

without close consideration of microscopic mechanisms of multiferroicity. In most ferroelectric materials the bulk polarization originates from atomic shifts of positively charged cations and their anionic environment. In terms of covalent bonding such displacements are energetically favourable when the d shell of the cation is empty. Contrary to that, long range magnetic orderings arise from the exchange interactions between unpaired electrons of partially filled d shell in case of transition metal ions. And here comes the problem that these two requirements, on filling of the d shell, make magnetism and ferroelectricity mutually exclusive [17]. Nevertheless there are some other mechanisms of polarization that help to avoid this d^0 versus d^n limitation. Essentially there is no single microscopic mechanism of ferroelectricity and polarization; it arises from an interplay between charge, orbital or spin ordering and structural distortions.

According to Cheong and Mostovoy ferroelectrics can be split into two groups: proper and improper ones [48]. For the first group the electric polarization results from some alterations in local structure, such as deformations or polyhedra tilts, appearing at the Curie temperature, and for improper ferroelectrics the polarization can be driven by structural transitions, charge or magnetic ordering. But from a different perspective, it might be handy to use another classification proposed by Khomskii, which also lies in dividing multiferroic materials into two groups: type-I and type-II multiferroics [5]. Type-II multiferroics consist of those within which ferroelectricity is induced by some particular types of long-range spin arrangements, whereas type-I are all the rest. Although there might be other ways of segregating ferroelectric materials [49], for the sake of the current project it would be more convenient to represent ferroelectric materials in terms of type-I and type-II multiferroics.

1.3.1 Multiferroics type-I

Type-I multiferroics were discovered the first, and as a result, the amount of materials representing type-I multiferroics is prevailing over type-II. Materials type-I are usually showing large values of polarization **P** and high transition temperatures, for both ferroelectric and magnetic transitions, which often lies above room temperature. However type-I multiferroics possess rather week magnetoelectric coupling. Here below the main mechanisms supporting ferroelectricity within this type of multiferroic materials will be listed.

Mixed perovskite phases. As it was already mentioned, ferroelectricity and magnetism are hard to combine since both of them counter each other. Strong covalent bonding is essential for ferroelectricity, it is achieved by cations with empty d states such as Ti^{4+}, Ta^{5+} or W^{6+} whereas magnetism emerges from non-compensated electron at the same d level carried by Cu^{2+}, Co^{2+}, Fe^{3+} and others. An obvious solution to overcome this problem is combining both types of ions within a single compound like it was realised in $PbFe_{0.5}Nb_{0.5}O_3$ for which the transition temperatures are relatively high: $T_{FE} = 387K$ and $T_N = 134K$, nonetheless the coupling between these two subsystems remains weak [11].

Lone pairs. This mechanism describes the case of $BiFeO_3$ in which Bi^{3+} pairs of outer *6s* valence electrons are not involved in chemical bonds. That creates an anisotropic charge distribution giving rise to a spontaneous polarization of around $100\mu Ccm^{-2}$ [18] below $T_c = 1103K$ [50]. Long range magnetic ordering in this system occurs below $T_N = 643K$ [51]. Such a scenario takes place not only in single phase compounds but also enhances ferroelectric properties in mixed systems like $Pb(Zr_xTi_{1-x})O_3$.

Geometric ferroelectricity. Structural phase transitions leading to displacements of structural elements can induce an electric polarisation in materials. That was observed

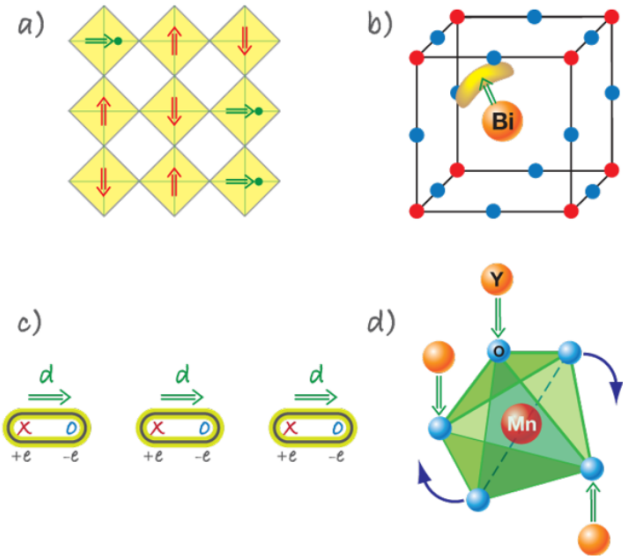

Figure 1.2: Microscopic mechanisms of ferroelectricity for type-I multiferroics. a) Mixed perovskites with a random distribution of d^0 (green arrows) and d^n (red arrows) cations. b) The lone pairs mechanism found in $BiFeO_3$. c) Charge ordering systems in which particular type of cationic distribution leads to inequivalent bond length causing ferroelectricity. d) The geometric mechanism. [5]

in h-$RMnO_3$ (R = Sc, Y, In or rare earth elements from Dy to Lu) in which MnO_5 polyhedra undergo an inclination to provide a closer packing after a unit cell tripling [52, 53, 54]. Similar structural shifts take place in a thin film of h-$LuFeO_3$ which shows a room temperature spin ordering [55]. Another manifestation of the very same mechanism was found in $BaNiF_4$ which gives an opportunity to reverse weak ferromagnetic moment along with the electric polarization [56, 57]. Another example of geometric ferroelectricity is $Ca_3Mn_2O_7$ in which a complex lattice distortion involving rotation of oxygen octahedra induces the ferroelectric transition.

Charge ordering. This effect could take place in compounds containing transition metal ions of different valence. In this case cations holding distinct charge can arrange into periodic superstructures or cause dimerization which in turn yield polarization. As an example one can consider $LuFe_2O_4$ having repetitive patterns of Fe^{2+} and Fe^{3+} cations within its crystal structure [58, 59]. Some nickelates $RNiO_3$ [48, 60] and mixed manganites such as $Pr_{1-x}Ca_xMnO_3$ also represents a corresponding mechanism.

1.3.2 Multiferroics type-II

Multiferroics of the second type are often referred as multiferroics of spin origin due to the fact that for these compounds the magnetic ordering itself is a driving force for an electric polarisation to occur [61]. Thus, it is obvious that compounds representing this type of multiferroicity possess a strong coupling between magnetic and electronic subsystems, which, in turn, permits a high tunability of magnetization under applied electric field as well as magnetic stimulation will cause a drastic change in polarization. However, the polarization shown by type-II multiferroics is usually weak in comparison to the values shown by compounds of the first type.

Another characteristic feature of type-II multiferroics is the relatively low magnetic ordering temperatures as complex spin arrangements, required for polarisation emergence,

are the result of multiple magnetic interactions, often competing ones, which prevent establishing of a long-range ordering at high temperatures.

Concerning microscopic mechanisms of magnetically driven ferroelectricity, multiferroics of spin origin may be split into three major groups. The first one is characterised by commensurate magnetic orderings bearing them to cause exchange striction along particular crystallographic directions, the second one is represented by magnets with special type of incommensurate spin structures, while the third one employs the geometry of electronic configuration of magnetic ions and their ligands. Regardless to the way the electric polarization is generated, all three groups of magnetic orderings are breaking the space-inversion symmetry.

1.3.2.1 Exchange striction mechanism

This mechanism exploits Heisenberg interaction exclusively and takes place in collinear or almost collinear magnets. The crucial point for the exchange striction is a presence of neighbouring magnetic cations of various valence that could undergo a dimerization at low temperatures. Prime example to illustrate this phenomenon is a quasi-one-dimensional Ising magnet Ca_3CoMnO_6 [62, 63]. Below the transition temperature alternating Co^{2+} and Mn^{+4} ions form one-dimensional spin chains resulting in so-called up-up-down-down ($\uparrow\uparrow\downarrow\downarrow$) magnetic structure (Fig. 1.3). This magnetic ordering distorts chains compressing chemical bonds between ferromagnetically coupled cations and expanding the ones coupled antiferromagnetically. Thus, the inversion symmetry is broken giving rise to an electric polarisation of P $\sim 90\mu C/m^2$ at 2 K.

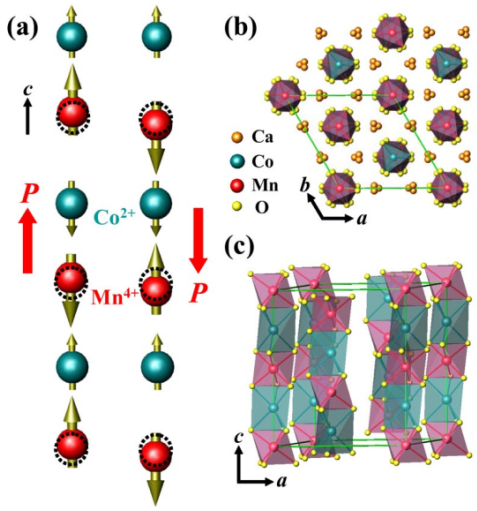

Figure 1.3: a) Alternating cationic arrangement of Co^{2+} and Mn^{4+} forming one-dimensional Ising chains. As a result an electric polarization is induced via exchange striction. Two different possible spin configurations are providing polarizations with opposing directions; b, c) The crystal structure of Ca_3CoMnO_6. Octahedra of CoO_6 and MnO_6 form chains along the crystallographic $c-$axis, while in the ab plane they are separate enough to exclude interactions between neighbouring chains. The green box corresponds to the crystallographic unit cell [62].

Another illustration of this mechanism can be found in orthorhombic manganites RMn_2O_5 where R is Y, Tb, Ho, Er or Tm [64]. Manganese atoms in octahedral and pyramidal environment are forming loops of ions with different oxidation states: $Mn^{4+} - Mn^{3+} - Mn^{3+} - Mn^{4+} - Mn^{3+}$. This rather complex cation arrangement causes significant

magnetic frustration which, in turn, is responsible for complex spin configurations. In case of YMn_2O_5 the system first orders in two-dimensional incommensurate phase below $T_{N1} \approx 45K$, then it enters a commensurate phase below $T_{CM} = 40K$ which is followed by another incommensurate magnetic phase transition, at $T_{N2} = 20K$. In the commensurate magnetic phase, half of $Mn^{2+}-Mn^{3+}$ are having almost antiparallel spin orientation whereas for the other half spins tend to align in parallel. That results in $\uparrow\uparrow\downarrow$ or $\downarrow\downarrow\uparrow$ zig-zag fragments which endure the same type of distortion as it was described above, symmetry breaking induces a net polarization along the b axis with the maximum magnitude of P $\sim 9\mu C/m^2$ at the temperature slightly above T_{N2}. Same kind of up-up-down-down zig-zag spin structures leading to ferroelectric transitions are observed in orthorhombic perovskite manganites $RMnO_3$ with R = Ho, Er, Tm, Yb and Lu reaching maximum polarization of P $\sim 5000\mu C/m^2$ in the case of Yb and Lu compounds [65, 66, 67].

1.3.2.2 Ferroelectricity and spiral spin orderings

A key component in understanding ferroelectricity in spiral magnets is Dzyaloshinskii-Moriya (DM) interaction or antisymmetric exchange [68, 69, 70, 71]. This interaction arises as the relativistic correction to exchange interactions in the presence of the spin-orbit coupling. Let us consider a chemical bond between metal ions via oxygen ligand (Fig. 1.4). In the ideal case the M-O-M bond angle is 180^o, however if the crystal structure is somehow distorted, which may occur due to different reasons, the M-O-M angle is no more straight, the rotation symmetry of the bond is broken, and the oxygen atom may be displaced from the middle point between its metal cations. This displacement will induce the DM interaction, which hamiltonian is

$$H_{DM} = \mathbf{D}_{ij} \cdot (\mathbf{S}_i \times \mathbf{S}_j), \tag{1.5}$$

whee $\mathbf{D}_{ij}$ is the vector of DM interaction, determined by the symmetry of the crystal structure. In the simplest approximation, the magnitude of the DM vector is proportional to the ligand displacement from its middle point $\mathbf{d}_0$:

$$\mathbf{D}_{ij} = \xi \mathbf{e}_{ij} \times \mathbf{d}_0, \tag{1.6}$$

where $\mathbf{e}_{ij}$ is the unit vector connecting site i and site j and ξ is a proportionality factor. In the high symmetry limit, $\mathbf{D}_{ij} = 0$.

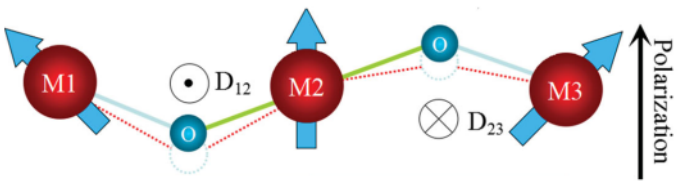

Figure 1.4: The Dzyaloshinskii-Moriya interaction appearing between metal ions (M) with distorted M-O-M bonds. The vector $\mathbf{D}_{ij}$ is perpendicular the M-M axis and pointing in or out the paper plane depending on the direction of the oxygen atom displacement [35].

It was shown that DM interaction, driven by oxygen displacements, plays an essential role in the stabilization of the incommensurate spin order in multiferroic $TbMnO_3$ perovskite [72]. Below 28 K this compound posesses $b-c$ plane cycloid with the propagation vector along the b-axis. The shift of charge distribution maximises the energy gain of DM interaction and the electric polarization appearing along the $c-$axis is:

$$\mathbf{P} \sim \mathbf{e}_{ij} \times (\mathbf{S}_i \times \mathbf{S}_j). \tag{1.7}$$

This is often referred as an inverse DM mechanism.

However, in the case of canted spins, an electric polarization may arise as a result of an electronic bias. This mechanism is often referred as the spin current model [73]. Let us consider a magnetic insulator, in such a material the momentum is quenched by the Coulomb interaction U, however there is a virtual electron hopping between neighbouring atoms that leads to an exchange interaction, which can be represented in the form of the Heisenberg Hamiltonian:

$$H = -\sum_{ij} J_{i,j} \mathbf{S}_i \cdot \mathbf{S}_j, \tag{1.8}$$

where $J_{i,j}$ is an exchange integral and $\mathbf{S}$ are spin operators. The spin current is then defined to satisfy the Heisenberg equation of motion for $\mathbf{S}_i^z$:

$$\frac{\partial \mathbf{S}_i^z}{\partial t} = (1/i\hbar)[\mathbf{S}_i^z, H] = -\sum_j j_{ji}^z \tag{1.9}$$

and the spin current itself is given by

$$j_{ij}^z = 2J_{ij}(S_i^+ S_j^- - S_i^- S_j^+). \tag{1.10}$$

Due to the spin orbit interaction, spin current is coupled to a vector potential $\mathbf{A}_s$, which role in the case of non-collinear magnets is played by the DM vector $\mathbf{D}$. As a consequence of this coupling, the electric polarization lies in the direction perpendicular to both the direction of the spin current and spin polarization:

$$\mathbf{P} \propto \sum_{i,j} \mathbf{e}_{ij} \times (\mathbf{S}_i \times \mathbf{S}_j) \tag{1.11}$$

and in the general case

$$\mathbf{P} = \eta \mathbf{e}_{ij} \times (\mathbf{S}_i \times \mathbf{S}_j), \tag{1.12}$$

where η is the coupling constant proportional to the spin-orbit interaction.

This may be illustrated with the case of hybridization of the d orbital of the magnetic ion and p orbitals of the oxygen atom (Fig. 1.10). Let us consider the inversion symmetry at the middle point between two magnetic ions is preserved. The non-collinear order in this case may occur due to the competition of exchange interactions and/or the symmetry breaking caused by the spin-orbit interaction. If $\mathbf{e}_1$ and $\mathbf{e}_2$ are directions of spins at magnetic sites, the electric polarization depends on matrix elements $I = \langle p_x|z|d_{zx}\rangle$ is given by:

$$\mathbf{P} \cong -\frac{4e}{9}\left(\frac{V}{\Delta}\right)^3 I \mathbf{e}_{12} \times (\mathbf{e}_1 \times \mathbf{e}_2), \tag{1.13}$$

where $\mathbf{e}_{12}$ is a unit vector connecting spins at M1 and M2 sites, Δ and V are the energy difference and the hybridization energy between the p and the d orbital.

Moreover, the same result for the electronic polarization may be independently derived using a phenomenological approach which does not put any restrictions on a crystal lattice symmetry [74]. Let us consider the simplest case of the cubic symmetry for which the electromagnetic coupling term of the thermodynamic potential has the form of

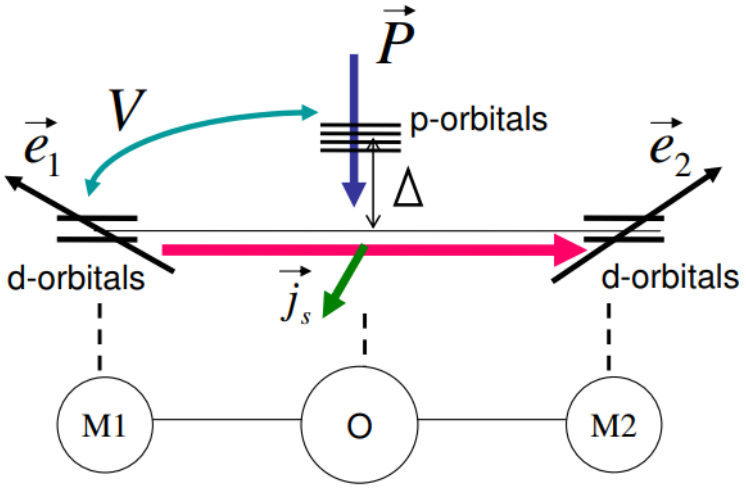

Figure 1.5: Non-collinear spins $\mathbf{e}_1$ and $\mathbf{e}_2$ of magnetic atoms M1 and M2 respectively produce a spin current $\mathbf{j}_s \propto \mathbf{e}_1 \times \mathbf{e}_2$ (green arrow) that drives an electric polarization $\mathbf{P}$ [73].

$$F_{em}(\mathbf{PM}) = \gamma \mathbf{P} \cdot [\mathbf{M}(\nabla \cdot \mathbf{M}) - (\mathbf{M} \cdot \nabla)\mathbf{M} + ...]. \tag{1.14}$$

Considering the system showing no instability towards ferroelectricity in absence of the magnetic ordering, one can keep only quadratic term in the pure electric part of the thermodynamic potential, $F_e(\mathbf{P}) = P^2/2\chi_e$, where χ_e is the dielectric susceptibility, and the variation of $F_e + F_{em}$ with respect to $\mathbf{P}$ provides

$$\mathbf{P} = \gamma \chi_e [(\mathbf{M} \cdot \nabla)\mathbf{M} - \mathbf{M}(\nabla \cdot \mathbf{M})]. \tag{1.15}$$

The magnetization of the SDW state with the propagation vector $\mathbf{Q}$ may be considered as

$$\mathbf{M} = M_1 \mathbf{e}_1 \cos\phi + M_2 \mathbf{e}_2 \sin\phi + M_3 \mathbf{e}_3, \tag{1.16}$$

where ϕ is the phase and $\mathbf{e}_i, i = 1, 2, 3$ are unit vectors in an orthogonal basis. In the case only M_1 or M_2 is non-zero, the SDW state adopts a sinusoidal wave form; if M_1 and $M_2 \neq 0$, the structure is helix with e_3 playing role of a rotation axis; when all three M coefficients are non-zero, the conical structure sets in. Now combining equations 1.15 and 1.16 one can predict the average polarization depending on the type of a spin structure:

$$\bar{\mathbf{P}} = \frac{1}{V} \int d^3x \mathbf{P} = \gamma \chi_e M_1 M_2 [\mathbf{e}_3 \times \mathbf{Q}] \tag{1.17}$$

Regardless to its simplicity, this approach shows some explanatory power, thus it explains the behavior of the $TbMnO_3$ [19]. At $T_S = 41$ K the compound undergoes a magnetic phase transition acquiring a sinusoidal SDW state, and since this ordering doesn't break the inversion symmetry, the equation 1.17 will give zero. However, the polarization is induced at T_H =28 K, when the magnetic structure of the compound changes to a helix with the propagation vector aligned with the $b-$axis and spins rotating in the $bc-$plane. Similar case take place in $Ni_3V_2O_8$ where the high-temperature incommensurate phase is the sinusoidal SDW [75].

Importantly, the spiral spin ordering may be represented as the combination of two non-collinear SDW states with the same propagation vector:

$$\mathbf{M} = M_1\mathbf{e}_1\cos(\mathbf{Q}\cdot\mathbf{x}+\phi_1) + M_2\mathbf{e}_2\cos(\mathbf{Q}\cdot\mathbf{x}+\phi_2). \tag{1.18}$$

In this case the interference between two states will induce a polarization

$$\bar{\mathbf{P}} = \gamma\chi_e M_1 M_2 \sin(\phi_2-\phi_1)[\mathbf{Q}\times[\mathbf{e}_1\times\mathbf{e}_2]]. \tag{1.19}$$

So it is seen that regardless to the microscopic mechanism of ferroelectricity, the direction of the electric polarization defined by equations 1.7, 1.12 and 1.19 is universal and inherent for any incommensurate modulated spin structure. To summarize possible scenarios within the inverse DM and spin current models, the figure 1.6 illustrates various types of incommensurate spin structures with the electric polarization they generate. Obviously if the $\mathbf{e}_{ij}$ vector is parallel to the cross product of spin operators at i-th and j-th sites, the resulting polarization induced by these mechanisms is zero.

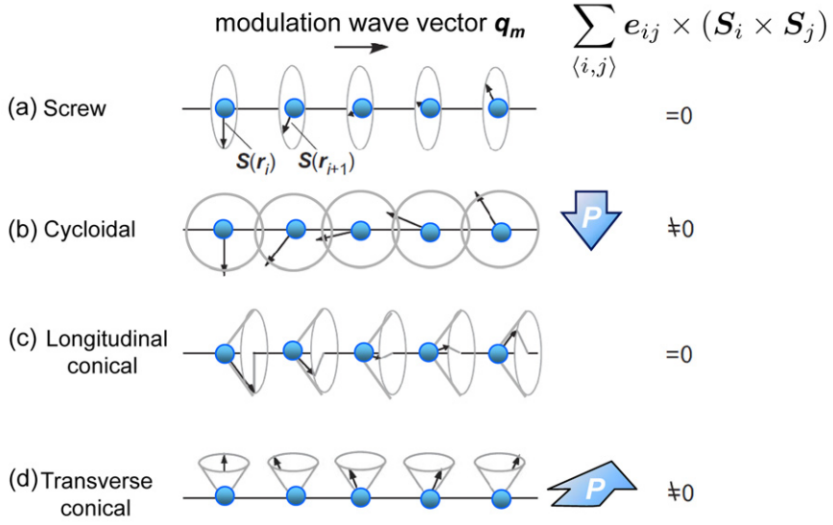

Figure 1.6: Several types of modulated magnetic structures with the corresponding electric polarisation they generate via the inverse Dzyaloshinskii-Moriya or spin current mechanisms [61].

Concerning examples of spiral magnets exhibiting multiferroic properties, one can take perovskite-type manganites $RMnO_3$ (R = Tb, Dy, $Eu_{1-x}Y_x$) as an example: magnetic ground state of this family is often described with a cycloidal spin ordering, which, as it was discussed above, may induce a ferroelectric transition [76, 77, 78]. Normally, when ionic sizes of Mn^{3+} and R atoms are relatively close, the case of $LaMnO_3$, the superexhange interaction between nearest Mn^{3+} spins in the ab-plane (J_1) is of a ferromagnetic nature, whilst the interaction along the $c-$axis is antiferromagnetic [79]. Reducing the size of the R site with Tb^{3+} or Dy^{3+} introduces orthorhombic distortions to the crystal structure, inflecting Mn–O–Mn bonds, that, in turn, modulates the in-plane second-nearest antiferromagnetic interaction J_2 to be of the same magnitude with J_1, causing significant magnetic frustrations. As a result, such crystal structures host long-range incommensurate spin modulations [80]. Similar to the above mentioned $TbMnO_3$, $DyMnO_3$ shows two successive magnetic phase transitions: sinusoidal spin order at $T_N = 41$ K followed by a cycloidal ordering at $T_C = 28$ K [81]. A partial substitution of Eu with Y averages the ionic size at the R site to those of Tb and Dy compounds, leading to the same scenario of magnetic transitions. The direction of polarization in each case fully obeys the one given by the inverse DM or spin current models. The magnitude of an electric polarization is

highly dependent on the cationic composition in this case and varies from P = $384\mu C/m^2$ to P ≈ $1200\mu C/m^2$ $Eu_{1-y}Y_yMnO_3$ for y = 0.9 and 0.4 respectively and P ≈ $600\mu C/m^2$ for Tb or Dy compounds. It was also shown that the spin helicity defined as

$$C = \sum_i \mathbf{S}_i \times \mathbf{S}_{i+1} \tag{1.20}$$

is reversed with the reversal of the electric polarization **P** induced by the applied electric field **E** [82].

In recent years extensive studies have led to the discovery of numerous different compounds possessing incommensurate helimagnetic structures inducing electric polarization where magnetic frustration is the main cause to stabilize such spin structures. Among examples there may be compounds with centrosymmetric nuclear structures like $Ni_3V_2O_8$ ($Cmca$) [75, 83] and $MnWO_4$ ($P2/c$) [84, 85]. In the first case the nuclear structure is a kagome lattice that is frustrated by the definition, while for the latter MnO_6 octahedra form zigzag chains where the frustration comes with the non-negligible exchange interaction of next-nearest-neighbouring magnetic moments. Geometric frustration plays an important role for magnetoelectric coupling in quasi-one-dimensional compounds $LiCu_2O_2$ [86, 87], $LiCuVO_4$ [88, 89] and $CuCl_2$ [90, 91]. The main structural element predetermining magnetism in these systems are chains composed of edge-sharing CuX_4 squares, characterized with ferromagnetic nearest-neighbour interaction and antiferromagnetic interaction between next-nearest-neighbouring Cu^{2+} spins, as a result of this competition, helical magnetic ground state is established at low temperatures. The same kind of competition between ferromagnetic and antiferromagnetic interaction results in the cycloidal-like spin modulation in the CuO in the temperature region between T_{N1} = 230 K and T_{N2} = 213 K [92]. The hallmark of all these compounds lays in the fact that the centrosymmetry of their nuclear structures is locally broken by the magnetic ordering and the emergent electric polarization is consistent with the spin current model. However, magnitudes of polarization in the case of this group of materials are rather low and the highest observed value is P ≈ $100\mu C/m^2$ for $Ni_3V_2O_8$. Remarkably, the spin helicity, and the direction of the electric polarization are also under field-induced control.

Some attention should be also pointed to the fact that even though some modulated magnetic structures don't naturally produce electric polarization in the spin current or inverse DM models, they can be manipulated externally with the magnetic field to do so. An example of such a behaviour is found in hexaferrite compound $Ba_2Mg_2Fe_{12}O_{22}$ [93]. This material demonstrate a set of magnetic phase transitions: collinear ferrimagnetic at T_1 = 553 K followed by a incommensurate proper screw phase at T_2 = 195 K and finally the system enters a longitudinal-conical spin state at T_3 = 50 K. As it is given by the spin current model, the longitudinal-conical magnetic structure cannot produce an electric polarization, however application of a magnetic field to tilt the cone angle from the original c-axis (**q** || c) gives rise to **P** ≈ $80\mu C/m^2$ normal to both the propagation vector **q** and the new cone axis co-aligned with the field.

1.3.2.3 Spin-dependent p-d hybridization mechanism

Spin-orbit interaction may also produce electric dipole between d orbitals of a transition metal ion and p orbitals of a ligand. To demonstrate that, one should consider a cluster consisting of two magnetic cations of a transition metal at **r** and **r+e** sites hybridized through a ligand oxygen anion situated in between them at the position **r+e/2**. A perturbative expansion to a generic $d-$electron configuration with respect to the hybridization

Δ and the charge transfer V between transition metal d and ligands p orbitals will provide the expression of the electric polarization on the bond between sites **r** and **r+e** [94, 95]:

$$\mathbf{P}_{r+1/2} = P^{ms}(\mathbf{m}_r \cdot \mathbf{m}_{r+1})\mathbf{e} + P^{sp}\mathbf{e} \times (\mathbf{m}_r \times \mathbf{m}_{r+1}) + P^{orb}[(\mathbf{e} \cdot \mathbf{m}_r)\mathbf{m}_r - (\mathbf{e} \cdot \mathbf{m}_{e+1/2})\mathbf{m}_{e+1/2}], \quad (1.21)$$

where $\mathbf{m}_r$ is the spin at the **r** site. Here the term $P^{ms} \propto (V/\Delta)^3$ is the magnetostriction, that has no dependence on the spin-orbit interaction, $P^{sp} \propto (\lambda/\Delta)(V/\Delta)^3$ is the spin current term, λ is the spin-orbit interaction energy. The last term $P^{orb} \sim min(\lambda/V, 1)(V/\Delta)$ is the orbital term due to p-d hybridization, found only in systems with partially filled t_{2g} systems and does not depend on the relative orientation of neighbouring $\mathbf{m}_r$ and $\mathbf{m}_{r+1}$ spins. Considering local environment, for each transition metal ion P^{orb} can be expressed in the form of [96]:

$$\mathbf{P} = \sum_i (\mathbf{S} \cdot \mathbf{e}_i)^2 \mathbf{e}_i, \quad (1.22)$$

where sum is taken over all the bonds and the **e** is the vector from the transition metal cation and ligand anions (Fig. 1.7). The mechanism described with the equation 1.13 is called spin-dependent p-d hybridization. The major difference between p-d hybridization and previously described exchange striction or spin current/inverse DM mechanism is that for latter two magnetic sites are required while the p-d hybridization mechanism produces electric polarization with only a single magnetic site.

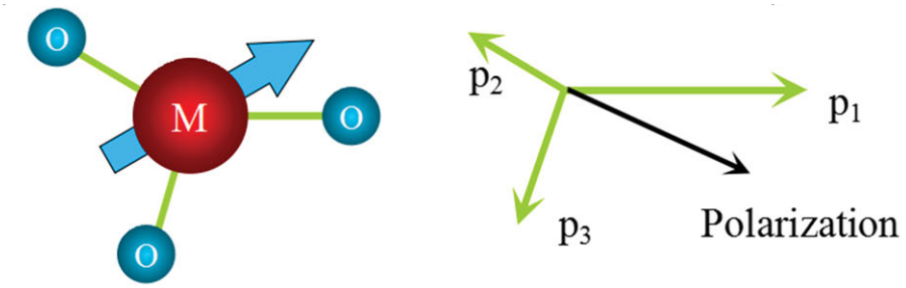

Figure 1.7: Left: a magnetic transition metal cation in the oxygen environment, breaking the inversion symmetry; Right: the net polarization induced by the metal-ligand hybridization [35].

This model nicely describes the multiferroic behaviour of compounds with triangular lattice and proper screw spin structures. Within the spin current model the proper screw can not induce electric polarization since $\mathbf{e}_{ij}$ is co-aligned with the cross product of neighbouring spins ($\mathbf{S}_i \times \mathbf{S}_j$). The simple screw axis is non-polar as it contains 2 and $2'$ axis orthogonal to each other (Fig.1.8a). When such a spin arrangement is hosted by a triangular lattice with $\bar{3}m$ trigonal symmetry of the magnetic site, which is centrosymmetric on its own, the symmetry reduction takes place and the system becomes polar [96]. This may occur in two typical triangular structure types: delafossite and CdI_2. In these compounds transition metal cation layer is adjacent to ligand layers, oxygen in case of delafossites and halogens (X = Cl, Br, I) for CdI_2 structures. As an example one can consider delafossite $CuFeO_2$ that shows several field-induced magnetic phase transitions [97]. Magnetic field of 7 T < H < 14 T applied along the c-axis, develops a proper screw spin order with the wave vector $\mathbf{q}||\langle 110\rangle$, breaking the twofold axis, which, in turn, allows the electric polarization $\mathbf{P}||\mathbf{q}, \mathbf{P} \approx 300\mu C/m^2$(Fig 1.8c). Such a state may be also achieved in zero field

with a partial substitution of Fe^{3+} with non-magnetic Al^{3+} or Ga^{3+} [98, 99]. Remarkably, electric control of spin chirality is also taking place as for multiferroic compounds based on the spin current mechanism [100]. Another possible scenario for the triangular lattices is $\mathbf{P} \perp \mathbf{q}$ in the case of a proper screw magnetic structure with $\mathbf{q}||\langle 1\bar{1}0\rangle$. Such an ordering will keep only an in-plane twofold rotation axis normal to $\mathbf{q}$ unbroken. Neutron diffraction studies confirmed such a spin ordering for the MnI_2, a representative of the CdI_2 structure family [101, 102]. Electric polarization $\mathbf{P} \perp \mathbf{q}$ was observed for MnI_2 ($\mathbf{P} \approx 150\mu C/m^2$) [103] and a similar compound NiI_2 ($\mathbf{P} \approx 50\mu C/m^2$) [104].

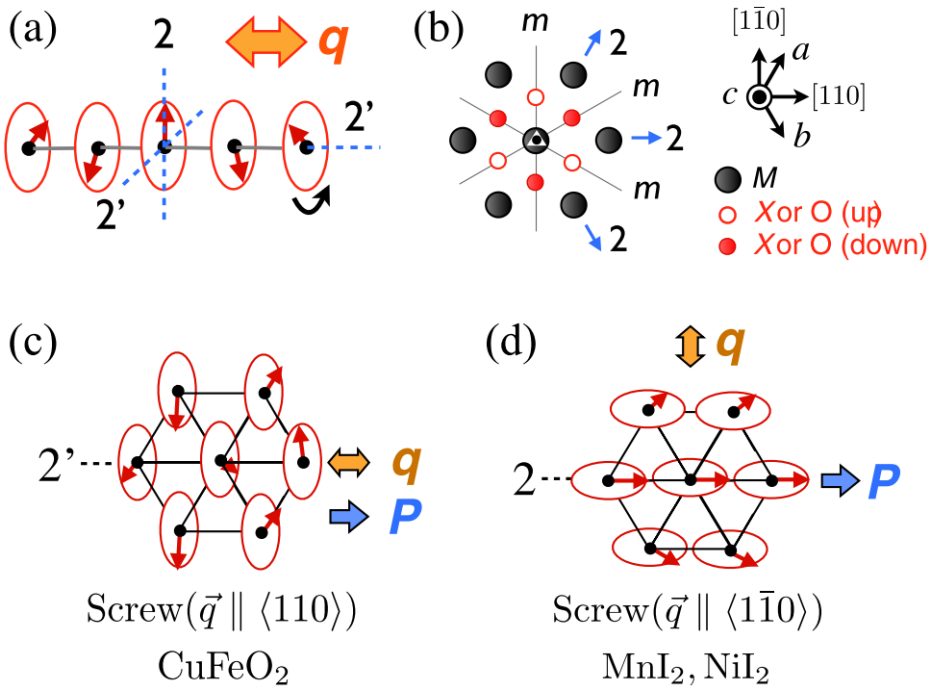

Figure 1.8: a) proper screw spin structure with the propagation vector $\mathbf{q}$ and symmetry elements compatible to it; b) Symmetry elements of the magnetic M site (black circles) in the delafossite or CdI_2 structures. A threefold rotation axis goes along the $c-$axis with the inversion centre (white triangle with the circle), mirror planes (m) and twofold rotation axis (2); crystallographic site symmetry $\bar{3}m$. Open (closed) circles denote the O or X sites lying above (below) the M layer; c) Proper screw magnetic structures and corresponding electric polarization of c) the delafossite $CuFeO_2$ d) MnI_2 and NiI_2 of CdI_2 structure [61].

Another way of inducing electric dipoles via spin dependent p-d hybridization is exploiting non-centrosymmetric lattices. They do not require complex incommensurate spin modulations since very basic collinear ferro- or antiferromagnetic structures are enough to turn an asymmetric but a non-polar crystallographic site into a polar one. An example is found in the Ba_2CoGeO_7, a non-centrosymmetric non-polar tetragonal $P\bar{4}2_1m$ compound with antiferromagnetic structure below $T_N = 6.7$ K [105]. The magnetism is carried by two inequivalent Co^{2+} cations in the tetrahedral oxygen environment. Multiferroic behaviour was found in this compound and the electric polarization is described with the equation 1.22 [106, 107], as the local dipole $\mathbf{p}$ is induced within a single CoO_4 tetrahedron and the polarization is non-zero due to non-centrosymmetric local geometry of Co^{2+} environment. The net polarization is a result of summation of local dipoles of two distinctive magnetic sites and is equal to $\mathbf{P} = 80\mu C/m^2$ at 2 K. One can set the direction of the magnetic moment by applying magnetic field and different resulting relative spin orientation may induce electric polarization of opposite sign (Fig. 1.9b). It was also found that field-

polarized ferromagnetic state under strong **H** || [110] produces electric polarization in a closely related compound $Ba_2MnGe_2O_7$ [108] (**P** $\approx 1\mu C/m^2$ at 2 K). Similar behaviour is shown by CuB_2O_4, a non-centrosymmetric tetragonal antiferromagnet of the same point group $\bar{4}2m$ [109].

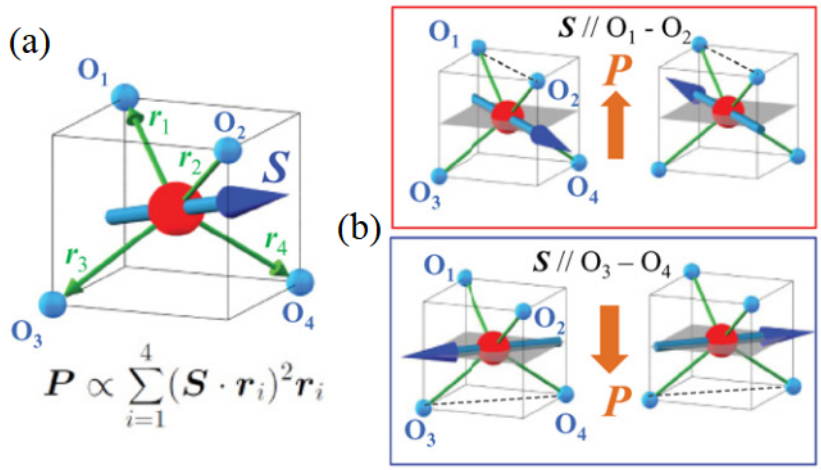

Figure 1.9: a) The coordination of the Co^{2+} cation in the Ba_2CoGeO_7. Local dipole appears as a sum of contributions of four Co-O bonds; b) Relative orientation of Co^{2+} spins and the according electric polarization **P** [108].

The lack of centrosymmetry give rise to the DM interaction that may lead to stabilization of a helical magnetic order. Remarkably, spin chirality of helimagnetics is fixed to the structural chirality, which for instance was found in chiral-structure multiferroic compounds $Ba_3NbFe_3Si_2O_{14}$ [110] and $NdFe_3(^{11}BO_3)_4$ [111]. Some chiral-structure magnets were found to host skyrmions, vortex-like spin textures with a typical size scale between 10 nm to 100 nm [112]. Originally, skyrmions were proposed as a field-theory model in application to nuclear physics, to describe localized particle-like configuration [113], however later it was found that such a model describes perfectly swirling spin textures, that can be also represented as a hybridization of three proper screw spin modulations with the same spin chirality, propagating at 120^o angle with respect to each other. Remarkably, skyrmions can host a spin-driven electric polarization as it was found in Cu_2OSeO_3 [114, 115]. This compound is of a chiral and non-polar cubic $P2_13$ structure, that provides no ferroelectric properties; skyrmion lattice, hosted by Cu_2OSeO_3 are also non-polar as under applied magnetic field it holds a sixfold rotation axis along **H** and orthogonal twofold rotation axis followed by a time reversal normal to **H**. When **H** || [111] most of the symmetry elements of the skyrmion lattice are lost and the system becomes polar with the emergence of the electric polarization **P** || **H** || [111] .

As it is seen, magnetoelectric effect and its special case, multiferroicity, holds a rich plethora of phenomena and in case of multiferroic type-II behaviour each particular system requires special consideration. The great interest to the investigation of such materials is dictated not only by a potential possibility of real-device applications, but mainly due to a fundamental concern of discovering novel compounds hosting unconventional magnetoelectric behavior.

1.4 Motivation to study spinel compounds with complex magnetic structures

Wthin all magnetic model systems spinel compounds $(A)[B_2]X_4$ are one of the most versatile families possessing an extraordinary plethora of magnetic phenomena [116]. A broad multitude of magnetic ground states arises with a chemical variability of these systems: *A*- and *B*-sites are occupied by transition metal cations of different valences and X is oxygen or chalcogens (sulphur, selenium, tellurium). The mineral spinel $MgAl_2O_4$ has a $Fd\bar{3}m$ cubic structure of parameter $a = 8.0625(7)$Å (Fig. 1.10).

The oxygen atoms form a close-packed network where the bivalent cations Mg^{2+} occupy the sites *A* (positions *8a*) corresponding to the tetrahedral sites $[MgO_4]$ and the trivalent cations Al^{3+}, occupy the sites *B* (crystallographic positions *16d*) corresponding to the octahedral sites $[AlO_6]$. All the octahedra $[AlO_6]$ are connected by the edges and form Kagome layers (Fig. 1.10) which are normal to the <111> direction and where reside cavities of a hexagonal section called Kagome window. Each Kagome window is surrounded on both sides by two tetrahedra $[MgO_4]$. When *A*-sites are occupied by M^{n+} cations and *B*-sites by $N^{n'+}$ cations the structure $(M^{n+})[N^{n'+}]_2X_4$ is called normal spinel. If A sites are occupied by $N^{n'+}$ with B sites randomly occupied by M^{n+} and $N^{n'+}$ cations the structure $(N^{n'+})[M_{1-x}^{n+1}N_x^{n'+}]_2X_4$ is called inverse spinel.

In oxides the main combinations of valence states are 2-3 spinels (with divalent M^{2+} and trivalent N^{3+} cations) and 4-2 spinels (with quadrivalent M^{4+} and bivalent N^{2+} cations). Nevertheless, many other valence states combinations are possible which can in certain cases yield to "ordered" spinels. Indeed, the higher the difference in valence states between cations the stronger their tendency to order [117]. When atomic ordering arises on the tetrahedral sites, cations M^{n+} and $N^{n'+}$ will occupy two different *A* and *A′*-sites corresponding to two distinct crystallographic positions of multiplicity m = 4. So the cubic symmetry is so lowered to $F\bar{4}3m$. The following spinels exhibit ordering on the A/A'-sites: $Li_{0.5}Ga_{0.5}Cr_2O_4$, $Li_{0.5}In_{0.5}Cr_2O_4$ [118], $Cu_{0.5}In_{0.5}Cr_2S_4$ [119], and $Fe_{0.5}Cu_{0.5}Cr_2S_4$ [120, 121]. Moreover, the cationic ordering on the *A*- and *A′*-sites should result in the appearance of magnetoelectricity [122].

Cationic ordering may also be obtained on the octahedral sites. Cations M^{n+} and $N^{n'+}$ of different valence states occupy two different *B*- and *B′*- sites corresponding to two distinct crystallographic positions of multiplicity 12 and 4. In that case, the cubic symmetry will be lowered to $P4_332$. For example $LiFe_5O_8$ $(Fe[Li_{0.5}Fe_{1.5}]O_4)$ [123], $Li_{0.5+0.5x}Fe_{2.5-1.5x}Ti_xO_4$ $(0 \leqslant x \leqslant 1.67)$ [124], $Zn[LiNb]O_4$ [125], $Zn[LiSb]O_4$, and $Fe[Li_{0.5}Fe_{1.5}]O_4$ [126] are spinels with cationic ordering on the B/B'-sites.

Spinel compounds played an important role in the evolution of general ideas in the field of solid state magnetism, particularly Louis Néel introduced ferrimagnetism as a type of cooperative magnetization with an example of ferrite compounds MFe_2O_4, where M is a metallic atom [127, 128]. Since spinel compounds are built of two substructures, A and B, the most simple magnetic Hamiltonian can be written as

$$\hat{H} = \sum_{x,y=A,B} J_{x,y} \sum_{i,j} (\hat{S}_i \cdot \hat{S}_j), \tag{1.23}$$

where the first sum refers to the nature of the exchange interaction: inter- or intra-substructure and the second one is taken over the neighbouring pairs of spins within the given exchange pathway. Thus, in the major part of cases concerning spinel compounds, the magnetic ground state is defined by the interplay between intra-substructure J_{AA} and J_{BB} and inter-sublattice J_{AB} exchange interactions.

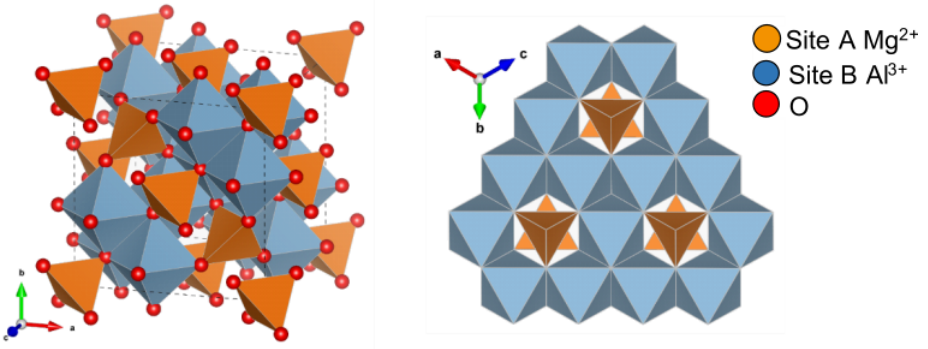

Figure 1.10: On the left: The crystal structure of the original spinel mineral, $MgAl_2O_4$. Magnesium cations caged in tetrahedral oxygen environment whereas aluminum cations are surrounded by eight oxygen atoms that form an octahedral environment. On the right: the projection of the structure along the [111] direction representing the polyhedron arrangement. Remarkably, edge-sharing octahedra form a Kagome layer.

One can exclude J_{AA} and J_{AB} terms from the equation 1.23 by simply filling A-sites with non-magnetic ions entirely. Spin-lattice coupling mechanisms can be examined within chromite spinels ACr_2O_4 and remarkably different magnetically neutral A-sites cations yield different types of magnetic order and lattice distortions associated with them. Neutron and synchrotron studies revealed that low temperature crystal symmetry of $CdCr_2O_4$ is tetragonal $I4_1/amd$ and the magnetic structure is an incommensurate antiferromagnet with the propagation vector $\mathbf{k} = (0, \delta, 1)$ [129], Zn compound undergoes tetragonal distortion to $I\bar{4}m2$ space group with a magnetic structure that can be described with two wavevectors $\mathbf{k}_1 = (0.5, 0.5, 0)$ and $\mathbf{k}_2 = (1, 0, 0.5)$ [130] and Hg as the magnetically neutral A-site cation leads to an orthorhombic $Fddd$ structure with two characteristic k-vectors $\mathbf{k}_1 = (1, 0, 0)$ and $\mathbf{k}_2 = (0.5, 0, 1)$ [131]. Other examples are spinel vanadates AV_2O_4 with A = Zn, Cd, Mg whose orbital degeneracy makes them perfect model systems for studying orbital ordering in frustrated antiferromagnets. Unlike chromites these compounds exhibit two phase transitions upon cooling: the first one is lifting orbital degeneracy by distorting of VO_6 octahedra and the second one is a magnetic phase transition [132, 133, 134]. Also complex magnetic orderings possessed by spinel compounds of this type can lead to emergence of unusual magnetic phenomena, such as gapless pseudo-Goldstone magnon exitations in the incommensurate magnetic phase of $ZnCr_2Se_4$ with the $\mathbf{k}$ $(0, 0, 0.44)$ [135, 136].

Magnetic behaviour gets more complicated when both A and B sites are occupied by magnetically active cations. The FeV_2O_4 spinel containing Fe^{2+} $(3d^6)$ with a high-spin $S = 2$ and two-fold orbital degeneracy goes through a series of structural transitions: $Fd\bar{3}m \rightarrow I4_1/amd \rightarrow Fddd \rightarrow I4_1/amd$. The second structural phase transition is accompanied by the magnetic phase transition into a collinear ferrimagnetic structure. Transition to the low-temperature orthorhombic phase drives Fe^{2+} spins inclination so they adopt a two-in-two-out configuration [137]. Another vanadate compound is MnV_2O_4 with a manganese having a high-spin configuration $S = 5/2$ $(3d^5)$ with quenched angular moment shows two sucessive magnetic phase transitions: a collinear ferrimagnetic with $\mathbf{k} = (0, 0, 0)$ first, and the second is a noncollinear state with an antiferromagnetic component in the ab plane that goes along with the structural phase transition to an orbitally ordered $I4_1/a$ tetragonal phase [138]. A rather simple case is found in the $NiCr_2O_4$ compound that is distorted into a tetragonal lattice below 310 K and becomes an orthorombic $Fddd$ at low temperatures. The ground state, in this case, is a collinear ferrimagnetic [139]. Generally, it has to be pointed out that that the B-site cations form a so-called pyrochlore structure

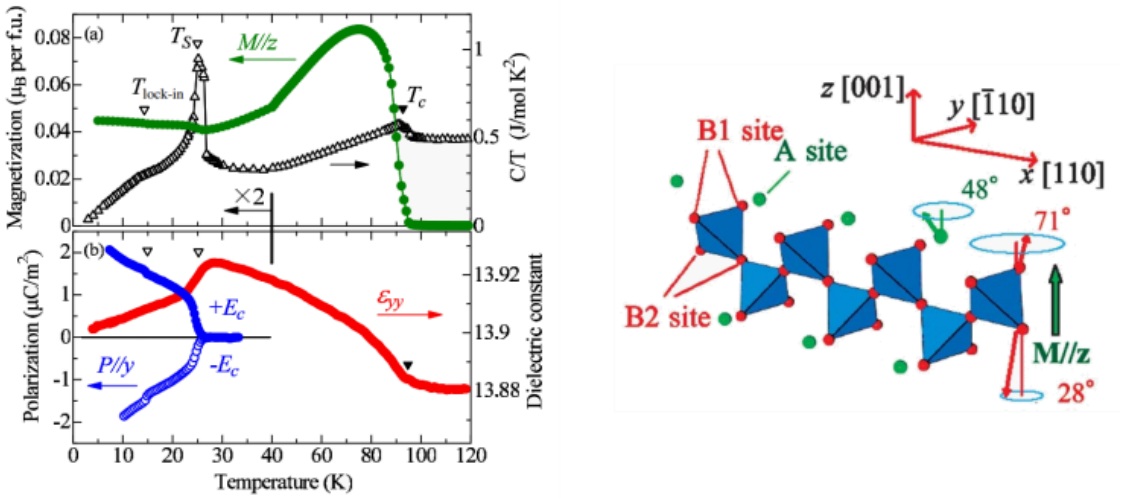

Figure 1.11: On the left: Macroscopic characteristics of $CoCr_2O_4$. Temperature evolution of a) magnetization **M** and specific heat divided by temperature (C/T), and b) dielectric constant measured along y direction at a frequency of 10 kHz and the induced electric polarization along y axis (|| [1̄10]). On the right: magnetic structure of $CoCr_2O_4$ [144].

well-known to hold geometric frustration [116].

However, for non-negligible J_{AA} and J_{BB} interactions some exotic ground states could be found. LKDM theory (Lyons, Kaplan, Dwight, Menyuk) [140, 141, 142] which is considering Heisenberg exchange interactions between nearest-neighbouring cations claims that the ground state of cubic spinel phases is completely described by the single parameter

$$u = \frac{4\, J_{BB}\, |\mu_B|}{3\, J_{AB}\, |\mu_A|}, \tag{1.24}$$

where μ_A and μ_B are magnetic moments of cations occupying A- and B-sites respectively. For $u \leqslant 8/9$ the spin structure adopts the Néel configuration which is represented by parallel orientation of A-site magnetic moments with respect to each other and antiparallel with respect to B-site. For larger values of u it was demonstrated that the lowest energy spin configuration is the so-called ferrimagnetic spin spiral state. Indeed neutron powder diffraction has proved these predictions. Such behaviour was found in $MnCr_2O_4$ ($u = 1.5$) that has two magnetic phase transitions: at $43K$ intensities of fundamental reflections show a strong enhancement indicating a transition to a ferrimagnetic state, and at T = 18 K a set of satellite reflections appears, which can be described with a ferrimagnetic conical structure with a satisfactory agreement [143].

To describe such a magnetic behaviour let us have a closer consideration of another chromate, $CoCr_2O_4$ ($u = 2$), that possess similar features. At room temperature $CoCr_2O_4$ has a cubic $Fd\bar{3}m$ structure with the cell parameter $a = 8.3294$Å [145]. Temperature variation of magnetization together with the specific heat (Fig. 1.11) show three distinct transitions at 93 K, 27 K and 13 K [144, 146]. This results lay in agreement with the neutron powder diffraction measurements [147] that reveal a clear gain in intensity of fundamental nuclear reflections below $T_C = 93K$ that occur as a consequence of a paramagnetic-ferrimagnetic phase transition. At $T_S = 27K$ NPD pattern display the emergence of a set of satellite reflections arising from an incommensurate magnetic phase. Ferrimagnetic spiral structure with a spin modulation propagating along [110] direction and the cone axis along [001] direction predicted by LKDM theory provided a

nice agreement with experimental observations. Later, this result was proved by neutron single crystal diffraction experiment that confirmed the presence of the propagation vector $\mathbf{k} = (\delta, \delta, 0)$ with $\delta = 0.626 \pm 0.009$ at 8 K [139]. The magnetic structure can be divided in three sublattices: a single A-site and two B-sites, Co^{2+} and Cr^{3+} are assumed to have spin-only magnetic moments of $3\mu_B$ (1.11). LKDM theory also predicts that for $u \geqslant 1.298$ long-range ferrimagnetic spiral configurations are locally unstable. In case of $CoCr_2O_4$ with $u = 2$ this instability arises from a weak magnetic geometrical frustration (MGF) due to equal magnitude of magnetic moments at tetrahedral and octahedral sites causes a spiral short-range order that results into a reentrant-spin-glass-like behaviour below $T_{lock-in} = 13K$.

On the side of the electronic subsystem $CoCr_2O_4$ also shows quite a rich picture. On cooling, dielectric constant reaches maximum at T_S that coincides with an emergence of electric polarization (1.11). Remarkably there is no structural phase transition down to the lowest temperatures and the nuclear structure remains $Fd\bar{3}m$ so the centrosymmetry is locally broken by the ferrimagnetic spiral ordering that drives the electric polarization to occur along the $[\bar{1}10]$ direction, which is in agreement with the spin current model (paragraph 1.3.2.2). Therefore $CoCr_2O_4$ is a type-II multiferroic compound. The magnitude of polarization $\mathbf{P} \sim 2\mu C/m^2$ is significantly lower than those exhibited by systems with the similar magnetic origin of electric polarization, by 2-3 orders of magnitude in comparison to $RMnO_3$ [77] and RMn_2O_5 [21]. However, the polarization itself shows curious behaviour under external stimuli. It was shown that the magnitude and direction of $\mathbf{P}$ is strongly dependent on the magnitude and sign of magnetic field applied along [001] direction. Moreover $\mathbf{P}$ exhibits full field-induced reversal signifying a robust magnetoelectric coupling in the system [144]. Furthermore, the sign of polarization in $CoCr_2O_4$ can be changed thermally: $\mathbf{P}$ flops abruptly from $2\mu C/m^2$ to $-2\mu C/m^2$ at $T_{lock-in}$ without the change of handedness or the $\mathbf{k}$ vector of the spiral modulation due to the change in magnitudes of electric dipole moments of $Co - Cr$ and $Cr - Cr$ bonds that have opposite signs of spin-orbit interaction [148].

At the same time, polarization in $CoCr_2O_4$ can be manipulated internally, by varying the chemical composition. It was demonstrated that admixing of non-magnetic d^{10} cations to the system at A-sites leads to a suppression of the spiral spin ordering. Introduction of Zn^{2+} alters the magnetism in the system to adopt frustrated antiferromagnetic behaviour that does not give rise to electric polarization (1.12) [150]. On the contrary a magnetic dilution on the B-site may drive an opposite effect. Magnetically inactive Co^{3+} cations at Cr^{3+} sublattice are likely to reduce the negative polarization and magnetization contribution of the B-site cations. That enhance both saturated electric polarization and magnetization under applied field with an increase of amount of magneto-diluting agent [149].

Thereby one can formulate a potential recipe for a type-II multiferroic compound that may possess some intriguing ferroelectric properties. First, it should be a cubic spinel that contains magnetic cations of the same or close magnitudes of magnetic moments at A- and B- sites to stabilize a long-range ferrimagnetic spiral structure. Second, there must be some room for a B-site magnetic dilution that can potentially boost up ferroelectric performance of the system.

Among the spinel compounds, Kasper reported in 1967 the synthesis of Co_5TeO_8, $CoZn_4TeO_8$ and $NiZn_4TeO_8$ phases with primitive cubic superstructure [151]. None of nuclear structures were published but it was assumed that the Te^{6+} cations can only occupy octahedral sites with the following formula $[(Co_2)[Co_3Te]O_8$. Since Co^{2+} and Te^{6+} have different valences and sizes it's possible to get an ordered Kagome layers (Fig.1.10)

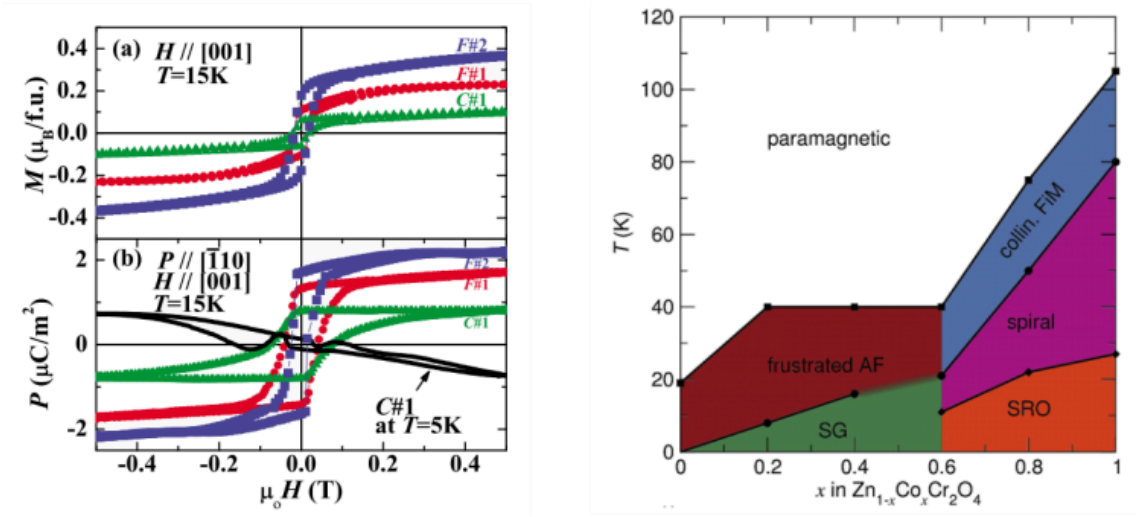

Figure 1.12: On the left: Magnetic field dependence of a) Magnetization along [001] direction b) Polarization along [$\bar{1}$10] direction measured at T = 15 K for $Co(Cr_{2-x}Co_x)O_4$. C#1, F#1 and F#2 denotes x = 0.0, 0.14 and 0.18 respectively [149]
. On the right: magnetic phase diagram of a $Zn_{1-x}Co_xCr_2O_4$ family. Following acronyms stand for AF - antiferromagnetism, FiM - ferrimagnetism, SG - spin-glass, SRO - short-range ordering [150].

with Te^{6+} and Co^{2+} cations both in octahedral environment but occupying two different crystallographic sites. Later, Rodriguez-Carvajal publish a first neutron diffraction study of Co_5TeO_8 [152]. He reported the presence of a first transition below 60 K with strong diffuse scattering that develops around the reflection (111). Then at lower temperature, the diffuse scattering condenses in satellites reflections corresponding to an incommensurate magnetic structure with a propagation vector $\mathbf{k} = (0, 0, \delta)$ with $\delta = 0.08$ at 30 K. On cooling, δ becomes smaller and the correlation length increases (reflection sharpening). Below 4.2 K, the magnetic ground state approximates a conventional ferrimagnetic state. Thus, it appears that the magnetic behaviour of Co_5TeO_8 resembles that of the spinel phase $CoCr_2O_4$. Since no magnetic measurements and no nuclear or magnetic structure of Co_5TeO_8 have been published, we have decided to re-examine this compound and the series $Co_{5-x}Zn_xTeO_8$, which are serious candidates to type II multiferroic materials.

Chapter 2

Methods

In the present chapter, a general overview on experimental and theoretical methods used within the scope of the current research will be given. The first part is dedicated to sample preparation techniques, the second part touches upon experimental methods and data acquisition and the last part is covering some aspects of data analysis.

2.1 Sample preparation

All the samples discussed below were exclusively synthesised for the current research project in both polycrystalline and single crystal forms, which makes sample preparation an essential part of the work. This section will outline the basic principles of sample preparation methods, however precise details will be provided in corresponding sections for each family of materials.

2.1.1 Solid-state reactions method

Solid-state reactions is the most common and widely used synthesis technique for polycrystalline inorganic sample preparation. This method employs a thermal-driven interdiffusion of two or more non- or low-volatile solids heated up below their melting point. For this type of preparation reactants of appropriate amount were first thoroughly grinded with agate mortar and pestle to achieve high homogeneity of the initial mixture of precursors. Mechanical grinding is also increasing the effective surface area of grains that enhances the quality of the synthesis. The prepared mixture is then placed in non-reactive container, namely platinum crucibles which melting point is 2041.5 K. The synthesis itself is carried out in horizontal tube furnaces under an atmosphere of N_2 gas to prevent oxidation to higher oxidation states. With all its simplicity solid state reaction method requires relatively high temperatures and significant amount of preparation time. The first is dictated by large lattice energy that should be overcome in order to initiate cationic diffusion in solids, and the second again is related to specificity of solid state in which the diffusion rate is generally slow. This process may be iterative and require several cycles of thermal treatment with subsequent regrinding of the product for homogenization.

2.1.2 Chemical vapour transport method

Chemical vapour transport (CVT) reactions were originally proposed by Harald Schafer in 1956 [153] and aims at crystallization of a large variety of chemical products: pure elements, halides, chalcogenides, oxides, sulfides, selenides, tellurides, pnictides, intermetallic phases and others. The method itself lies in the transportation of a condensed phase via

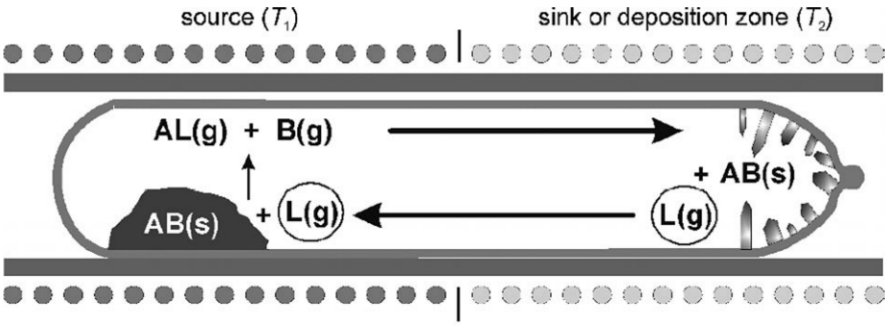

Figure 2.1: Schematic illustration of a vapour transport process inside of the ampoule in the temperature gradient of a two-zone furnace. A transport agent L(g) reacts with the precursor solid AB to form the transport gas species AL(g) and B(g) that are driven to the deposit zone [154].

transport agent in a presence of a temperature gradient. The process of CVT synthesis is schematically described in the 2.1 section. An evacuated and sealed silica tube containing initial precursors mixed with a transport agent is placed into a two-zone furnace in a way that the side of the tube accommodating the initial mixture is placed in the "hot" zone of the furnace whereas the empty side of the tube is located at the "cold" zone. Temperature difference between two zones together with the transport agent provokes a gas flow inside of the tube that induces chemical reactions. The process of synthesis can be split in three major steps [154]:

1. Forward reaction. At this step the transport agent reacts with condensed phases of precursors.
2. Gas flow that circulates evaporated phases.
3. Back reaction which is essentially a deposition of the condensed phase with the release of the transport agent. Nucleation and the crystal growth are taking place at this step.

Each class of materials require special synthesis conditions that put special demands over temperature regime, pressure inside of the tube and nature of the transport agent. CVT reactions are taking place in a wide range of internal pressure between 10^{-3} bar to 3 bar and needs rather high temperatures: 300 - 1000 °C. Concerning transport agents the most common ones are chlorine and iodine compounds: Cl_2, HCl, $TeCl_4$, $NbCl_5$, $PtCl_2$, I_2, HgI_2.

2.2 Sample characterization

2.2.1 Laboratory techniques

2.2.1.1 Magnetometry

Magnetometry is the first-step technique in characterizing magnetic behaviour of a given material and represents measurements of macroscopic magnetization M of the sample as the function of magnetic field or temperature. There are numerous experimental realizations for such measurements, however the most precise and accurate are techniques based on superconducting quantum interference devices (SQUID) [155].

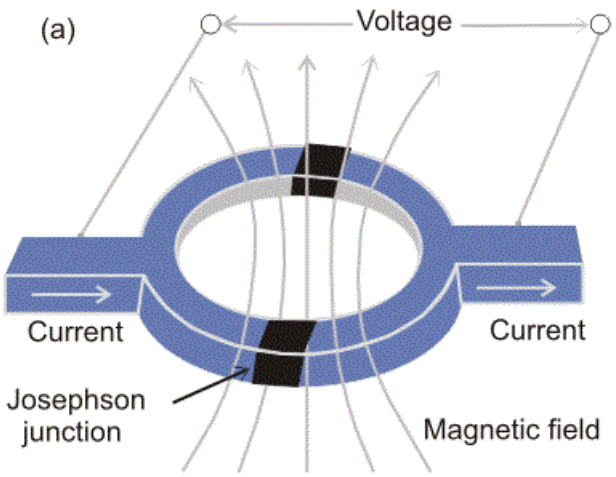

Figure 2.2: Dual-junction SQUID loop scheme [155].

SQUID is essentially a superconducting loop containing one or two Josephson junctions (figure 2.2) that exploits the fact that the magnetic flux in the ring is quantized and exist only as multiples of the flux quantum $\Phi_0 = 2.068 \times 10^{-15}$Wb. Which means that for a ring of an area 1 cm^2 the field inside the ring will have discrete steps of $\Phi_0 = 2.068 \times 10^{-11}$T. This allows SQUID devices to detect magnetic fields with an extraordinary precision [156]. Cooper pairs, driven by the biasing current are tunneling through the junctions, however the flow can be alternated by a magnetic field that is applied to the ring. This in turn changes a phase difference across each of two junctions that affects the critical current of the SQUID. This change in magnetic field drives the oscillation of the critical current. Monitoring the change in voltage provides a possibility to assess the magnetic flux that has been coupled into the SQUID loop.

A basic SQUID setup is illustrated in figure 2.3. The sample placed inside of a plastic straw attached to a sample holder that moves the sample through the set of detection coils in discrete steps. This movement induces a change of the flux in the detection coils and hence leads to the change of the current in the SQUID circuit. The magnetic moment is then determined by the shape of the SQUID voltage collected as a function of the sample position inside the gradiometer. It is also worth mentioning that SQUID can be operated in AC and DC modes. DC magnetic measurements determine magnetization of the sample at the equilibrium state whereas the AC measurements can provide an information on magnetization dynamics. In the case of AC measurements an applied AC magnetic field induces a time-dependent magnetic moment in the sample. The AC measurement is capable of detecting subtle changes in the value of $M(H)$, so this technique can resolve small changes in magnetic behaviour of the sample even with the presence of a large magnetic moment.

One can perform two types of magnetic measurements: magnetization at constant temperature as a function of applied field $\mathbf{M}(H)$ and magnetization at constant field as a function of temperature $\mathbf{M}(T)$. The behaviour of this two functions can provide an important insights into the microscopic nature of the studied material. Another important inherent characteristic of magnetic materials is the magnetic susceptibility χ that represents the linear response of a material to an applied magnetic field:

$$\mathbf{M} = \chi \mathbf{H} \tag{2.1}$$

In case of purely paramagnetic materials magnetization and applied magnetic field are

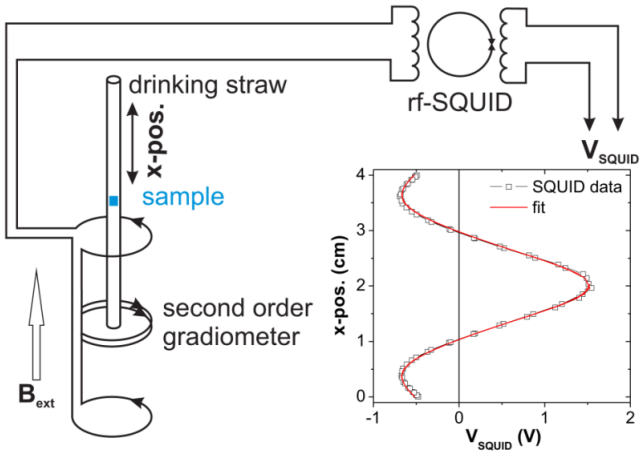

Figure 2.3: A setup of a SQUID magnetometer. The inset demonstrates the change of a voltage as a function of the sample position inside the detection coil [157].

coupled linearly and this dependence is given by the Curie law, that can be expressed as

$$\chi(T) = \frac{C}{T} \tag{2.2}$$

where C is the Curie constant

$$C = \frac{\mu_0 \mu_B^2}{3k_B} N g^2 J(J+1), \tag{2.3}$$

here N is the number of magnetic atoms per unit volume, g is the g-factor and J is an angular momentum quantum number.

Combining equations 2.2 and 2.3 together one can obtain a simple numerical equation for the effective magnetic moment:

$$\mu_{eff} = 2.282\sqrt{C} \tag{2.4}$$

In case of interacting moments systems one should apply Curie-Weiss law to describe the temperature evolution of magnetic susceptibility:

$$\chi(T) = \frac{C}{T - T_c} \tag{2.5}$$

where T_c is the Curie temperature, a point below which the energy of magnetic interactions overcomes the energy of thermal fluctuations and atomic spins become ordered. However equation 2.5 describes the behaviour of $\chi(T)$ only above the Curie temperature, the law is then applicable in the paramagnetic state ($T \gg T_c$) with the T_c replaced by Θ - Weiss temperature. Below the ordering temperature the susceptibility is not well-defined because the dependence of M/H is non-linear and depends on both the applied magnetic field and the characteristics of the magnetic structure. Whereas the $\chi(T)$ plot may pinpoint temperatures of magnetic phase transitions, $1/\chi(T)$ dependence can help to specify the predominant type of magnetic interactions of the studied system. A linear approximation of the paramagnetic part of the inverse susceptibility will provide C as an inverse of the slope of the linear part of $1/\chi(T)$ plot and the Weiss temperature is given by the intersection with abscissa. Hereby the Weiss temperature is a key characteristic

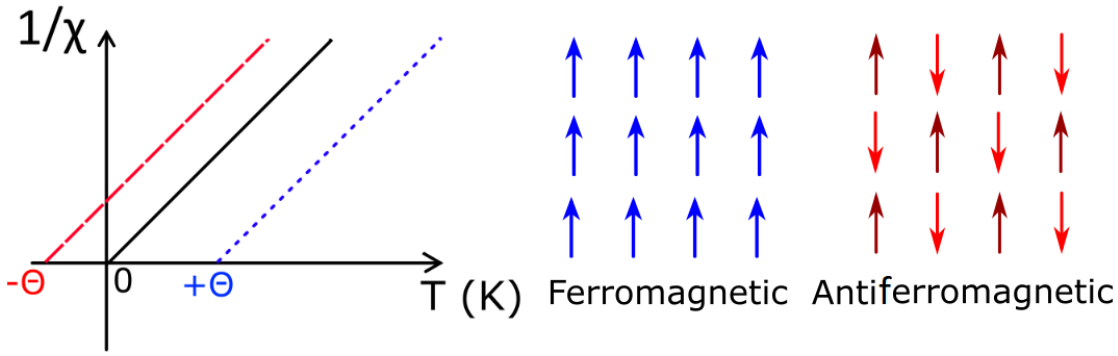

Figure 2.4: Three extreme scenarios for the Curie-Weiss behaviour plotted for a simple Bravais lattice as a temperature variance of the inverse susceptibility. The positive value of Θ (in blue) is given by parallel spin alignment and the negative Θ values (in red) are due to an antiparallel spin correlation in the studied compound.

extracted from such a lay out: if $\Theta > 0$ predominant interactions in the material are ferromagnetic, if $\Theta < 0$ - predominant interactions are antiferromagnet. In case if material clearly shows magnetic transitions but $\Theta \approx 0$ - there is a delicate balance between ferro- and antiferromagnetic type of interactions (Figure 2.4).

2.2.1.2 Dielectric measurements

A knowledge of the response to an electromagnetic field is crucial for understanding properties of ferroelectric materials. Dielectric spectroscopy is a method to study the permittivity of a system at a fixed or changing frequency. Dielectric spectroscopy provides information about storage properties of a capacitor and is widely used to characterize electrochemical systems. Generally, it is sensitive to the presence of polarization and relaxation processes and thereby can help to identify ferroelectric transitions [158].

This type of measurements are aimed to retrieve the relative permittivity of a material ϵ_r which sets the relationship between the electric displacement field $\mathbf{D}$ caused by an applied electric field $\mathbf{E}$

$$\mathbf{D} = \epsilon\mathbf{E} = \epsilon_r\epsilon_0\mathbf{E} \tag{2.6}$$

where ϵ_0 is the vacuum permittivity. The relative permittivity depends on the frequency of the applied field:

$$\epsilon_r(\omega) = \epsilon_r'(\omega) - i\epsilon_r''(\omega) \tag{2.7}$$

and in the general case, is a dimensionless complex number that describes the interaction between a material and an applied electric field. In the equation 2.7 ϵ_r' and ϵ_r'' are real and imaginary parts of the relative permittivity respectively. The real part ϵ_r' represents how much energy is stored and associated with materials capacitance; ϵ_r' is often referred as dielectric constant which may be confusing as, in general, this value is not constant and depends on the temperature and the frequency of the applied electric field. The imaginary part ϵ_r'' represents energy dissipation and called dielectric losses.

A commercial AG4284A LCR meter was used for complex impedance measurements allowing to retrieve values of dielectric constants of the studied materials. A special four-coaxial-cable sample holder that allows controlling the magnetic field inside of a Quantum

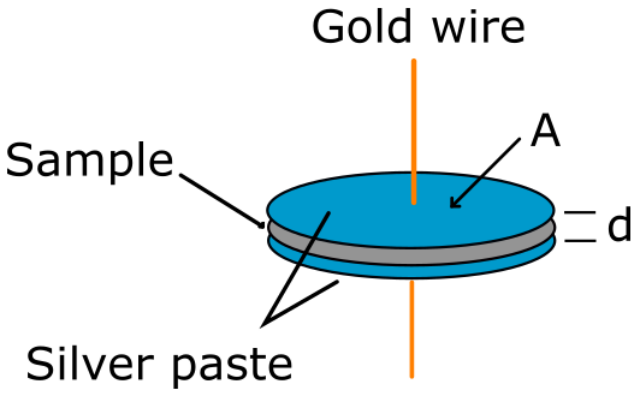

Figure 2.5: A parallel capacitor used for dielectric spectroscopy measurements

Design PPMS was used. During the measurements an AC voltage of 1 V was applied to the sample, frequencies of the voltage varied in between 100 and 500 kHz. To exclude possible frequency and amplitude dependence of results, a systematic check was performed. Frequency dependence of the complex impedance allows to represent the sample as a circuit of a parallel-connected capacitor and a resistance, so the dielectric constant is derived from the capacitance value by using the sample dimensions.

All dielectric measurements were performed using a parallel plate geometry (fig. 2.5). The studied samples, single crystals of plate-like sintered powder pellets, were placed between two golden wires ($25\mu m$) attached to the sample using silver epoxy (EPOTEK H2OE), which covers top and bottom parallel faces of the sample to form a capacitor. The dielectric constant in this case is given by the following formula:

$$\epsilon_r' = \frac{d\ C_p}{A\ \epsilon_0} \tag{2.8}$$

where C_p and d - are the capacitance and the thickness of the sample, A - is the surface area of the electrode and ϵ_0 is the permittivity of the vacuum.

2.2.2 Neutron and X-ray scattering

Neutron and X-ray scattering allow to investigate structural properties of materials at the atomic level. While X-ray diffraction was used for structural characterization of the studied materials, the major part of the present work, dedicated to understanding the microscopic mechanisms of magnetic behaviour, was carried out via neutron scattering techniques. Neutron properties, and the possibility to manipulate them, makes neutron scattering almost the ideal probe to study magnetism on a wide range of inter-atomic distances and energy scale.

2.2.2.1 Basic neutron properties and neutron production

All possible neutron applications and their limitations are of course defined by the properties of the neutron itself. From particle physics it is known that the neutron is a composite particle that is built up of one up and two down quarks, carrying charges 1/3 and -2/3 respectively, so the resulting charge is equal to 0. The absence of charge determines the way neutron interacts with the matter: since there is no Coulomb potential to overcome neutrons are scattered via nuclear forces. Nuclei in a scattering process act like point-like objects. Thus, the neutron cross section is not monotonous with the atomic number, like

in the case of X-rays, but depends on the internal structure of nuclei and has no regular dependence on Z. That, in turn could provide a better contrast for studying elements lying close in the periodic table. Zero charge also conditions a deeper penetration length of neutrons in comparison to photons.

Table 2.1: Properties of the neutron

mass	$\mathrm{m} = 1.657 \times 10^{-27} kg$
charge	0 e
spin	$\frac{1}{2}$
magnetic moment	$\mu = 1.913 \mu_N$
life time	$\tau = 888 \pm 3s$

One should keep in mind that neutrons are microscopic objects that obey laws of quantum mechanics, so, as all other particles, neutrons are described in terms of particle-wave duality. Essentially, this means that the neutron with speed v and mass m can be also described as a de Broglie wave with wavelength:

$$\lambda = \frac{2\pi\hbar}{mv}, \tag{2.9}$$

so the corresponding wavenumber is:

$$k = \frac{2\pi}{\lambda}, \tag{2.10}$$

which can be also written in vector form and has the same direction as the speed $\mathbf{v}$. And the momentum of neutron is then:

$$\mathbf{p} = \hbar\mathbf{k}. \tag{2.11}$$

The kinetic energy of a neutron can be expressed in several different manners:

$$E = \frac{mv^2}{2} = k_B T = \frac{h^2}{2m\lambda^2} = \frac{\hbar^2 k^2}{2m}, \tag{2.12}$$

where $k_B T$ refers to the fact that the energy distribution of neutrons nicely follows Maxwellian statistics. Consequently, the energy of a free neutron can be moderated by media, which is always used to tailor beams with the right parameters for a particular experiment. The table 2.2 shows typical parameters of neutrons produced by sources of various temperatures pointing out features of high importance. Depending on initial conditions, neutrons could be produced with wavelengths of the same order of interatomic distances in condensed matter or even higher. This allows to study the structure of materials at the angstrom and nanometer scale. Moreover, energies of cold and thermal neutrons correspond to energies of excitations found in solids. Thus, a neutron of such energies could create or annihilate an exited state. So a precise knowledge of the energy of neutrons before and after a scattering event could provide insights on interatomic forces of a studied material [159].

There is no experimental evidence of electric charge of the neutron to be larger than $(-2 \pm 8) \times 10^{-22} e$ [160], an internal charge distribution caused by neutron structure leads to the fact that neutron has a magnetic moment. This means that each single neutron represents a microscopic magnet which can interact with local magnetic fields produced by

Table 2.2: Typical values of neutron energy and wavelength for different source temperatures

Source type	**Temperature** T, K	**Energy** E, meV	**Wavelength** $\lambda, Å$
Cold	1 - 110	0.1 - 10	30 - 3
Thermal	60 - 1000	5 - 100	4 - 1
Hot	1000 - 6000	100- 500	1 - 0.4

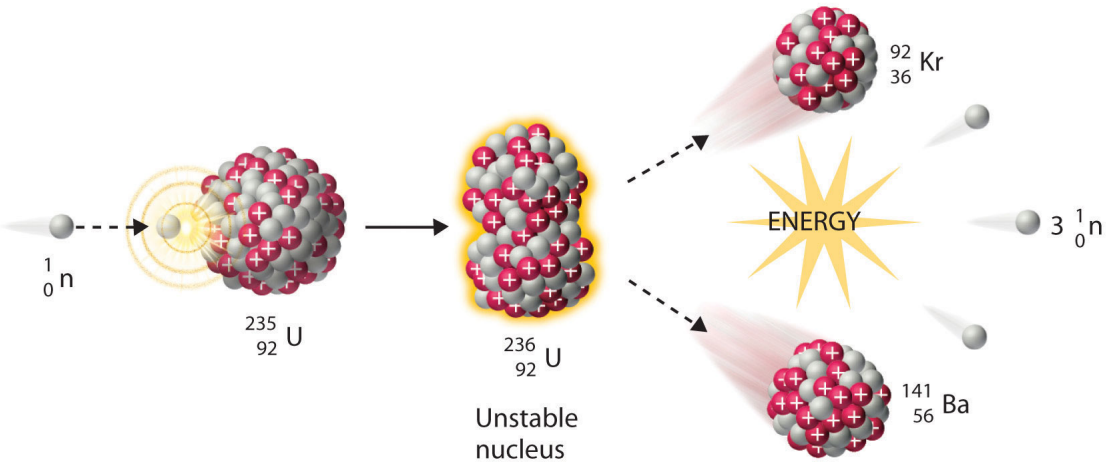

Figure 2.6: A fission reaction. Neutron is captured by 235^{U} nucleus which splits into to fragments with release of a few neutrons with energies around 1 MeV

unpaired electrons of magnetic atoms, thereby it is also possible to study spatial distribution of electronic spins and magnetic excitations. Furthermore, the possibility to polarize neutrons, and to manipulate this polarization, opens up opportunities of studying chiral magnetic structures and disordered magnetic phases.

There are two methods of neutron production for scattering experiments, fission which is used in nuclear reactors and spallation that is exploited at sources based on particle accelerators.

Nuclear reactors provide a constant flux of neutrons and, due to that, are often referred as continuous sources. Fission which happens in a reactor core is a process of neutron capture by ^{235}U. In this reaction a highly exited unstable nucleus splits into two medium-heavy elements, for instance:

$$^{1}_{0}\mathrm{n} + ^{235}_{92}\mathrm{U} \rightarrow ^{92}_{36}\mathrm{Kr} + ^{141}_{56}\mathrm{Ba} + 3^{1}_{0}\mathrm{n}, \tag{2.13}$$

Each reaction produces 2 to 3 neutrons, 1.5 of which on average is used to maintain the chain reaction and roughly 200 MeV of heat energy that should be cooled away. Thus, each event of fission reaction provides one neutron that typically has a kinetic energy of 2 MeV and can be moderated and delivered to instruments. For purposes of a neutron scattering experiment, the most important reactor parameter is of course the flux density: the number of neutrons per time unit and area. For instance, the high flux-reactor of the Institut Laue-Langevin has a flux density of $1.5 \times 10^{15} n \cdot cm^{-2} \cdot s^{-1}$.

The second technical solution for neutron production is bombarding heavy-element

target like mercury, tantalum or lead, with high-energy protons with a typical energy of 1 GeV [161], thus, one of the basic parts of every spallation source is proton accelerator. In the existing spallation neutron sources there is no unified approach for proton acceleration and different facilities use different types of accelerators: a linear accelerator (European Spallation Source, Lund, Sweden), a combination of linac and synchrotron (ISIS neutron source, Oxfordshire, United Kingdom) or cyclotron (Paul Scherrer Institute, Villigen, Switzerland). As a result of collision, target nuclei get excited with a subsequent release of subatomic particles, like protons, pions, muons and neutrinos. And also from 20 to 30 neutrons are ejected from each nuclei in each spallation event, with a the resulting spectrum close to that obtained with fission reaction. The main difference compared to reactor based sources is that the spallation source produces pulsed beams with a repetition rate of 10 to 50 Hz which requires different experimental approaches for neutron instrumentation. However a time averaged flux of pulsed sources is somehow comparable with reactor flux which makes both types of sources competitive.

It is also worth mentioning that not all fission- and spallation- based sources are continuous and pulsed respectively. For instance, SINQ facility at Paul Scherrer institute is a continuous-type spallation source, another example would be IBR-2 pulsed reactor located in Dubna, Russia.

Yet another important stage of neutron preparation is a pre-tuning of its energy called moderation. Neutrons produced in fission or spallation reactions are too energetic for scattering studies, having their energy spectrum distributed around several MeV. To slow them down one should put a medium on their pathway, passing through which neutrons undergo inelastic collisions transferring their energy to atoms of the medium. This simple approach brings neutrons to thermal equilibrium and shapes their energy spectrum to a Maxvellian type. To obtain a flux of thermal neutrons H_2O or D_2O moderators are typically used. However some experimental purposes could require neutrons with energies different from the thermal region; for that, spectra could be moved towards higher or lower energies by using moderators with high or low temperatures respectively. Achieving cold neutrons is done via the so-called a "cold" source, a reservoir filled with liquid H_2 or D_2 at temperatures below 20 K. Hot neutrons are thermalized by passing through a graphite block heated up to roughly 2000 K.

2.2.2.2 Basic neutron scattering theory

In any kind of scattering experiment one is interested in a particular quantity called cross-section. Let's consider an incident beam having a constant energy E coming at a scattering system, thus the most exhaustive information would be given by the number of scattered particles N per unit of time t into a small solid angle $d\Omega$ with the final energy between E_f and $E_f + dE_f$:

$$\frac{d^2\sigma}{d\Omega dE_f} = \frac{\text{N} \times \text{t scattered into } d\Omega}{\Phi d\Omega dE_f}, \tag{2.14}$$

where Φ - is the flux of incident particles. The quantity defined by the equation 2.14 is called the partial differential cross-section and and has dimensions of area divided by energy. It should be also mentioned that the area covered by the solid angle $d\Omega$ is negligibly smaller than the distance between the scattering system and the solid angle.

If there is no interest in analyzing energy of scattered particles, one can consider a differential cross-section which is:

$$\frac{d\sigma}{d\Omega} = \int_0^\infty \left(\frac{d^2\sigma}{d\Omega dE_f}\right) dE_f, \tag{2.15}$$

and has a physical meaning of the number of particles scattered per the unit of time into $d\Omega$ normalized to the flux and the area of $d\Omega$.

And integration of 2.15 gives a total scattering cross-section, a total number of particles scattered in all directions:

$$\sigma_{tot} = \int_0^\infty \left(\frac{d\sigma}{d\Omega}\right) d\Omega. \tag{2.16}$$

These cross-sections are experimentally observed values and can be applied to X-ray and neutron techniques. However these expressions do not explicitly contain any information neither on a scattering system nor the initial and the final state of a scattered particle, which are required to structural or dynamic characterization of the system.

Let us consider now the neutron scattering at a single nucleus at a fixed position. Typical distance of interaction for nuclear forces via which neutrons are scattered by nuclei are around femtometers - 10^{-15} m while thermal neutron wavelength is of the order of angstroms - 10^{-15} m. This means that nuclei scatter neutrons as if they were point-like objects. Thus the incident neutron on a nucleus could be described as a plane wave, whereas the scattered neutron is a spherical wave.

For neutrons with wavevector $\mathbf{k}$ along the z-axis scattered by a nucleus located at the origin, the incident neutron wave function is:

$$\psi_{inc} = e^{i\mathbf{kz}}. \tag{2.17}$$

The wave function of scattered neutrons at the position $\mathbf{r}$ is:

$$\psi_{sc} = -\frac{b}{r} e^{i\mathbf{kr}}, \tag{2.18}$$

where b is a constant defined by the nature of the nucleus and independent from the scattering direction. The quantity b is known as scattering length and it is described with a complex number $b = \alpha + i\beta$. However the $i\beta$ term becomes significant only for highly absorbing elements like boron or cadmium.

Scattering length is related to the cross section because they represent a scattering amplitude. Lets first consider a monoatomic scattering system in which b values vary from one nucleus to another due to the presence of isotopes or variations of nuclear spins. The frequency at which a certain b_i value occurs is f_i and:

$$\sum_i f_i = 1. \tag{2.19}$$

The average value of b for the considered system is then given by:

$$\bar{b} = \sum_i f_i b_i \tag{2.20}$$

so the average value of b^2 would be:

$$\bar{b^2} = \sum_i f_i {b_i}^2. \tag{2.21}$$

Assuming that there is absence of correlation between scattering lengths of different nuclei b values could be written in the following form of:

$$\overline{b_j b_{j'}} = (\bar{b})^2 \quad \text{for} \quad j \neq j' \tag{2.22}$$

$$\overline{b_j b_{j'}} = \overline{b^2} \quad \text{for} \quad j = j' \tag{2.23}$$

The most general case would be a scattering from a system containing a single isotope of a zero spin, so all scattering lengths b are equal and the scattering itself is fully coherent:

$$\sigma_{coh} = 4\pi(\bar{b})^2. \tag{2.24}$$

But in the real case the differential cross-section contains both coherent and incoherent contributions:

$$\frac{d\sigma}{d\Omega_f} = \left(\frac{d\sigma}{d\Omega_f}\right)_{coh} + \left(\frac{d\sigma}{d\Omega_f}\right)_{incoh}, \tag{2.25}$$

so the total scattering would contain both contributions as well:

$$\sigma_{tot} = 4\pi \sum_i f_i b_i = 4\pi \overline{b^2}, \tag{2.26}$$

simply subtracting σ_{coh} from σ_{tot}, one can obtain the equation for incoherent scattering:

$$\sigma_{incoh} = 4\pi \left(\overline{b^2} - (\bar{b})^2\right). \tag{2.27}$$

In the most general case the total scattering cross-section should be represented as the sum of coherent and incoherent contributions:

$$\sigma_{tot} = \left.\frac{d\sigma}{d\Omega}\right|_{coh} + \left.\frac{d^2\sigma}{d\Omega dE_f}\right|_{coh} + \left.\frac{d\sigma}{d\Omega}\right|_{incoh} + \left.\frac{d^2\sigma}{d\Omega dE_f}\right|_{incoh}. \tag{2.28}$$

Each term in the equation 2.28 stands for a different origin: the first one describes Bragg scattering, the second - scattering from collective excitations like phonons or magnons, third - arises from structural imperfections and the last one - provides information on individual atom motion like diffusion or confined vibrations.

Before considering theoretical expressions for cross-sections one important point should be mentioned. Every physical event do obey some universal rules and in the case of scattering experiments these are the laws of momentum and energy conservation:

$$\mathbf{Q} = \mathbf{k}_f - \mathbf{k}_i, \tag{2.29}$$

$$\hbar\omega = E_i - E_f, \tag{2.30}$$

where i and f indices stand for properties of the incident and final neutron beam and the value $\hbar\omega$ is the energy transferred to the scattering system. Therefore a neutron scattering experiment is nothing else but probing a transition between neutron states with $\mathbf{k}_i$ and $\mathbf{k}_f$. So it is obvious that one can split scattering experiments in two major groups. In the first one there is no energy transfer from neutrons to the scattering system and vice versa, i.e. neutrons are scattered elastically. These are diffraction techniques aimed to study the structure of matter. For the second group $|\mathbf{k}_f| \neq |\mathbf{k}_i|$ and the energy difference between the incident and final neutron states is spent to create or annihilate excitations, so the scattering, in this case, is inelastic and methods exploiting this approach are called spectroscopy, whose main concern is obviously the dynamical aspects of solids. No spectroscopic technique was used within the present project, thus for the sake of brevity discussions on inelastic aspects of neutron scattering will be avoided.

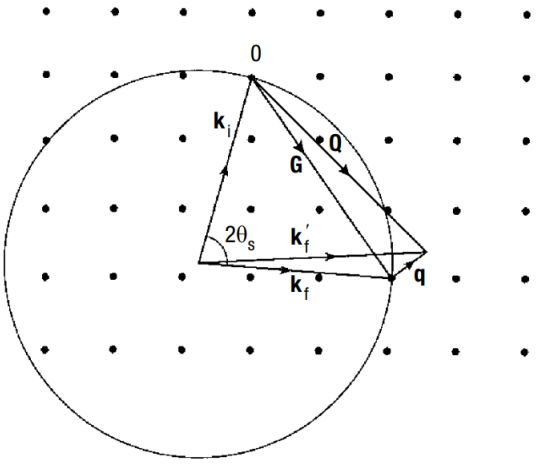

Figure 2.7: Two-dimensional representation of reciprocal space showing the Ewald circle and the vector representation for elastic and inelastic scattering. Here **G** is a reciprocal-lattice vector and **q** the momentum transfer within the first Brillouin zone[162].

2.2.2.3 Elastic nuclear scattering

Let us now have a closer look at the elastic scattering in crystalline materials. From the definition one can say that $|\mathbf{k}_f| = |\mathbf{k}_i| = k$. It is convenient to represent scattering in the reciprocal space, so the figure 2.7 shows the reciprocal lattice of a two-dimensional crystalline solid, where each node corresponds to a reciprocal-lattice vector. One can plot the Ewald sphere - a sphere or, in case of a two-dimensional lattice, a circle of the radius k. Whenever this circle passes through two nodes the Bragg condition is fulfilled:

$$\mathbf{Q} = \mathbf{G} = \mathbf{k}_f - \mathbf{k}_i, \tag{2.31}$$

where **G** is the reciprocal-lattice vector. In the figure 2.7 $\mathbf{k}_i$ and $\mathbf{k}_f$ have relative directions of the incident and diffracted beams respectively.

Using Ewald's sphere and the following formula:

$$|\mathbf{Q}| = k_i^2 + k_f^2 - 2k_i k_f \cos\theta_S, \tag{2.32}$$

one will obtain

$$|\mathbf{Q}| = |\mathbf{G}| = 2|\mathbf{k}_i| \sin\theta_S, \tag{2.33}$$

where $2\theta_S$ is the angle between the incident and the diffracted beam. The equation 2.33 represents the Bragg's law, which can be represented in terms of d spacing between direct lattice planes (inverse of the module of reciprocal lattice vectors)

$$\lambda = 2d \sin\theta_S, \tag{2.34}$$

so the magnitude of the reciprocal lattice vector

$$|\mathbf{G}| = \frac{4\pi \sin\theta_S}{\lambda}. \tag{2.35}$$

In a typical diffraction experiment three parameters are used to manipulate the momentum transfer: $\mathbf{k}_i$, $2\theta_S$ and the crystal orientation ϕ. By varying the angle $2\theta_S$ one modifies the magnitude of **Q** while its orientation is achieved by rotating the sample [162].

A couple of words about the relation between the real and the reciprocal space. Lets define primitive unit cell parameters as $\mathbf{a}_1$, $\mathbf{a}_2$, $\mathbf{a}_3$, so the volume of the unit cell is

$$v_0 = \mathbf{a}_1 \cdot [\mathbf{a}_2 \times \mathbf{a}_3]\,. \tag{2.36}$$

The reciprocal-lattice vector can be decomposed in three-dimensional form of

$$\mathbf{G} = h\boldsymbol{\tau}_1 + k\boldsymbol{\tau}_2 + l\boldsymbol{\tau}_3 \tag{2.37}$$

where h, k, l denote Miller indexes having integer values. So the unit cell vectors $\boldsymbol{\tau}_1$, $\boldsymbol{\tau}_2$ and $\boldsymbol{\tau}_3$ could be defined as:

$$\begin{aligned} \boldsymbol{\tau}_1 &= \frac{2\pi}{v_0}\,[\mathbf{a}_2 \times \mathbf{a}_3]\,, \\ \boldsymbol{\tau}_2 &= \frac{2\pi}{v_0}\,[\mathbf{a}_3 \times \mathbf{a}_1]\,, \\ \boldsymbol{\tau}_3 &= \frac{2\pi}{v_0}\,[\mathbf{a}_1 \times \mathbf{a}_2]\,. \end{aligned} \tag{2.38}$$

The volume of the unit cell in the reciprocal lattice is

$$v_r = \mathbf{a}_1 \cdot [\mathbf{a}_2 \times \mathbf{a}_3] = \frac{2\pi^3}{v_0}. \tag{2.39}$$

From the equation 2.36 one can retrieve the following relationship between direct and reciprocal space vectors:

$$\mathbf{a}_i \cdot \boldsymbol{\tau}_j = 2\pi\delta_{ij} \quad \delta_{ij} = \begin{cases} 0 & \text{if} \quad i \neq j \\ 1 & \text{if} \quad i = j \end{cases} \tag{2.40}$$

Notice that in crystallography the factor 2π is removed from the definition of the reciprocal lattice. The most common equation for coherent scattering cross section can be written concerning scattering system that contains atoms with various scattering lengths b in the following form

$$\left.\frac{d^2\sigma}{d\Omega dE_f}\right|_{coh} = N\frac{k_f}{k_i}(\bar{b})^2 S(\mathbf{Q},\omega), \tag{2.41}$$

which, taking into account 2.24, can be rewritten as

$$\left.\frac{d^2\sigma}{d\Omega dE_f}\right|_{coh} = N\frac{k_f}{k_i}\frac{\sigma_{coh}}{2\pi} S(\mathbf{Q},\omega), \tag{2.42}$$

where $S(\mathbf{Q},\omega)$ is called the scattering function. This formula is valid for the case of single-element scattering systems, but in the general case the site dependence of b should be taken into account.

An explicit form of the scattering function can be represented via the atomic density operator[163]:

$$\rho_{\mathbf{Q}}(t) = \sum_l e^{i\mathbf{Q}\mathbf{r}_l(t)}. \tag{2.43}$$

So $S(\mathbf{Q}\omega)$ is then

$$S(\mathbf{Q}\omega) = \frac{1}{2\pi}\int_{-\infty}^{\infty} dt\ e^{-i\omega t}\langle \rho_{\mathbf{Q}}(0)\rho_{\text{-}\mathbf{Q}}(t)\rangle \tag{2.44}$$

In case of a purely nuclear scattering from a Bravis lattice elastic coherent cross section can be written in terms of **Q** and **G**:

$$\left.\frac{d\sigma}{d\Omega}\right|_{coh}^{el} = N\frac{(2\pi)^3}{v_o}(\bar{b})^2\sum_{\mathbf{Q}}\delta(\mathbf{Q}-\mathbf{G}). \tag{2.45}$$

Equation 2.45 implies that the lattice is rigid. However, it is known that even at T = 0 atoms oscillate around their equilibrium positions and magnitude of this motion only increases with the temperature. The effect of such a motion lies in the reduction of Bragg intensities. Let us introduce **u** as the vector describing instantaneous displacement of an atom from its equilibrium position **r**. This consideration should now be taken into account for $S(\mathbf{Q}\omega)$ function as an extra factor, which is known as the Debye-Waller factor:

$$W = \frac{1}{2}\langle(\mathbf{Q}\cdot\mathbf{u})^2\rangle, \tag{2.46}$$

but for crystallographic purposes the same value is used in a different notation:

$$\begin{aligned} W &= B\left(\sin\theta/\lambda\right)^2, \\ B &= \frac{(8\pi)^2}{3}\langle u^2\rangle. \end{aligned} \tag{2.47}$$

The next step is to take into account a more general case of lattice with more than one atom per unit cell. Lets define $\mathbf{d}_j$ as the position of jth atom within the unit cell, then the coherent elastic differential cross section gains another factor:

$$\left.\frac{d\sigma}{d\Omega}\right|_{coh}^{el} = N\frac{(2\pi)^3}{v_o}\sum_{\mathbf{Q}}\delta(\mathbf{Q}-\mathbf{G})|F_N(\mathbf{G})|^2, \tag{2.48}$$

where

$$F_N(\mathbf{G}) = \sum_j \bar{b}_j e^{i\mathbf{G}\mathbf{d}_j}e^{-W_j} \tag{2.49}$$

is called the static nuclear structure factor that contains information on atomic positions $\mathbf{d}_j$ within the unit cell and the mean square displacements $\langle u_{j\alpha}^2\rangle$. In a diffraction experiment one measures the square of the nuclear structure factor and with the collection of a large number of reflections structural models could be fitted. Explicit form of the formula describing integrated intensity depends in general on the geometrical characteristics and the way the reflections are collected for each particular instrument. However some simple cases could be easily described.

For a single crystal diffraction measurement with monochromatic incident beam of wavelength λ the integrated intensity of an observed reflection (hkl) at the angular position θ and 2θ angle between incident and diffracted beam is given by

$$\mathcal{I} = A\frac{\lambda^3|F_N(hkl)|^2}{v_0\sin 2\theta}, \tag{2.50}$$

Where A depends on the incident flux, sample volume and the counting time. If this parameters remain constant for a single experiment, then A is simply a scale factor [162]. There is also no need to say that $F_N(hkl) = F_N(\mathbf{G})$.

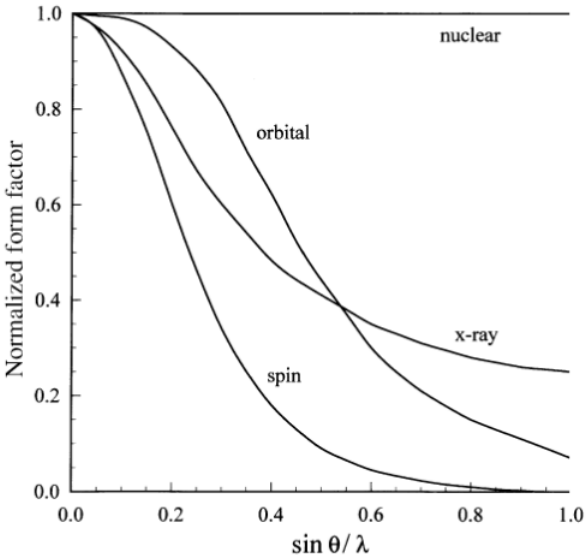

Figure 2.8: The angular dependence of the normalized form factor for nuclear, and spin and orbital magnetic scattering for chromium metal. The comparable values for X-ray scattering are given for comparison[164]

2.2.2.4 Elastic magnetic scattering

As it was already mentioned in the paragraph 2.2.2.1 a neutron has a magnetic dipole moment that could be represented as

$$\boldsymbol{\mu}_n = -\gamma\mu_N\boldsymbol{\sigma}, \tag{2.51}$$

where γ is the gyromagnetic ratio, μ_N is the nuclear magneton and $\boldsymbol{\sigma}$ is the Pauli spin operator with the eigenvalues for its components of ± 1. Thus, neutrons have a scattering channel due to dipole-dipole interactions with the magnetic moment of the atom. To simplify here it will be assumed that atomic moment is caused purely by spin, however one should keep in mind that the orbital contribution should be also taken into account. By the analogy to 2.43 magnetic scattering also depends on the density of scattering objects $\rho_s(\mathbf{r})$, which in this case are unpaired electrons. Then its Fourier transform

$$f(\mathbf{Q}) = \int \rho_s(\mathbf{r}) e^{i\mathbf{Q}\mathbf{r}} d\mathbf{r} \tag{2.52}$$

will be the magnetic form factor.

In comparison to the nuclear scattering where neutron interacts with point-like potential, the magnetic neutron scattering is conditioned by the electronic density distribution and resembles to that of X-ray scattering by electrons [164]. For small scattering angles i.e. small $\mathbf{Q}$ values the magnetic form factor is normalized to unity:

$$f(\mathbf{Q}) \equiv 1, \tag{2.53}$$

however with the increase of the scattering angle it drops dramatically. The angular behaviour of the magnetic form factor is illustrated on the figure 2.8, therefore it is obvious that the area of the interest for the magnetic neutron scattering experiments lies at the low $\mathbf{Q}$ (low 2θ) region.

In the case of magnetic scattering, elastic coherent cross section for a single atom can be expressed as the square of the magnetic scattering amplitude absolute value:

$$\left.\frac{d\sigma}{d\Omega}\right|_{coh}^{el} = |\mathbf{F}_M(\mathbf{Q}|^2 \tag{2.54}$$

where the magnetic scattering amplitude itself is

$$\mathbf{F}_M(\mathbf{Q}) = pf(Q)\mathbf{m}_\perp. \tag{2.55}$$

In the equation 2.55 the prefactor $p = r_0\gamma/2$, where r_0 is the classical electron radius:

$$r_0 = \frac{e^2}{4\pi\epsilon_0 mc^2} \tag{2.56}$$

and the $\mathbf{m}_\perp$ as given by

$$\mathbf{m}_\perp = \frac{\mathbf{Q}\times(\mathbf{m}\times\mathbf{Q})}{Q^2}, \quad Q = |\mathbf{Q}| \tag{2.57}$$

is the component of the atomic magnetic moment perpendicular to the scattering vector $\mathbf{Q}$ to which neutrons are sensitive in a scattering experiment.

Considering the magnetic structure as the average over quantum and thermal fluctuations, the magnetization $\mathbf{m}_{jl}$ of the magnetic ion j at the l-th unit cell is given by:

$$\mathbf{m}_{jl} = \sum_{\mathbf{k}} \mathbf{S}_{\mathbf{k}j} exp(i\mathbf{k}\cdot\mathbf{R}_l), \tag{2.58}$$

where $\mathbf{k}$ are propagation vectors, $\mathbf{R}_l$ is the vector position of the origin of the l-th unit cell and $\mathbf{S}_{\mathbf{k}j}$ are complex vectors called Fourier coefficients given by:

$$\mathbf{S}_{\mathbf{k}j} = \frac{1}{2}\{\mathbf{R}_{\mathbf{k}j} + \mathbf{I}_{\mathbf{k}j}\}exp(i\phi_{\mathbf{k}j}) \tag{2.59}$$

that should fulfill the equation $\mathbf{S}_{-\mathbf{k}j} = \mathbf{S}^*_{\mathbf{k}j}$ since the $\mathbf{m}_{jl}$ vectors are real.

The elastic intensity of magnetic neutron scattering is proportional to the magnetic interaction vector:

$$\mathbf{M}^T_\perp(\mathbf{Q}) = p\sum_{jl} f_j(Q)\mathbf{m}_{\perp jl} exp(i\mathbf{Q}\cdot\mathbf{R}_{jl}) = \frac{1}{Q^2}\mathbf{Q}\times\mathbf{M}^T(\mathbf{Q})\times\mathbf{Q}. \tag{2.60}$$

Here $\mathbf{M}^T$ is the magnetic structure factor of the crystal and R_{jl} is the vector position of the magnetic atom j at unit cell l. In a magnetically ordered crystal described by the equation 2.58, the magnetic structure factor crystal is given by

$$\mathbf{M}^T(\mathbf{Q}) = p\sum_j f_j(Q)exp(i\mathbf{Q}\mathbf{r}_j)\sum_{\mathbf{k}}\mathbf{S}_{\mathbf{k}j}\sum_{\mathbf{G}}\delta(\mathbf{Q}-\mathbf{k}-\mathbf{G}). \tag{2.61}$$

As a result the equation 2.61 postulates that the magnetic intensity appears in the reciprocal space positions that are given by

$$\mathbf{Q} = \mathbf{G} + \mathbf{k}. \tag{2.62}$$

Obviously, for $\mathbf{k} \neq 0$ nuclear and magnetic reflections do not overlap and for the magnetic reflection described with 2.62 relation, the magnetic structure factor of the crystal unit cell is

$$\mathbf{M}(\mathbf{Q} = \mathbf{G} + \mathbf{k}) = p\sum_j^{n_c} f_j(Q)\mathbf{S}_{\mathbf{k}j} exp(i(\mathbf{G}+\mathbf{k})\mathbf{r}_j) \tag{2.63}$$

where the sum is taken over the unit cell having n_c magnetic atoms.

2.2.2.5 Neutron diffraction techniques

As mentioned previously, diffraction techniques are exploiting the elastic scattering channel and they are mainly used for an accurate structure characterization at atomic level. Since the discovery of X-rays, monochromatic beam diffraction has become one of the most widely used methods recovering the structure factor $F(\mathbf{G})$ amplitudes for a series of reflections hkl with scattering vector $\mathbf{G}$. Technical implementation of this seemingly simple task, however, is strictly dependent on the type of sample: a structural determination of solids could be carried out for both single crystal and powder forms. In this paragraph the basic principles and examples of used instruments for both cases will be given.

Neutron powder diffraction

For several reasons powder diffraction is one of the most common technique used for phase analysis and structural characterization of crystalline materials. This is mainly due to the fact that this method is fairly straightforward, it provides not only the structural information but also helps to investigate crystalline texture and microstructure. On top of that powder diffraction patterns are unique for each single material which makes this method an ideal tool for phase identification. It is also worth mentioning that some materials like catalysts, zeolites, fast-ion conductors etc. are hardly achievable in single crystal forms, so the powder diffraction is the only method study structures of this compounds.

To obtain good averaging the powder should contain a large number of randomly oriented crystallites of a small size preferably tens of microns. Coarse grain sizes could lead to problems like extinction, microabsorption and particle statistics. Another typical issue encountered in powders is preferred orientation which should be also taken into account during the sample preparation.

From the Bragg equation 2.34 it is obvious that there could be two types of diffraction experiments. In the first one, the sample is illuminated with a monochromatic radiation and reflections associated with different d-spacing are collected at different angular detector positions. The second type uses a white beam and fixed scattering angle, so the diffracted radiation is discriminated by energy. In the current work only instruments of the first type have been used, so below details of neutron powder diffraction with a fixed incident wavelength are given.

The intensity of a diffraction line $\mathbf{G}$ is given by the following expression:

$$\mathcal{I}_{\mathbf{G}} = S\ j_G\ L_{pG}\ |F(\mathbf{G})|^2 \tag{2.64}$$

where S is the scale factor depending on technical specifications of each particular setup, wavelength and sample density, j_G is the multiplicity of the reflection $\mathbf{G}$.

A perfect sample would give narrow diffraction lines, however the real powder diffraction peaks are of a finite width, meaning fact that the diffraction signal is the convolution of the instrumental resolution, determined by the initial wavelength distribution, monochromator mosaicity and scattering effects related to a sample's morphology.

The first type of effects are related to the particle size distribution. A finite number of scattering planes leads to the fact that for particles of a small size the incident beam is not fully scattered coherently, in other words the reciprocal lattice points are no longer δ-functions but smeared around their centers according to the particle size. To describe the most simple isotropic case one can use the Scherrer formula [165]:

$$D = \frac{K\lambda}{\beta \cos\theta}, \tag{2.65}$$

where D is the volume-averaged apparent size of crystallites in the direction normal

to the scattering planes, β is the integral breadth of the diffraction line at the position **G** and K is a dimensionless numerical constant with a typical value around 0.9.

Another mechanism of a peak shape broadening are microstrains, which emerge as the result of local fluctuations of interatomic distances due to lattice strains distributed within crystallines in a non-uniform way. The apparent strain is defined as [166]:

$$\eta = \beta \cot \theta \tag{2.66}$$

Equations 2.65 and 2.66 describe isotropic size and strain broadening effects and there is no need to say that some more complicated microstructures can be encountered within the real materials [167]. It should be also mentioned that both types of effects can occur in the same sample simultaneously [168].

Every single diffraction pattern can be decomposed in four sets of observables that carry an information about the scattering system, namely the peak positions and their intensities, the intensity of the background and the profile shapes.

Peak positions obviously characterize the lattice and provide a finger-print information for the phase identification. This is already fairly informative for phase diagram investigations, measurements of thermal expansion coefficients and residual stresses in materials.

Since the integrated intensities are proportional to the structure factors, a careful integration of diffraction profile is essential for obtaining an accurate description of an atomic arrangement. Moreover intensities are proportional to the amount of corresponding phase in a sample. Usually peak integration is straightforward if there is no severe peak overlapping, nevertheless peak intensities can be affected by preferential orientation, thus powder experiment requires an accurate sample preparation. On the other hand, grain orientation itself can be an object of interest for metallurgic or geophysical studies.

As mentioned above, peak shape can provide an insight on the microstructure characteristics of a sample: crystalline size distribution and strains. Peak shape parameters of powder diffraction profiles $\Omega(2\theta)$ are usually described in terms of their full widths at half maximum (FWHM). The most common mathematical function to describe powder diffraction line is the pseudo-Voigt function:

$$pV(2\theta) = \eta L(2\theta) + (1-\eta)G(2\theta) \tag{2.67}$$

where L and G stand for Lorentzian and Gaussian components and η is the mixing coefficient:

$$G(2\theta) = \frac{2}{H}\left(\frac{ln2}{\pi}\right)^{1/2} exp\left(\frac{-4ln2}{H^2}(2\theta - 2\theta_c)^2\right) \tag{2.68}$$

$$L(2\theta) = \frac{2}{\pi H}\left(1 + \frac{4(\sqrt{2}-1)}{H^2}(2\theta - 2\theta_c)^2\right)^{-1} \tag{2.69}$$

and H_L and H_G are their respective full-width at half maximum. H_G and H_L themselves have angular dependence:

$$H_G = \left(U + (1-\xi)^2 D_{ST}^2(\boldsymbol{\alpha}_D)\tan^2\theta + V\tan\theta + W + \frac{I_G}{\cos^2\theta}\right)^{1/2} \tag{2.70}$$

$$H_L = (X + \xi^2 D_{ST}^2(\boldsymbol{\alpha}_D))\tan\theta + \frac{Y + F(\boldsymbol{\alpha}_z)}{cos\theta}. \tag{2.71}$$

Considering non-negligible microstructure, V and W are put to zero, while there rest of parameters have a physical meaning and can be split in two groups: U, $\boldsymbol{\alpha}_D$ and X describe strains, while Y, I_G and $\boldsymbol{\alpha}_Z$ characterize. The functions $2D^2_{ST}(\boldsymbol{\alpha}_D)$ and $F(\boldsymbol{\alpha}_z)$ may have different explicit forms depending on the particular microstructure model, describing strain and size contribution to diffraction peaks broadening.

Experimental setups are usually designed in a way to minimize the signal-to-background ratio since it is the least informative part of a pattern. Nevertheless, there are some cases in which the background is enhanced due to the incoherent scattering arising from local ordering. This case deserves a special attention because the modulation of the background may shed light on the nature of the short-range ordering[168].

Several neutron powder diffractometers were used in the framework of the current work, namely a high-resolution two-axis diffractometer D2B, two-axis diffractometer D1B and high intensity two-axis diffractometer D20 located at the ILL, high-resolution diffractometer 3T2 and cold neutron two-axis diffractometer G4-1 located at the Orphee reactor (Laboratoire Léon Brillouin, Saclay, France). Conceptually every single neutron powder diffractometer consists of the same principal parts, so for the sake of brevity lets focus on the layout of D1B.

A narrow spectral line is selected from the white beam of the thermal guide H22 by the focusing monochromator represented by the assembly of seven pyrolitic graphite (002) crystals. Higher harmonic wavelengths are then cut by the graphite filter and the beam arrives to the sample position throughout an evacuated flight tube to reduce the scattering on air. The instrument allows one to use various sample environment to cover the temperature range from $1.5K$ to $1200K$. A radial oscillating collimator is placed between the sample position and the detector to eliminate the parasitic scattering signal coming from the sample environment devices. Diffracted neutrons are detected by a ^{3}He multidetector containing 1280 cells that covers an angular range of 128^o.

2.2.2.6 Small angle neutron diffraction

Considering that the wavelength λ is constant in the Bragg equation 2.34, if one wants to study systems with large d-spacing, the scattering will appear at low scattering angles θ. For objects with d values in between tens to thousands of Angstroms small angle scattering becomes a perfect probe for structural studies. It is obvious that the small angle scattering probes distances that are significantly larger than interatomic ones, so in this case neutrons are sensitive to inhomogeneities of the scattering length density. Typical samples for small angle scattering are proteins, colloids, polymers and glasses, amorphous solids and particle solutions i.e. objects which do not possess any long-range ordering.

With the lack of long-range ordering there is no need of detailed description of atomic arrangement within the studied system. To understand its properties only the most general features investigated. In the case of a single-phase monodisperse system one can write the so-called Patterson function:

$$P(\mathbf{r}) = \sum_{\mathbf{Q}} I(\mathbf{Q}) \cos \mathbf{Qr} \tag{2.72}$$

where r is the distance in the real space. This formula provides information about typical distances between atoms in gases and liquids, particle dimensions in solutions, dimensions of clusters or pores in solids [170]. This approach is of course oversimplified and the small angle scattering from disordered media is more complex and requires a special consideration. However, small angle scattering could be also on ordered objects as flux line lattices in superconductors [171], skyrmions and helical orders [172]. In this case

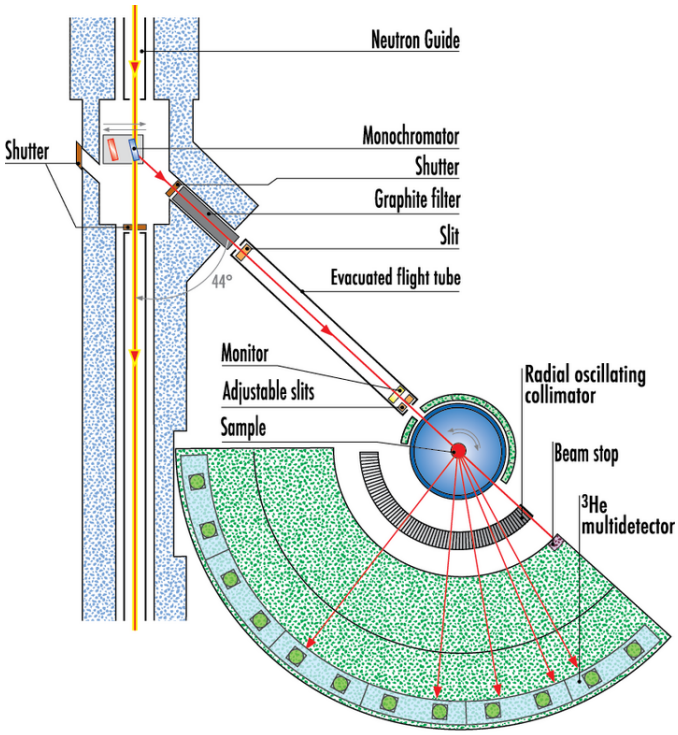

Figure 2.9: Scheme of the high intensity two-axis powder diffractometer D1B [169].

one can say that diffraction at small angles takes place and all the considerations applied for the wide-angle diffraction are also valid here.

D33 - a massive dynamic q-range small-angle diffractometer installed at the H14 cold neutron guide was used to perform small angle diffraction studies for the present project. The layout of the instrument is represented in figure 2.10. The instrument works in two modes: (1) monochromatic, using velocity selector that provides neutrons with wavelength between 4.5 and 40 Å with a wavelength spread of 10% and (2) time-of-flight mode exploiting the chopper system which consists of four choppers and a wavelength filter that cuts off long wavelengths to avoid frame overlaps. Then the beam goes through the collimation system that defines the angular divergence of the beam at the sample position. Then that the beam scattered by the sample is detected by detectors located at the detector tank. There are two ^{3}He detectors, front and rear. The first is constituted by four monoblock panels mounted horizontally and vertically, the second one is a single monoblock panel, covering together sample-detector distance between 1.2 and 12.8 meters in order to cover a wide **Q** range.

2.2.2.7 XYZ neutron polarization analysis

As already mentioned the total scattering consist of several contributions and contains a certain degree of disorder which comes form nuclear isotopes, nuclear spin-incoherent scattering and local structural disorder like atomic irregularities, structural defects and internal strains. Moreover, magnetic compounds, diffuse scattering arises from disordered magnetic moments in paramagnetic state as well as from magnetic defects perturbing long-range spin ordering. Magnetic diffuse scattering is usually drowned out by the nuclear diffuse scattering and thermal diffuse scattering. However there is a powerful tool, using neutron polarization, capable of unambiguous separation of nuclear, magnetic and spin-

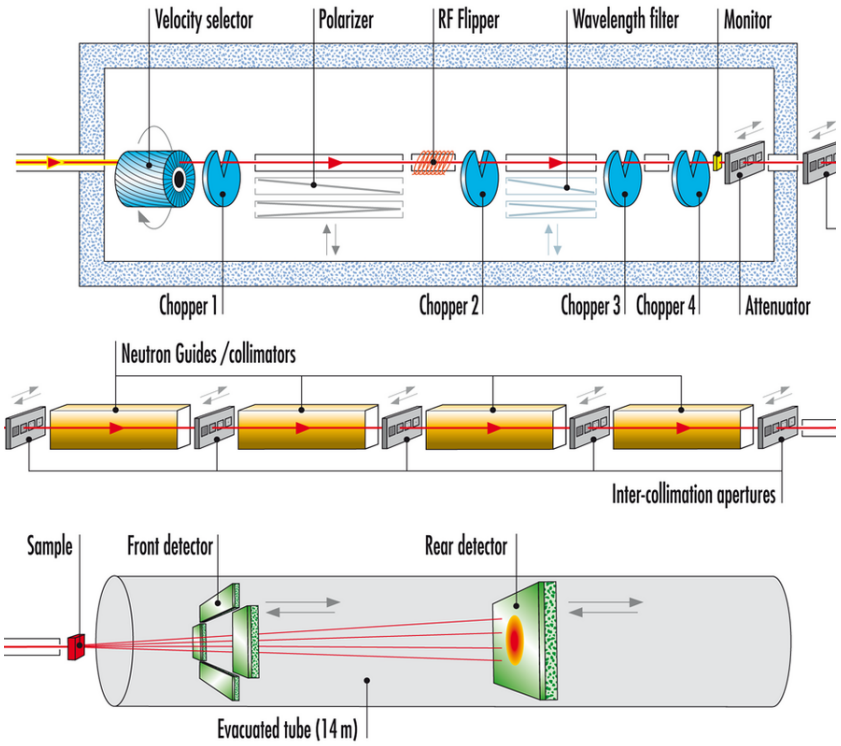

Figure 2.10: Layout of D33. Top: neutron selection either with a neutron velocity selector (monochromatic mode) or with choppers (time-of-flight mode); middle: collimation part; bottom: front and rear detector moving in the vacuum tube from 1.2 m to 12.8 m after the sample position.[173].

incoherent scattering. It is called XYZ-polarization analysis [174].

One can apply a magnetic field over a neutron beam, so that Zeeman level splitting aligns neutron spin either parallel or anti-parallel to the quantization axis set by the direction of the magnetic field. The polarization of a neutron beam can be defined as

$$\mathbf{P} = \langle \boldsymbol{\sigma} \rangle, \tag{2.73}$$

where $\boldsymbol{\sigma}$ is Pauli spin operator, given by

$$\sigma_x = \begin{bmatrix} 0 & 1 \\ 1 & 0 \end{bmatrix}, \ \sigma_y = \begin{bmatrix} 0 & -i \\ i & 0 \end{bmatrix}, \ \sigma_z = \begin{bmatrix} 1 & 0 \\ 0 & -1 \end{bmatrix}. \tag{2.74}$$

The scattering of thermal neutrons by a nucleus can be described with the Fermi pseudo-potential

$$\hat{V} = \left(\frac{2\pi\hbar^2}{m_n} \right) \hat{b}\delta(r). \tag{2.75}$$

In the absence of external fields the angular momentum of a combined neutron -nucleus system $\mathbf{J} = \mathbf{I} + \mathbf{S}$ is a conserved quantity, so $J = I \pm 1/2$ is a good quantum number. There are $2I + 2$ scattering channels for the neutron spin co-aligned with the nuclear spin $\mathbf{I}$ and $2I$ for the antiparrallel orientation. Lets denote the scattering channel $2I + 2$ as b_+ and the scattering channel $2I$ as b_-, so in the general case one can describe the spin dependent nuclear scattering via scattering length operator [159]

$$\hat{b} = A + B\boldsymbol{\sigma} \cdot \mathbf{I} \tag{2.76}$$

where

$$A = \frac{(I+1)b_+ + Ib_-}{2I+1} \quad \text{and} \quad B = \frac{b_+ - b_-}{2I+1}. \tag{2.77}$$

So the spin dependent scattering amplitudes will be given by

$$\begin{aligned} U_n^{++} &= \langle + | \hat{b} | + \rangle = A + BI_z, \\ U_n^{--} &= \langle - | \hat{b} | - \rangle = A - BI_z, \\ U_n^{+-} &= \langle + | \hat{b} | - \rangle = B(I_x + iI_y), \\ U_n^{-+} &= \langle - | \hat{b} | + \rangle = B(I_x - iI_y). \end{aligned} \tag{2.78}$$

Here the first two scattering amplitudes conserve the neutron state so they are called the non-spin-flip amplitudes (NSF), whereas the last two involve a change of the spin state so they the spin-flip amplitudes (SF).

Taking into account that the magnetic scattering potential is

$$V_m(\mathbf{Q}) = -\left(\frac{\gamma r_0}{2}\right) \boldsymbol{\sigma} \cdot \mathbf{m}_\perp(\mathbf{Q}), \tag{2.79}$$

where r_0 is the classical electron radius and the $\mathbf{m}_\perp$ is given by the equation 2.57, one can obtain nuclear and magnetic scattering amplitudes together

$$\begin{aligned} U^{++} &= A - pM_{\perp z} + BI_z, \\ U^{--} &= A + pM_{\perp z} - BI_z, \\ U^{+-} &= -p(M_{\perp x} + iM_{\perp x}) + B(I_x + iI_y), \\ U^{-+} &= -p(M_{\perp x} - iM_{\perp x}) + B(I_x - iI_y), \end{aligned} \tag{2.80}$$

where p is the magnetic prefactor $\gamma r_0/2$. This equations are also known as Moon-Riste-Koeller equations for the spin-dependent amplitudes [175]. Remembering that the neutron polarization is aligned along the $\mathbf{z}$ direction, it is easy to notice that the NSF scattering is only sensitive to magnetization components parallel to the neutron spin, while SF scattering - to those which are perpendicular.

Considering the case of a paramagnet magnetic-only, the NSF and SF cross sections are given by

$$\left(\frac{d\sigma}{d\Omega_f}\right)_{nsf} = \frac{1}{2}\left(\frac{d\sigma}{d\Omega_f}\right)_{mag} \left(1 - (\hat{\mathbf{P}} \cdot \hat{\mathbf{Q}})^2\right), \tag{2.81}$$

$$\left(\frac{d\sigma}{d\Omega_f}\right)_{sf} = \frac{1}{2}\left(\frac{d\sigma}{d\Omega_f}\right)_{mag} \left(1 + (\hat{\mathbf{P}} \cdot \hat{\mathbf{Q}})^2\right) \tag{2.82}$$

where

$$\left(\frac{d\sigma}{d\Omega_f}\right)_{mag} = \frac{2}{3}\left(\frac{\gamma}{2}\right)^2 f(\mathbf{Q}) g_s^2 S(S+1) \tag{2.83}$$

and an incident beam polarization **P** alternately aligned along the **z**, **x** and **y** directions, one can deduce the spin dependent scattering cross sections for an XYZ-polarization measurements done on a paramagnetic sample:

$$\begin{aligned}
\left(\frac{d\sigma}{d\Omega}\right)_x^{nsf} &= \frac{1}{2}\sin^2\alpha\left(\frac{d\sigma}{d\Omega}\right)_{mag} + \frac{1}{3}\left(\frac{d\sigma}{d\Omega}\right)_{si} + \left(\frac{d\sigma}{d\Omega}\right)_{nuc}, \\
\left(\frac{d\sigma}{d\Omega}\right)_x^{sf} &= \frac{1}{2}(\cos^2\alpha + 1)\left(\frac{d\sigma}{d\Omega}\right)_{mag} + \frac{2}{3}\left(\frac{d\sigma}{d\Omega}\right)_{si} \\
\left(\frac{d\sigma}{d\Omega}\right)_y^{nsf} &= \frac{1}{2}\cos^2\alpha\left(\frac{d\sigma}{d\Omega}\right)_{mag} + \frac{1}{3}\left(\frac{d\sigma}{d\Omega}\right)_{si} + \left(\frac{d\sigma}{d\Omega}\right)_{nuc}, \\
\left(\frac{d\sigma}{d\Omega}\right)_y^{sf} &= \frac{1}{2}(\sin^2\alpha + 1)\left(\frac{d\sigma}{d\Omega}\right)_{mag} + \frac{2}{3}\left(\frac{d\sigma}{d\Omega}\right)_{si} \\
\left(\frac{d\sigma}{d\Omega}\right)_z^{nsf} &= \frac{1}{2}\left(\frac{d\sigma}{d\Omega}\right)_{mag} + \frac{1}{3}\left(\frac{d\sigma}{d\Omega}\right)_{si} + \left(\frac{d\sigma}{d\Omega}\right)_{nuc} \\
\left(\frac{d\sigma}{d\Omega}\right)_z^{sf} &= \frac{1}{2}\left(\frac{d\sigma}{d\Omega}\right)_{mag} + \frac{1}{3}\left(\frac{d\sigma}{d\Omega}\right)_{si},
\end{aligned} \tag{2.84}$$

where x, y and z subscripts stand for the direction of the incident polarization, *sf* and *nsf* superscripts stand for spin-flip and non-spin-flip cross sections respectively and *nuc* subscript refers to nuclear and isotope-incoherent, *si* - spin-incoherent contribution. Then, the nuclear, spin-incoherent and magnetic cross sections can be calculated as linear combinations of equations 2.84. There are two independent ways to calculate the magnetic cross section:

$$\begin{aligned}
\left(\frac{d\sigma}{d\Omega}\right)_{mag} &= 2\left(\frac{d\sigma}{d\Omega}\right)_x^{sf} + 2\left(\frac{d\sigma}{d\Omega}\right)_y^{sf} - 4\left(\frac{d\sigma}{d\Omega}\right)_z^{sf}, \\
\left(\frac{d\sigma}{d\Omega}\right)_{mag} &= 4\left(\frac{d\sigma}{d\Omega}\right)_z^{nsf} - 2\left(\frac{d\sigma}{d\Omega}\right)_x^{nsf}\left(\frac{d\sigma}{d\Omega}\right)_y^{nsf}.
\end{aligned} \tag{2.85}$$

Nuclear and spin incoherent scattering are expressed in the following way:

$$\begin{aligned}
\left(\frac{d\sigma}{d\Omega}\right)_{nuc} &= \frac{1}{6}\left(2\left(\frac{d\sigma}{d\Omega}\right)_{Tnsf} - 2\left(\frac{d\sigma}{d\Omega}\right)_{Tsf}\right) = \\
&= b^2 s(\mathbf{Q}) + \overline{b^2} - (\bar{b})^2, \qquad (2.86) \\
\left(\frac{d\sigma}{d\Omega}\right)_{si} &= \frac{1}{2}\left(\frac{d\sigma}{d\Omega}\right)_{Tsf} - \left(\frac{d\sigma}{d\Omega}\right)_{mag} = \\
&= B^2 I(I+1), \qquad (2.87)
\end{aligned}$$

where T_{NSF} and T_{SF} stand for the total non-spin-flip and spin-flip cross sections respectively. In order to separate nuclear coherent and spin-incoherent scattering in the absence of magnetic scattering only z components of the spin-dependent and cross sections should be measured [176].

This method was applied in the D7 diffuse scattering spectrometer located at H15 cold neutron guide of the ILL. A monochromatic neutron beam of $\lambda = 3.1\text{Å}, 4.8\text{Å}$ or 5.7Å is prepared by vertically and horizontally focusing (002) pyrolitic graphite crystals

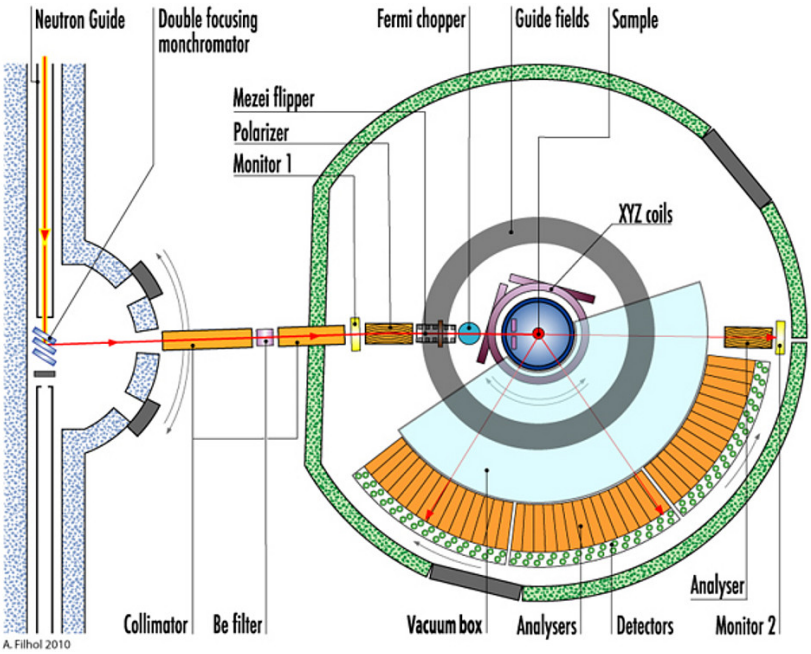

Figure 2.11: D7 diffuse scattering spectrometer layout [177].

and then polarized with the focusing (Co/Ti, $m = 2.8$) Schärpf bender-type supermirror polarizer. A magnetic guide field of around 10 to 20 G exists everywhere within D7 to preserve the neutron polarization during the experiment. The neutron polarization is manipulated with a Mezei flipper [178], which is switched *off* during non-spin-flip cross-sections measurements, and *on* when measuring spin-flip cross-sections. The spin-flipper is followed by by a set of orthogonal Helmotz coils that adiabatically rotate an incoming beam polarization into **x**, **y** or **z** directions. Scattered neutrons are analyzed by 66 Schärpf-type bender supermirrors (Co/Ti, $m = 2.8$) and, after that, arrive to the detector system of three banks, each containing forty four ^{3}He tubes, covering the total angular range between 10^o and 155^o.

2.2.2.8 X-ray diffraction

Phase analysis and basic structural characterization of a material are the primary steps towards understanding its properties. X-ray diffraction is the most straightforward technique for a basic material description.

X-rays are attractive for structural applications mainly because of two reasons:

- First, they can be relatively easy produced to have a wavelength that has the same order of magnitude as interatomic distances in solids, which is essential for interference effects responsible for diffraction to occur.
- Second, photons are scattered by electron density, so it makes possible to localize atomic positions of scattering systems. On the other hand that also means that the scattering magnitude is highly dependent on the atomic number Z. Thus light elements have less contrast in the presence of elements of high atomic numbers.

Mathematical description as well as the technical realization are pretty close to that used for neutron scattering, as discussed in details in 2.2.2.3 and 2.2.2.5. Within the

current project X-ray diffraction was used as a supporting technique, thereby there is no need to elaborate a detailed description of the method.

Conventional commercially produced Panalytical X'PERT Pro MPD x-ray powder diffractometer with Co tube (λ = 1.7892 Å) was used for structural characterization of studied compounds.

2.3 Data analysis

2.3.1 Rietveld refinement

Introduced in 1969 by Hugo Rietveld the method originally worked with neutron powder data and later extended for X-ray radiation as well [179]. Since then it has become the most widely used tool for structural refinement. The Rietveld method itself is essentially a fitting algorithm that fits the experimental powder diffraction pattern by minimizing the function:

$$\chi^2 = \sum_{i=1}^{n} w_i (y_i - y_{ci})^2 \tag{2.88}$$

where y_i is the observed intensity at the i^{th} step of the pattern, y_{ci} is the calculated intensity at the i^{th} step of the pattern, $w_i = 1/\sigma_i^2$ is th weight of the individual step y_i and σ_i^2 is is the variance of the y_i observation. The sum is taken over all data points of the pattern. The calculated intensity is given by the following expression:

$$y_{ic} = y_{bi} + \sum_{\phi} S_\phi \sum_{G} j_{\phi G}\ L_{\phi G}\ A_{\phi G}\ O_{\phi G}\ |F_\phi(\mathbf{G})|^2\ \Omega_{i\phi G} \tag{2.89}$$

where y_{bi} is the background intensity at the angular position $2\theta_i$, S is the scale factor, proportional to the volume fraction of the phase ϕ, j_G is the multiplicity factor of the reflection appearing at $\mathbf{G}$, L is the Lorentz polarization factor, A is the absorption correction, O is the preferred orientation correction and Ω_{iG} is the peak shape function that includes both instrumental resolution and the microstructure parameters of the sample.

The first sum is taken over all contributing phases ϕ and the second one over neighbouring reflections contributing to a given data step i. The calculation of the peak profile for a given reflection $\mathbf{G}$ is done over a limited angular range around the peak centre position $2\theta_G$ due to a rapid fall of peak tails defined by the peak shape function. Background intensity is usually calculated by a linear interpolation between the data points where no peaks are observed or estimated by polynomial functions.

Minimization of χ^2 is done with least-squares procedures exploiting variation of Newton's method such as the Newton-Raphson algorithm [180] or Gauss-Newton method [181]. To estimate the goodness of fit several residual measures are introduced and defined as follows.

Profile factor:

$$R_p = 100 \frac{\sum_i |y_i - y_{ci}|}{\sum y_i} \tag{2.90}$$

shows the agreement between calculated profile and the data.

Weighted Profile Factor:

$$R_{wp} = 100 \left(\frac{\sum_i w_i (y_i - y_{ci})^2}{\sum_i w_i |y_i|^2} \right)^{1/2} \tag{2.91}$$

is rather a more straightforward agreement factor as it derived directly from the square root of the minimized quantity, scaled by the weighted intensities.

Expected Weighted Profile Factor:

$$R_{exp} = 100 \left(\frac{N - P + C}{\sum_i w_i y_i^2} \right)^{1/2}, \tag{2.92}$$

where N and P are the number of data points and refined parameters respectively and C is the number of constraints if any of them are introduced into the model. This quantity defines the best possible R_{wp} value that can be obtained for the given set of data. And the ratio between above two R-factors gives the reduced χ^2 of the fit:

$$\chi^2_\nu = \left(\frac{R_{wp}}{R_e xp} \right)^2 = S^2, \tag{2.93}$$

where S is the goodness of fit. Obviously, χ^2 should never be less than unity.

Bragg Factor:

$$R_{Bragg} = 100 \frac{\sum_i |\mathcal{I}_i - \mathcal{I}_{ci}|}{\sum \mathcal{I}_i}, \tag{2.94}$$

shows the agreement between calculated Bragg peak intensities and the data.

It is important to mention that the Rietveld method does not solve structures, thus a reasonably good starting model is required to perform the structure analysis. All structural refinements done within the present work were carried out using the FullProf program [152].

2.3.2 Reverse Monte Carlo technique in application for powder magnetic diffuse scattering

When it comes to description of disordered materials the reverse Monte Carlo (RMC) method becomes a perfect instrument to characterise local structural features [182, 183]. In some particular cases RMC has proven itself a valuable technique to describe magnetic materials in ordered states [184, 185]. However, the method can be extended to obtain an information about three-dimensional spin correlations of magnetic materials in paramagnetic state from powder diffuse magnetic scattering data [186]. The RMC method is model-independent, it means that it has nothing to do with a spin Hamiltonian. like it is done in the direct Monte Carlo simulations. In comparison to that, RMC method, instead of some energy term, minimizes the sum of square residuals that characterizes the disagreement between the experimental data and the fit.

In case of the magnetic RMC a large configuration of spins is initially defined in such a way as their positions are fixed to their crystallographic sites while a three-dimensional orientations are refined in order to fit the data. On the first step a supercell containing several thousands atoms with an appropriate boundary conditions is generated. Each atom is assigned with a classical spin vector with a random orientation, and the sum of square residuals is calculated:

$$\chi^2 = \sum_Q \left(\frac{I_{calc}(Q) - I_{exp}(Q)}{\sigma(Q)} \right)^2 \tag{2.95}$$

where I_{calc} and I_{exp} are calculated and experimental powder-averaged magnetic scattering intensies respectively, $\sigma(Q)$ is an experimental uncertainty. Next a random spin

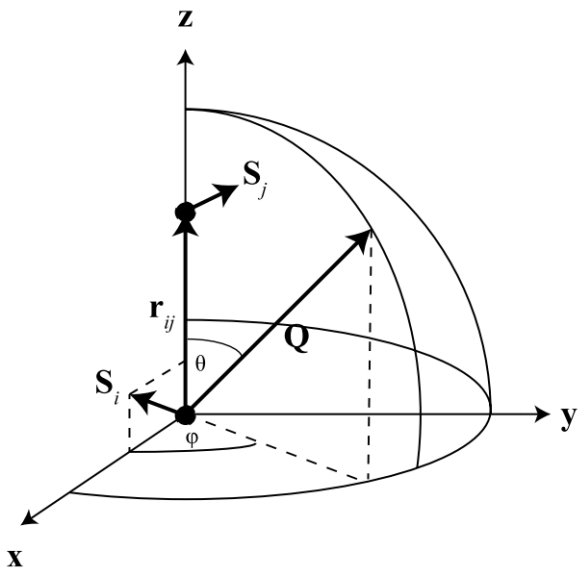

Figure 2.12: Local spherical coordinate system used for calculation of the powder-averaged magnetic neutron scattering intensity [188]

from the supercell is chosen and rotated by a small amount. A new spin vector is defined as

$$\mathbf{S}_i^{new} = \frac{\mathbf{S}_i + \Delta\mathbf{s}}{|\mathbf{S}_i + \Delta\mathbf{s}|} \tag{2.96}$$

where $\mathbf{s}$ is a unit vector with a random orientation and $0 < \Delta \leqslant 1$ is the maximum spin move length. After a move is proposed, the change in χ^2 is calculated and the proposed move is either accepted or rejected according to the Metropolis criterion [187]. This process is iteratively repeated until χ^2 is reduced to its limit. The final spin configuration represent correlations that are in agreement with experimental data.

In order to fit the data, the scale factor s is also being refined, which best value can be calculated after each step by minimizing χ^2 with respect to s which yields

$$s = \frac{\sum_Q (I_{calc}(Q) I_{obs}(Q))/(\sigma(Q)^2)}{\sum_Q (I_{calc})/(\sigma(Q)^2)}, \tag{2.97}$$

and if the data is placed on an absolute scale, the effective magnetic moment is then given by

$$\mu^2 = g^2 S(S+1) = s, \tag{2.98}$$

where g is the g-factor [188].

Scattering cross-section in this case can be written in terms of correlations between pairs of spins:

$$I(\mathbf{Q}) = \left(\frac{\gamma r_e}{2}\right)^2 (\mu F_M(\mathbf{Q}))^2 \left(\frac{2}{3} + \frac{1}{N}\sum_{i,j} \mathbf{S}_i^{\perp} \cdot \mathbf{S}_j^{\perp} \cos \mathbf{Q} \cdot \mathbf{r}_{ij}\right), \tag{2.99}$$

where $\mathbf{r}_{ij} = \mathbf{r}_i - \mathbf{r}_j$. The double sum in 2.99 excludes terms in which $i = j$. Self correlations are taken into account as the additive term 2/3.

The exact expression for $I(\mathbf{Q})$ implemented in SPINVERT program that was used for D7 data treatment was originally introduced in [189] and derived as follows. First, one should define a local coordinate system for each pair of spins $\mathbf{S}_i$ and $\mathbf{S}_j$ in the way as it is illustrated in figure 2.12. The $\mathbf{z}$ axis matches with the vector connecting $\mathbf{S}_i$ and $\mathbf{S}_j$; $\mathbf{x}$ axis is perpendicular to $\mathbf{z}$ and lies in the plane of $\mathbf{S}_i$; and the $\mathbf{y}$ axis is the remaining vector in the right-handed set. The new coordinate system is then

$$\begin{aligned} \mathbf{z} &= \frac{\mathbf{r}_{ij}}{r_{ij}} \\ \mathbf{x} &= \frac{[\mathbf{S}_i - (\mathbf{S}_i \cdot \mathbf{z})\mathbf{z}]}{|\mathbf{S}_i - (\mathbf{S}_i \cdot \mathbf{z})\mathbf{z}|} \\ \mathbf{y} &= \mathbf{z} \times \mathbf{x}. \end{aligned} \tag{2.100}$$

With the local coordinates one can put down

$$\mathbf{S}_i^{\perp} \cdot \mathbf{S}_j^{\perp} = \sum_{\alpha,\beta} \left(\delta^{\alpha\beta} - \frac{Q^{\alpha} Q^{\beta}}{Q^2} \right) S_i^{\alpha} S_j^{\beta} \tag{2.101}$$

where the components $\alpha, \beta \in [x, y, z]$ of $\mathbf{Q}$ are given in spherical coordinates:

$$\mathbf{Q} = [Q \sin\theta \cos\phi, Q \sin\theta \sin\phi, Q \cos\theta]. \tag{2.102}$$

Combining equations 2.99, 2.3.2 and 2.101 one arrives to the final expression for the scattered intensity

$$I(\mathbf{Q}) = \left(\frac{\gamma r_e}{2}\right)^2 (\mu F_M(\mathbf{Q}))^2 \left\{ \frac{2}{3} + \frac{1}{N} \sum_{i,j} \left(A_{i,j} \frac{\sin Q r_{ij}}{Q r_{ij}} + B_{ij} \left(\frac{\sin Q r_{ij}}{(Q r_{ij})^3} - \frac{\sin Q r_{ij}}{(Q r_{ij})^2} \right) \right) \right\} \tag{2.103}$$

where

$$A_{i,j} = S_i^x S_j^x, \tag{2.104}$$

$$B_{i,j} = 2 S_i^z S_j^z - S_i^z S_j^z. \tag{2.105}$$

The sum in the equation 2.103 is taken over all pairs of spins in the range of $0 < r_{ij} \leqslant r_{max}$. The maximum radial distance r_{max} is defined as the half length of the shortest side of the supercell.

Once the global spin configuration is obtained after minimization of residual between calculated and observed profile intensities, one can plot a radial spin correlation function that represents the average scalar product of pairs of spins at a distance r:

$$\langle \mathbf{S}(0) \cdot \mathbf{S}(r) \rangle = \frac{1}{n(r)} \sum_{i}^{N} \sum_{j}^{Z_{ij}(r)} \mathbf{S}_i \cdot \mathbf{S}_j, \tag{2.106}$$

where

$$n(r) = \sum_{i}^{N} Z_{ij}(r), \tag{2.107}$$

with $Z_{ij}(r)$ representing the number of spins j coordinating a central spin i at a distance r.

Chapter 3

Ordered and disordered cobalt-based spinel

In this chapter Co_5TeO_8 is considered in details. Indeed, this material belongs to a spinel family and the common notation is $(Co)[Co_{1.5}Te_{0.5}]O_4$. Depending on a synthesis routine this material could be obtained in two structural forms: disordered and ordered. Structural variance between these polymorph give rise to different magnetic behaviour that was thoroughly studied using bulk characterization methods and the neutron powder diffraction. To examine a possible tenability of magnetism and physical properties related to it, $A-$site magnetic dilution was introduced to the system. This eventually let us to plot a magnetic phase diagram of $(Co_{1-x/2}Zn_{x/2})[Co_{1.5}Te_{0.5}]O_4$ ordered spinel series. Magnetic field response of the ordered Co_5TeO_8 and $Co_4Zn_1TeO_8$ was studied with the small angle neutron scattering. All scattering techniques showed non-negligible diffuse scattering in the wide temperature range for all studied samples, which have become a reason to study short-range ordering in the system using XYZ-polarization analysis. Altogether, neutron scattering experiments carried out in the framework of the current research provided an exhaustive characterization of magnetism in the system, which was then compared to the results of the dielectric spectroscopy.

3.1 Synthesis and structural characterization

All studied samples of pure Co_5TeO_8 and $Co_{5-x}Zn_xTeO_8$ family are available only in powder form and were prepared by solid-state reactions method. There are two synthesis routines to prepare pure Co_5TeO_8 compound (Fig. 3.1). The first one lays in preparing a stoichiometric mixture of $Co(OH)_2$ (Aldrich 99%) and TeO_3 (Cerac 99.9%) with 5 to 1 ratio. These precursors are thoroughly ground in an agate mortar and then heated in platinum crucible at 750^oC for 20 hours under nitrogen flux with a heating rate of $2^oC/min$ followed up by a rapid cooling following the furnace inertia. After initial synthesis the sample is regrinded and heated for a second time at 750^oC for 10 hours with the same heating and cooling protocol. Another way is to mix $Co(OH)_2$ (Aldrich 99%) with $Te(OH)_6$ (Alfa Aesar 99%) with a ratio of 5:1.1. A slight excess of $Te(OH)_6$ is necessary to prevent unnecessary Co oxidation due to a tendency of Te to volatilize at high temperatures. This precursors are also ground in an agate mortar, and heated at 940^oC for 20 hours under nitrogen flux with a heating rate of $2^oC/min$, after the sample is slowly cooled down to the temperature in 24 hours.

To study the magnetic behaviour of the system upon magnetic dilution a series of $Co_{5-x}Zn_xTeO_8$ with $0 \leqslant x \leqslant 1$ powder samples were synthesized via solid-state reactions.

For this purposes $Co(OH)_2$ (Aldrich 99%), ZnO (Alfa Aesar 99%), $Te(OH)_6$ (Alfa Aesar 99%) with the respective ratio of 5-x:x:1.1. After grinding in an agate mortar, precursors were heated at 740^oC in platinum crucibles for 20 hours under a constant flux of nitrogen gas, with a heating rate of $2^oC/min$. Then samples were cooled in two ways: first, rapid cooling following the furnace inertia, second slow cooling to the room temperature in 24 hours.

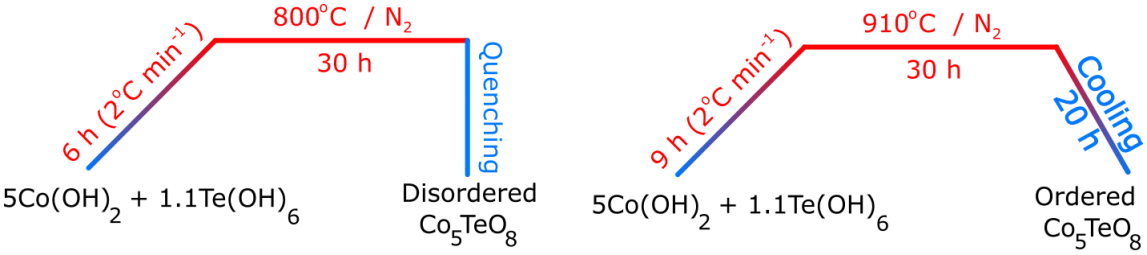

Figure 3.1: A schematic representation of synthesis routine of the disordered (left) and ordered (right) Co_5TeO_8 phases.

Rietveld refinement of the NPD data recorded at the 3T2 diffractometer on the sample prepared with the first routine (Fig. 3.2) revealed the nuclear structure to be of $Fd\bar{3}m$ (#227) space group with the unit-cell parameter $a = 8.5572(2)$Å. The model used for the refinement assumed mixed occupancy of Co^{2+} and Te^{6+} at the octahedral site with a ratio 0.75/0.25 respectively in agreement with the nominal chemical composition and no mixing at the A-site since Te^{6+} cannot adopt tetrahedral environment. Atomic positions and isotropic thermal parameters were refined for all sites as well as the occupancy parameters of the mixed octahedral $16d$ site. No significant deviation from the nominal values 0.75/0.25 for Co/Te ratio was observed. Since the cationic distribution at the B-site is random, later in the text this polymorph will be referred as the disordered Co_5TeO_8. Besides peaks of the main Co_5TeO_8 phase several impurity reflections were observed. The phase analysis revealed presence of three phases within the sample: Co_5TeO_8, Co_3TeO_6 and Co_3O_4 with a respective mass concentration of 92.21(81)%, 0.33(71)% and 7.45(24)%. Details of the Rietveld refinement of Co_5TeO_8 polymorphs are provided in the table A.1 in the appendix A.

Combined X-ray and Neutron powder diffraction studies at room temperature revealed that the sample prepared with the second routine is impurity-free. In addition to main spinel peaks both XRPD and NPD patterns show the existence of additional reflections at low 2θ angles typical for ordered spinel phases [190]. These patterns were indexed and refined with the non-centrosymmetric $P4_332$ (#212) space group with the unit cell parameter $a = 8.5531(1)$Å (Fig. 3.3). A significant anisotropic peak broadening breaking the F-centring of the cubic structure is observed. This is a well-known phenomenon within ordered spinel materials that indicates the presence of antiphase domains [191]. Considering this effect required the use of anisotropic size-model-function "-2" in FullProf that allows an independent fitting of broadened peaks widths with a certain set of (hkl) indices, $h + k = 2n + 1$ and $k + l = 2n + 1$ particularly in this case. In this structure the B-site corresponds to two crystallographic sites with $4b$ and $12d$ Wyckoff positions. For the initial model it was assumed that the $4b$ and $12d$ positions are fully occupied with Te^{6+} and Co^{2+} respectively. Rietveld refinement does not show any disorder between $4b$ and $12d$ sites, so this particular cationic arrangement as well as the polymorph adopting this structure will be further referred as the ordered Co_5TeO_8.

The atomic coordinates and thermal displacement parameters of both Co_5TeO_8 polymorphs are summarized in the table 3.1. Selected interatomic distances are given in the

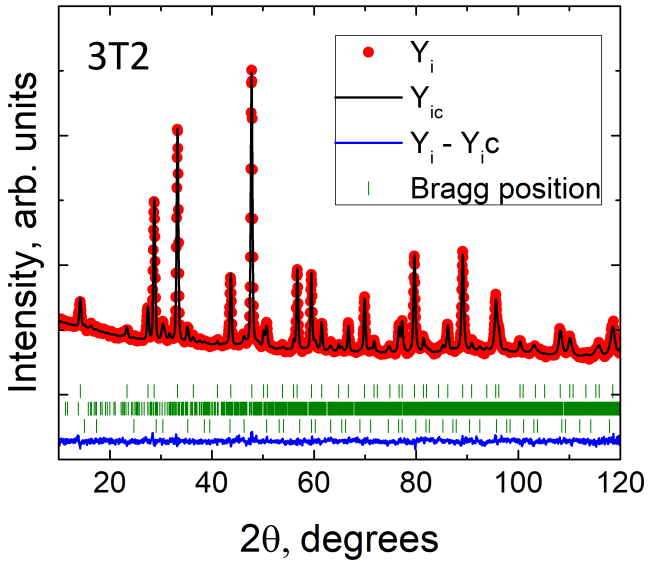

Figure 3.2: Rietveld refinement results performed on a room temperature NPD pattern of the disordered Co_5TeO_8. Red dots - experimental data, black line - calculated intensity, blue line - difference between the experimental data and the calculated intensity, vertical green ticks represent position of Bragg reflections of (top row) Co_5TeO_8 ($Fd\bar{3}m$), (middle) Co_3TeO_6 and (bottom) Co_3O_4. Reliability factors: $R_p = 2.42$, $R_{wp} = 2.99$, $R_{exp} = 2.29$, $\chi^2 = 1.71$.

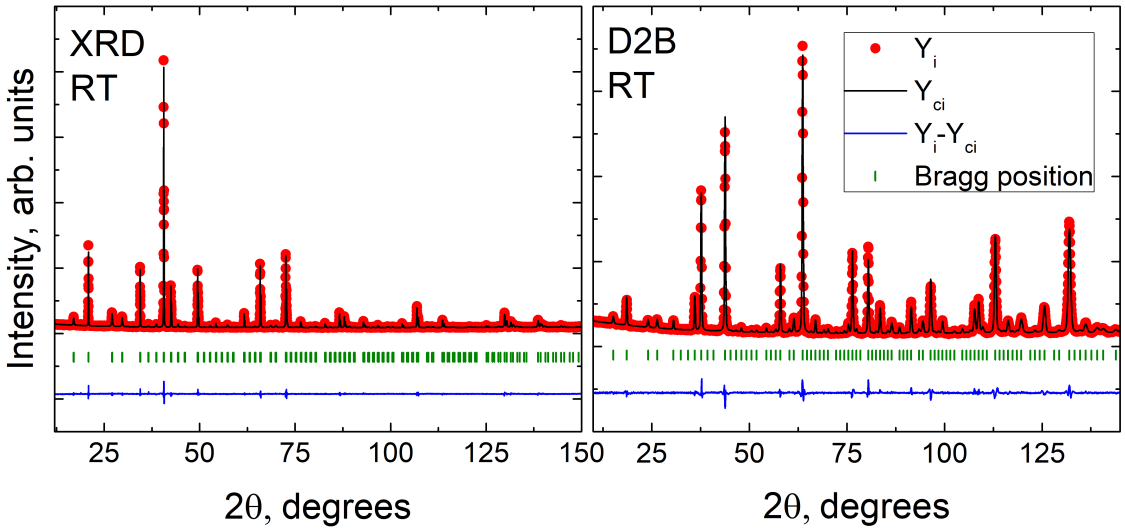

Figure 3.3: Results of the combined X-ray and neutron Rietveld refinement performed on room temperature NPD patterns of the ordered Co_5TeO_8. Red dots - experimental data, black line - calculated intensity, blue line - difference between the experimental data and the calculated intensity, vertical green ticks represent position of Bragg reflections. Reliability factors: XRD) $R_p = 2.93$, $R_{wp} = 3.10$, $R_{exp} = 2.98$; NPD) $R_p = 2.71$, $R_{wp} = 3.37$, $R_{exp} = 4.57$; $\chi^2 = 2.54$.

table A.2 in the appendix A. The bond valence sums (BVS) calculated with parameters given in the reference [192] together with polyhedra distortions for the ordered Co_5TeO_8 were determined with the use of BondStr program of the FullProf Suite and are presented

in the table A.3 in the appendix A as well.

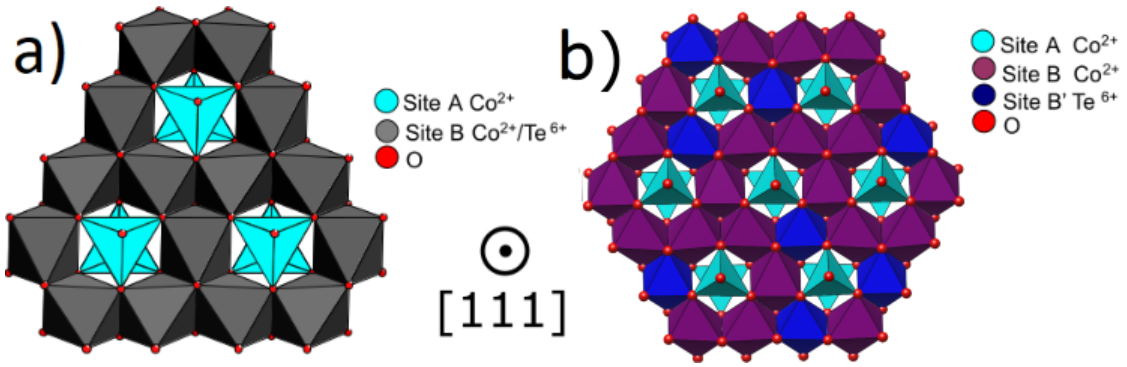

Figure 3.4: Kagome layers of a) the ordered and b) the disordered polymorph of Co_5TeO_8

Within the ordered Co_5TeO_8 structure two types of octahedral sites are identified: B and B' (Fig 3.4a). Hexagonal cavities found in Kagome layers are alternately surrounded by three B and three B' octahedra and then five B octahedra and one B' octahedron. Likewise the original spinel structure, two out-of-Kagome-plane tetrahedrons corresponding to the *A*-site are adjacent to hexagonal cavities. The disordered polymorph structure is built of regular polyhedra, all pairs of Co_1/Te_1-O_1 and Co_2-O_1 distances are of 2.0577(5) Å and 2.0000(4) Å for octahedral and tetrahedral environments respectively. Considering ionic radii [193] of Co^{2+} at the high-spin state (r_i = 0.58Å for coordination number 4, r_i = 0.745Å for coordination number 6) one can get Co−O distances for octahedral and tetrahedral coordination to be of 2.125 Å and 1.96 Å respectively; Te−O bonds for Te^{6+} in octahedral oxygen environment is 1.94 Å. The observed bond distance of an octahedral site lies in between the calculated values for Co^{2+} and Te^{6+} cations and the size and the charge difference between these two cations, occupying the same octahedral site, r = 0.65Å for Co^{2+} and r = 0.56Å for Te^{6+}, must be the reason of the disordered Co_5TeO_8 phase metastability. Distortions of cobalt polyhedra are involved in the transformation from the disordered cubic F to the ordered cubic P structure. In ordered Co_5TeO_8, the distortions of 12.522×10^{-4} and 3.98×10^{-4} for $[CoO_6]$ and $[CoO_4]$ respectively while the no distortion is observed for $[TeO_6]$ octahedra. These distortions also cause a shortening of Co−Co distances between neighbouring octahedra, reducing them from 3.0254(1)Å in the disordered phase to 2.9528(18) and 2.9532(24)Å in the ordered phase. As a consequence, the J_{BB} magnetic exchange should be also modified, which can result in a variation of magnetic properties of the ordered polymorph.

All samples of the $Co_{5-x}Zn_xTeO_8$ family were found to be impurity-free. XRD and NPD displayed a presence of superstructure reflections similar to those observed for the ordered polymorph and a subsequent combined X-ray and neutron Rietveld refinement at room temperature revealed that regardless to the way samples were cooled down during the synthesis routine, all $Co_{5-x}Zn_xTeO_8$ adopt ordered $P4_332$ structure. Remarkably, up to x = 1, Zn^{2+} occupies exclusively *A*-site 8*c* position, which allows both: a release of magnetic frustration at tetrahedral site and a fine tuning of the J_{AB} exchange interaction crucial for the stabilization of spiral-spin ordering. All studied samples of the $Co_{5-x}Zn_xTeO_8$ are listed in the table 3.2, atomic positions are listed in tables A.4 - A.9 in the appendix A.

Table 3.1: Atomic positions and U_{iso} parameters for both Co_5TeO_8 polymorphs.

Atom	Wyckoff pos.	Occ.	x	y	z	U_{iso} (Å^2)
Disordered, space group $Fd\bar{3}m$, a = 8.5541(1) Å, V = 625.94(1) Å^3.						
Co_1	8a	1	1/8	1/8	1/8	0.0113(9)
Co_2	16d	0.772(7)	1/2	1/2	1/2	0.0070(5)
Te_2	16d	0.228(7)	1/2	1/2	1/2	0.0070(5)
O_1	32e	1	0.25984(6)	0.25984(6)	0.25984(6)	0.01106(20)
Ordered, space group $P4_332$, a = 8.5531(1) Å, V = 625.43(1) Å^3.						
Co_1	8c	1	0.5008(3)	0.4992(3)	-0.0008(3)	0.0047(3)
Co_2	12d	1	0.3871(2)	0.8629(2)	1/8	0.0042(5)
Te_3	4b	1	1/8	7/8	3/8	0.0035(4)
O_1	8c	1	0.3707(3)	0.6293(3)	0.1293(3)	0.0061(8)
O_2	24e	1	0.35193(17)	0.8658(3)	0.3733(2)	0.0048(4)

Table 3.2: Cell parameters and the A-site zinc content of the $Co_{5-x}Zn_xTeO_8$ family.

x	a, Å	A-site Zn^{2+} content, %
0.04	8.5543(2)	2.04
0.21	8.5533(1)	11.5
0.38	8.5527(2)	19
0.58	8.5524(1)	29
0.76	8.5512(2)	39.9
1.01	8.5514(2)	50.6

3.2 Magnetic behaviour

The magnetic behaviour of both Co_5TeO_8 polymorphs was firstly characterized by magnetic susceptibility measurements at low temperature (Fig. 3.5 left). Comparing both $1/\chi$ curves as a function of temperature and despite structural differences, both samples seem to present rather similar behaviour: high temperature paramagnetic parts of $\chi(T)$ for the ordered and disordered Co_5TeO_8 match and nicely follow a Curie-Weiss behaviour and a linear fitting of an inverse susceptibility in both cases gives the same results: $\mu_{eff} = 10.6\mu_B$ per formula unit, i.e $4.7\mu_B$ per Co^{2+} ion, and a strongly negative Weiss temperature $\Theta = -148K$ revealing predominance of antiferromagnetic interactions. The resulting value of the μ_{eff} is in agreement with a calculated value for Co^{2+} cation ($3d^7$) in high spin state with a largely unquenched orbital moment. Remarkably, $1/\chi$ temperature evolution deviates from the Curie-Weiss law below $T \leq 140K$. This, in fact, may have several explanations: first, a magnetic clustering can take place at temperatures well above the temperature of the long-range ordering [194]; second, it can be a characteristic feature of a ferrimagnetic structure with different sublattices [127]. Strong increase of the mag-

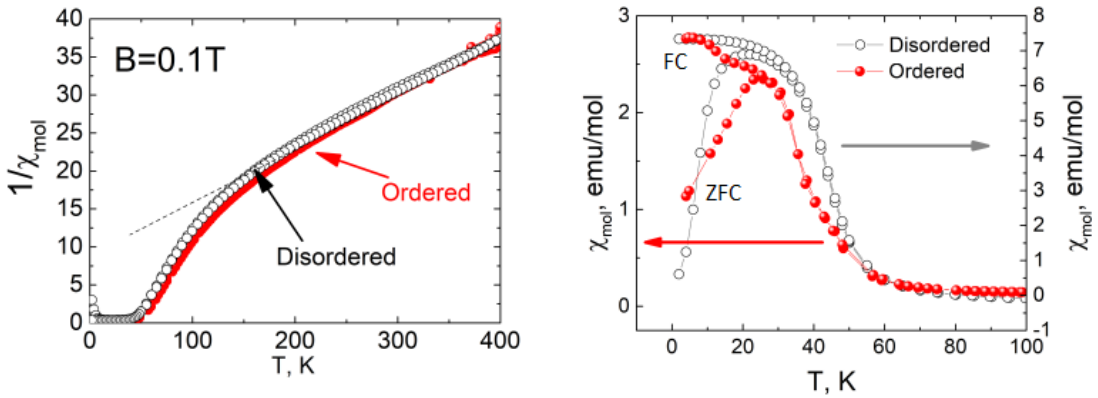

Figure 3.5: Temperature evolution of the inverse magnetic DC susceptibility (left) and magnetic DC susceptibility (right) measured at B = 0.01 T.

netic response is observed below 50 K as well as thermal hysteresis after field and cooling (FC) and zero field cooling procedure (Fig. 3.5 right). Regardless to all similarities, the ordered polymorph demonstrate lower magnitude of χ as well as some difference in the shape of $\chi(T)$ can be spotted.

Figure 3.6 illustrates magnetization loops measured at $T = 4K$. Again, both polymorphs share the same ferrimagnetic magnetization $M_S = 2.5\mu_B$ per formula unit for $B = 5$ T. However, $M(B)$ dependence reveal a certain difference in behaviour of these two polymorphs. The disordered Co_5TeO_8 shows a typical hysteresis loop shape of a long-range ordered ferro- or ferrimagnet, with a coercivity $B_c = 0.38T$ and remnant magnetization $M_r = 1.4\mu_B/f.u.$. Contrary to that, the ordered Co_5TeO_8 shows features of a rather soft magnetic material with small coercivity $B_c = 0.06$ T and remnant magnetization $M_r = 0.7\mu_B/f.u.$ that resembles the $M(B)$ behaviour of $CoCr_2O_4$ spinel [62, 144]. Remarkably, the magnetization is far from the expected value for the fully ordered system, which may also imply two scenarios. A non-collinear ferrimagnetic ground state with Yafet-Kittel triangular spin arrangement [195] is possible in this case as well as a presence of some sort of short-range magnetic ordering that is persisted down to the low temperatures.

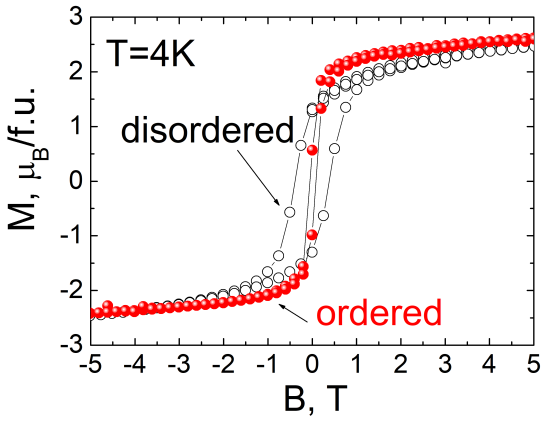

Figure 3.6: Magnetization hysteresis loops of both Co_5TeO_8 polymorphs measured at 4 K.

For a more accurate characterization of the magnetic transitions appeared on DC susceptibility curves, the AC magnetic susceptibilities were measured on the ordered polymorph. The advantage of this measurement is that it is more sensitive to subtle changes in magnetization and happens to be a perfect tool for determining the temperatures of the magnetic phase transitions. Figure 3.7 illustrates the temperature evolution of the AC magnetic susceptibility of the ordered Co_5TeO_8. The $\chi'(T)$ curve shows two distinct maxima at 40 K and 27 K pointing out a possible presence of two magnetic phase transitions in the compound. The imaginary component of the magnetic susceptibility $\chi(T)$, representing dissipative processes, is fairly small, however it coincides with the shape of the $\chi'(T)$, which is consistent with the presence of two consecutive magnetic transitions at 40 and 27 K at B = 0.01 T for the ordered Co_5TeO_8.

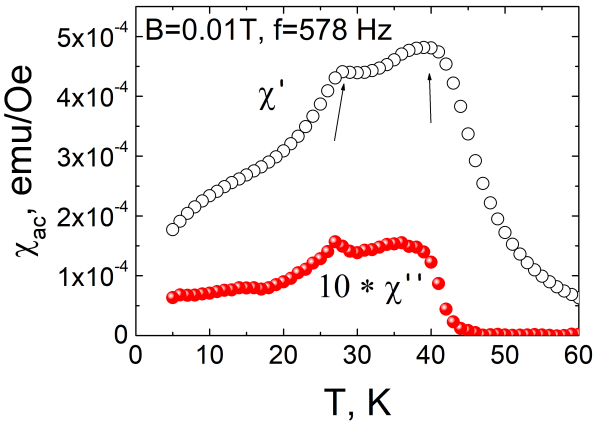

Figure 3.7: The AC magnetic susceptibility of the ordered Co_5TeO_8 polymorph measured with an applied field B= 0.01 T and operating frequency $f = 578$ Hz; χ' and χ" are the real and imaginary components of the AC susceptibility.

Eventually, field-dependent AC susceptibility measurements were able to provide first insights on $B(T)$ magnetic phase diagram of both polymorphs (Fig. 3.8). The disordered Co_5TeO_8 exhibits a single magnetic phase transition up to B = 0.2 T with a probable phase of a long-range ferro- or ferrimagnetic ordering. The ordered polymorph, in turn, shows two different ordered magnetic phases named FM/FI-1 and FM/FI-2 (Fig. 3.8 right). The first phase only exists between 38 and 27 K and is suppressed by applying a magnetic field B = 0.08 T. It is clear that the Co^{2+}/Te^{6+} ordering on the B and B' octahedral sites induces an intricate magnetic behaviour. Nevertheless, the true nature of the ordered magnetic phases at low temperature for both polymorphs can only be determined by neutron scattering.

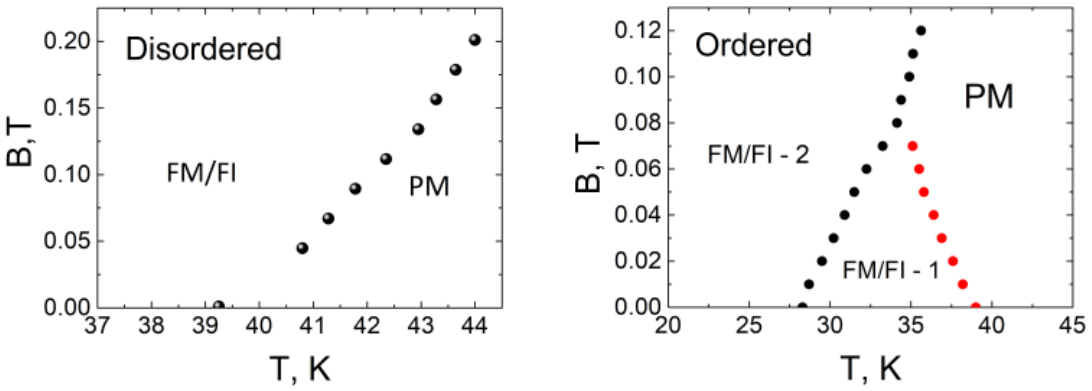

Figure 3.8: Magnetic phase diagrams for the disordered (left) and the ordered (right) Co_5TeO_8 polymorphs. PM stands for paramagnetic, FM - ferromagnetic, FI - ferrimagnetic.

3.3 Magnetic structures of Co_5TeO_8

3.3.1 Disordered Co_5TeO_8

Let us first consider the disordered Co_5TeO_8. Temperature evolution of NPD patterns, obtained at G4-1 diffractometer, shows two important characteristic features: first, a significant background enhancement at low diffraction angles appearing below 195 K, followed by a large increase of (111) and (220) diffraction peaks intensity below 40 K (Fig. 3.9 left). The diffuse scattering development at high temperatures corresponds to the emergence of short-range-ordered magnetic clusters as previously observed in various magnetic spinels [196, 197, 198]. The right graph on the figure 3.9 displays the variations of the integrated intensity of the magnetic diffuse halo and the (111) Bragg reflection, as a function of the temperature. Diffuse scattering arises well above the temperature of the long-range ordering, reaching its maximum intensity at 50 K. Below 50 K, the diffuse scattering loses part of the intensity and below 40 K the intensity of (111) reflection increases significantly, pointing out the development of the long-range magnetic ordering. Remarkably, at the lowest temperature of 1.7 K the intensity of the diffuse scattering is not reduced to zero.

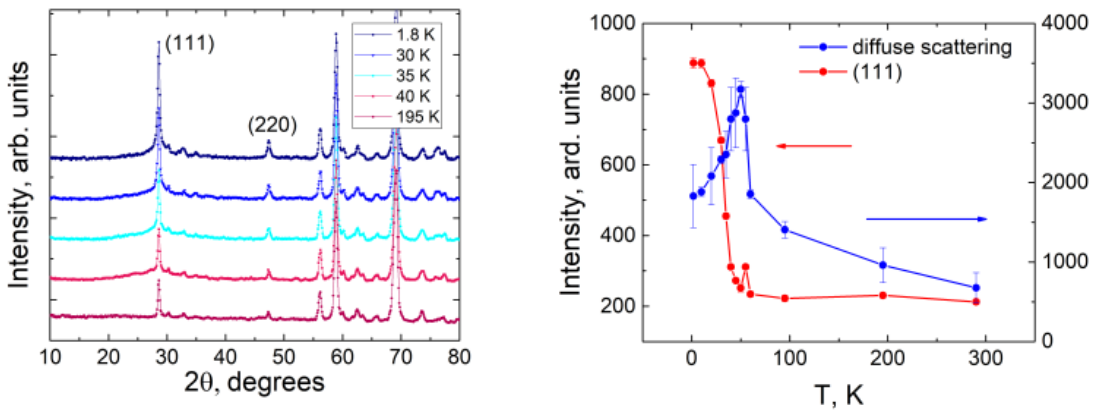

Figure 3.9: Disordered Co_5TeO_8. Evolutions as a function of the temperature of; - left, a set of NPD diagrams; -right, integrated intensities of the diffuse scattering and the Bragg peak (111).

Since Neutron Powder Diffraction (NPD) exhibits no additional Bragg reflections below T_N =40 K, but only the increase of some nuclear peaks intensity, the magnetic unit cell matches with the nuclear one and the propagation vector of the magnetic structure is therefore $\mathbf{k}$ =0. A list of ten (four cubic, four tetragonal and two orthorhombic) maximal magnetic symmetries for the given $\mathbf{k}$-vector and the parent $Fd\bar{3}m1'$ paramagnetic space group was determined with the MAXMAGN program of the Bilbao Crystallographic server [199]. Rietveld refinement revealed that only one magnetic space group, tetragonal $I4_1/am'd'$ (#144.557), provides a model that fits NPD patterns with an acceptable agreement (Fig. 3.10).

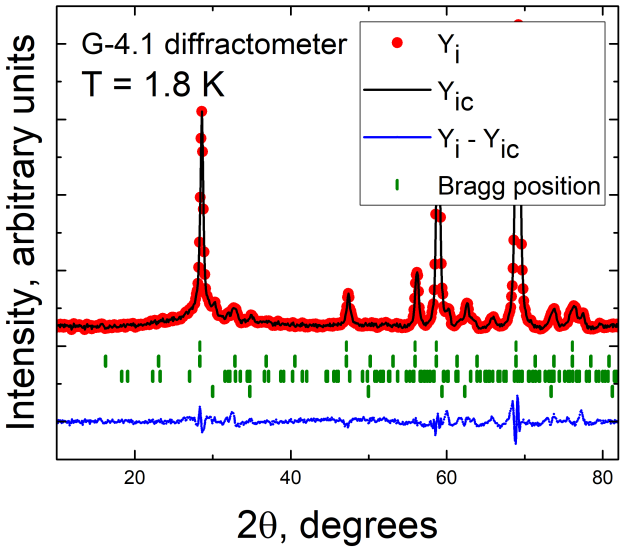

Figure 3.10: Results of the Rietveld refinements of the magnetic structure of disordered Co_5TeO_8 polymorph.

The magnetic structure of the disordered Co_5TeO_8 at T = 1.7 K was found to be collinear ferrimagnetic with magnitudes of magnetic moments for Co^{2+} cations at tetrahedral and octahedral sites of $\mu_{Co1} = 2.39(7)\mu_B$ and $\mu_{Co2} = -1.96(6)\mu_B$ respectively at T = 1.7 K. Magnetic structure and the evolution of magnetic moments as the function of the temperature are presented in the figure 3.11, parameters of the magnetic structure are given in the table A.10 in the appendix A. Reduced value of magnetic moments (Spin-only magnetic moment $\mu = 3.88\mu_B$ for Co^{2+} at a high-spin state) at both sites together with the presence of the magnetic diffuse scattering at low-temperature indicate that the magnetic subsystem is not perfectly ordered even at low temperatures. Explanations of such behaviour might be as follows: the random distribution of non-magnetic Te^{6+} cations on B-sites breaks the regularity in J_{AB} and J_{BB} exchange pathways, which, in turn, prevents the system from complete ordering. Short-range-ordered clusters, responsible for the magnetic diffuse scattering, however, should have magnetic correlations resembling those of the ferrimagnetic structure of the long-range ordered state, since the diffuse magnetic halo is centered around the (111) Bragg peak.

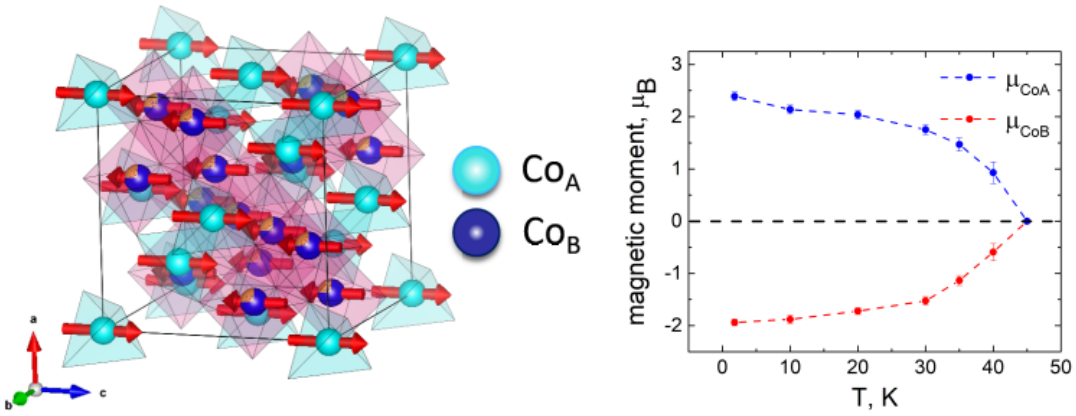

Figure 3.11: The magnetic structure at T = 1.7 K (left) and the evolution of the magnitude of magnetic moments as the function of the temperature of the disordered Co_5TeO_8 polymorph.

3.3.2 Ordered Co_5TeO_8

While the magnetic behaviour of the disordered polymorph stays relatively simple, the behaviour of the ordered Co_5TeO_8 is rather complex. The evolution of NPD patterns with the temperature is illustrated in the figure 3.12 (left). As observed for the disordered polymorph, the diffuse magnetic scattering is centered around the fundamental (111) Bragg peak, it emerges below 200 K and its intensity increases until 50 K. Again, this feature points out an appearance of short-range magnetic correlations. At T_{C1} = 45 K satellite reflections appears on NPD patterns. The sharper ones are located on either side of fundamental reflections with (hhh) and $(hh0)$ indices. These satellite reflections are indexed with a propagation vector $\mathbf{k}_i = (0, 0, \delta)$ with $\delta = 0.126$ at T_{C1}. Therefore the long-range magnetic ordering that sets in, corresponds to an incommensurate magnetic structure. Between 45 K and 30 K a considerable decrease of magnetic diffuse scattering intensity is counterbalanced with the increase of the satellites intensities. The k_z component of the propagation vector also decreases to $\delta = 0.086$. Thus, in this temperature interval, the increase of the incommensurate modulation period follows the extension of long-range magnetically ordered domains.

At T_{C2} = 27 K some substantial changes on NPD patterns take place. Magnetic satellites abruptly drift away from fundamental reflections, acquiring the position corresponding to the $\mathbf{k}_z \approx 0.14$ that remain stable down to 1.7 K (Fig. 3.12 right). A change of the value of propagation vector occurs simultaneously with the enhancement of the intensity of the main (111) reflection and the decrease of the intensity of the satellite reflections. This behaviour looks like the case of $CoCr_2O_4$ spinel, implying that below T_{C2} two magnetic components, an incommensurate modulated and ferrimagnetic one, described with $\mathbf{k}_0 = 0$, coexist. Furthermore, below T_{C2} no diffuse scattering is observed anymore, meaning that long-range magnetic domains are completely ordered.

Incommensurate magnetic structure of the ordered Co_5TeO_8 was solved, using the NPD pattern collected at 30 K, as satellite reflections are most pronounced at these temperatures. On the first step, integrated intensities of magnetic peaks were retrieved using profile matching fit (Jbt = 2 option in FullProf). Next step was to deduce possible symmetry constraints. For that a simulated annealing search was done for a triclinic $P1$ unit cell with 20 Co^{2+} atoms (8 at tetrahedral and 12 at octahedral sites) respecting cell translation. Intensities of magnetic reflections were calculated, considering conical magnetic structure in real space (Jbt = 5 option in FullProf). In this routine each Co^{2+} cation

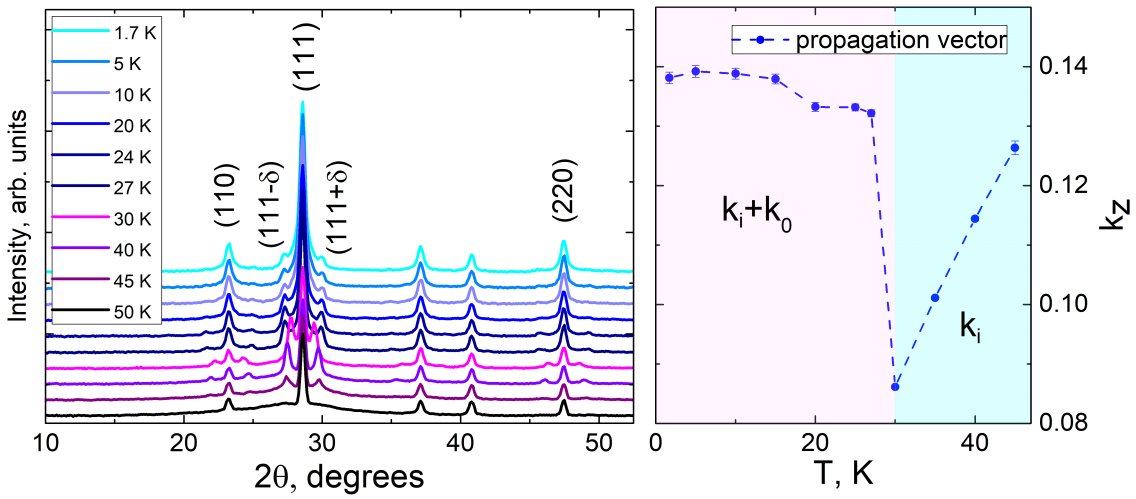

Figure 3.12: Evolution as a function of the temperature of the low-angle part of the NPD patterns (left) and $\mathbf{k}_z$ component of the propagation vector (right) of the ordered Co_5TeO_8 polymorph. In the temperature region between T_C1 and T_C2 only incommensurate $\mathbf{k}_i$ contribution is present on NPD patterns, whereas below T_C2, the magnetic structure is described with a sum of incommensurate $\mathbf{k}_i$ and commensurate $\mathbf{k}_0$ components.

was assigned with three parameters, describing magnetic moments: M - magnitude of the magnetic moment in Bohr magnetons, Φ_c - half of a cone angle in degrees, and P - magnetic phase in fractions of 2π. At first, all parameters of each Co^{2+} cation were set free, however several independent simulated annealing runs revealed that atoms within the same oxygen environment tend to adopt close values of M, Φ_c and P parameters. So Co^{2+} cations sharing same positions in $P4_332$ structure were restrained to have the same M, Φ_c and P. Simulated annealing search and a subsequent Rietveld refinement using this model provided good agreement with the results of powder diffraction, giving final parameters $\mu_{Co1} = 2.49(5)\mu_B$, $\Phi_c^{Co1} = 62.33^o(1.96^o)$, $P_{Co1} = 0$ for Co_1 and $\mu_{Co2} = 3.05(4)$, $\Phi_c^{Co2} = 124.51^o(1.47^o)$, $P_{Co2} = 0.57(1)$ for Co_2 (the phase of Co_1 was fixed to zero to to take an origin of the arbitrary global phase that is lost a diffraction experiment). This results in ferrimagnetic spiral spin structure with magnetic moments of Co_1 and Co_2 (Co^{2+} cations at A- and B-sites respectively) coupled antiferromagnetically along c-axis.

Possible magnetic space groups were sought using ISODISTORT tool [200, 201]. The notations for the irreducible representations and the number of superspace groups used below are adopted from ISODISTORT. Since there are two magnetic contributions to NPD patterns, a commensurate $\mathbf{k}_0$, providing strong enhancement of the fundamental (111) reflection at low temperatures and an incommensurate modulation, giving rise to satellite reflections with the propagation vector $\mathbf{k}_i = (0, 0, \delta)$, the combination of these two vectors was used to build a magnetic superspace groups. Together $\mathbf{k}_i$ and $\mathbf{k}_0$ provide a superposition of the corresponding magnetic irreducible representations, that, in turn provided 72 possible magnetic superspace group models. All these models obtained with ISODISTORT were then tested with simulated annealing search using the superspace formalism in spherical coordinates implemented in FullProf (jbt = -7). The best agreement factors were found for the $P4_3(00\gamma)0$ (#78.1.19.1.m19.1) magnetic superspace group, which is given independently by three combinations of magnetic irreducible representations: $m\Gamma_1 + m\Delta_3$, $m\Gamma_2 + m\Delta_3$, $m\Gamma_4 + m\Delta_3$. The Rietveld refinement using the obtained model revealed that magnetic structure of the ordered Co_5TeO_8 is described with $P4_3(00\gamma)0$ magnetic

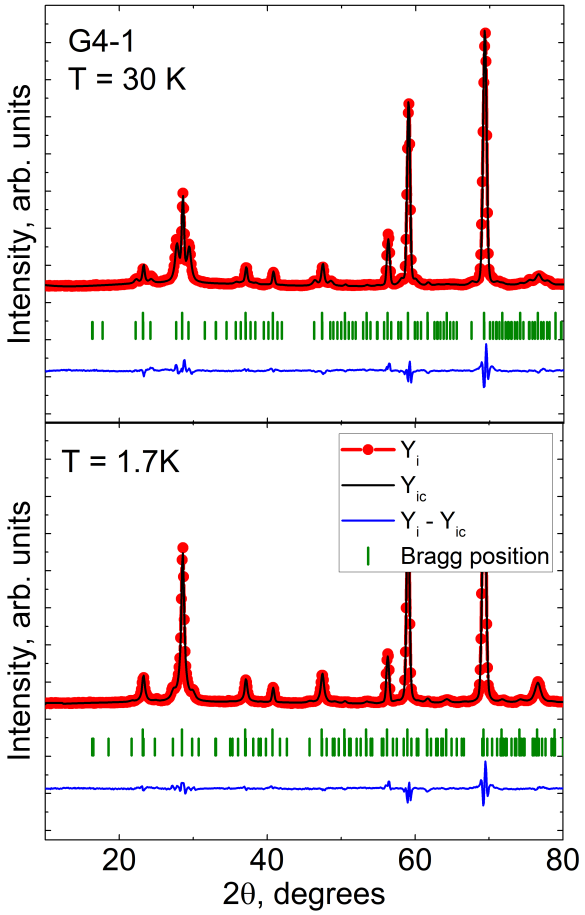

Figure 3.13: Results of Rietveld refinement of Co_5TeO_8 NPD patterns with $P4_3(00\gamma)0$ (#78.1.19.1.m19.1) magnetic superspace group: top) 30 K, bottom) 1.7 K . Red dots - experimental data, black line - calculated intensity, blue line - difference between the experimental data and the calculated intensity, vertical green ticks represent position of Bragg reflections.

superspace group in both high ($T_{C1} < T < T_{C2}$) and low ($T_{C2} < T < 1.7K$) temperature regions (Fig. 3.13).

Symmetry reduction from the original paramagnetic $P4_332'$ cubic space group to tetragonal $P4_3(00\gamma)0$ implies position splitting. Both Co^{2+} positions, A-site *8c* and B-site *12d* are split in two and three *4a* positions respectively. No symmetry constraints are imposed on magnitudes and orientation of modulation functions of any Co^{2+} site within the obtained $P4_3(00\gamma)0$ superspace group and the total number of free parameters describing magnetic structure within this model is 45 (three parameters to describe the direction of a magnetic moment in polar coordinates and six parameters describing magnetic moment modulation, all together $(3 + 6) \times 5 = 45$). At this moment, to reduce the number of refined parameters, symmetry constraints deduced from simulated annealing in $P1$ space group mentioned above were applied: magnetic moments of Co with the same oxygen environment were forced to have the same parameters; A- and B- site spins were set to have antiparallel directions along crystallographic c-axis.

The magnetic structure itself is represented by the conical spin arrangement with Co^{2+} magnetic moments at tetrahedral and octahedral sites coupled antiferromagnetically along the crystallographic c-axis on the entire temperature range where the long-range

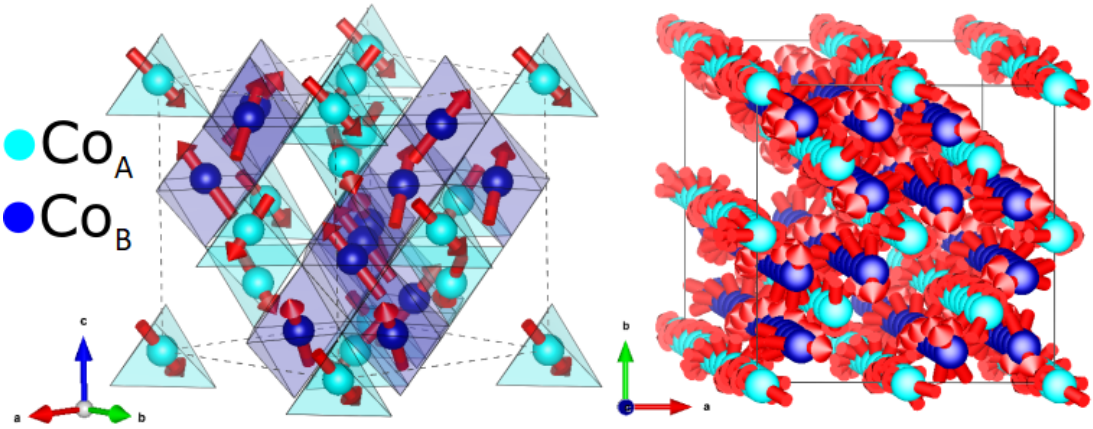

Figure 3.14: Magnetic structure of the ordered Co_5TeO_8 polymorph at 30 K.

ordering exists (Fig. 3.14). Remarkably, the same magnetic superspace group describes the magnetic structure of the ordered Co_5TeO_8 polymorph in both high temperature ($T_{C1} < T < T_{C2}$) and low temperature ($T_{C2} < T < 1.7K$) regions, so the second phase transition indicates a spin reorientation represented by an abrupt change in the magnetic moments cone angles. Magnetic moments of *A*- and *B*- site spins also reach saturation below T_{C2} with $\mu_{Co1} = 2.68(7)\mu_B$ and $\mu_{Co2} = 3.36(7)\mu_B$ at 1.7 K (Fig. 3.15). Large non-zero values of magnetic moments at both tetrahedral and octahedral sites at T_{C1} indicate that above 45 K the system is not purely paramagnetic but contains short-range ordered domains. Eventually, one can think about the magnetic structure of the ordered polymorph as the ferrimagnet with a modulated distortion perpendicular to the *c*-axis. An incommensurate spin modulation is obviously originated from the cationic arrangement, however at T_{C2} the periodicity of the modulation decreases together with the tilt of the spins from the c -axis, so the low-temperature phase is less distorted. The latter means that even though the magnetic structure is incommensurate ferrimagnetic at the temperatures below T_C1 down to 1.7 K, the spin configuration of the low temperature phase is closer to be a conventional ferrimagnet in comparison to the high temperature one. Parameters of the ordered Co_5TeO_8 polymorph magnetic structure at 30 K and 1.7 K are given in the table A.11 in the appendix A. Section A.2 in the appendix contains .mcif files for disordered Co_5TeO_8 at T = 1.7 K and ordered Co_5TeO_8 at T = 1.7 K and 30 K.

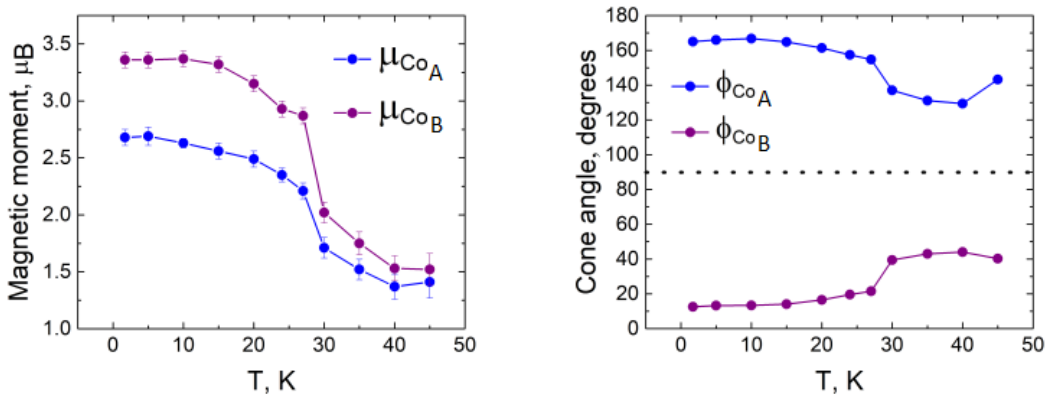

Figure 3.15: Temperature variation of the magnetic moment (left) and the cone angle (right) of the ordered Co_5TeO_8 polymorph.

3.4 *A*-site magnetic dilution

This paragraph discusses the evolution of magnetism in the ordered Co_5TeO_8 polymorph upon increase of Zn^{2+} in the system. For readers' convenience, it's better to remind that $Co_{5-x}Zn_xTeO_8$ notation that will be used frequently down below may be rewritten in the common spinel notation as $(Co_{1-x/2}Zn_{x/2})[Co_{1.5}Te_{0.5}]O_4$, which explicitly shows that the magnetic dilution takes place exclusively at the tetrahedral position.

Influence of the *A*-site magnetic dilution were first studied by SQUID magnetometry technique. Temperature evolution of the magnetic susceptibility (Fig. 3.16) revealed that upon increase of the Zn^{2+} content in $Co_{5-x}Zn_xTeO_8$, the system exhibits a decrease of the magnetic response together with a shift of the $\chi(T)$ maxima towards lower temperatures. However, even large magnetic dilution in case of x = 1, where the half of the 8*c* site is occupied with the non-magnetic cation, does not eliminate magnetic signal entirely.

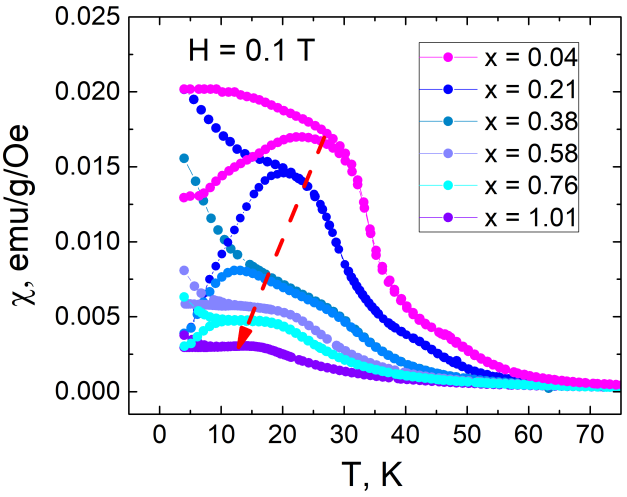

Figure 3.16: Temperature evolution of magnetic susceptibility of the $Co_{5-x}Zn_xTeO_8$ family. For each x value a top curve represents a FC scan, a bottom curve is a ZFC scan.

Some important insights on the evolution of magnetism in $Co_{5-x}Zn_xTeO_8$ series are

evidenced from magnetization measurements (Fig. 3.17 left). All diluted compounds shows almost zero coercivity, which relates them to the parent system, however increasing of the magneto-diluting agent leads to noticeable alterations in $M(B)$ curves. Low values of Zn^{2+}, up to $x = 0.38$, just increase the saturated magnetization, the shape of magnetization loops is preserved. At $x = 0.56$ the magnetization curve gains a tilt, that increases at $x = 0.76$. At the same time magnetization of $Co_{5-x}Zn_xTeO_8$ compounds with $x \leq 0.56$ doesn't reach saturation at $B = 5$ T reaching $M \approx 4\ \mu_B/f.u.$ At $x = 1.01$ the $M(B)$ curve adopts a Brillouin function-like shape, pointing out that heavy $A-$site magnetic dilution drives system towards a paramagnetic behavior. At the same time, for $x > 0.38$ coercivity was found to be almost zero, thus magnetic dilution decreases the average size of magnetic domains in the system.

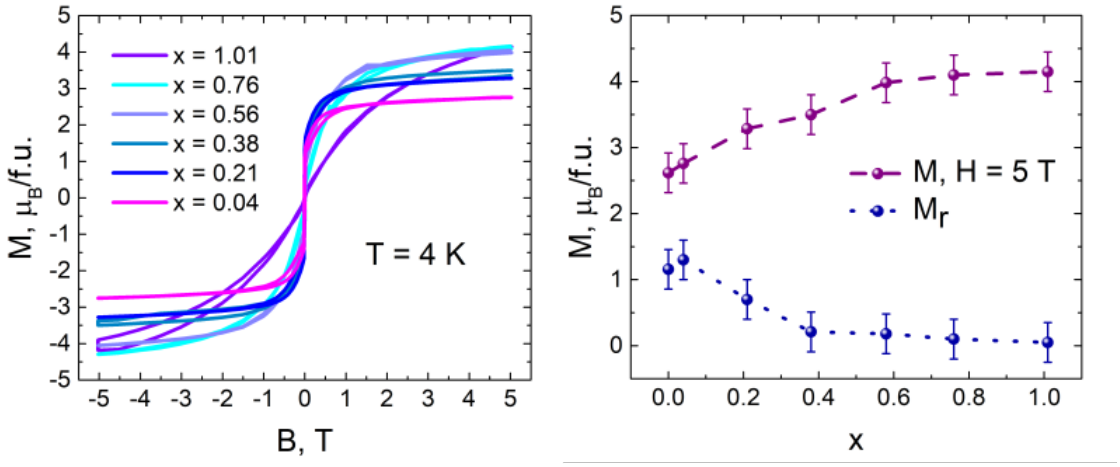

Figure 3.17: Left: Magnetization loops of studied compounds with various Zn^{2+} content measured at T = 4 K; Right: Variation of magnetization at B = 5 T and remanent magnetization of $Co_{5-x}Zn_xTeO_8$ family.

NPD patterns of $Co_{5-x}Zn_xTeO_8$ family confirms the corresponding behaviour (Fig. 3.18). First, it has to be said that as well as the parent compound, Co_5TeO_8, samples diluted with Zn^{2+} exhibits distinct emergence of a magnetic diffuse scattering centered around (111) reflection at relatively high temperatures. On cooling all studied samples except the one with x = 1.01, undergo an incommensurate long-range ordering transition with propagation vector $\mathbf{k} = (0, 0, \gamma)$. For $Co_{3.99}Zn_{1.01}TeO_8$ only the diffuse scattering is observed down to 1.7 K indicating that system is diluted enough to possess only a short-range ordering. Small Zn^{2+} content, $x = 0.04$ in particular, does not have any substantial effect on the behaviour of the neutron diffraction patterns and the temperature evolution of the propagation vector of $Co_{4.96}Zn_{0.04}TeO_8$ coincides with the one of the parent compound. However, for larger values of x some notable changes were observed. Increasing the amount of Zn^{2+} in the system diminishes both the temperature of the magnetic diffuse scattering emergence and the long-range ordering transition temperature. Together with a lower T_C NPD patterns reveal a significant satellite reflections broadening for larger x, indicating that the magnetic dilution reduces the average domain size of the modulated magnetic phase. At $x = 0.21$ the second magnetic phase transition present in $Co_{5-x}Zn_xTeO_8$ with $x = 0, 0.04$ is entirely eliminated and, instead of a sharp increase, the propagation vector of $Co_{4.79}Zn_{0.21}TeO_8$ continues decreasing and stabilizes below 15 K. Propagation vectors of compounds with $x = 0.38$ and 0.58 follow the same trend. Remarkably, for $x = 0.21$

and 0.38 the magnitude of the propagation vector at T = 1.7 K is considerably lower than the one of the non-diluted compound, $\mathbf{k}_z$ = 0.065 and 0.091 for $Co_{4.79}Zn_{0.21}TeO_8$ and $Co_{4.62}Zn_{0.38}TeO_8$ respectively against 0.134 in case of Co_5ZnTeO_8, thus, the intermediate dilution favours raise of the Zn^{2+} content only increases the magnitude of $\mathbf{k}_z$.

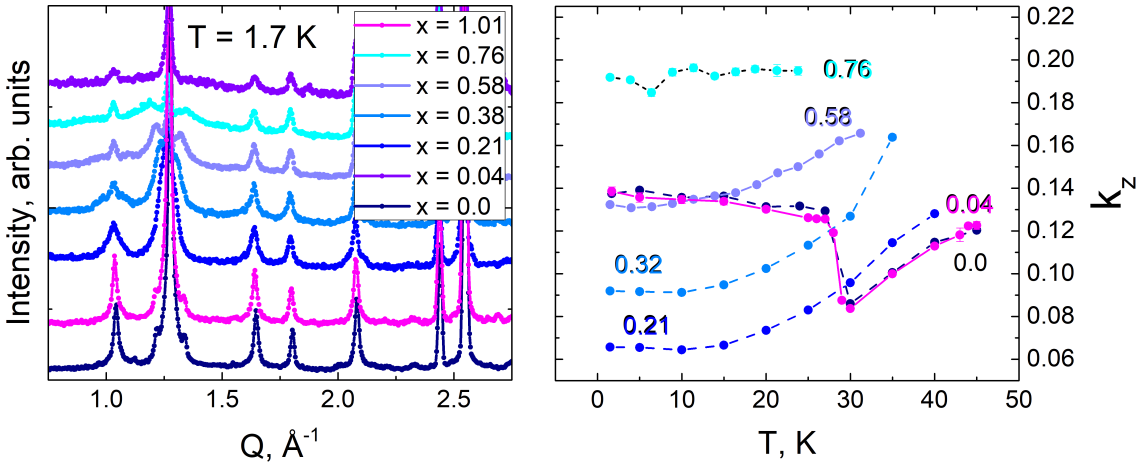

Figure 3.18: NPD patterns at T = 1.7 K (left) and the temperature evolution of the $\mathbf{k}_z$ component of the propagation vector (right) of the $Co_{5-x}Zn_xTeO_8$ family ($0 \leq x \leq 1.01$).

The magnetic structure of the $Co_{5-x}Zn_xTeO_8$ family is described with the same $P4_3(00\gamma)$ (#78.1.19.1.m19.1) superspace group on the entire x range where the long-range ordering is observed. For the magnetic structure refinement the same assumptions discussed in the paragraph 3.3 were exploited, so the evolution of long-range spin correlations with the Zn^{2+} content in the system can be described in terms of four parameters: magnetic moments and cone angles of Co^{2+} cations at A- and B-sites (Fig. 3.19). Regardless to the identical behaviour of propagation vectors, the magnetic moment magnitudes of $Co_{4.96}Zn_{0.04}TeO_8$ are significantly lower than those shown by the parent compound. Further increase of x diminishes both $\langle\mu_{Co1}\rangle$ and $\langle\mu_{Co2}\rangle$ leading them to be around $1.5\mu_B$ at both sites for $x < 0.38$. As for the cone angles, the A-site dilution affects mainly Co^{2+} spins occupying B-sites. While ϕ_{Co1} remains stable, ϕ_{Co2} is increasing from approximately ten degrees for low Zn^{2+} concentration corresponding to almost antiparallel orientation of Co_1 and Co_2 spins, to values close to 90^o for $x = 0.58$ and 0.76, implying B-site magnetic moments rotating almost within the crystallographic $a-b$ plane. Thus, the A-site magnetic dilution leads to a weakening of the antiferromagnetic coupling along the c-axis. The results of NPD experiments for $Co_{5-x}Zn_xTeO_8$ family are presented in the appendix (Tables A.12 - A.16).

The magnetic phase diagram of the $Co_{5-x}Zn_xTeO_8$ family with $0 \leq x \leq 1.01$ is illustrated in the figure 3.20. From the NPD data it follows that there is a narrow region of Zn^{2+} concentration where the phase transition taking place at T_{C2} is preserved, so the almost-collinear modulated phase in the system requires a high level of regularity of the cationic arrangement.

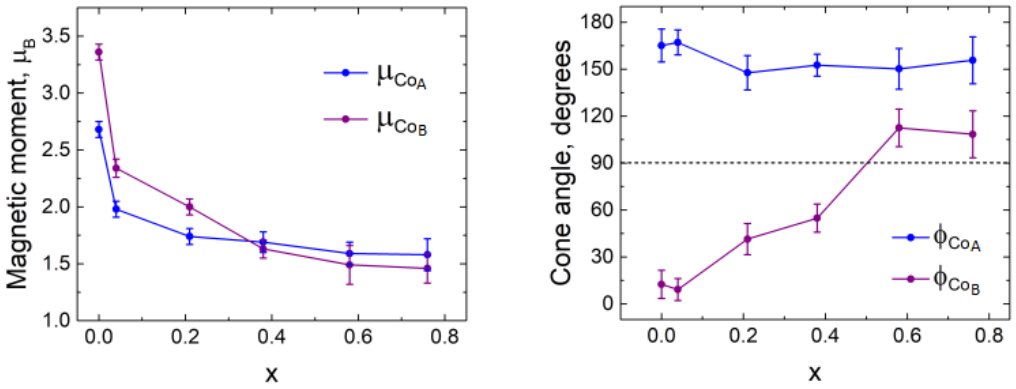

Figure 3.19: Variation of magnetic moments (left) and cone angles (right) at A- and B-sites of the modulated spin structure of the $Co_{5-x}Zn_xTeO_8$ family at T = 1.7 K

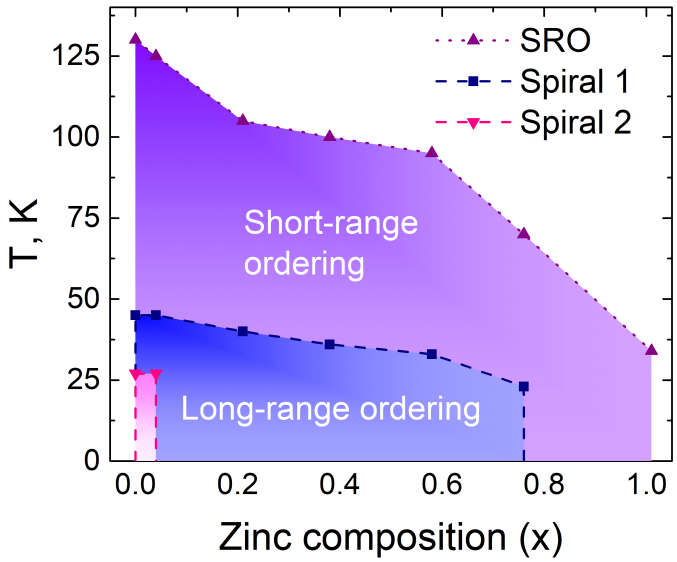

Figure 3.20: Magnetic phase diagram of the $Co_{5-x}Zn_xTeO_8$ family.

3.5 SANS studies and field dependent behaviour

For the further analysis of the magnetic ordering in $Co_{5-x}Zn_xTeO_8$ family, Small-Angle Neutron Scattering (SANS) experiments were carried out for the ordered polymorph of Co_5TeO_8 and $Co_4Zn_1TeO_8$ with the use of D33 small angle diffractometer. This technique may shed light on the nature of the magnetic phase transition at T_{C2} in the ordered polymorph and also allows one to study a magnetic-field induced behaviour of the system. Both polycrystalline samples were sintered as pellets by Spark Plasma Sintering (SPS). All measurements were performed with the acquisition time of five minutes.

3.5.1 Zero field Co_5TeO_8 SANS

Let us first consider the zero-field SANS of the ordered Co_5TeO_8 compound. Above T_{C1} SANS patterns show smooth featureless signal, however as soon as the temperature goes

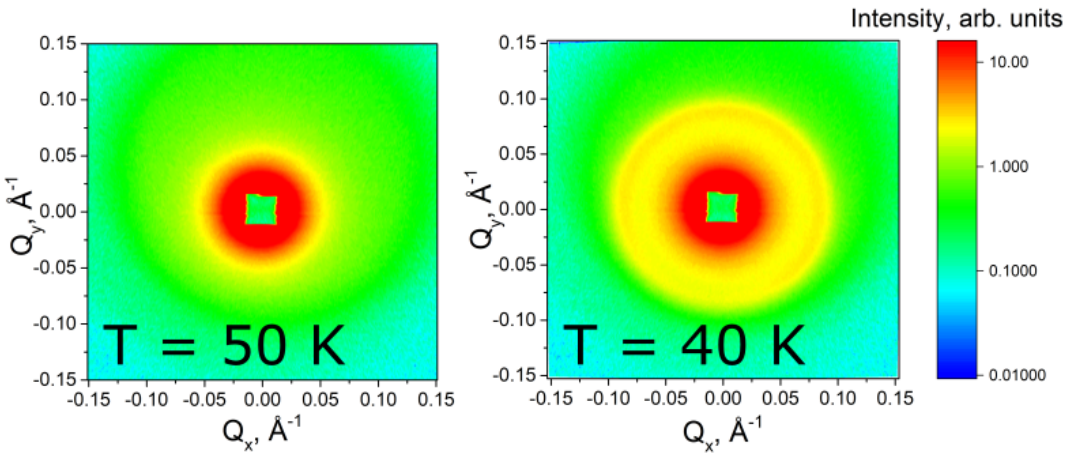

Figure 3.21: The comparison of SANS pattern for the ordered Co_5TeO_8 at 50 K and 40 K.

down to T_{C1} a homogeneous ring corresponding to (00δ) Bragg peak of the ferrimagnetic spiral structure is observed (Fig. 3.21).

To obtain characteristic features, SANS patterns were treated via the GRASP program [202]: the integration was done over the entire detector area excluding the area covered by the beamstop and, then obtained 2D plots were refined with the use of the following expression:

$$Y = Y_0 + \frac{m}{Q^{-n}} + I\frac{2}{H_G}\left(\frac{ln2}{\pi}\right)^{1/2} exp\left(-\frac{4ln2}{H_G^2}(Q - Q_c)^2\right), \tag{3.1}$$

where the first term describes the background intensity; the second term describes the low-**Q** part of SANS patterns, here m is the multiplier and n defines the slope of the SANS curve; and the third term is a Gaussian function where H_G is its full width on half maximum and Q_c is the peak centre position. The typical notation for the diffraction peak position in SANS measurements is the **Q**-vector, below it will be used to describe features of SANS patterns corresponding to ferrimagnetic spiral ordering of the ordered Co_5TeO_8. In principle, absolute values of **k**-vector and **Q**-vector should be equal, however the **Q**-vector has dimensions of $Å^{-1}$ while the **k**-vector is dimensionless. Temperature evolution of the **Q**-vector of the observed magnetic reflection follows the same trend as the $\mathbf{k}_z$ component of the propagation vector observed in NPD. Appearing at 45 K with $|Q| = 0.091Å^{-1}$, the ring first moves towards the direct beam reaching $|Q| = 0.065Å^{-1}$, and then spreads out to reach a stable magnitude of $|\mathbf{Q}| \approx 0.11Å^{-1}$ below T_{C2} (Fig. 3.22). However, the magnitude of the **Q**-vector observed in SANS experiment is lower than the one observed in the wide-angle diffraction by $\approx 20\%$. This may be due to general drawbacks of SANS technique such as a low resolution as well as the diffraction peak shift at low angles. It should be also mentioned that one diffraction peak is not enough for a precise wave vector determination.

To retrieve SANS intensity as a function of the momentum transfer SANS patterns were averaged over a radial sector of 360^o with the radius equal to the half of the 2D detector dimensions excluding the area close to the primary beam. Left graph in the figure 3.23 illustrates the temperature evolution of the SANS intensity for the ordered polymorph in log-log scale. An important characteristic of any SANS pattern is the slope of its low-**Q** part defined by the second term in the equation 3.1, which is defined by the morphology of the sample. If the intensity of small-angle scattering is proportional to

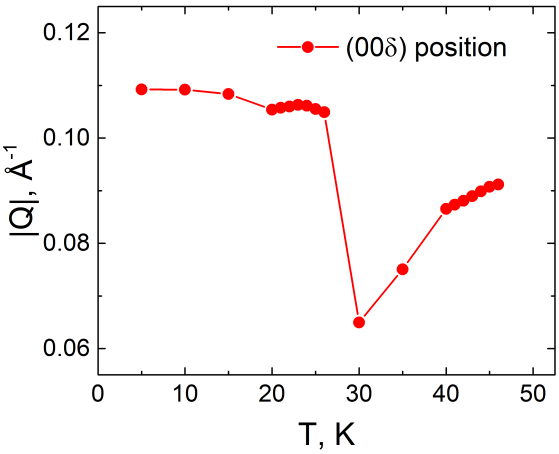

Figure 3.22: The temperature evolution of the (00δ) diffraction peak position of the ordered Co_5TeO_8 polymorph.

Q^{-4}, a system exhibits so-called Porod behaviour [203]: typical scattering picture caused by inhomogeneous systems as a result of scattering on interfaces and, in case of magnetic systems, represents the scattering on domain walls [204]. As the right graph in the figure 3.23 shows, on cooling, n is decreasing from $n \approx 3.59$ at T = 95 K to $n \approx 3.55$ at T = 46 K. Below T_{C1} $n(T)$ undergoes a rapid increase, reaching $n \approx 3.78$ at T = 5 K. Thus, below the temperature of the long-range ordering the ordered Co_5TeO_8 starts developing a domain structure that is well-defined at low temperatures, however the difference from the ideal Porod behaviour indicates the presence of a slight degree of the magnetic disorder in the system.

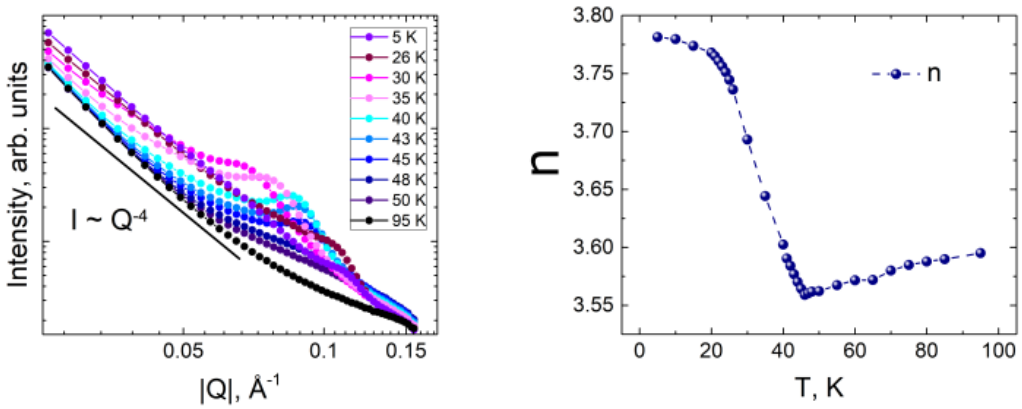

Figure 3.23: Temperature evolution of the SANS intensity (left) and n from the equation 3.1 for the ordered Co_5TeO_8.

Magnetic SANS is typically Q-selective as different contributions manifest themselves at different Q-range [205]. In case of magnetic scattering, the intensity varies with the order parameter and, in fact, is proportional to the square of magnetization M^2. Since the magnetic form factor decreases significantly with **Q**, the low-Q part of SANS patterns contains information on static magnetic correlations. Left part of the figure 3.24 illustrates an increase of the scattering signal below T_{C1} as the long-range magnetic ordering sets

in. The intensity at $|\mathbf{Q}| = 0.027\text{Å}^{-1}$ grows gradually and reaches its saturation at low temperatures without any remarkable feature at $T_{C2} = 27K$. High-Q part, in turn, contains contributions due to dynamical correlations. In the case of the ordered Co_5TeO_8, the temperature dependence of the high-Q part of SANS signal demonstrates a critical scattering behaviour associated with the second-order paramagnetic to long-range order transition. The additional scattering intensity at $T > T_{C1}$ arises with spin correlations and reaches its maximum at the transition temperature. For $T < T_{C1}$ the intensity at $|\mathbf{Q}| = 0.125\text{Å}^{-1}$ is due to quasielastic scattering from spin waves. Such a behaviour is similar to that present in the pyrochlore compound $Tl_2Mn_2O_7$ described in [206].

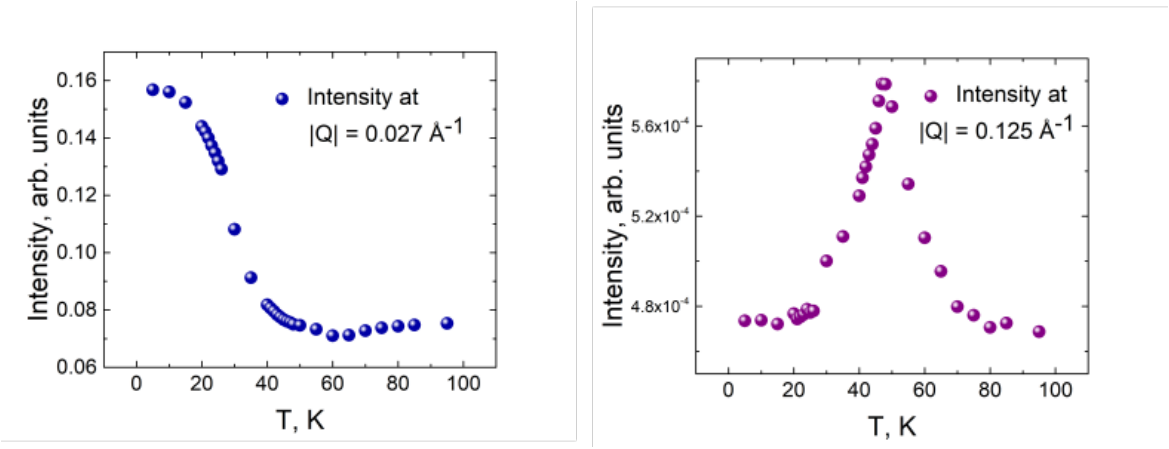

Figure 3.24: Temperature evolution of the low-Q ($|\mathbf{Q}| = 0.027\text{Å}^{-1}$) and high-Q ($|\mathbf{Q}| = 0.125\text{Å}^{-1}$) SANS intensity of the ordered Co_5TeO_8.

3.5.2 In-field Co_5TeO_8 SANS

To study the evolution of magnetic scattering density the ordered Co_5TeO_8 under an applied magnetic field, three temperatures, covering different areas of interest, were selected according to the magnetic phase diagram obtained by magnetic susceptibility (Fig. 3.8 right) and the low temperature NPD (Fig. 3.20, x = 0). The first is 20 K, where the low-temperature ferrimagnetic spiral spin structure (spiral 2) undergoes no field-induced magnetic phase transition, the second is 32 K, as the field induces a phase transition from spiral 2 to spiral 1 phase. And the last, but not least, is 36 K; when the applied magnetic field suppresses the long-range spiral 1 ordering in favour of a paramagnetic state. The applied magnetic field direction was set to be perpendicular to the neutron beam along the q_x direction as shown on a figure 3.28.

Let us first consider the in-field SANS at 20 K. A set of SANS patterns of the system under an applied magnetic field up to 1 T with the step of 0.2 T was collected. As soon as the magnetic field is applied, the scattering pattern is no more homogeneous and the (00δ) reflection splits into two distinct arc-like peaks on both sides of the direct beam along the Q_x-direction of the detector. On increase of the magnetic field, these features shrink along the Q_y-direction and at B = 1 T almost merge into spots (Fig. 3.25).

Q-vector corresponding to the (00δ) Bragg peak is stable with magnitude $|\mathbf{Q}| \approx 0.105\text{Å}^{-1}$ on the entire field range and changes slightly to $|\mathbf{Q}| \approx 0.106\text{Å}^{-1}$ at B = 1 T, indicating almost no field effect on the periodicity of the spin modulation for the studied magnetic field range (Fig. 3.26 left).

Considering $R_0 = 0$ Å^{-1} the centre of the direct beam, one can define a circle of

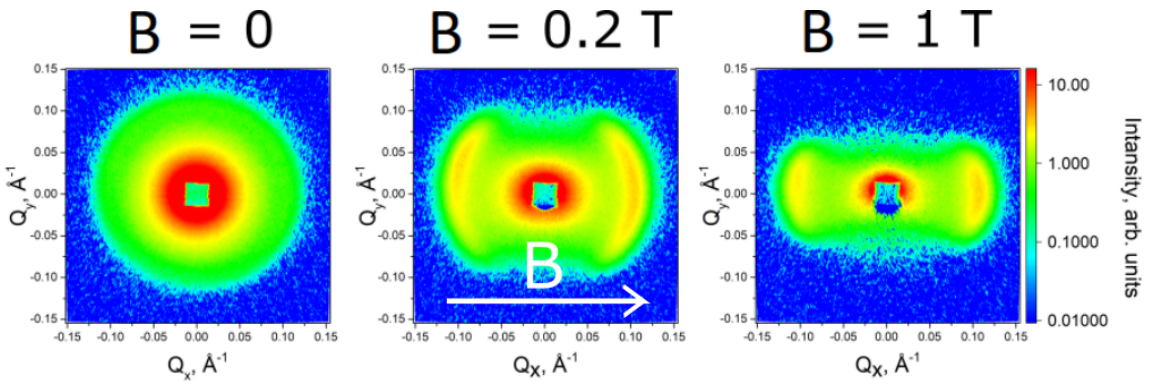

Figure 3.25: Evolution of SANS patterns for the ordered Co_5TeO_8 polymorph under applied magnetic field (**B** || q_x) at T = 20 K.

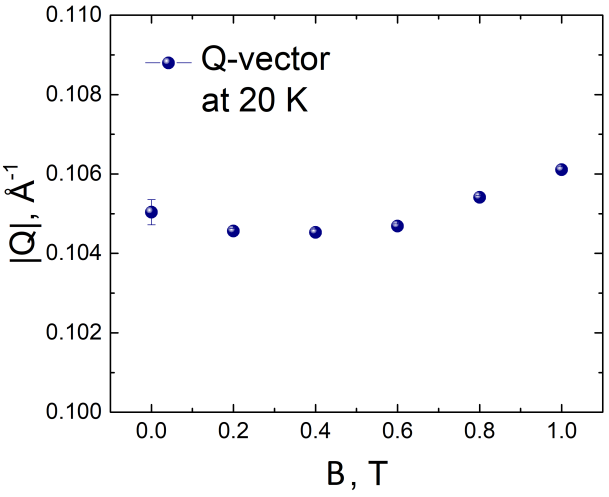

Figure 3.26: Evolution of the **Q**-vector, describing (00δ) Bragg peak position for the Co_5TeO_8 polymorph under applied magnetic field (**B** || q_x) at 20 K.

the radius R_{min} = 0.066 Å^{-1} as the area of the detector containing mainly the direct beam signal and for all $R > R_{max}$ where R_{max} = 0.14 Å^{-1} the intensity is given by the background scattering. To follow the evolution of diffraction peaks intensity a circle area between R_{min} and R_{max} was selected (Fig. 3.27 left). To exclude the non-magnetic contribution, data collected at 155 K was subtracted from each SANS pattern. The scattering intensity within the circle area defined by $R_{min} > R > R_{max}$ first increases abruptly from zero field to B = 0.2 T and then decreases gradually reaching its lowest value at B = 1 T (Fig. 3.27 right).

Such a behaviour can be described as follows. With no field applied each magnetic domain of the polycrystalline sample, oriented randomly with respect to each other, participates in scattering resulting in homogeneous SANS pattern with the Bragg peak in a form of Debye-Scherrer ring. As soon as the magnetic field is applied, only those magnetic domains for which the **k** || **B** contribute to the scattering pattern. Neutron scattering with H perpendicular to the neutron beam on single crystal with a conical spin arrangement will produce a SANS pattern with two Bragg peaks in the Q_x direction on either sides of the direct beam [172] as illustrated on the figure 3.28. But in a polycrystalline

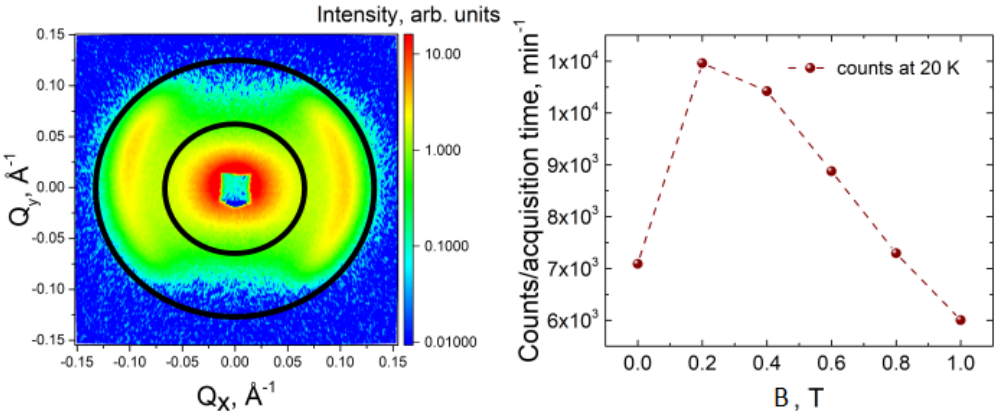

Figure 3.27: Left: SANS pattern for the ordered Co_5TeO_8 polymorph collected at 20 K and H = 0.2 T || q_x. Small and large rings represent R_{min} and R_{max} respectively. Right: the evolution of detector counts in the area of interest ($R_{min} > R > R_{max}$) as the function of the applied magnetic field (**B** || q_x) at 20 K.

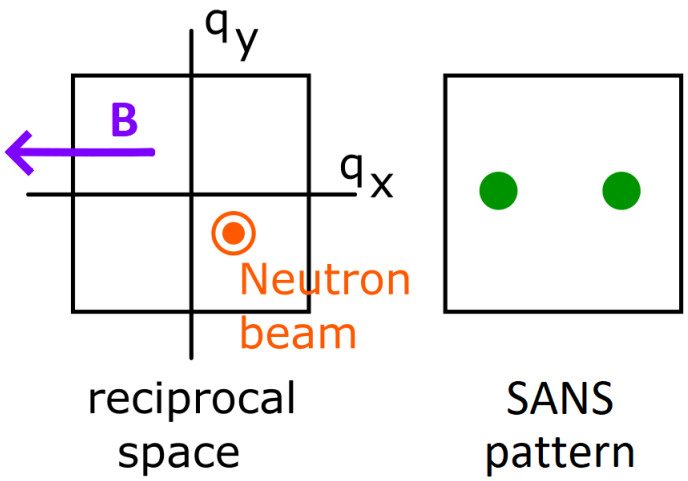

Figure 3.28: Schematic representation of a small-angle neutron diffraction pattern produced by a conical spin arrangement in the geometry where neutron beam is perpendicular to the applied magnetic field **B**

conical magnet, some domains that are slightly misoriented with respect to the applied magnetic field are still involved in scattering events. So the Bragg peaks are smeared into arc-like features illustrated in figure 3.25. The increase of the scattering intensity at B = 0.2 T indicates that in some domains the propagation vector of the ferrimagnetic spiral modulation rotates to fulfill the **k** || **B** condition (Fig. 3.27 right). The subsequent loss of the intensity in the area of interest corresponds to a decrease of the number of domains involved in the scattering process as the field increases. Thus, the applied magnetic field suppresses the ferrimagnetic spiral in favour of a field-induced ferromagnetic state.

Field scans at 32 K show rather complex behaviour (Fig. 3.29). Starting with the (00δ) Bragg peak with $|\mathbf{Q}_1| = 0.07\text{Å}^{-1}$ at H = 0.01 T, the **Q**-vector increases gradually up to $|\mathbf{Q}_1| \approx 0.072\text{Å}^{-1}$ at at H = 0.05 T with the scattering preserving the same homogeneous SANS patterns. However, as the magnitude of the applied magnetic field reaches B_{C1} = 0.06 T two arc-shaped peaks with $|\mathbf{Q}_2| \approx 0.097\text{Å}^{-1}$ appear on left and right sides with respect to the direct beam while $\mathbf{Q}_1$ ring is still partially observed. This coexisting state

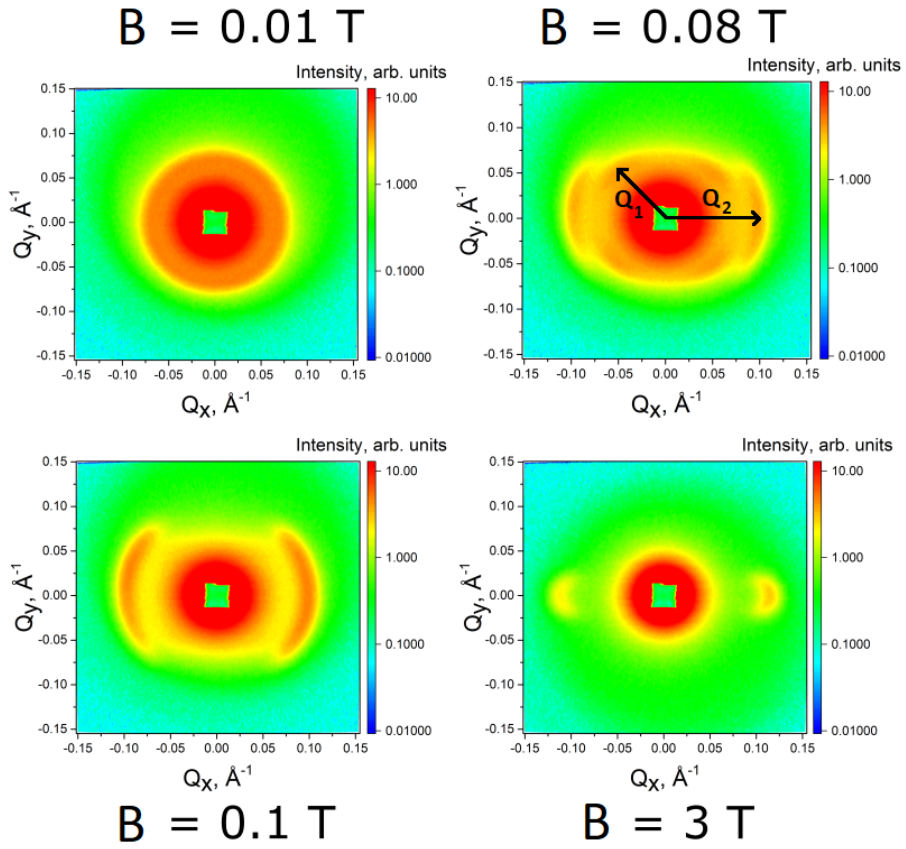

Figure 3.29: Evolution of SANS patterns for the ordered Co_5TeO_8 polymorph under applied magnetic field ($\mathbf{B} \parallel q_x$) at T = 32 K.

remains up to $B_{C2} = 0.09$ T at which the $\mathbf{Q}_1$ feature is suppressed entirely. Above B_{C2} only arc-shaped $\mathbf{Q}_2$ Bragg peaks are preserved with the $\mathbf{Q}$-vector $|\mathbf{Q}_2| \approx 0.1$Å^{-1} up to 1 T. With the further increase of H the magnitude of the $\mathbf{Q}_2$ grow finally reaching the value of ≈ 0.124Å^{-1} at B = 7 T. However, at high applied fields the intensity of the $\mathbf{Q}_2$ peak drops significantly almost to 0. Figure 3.30 illustrates field evolution of $\mathbf{Q}$-vectors and integrated intensity of diffraction peaks at 32 K for Q_1 and Q_2 phases.

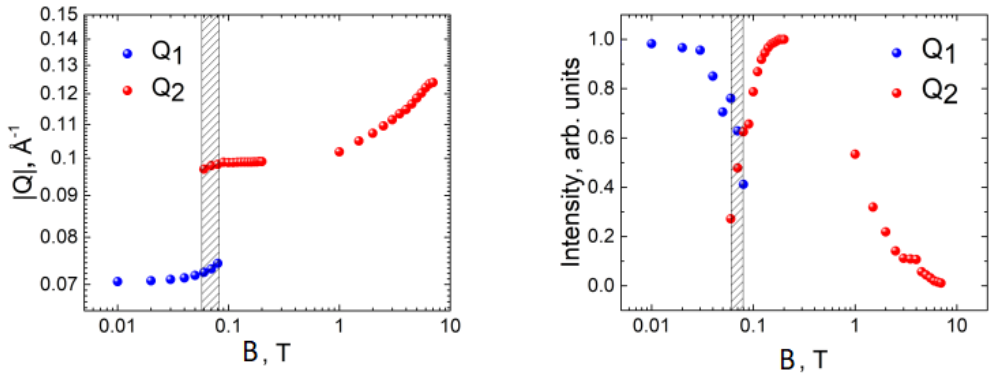

Figure 3.30: Evolution of $\mathbf{Q}$-vectors (left) and integrated intensity of diffraction peaks of Q_1 and Q_2 phases of the ordered Co_5TeO_8 polymorph under applied magnetic field ($\mathbf{B} \parallel q_x$) at T = 32 K.

To unveil domain behaviour under the applied magnetic field, detector counts were integrated within the circle with $R_{min} = 0.054$ Å and $R_{max} = 0.13$ Å (Fig. 3.31). Below B_{C1} the ordered polymorph of Co_5TeO_8 is in a single domain state that is stable at low fields. Up to 0.03 T both the integrated intensity of the Q_1 diffraction peak and detector counts for $R_{min} > R > R_{max}$ changes insignificantly. At $B_{C1} = 0.06$ T the system enters a field-induced multidomain state which represent itself with two separate sets of diffraction peaks on SANS patterns. Critical field B_{C1} drives a part of magnetic domains, co-aligned with the direction of the applied magnetic field, to undergo a magnetic phase transition characterized with a sharp decrease of the spin modulation periodicity. At the same time the part of magnetic domains, close enough to provide diffraction but misaligned with respect to the field direction, stays at the Q_1 state, as it requires a larger magnetic field to induce the transition in this fraction of domains. Finally at $B_{C2} = 0.09$ T the low-Q Q_1 feature merges into the Q_2 feature, thus the system enters a field-induced single-domain state. Remarkably, the intensity evolution under applied magnetic field within the ring area $R_{min} > R > R_{max}$ shows a peak at B_{C1}, indicating a rotation of propagation vector in some domains. At fields $B > 1T$ the system shows a rapid decrease of the scattering intensity, representing the increase of the sample fraction in the field-induced ferromagnetic state. And finally at $B \geq 7$ T there is no scattering intensity observed at the **Q** positions of Bragg reflections, thus the system enters a fully field-polarized ferromagnetic state.

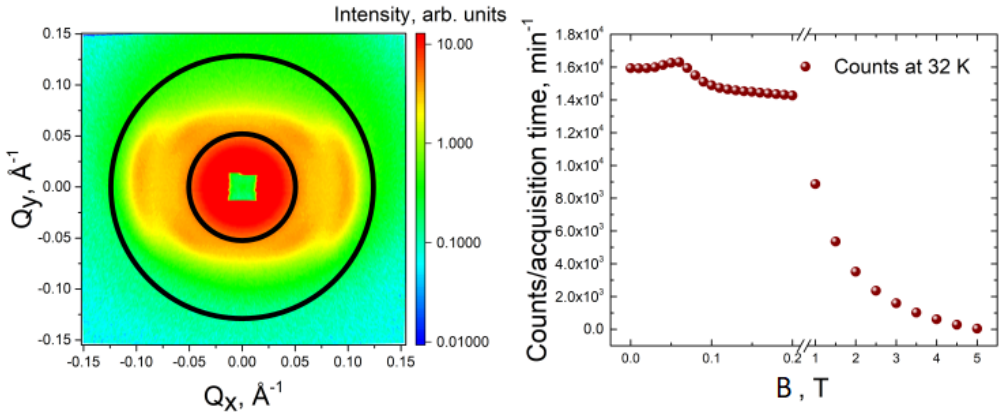

Figure 3.31: Left: SANS pattern for the ordered Co_5TeO_8 polymorph collected at 32 K and B = 0.08 T. Small and large rings represent R_{min} and R_{max} respectively. Right: the evolution of detector counts in the area of interest ($R_{min} > R > R_{max}$) as the function of the applied magnetic field (**B** || q_x) at 32 K.

The behaviour of the ordered Co_5TeO_8 polymorph under applied magnetic field at 36 K resembles that exhibited by the system at 20 K (Fig. 3.32). Already at B = 0.024 T powder-averaged ring of (00δ) reflection splits in two arc-shaped peaks. At $B = 0.2$ T they are distinct and well-shaped, and upon further increase of the applied magnetic field they loose their intensity. The diffraction peaks are suppressed entirely above $B_C = 5$ T.

Increasing B, the **Q**-vector magnitude, describing the position of the (00δ) diffraction peaks, first remains stable with a magnitude of $|\mathbf{Q}| \approx 0.081$Å^{-1} up to B = 0.032 T and then grows rapidly with further increase of the applied field, reaching its highest magnitude of $|\mathbf{Q}| \approx 0.199$Å^{-1} at 5 T (Fig. 3.33).

SANS patterns of the ordered Co_5TeO_8 polymorph under applied magnetic field at 36 K were also integrated within the same circle area as those of 32 K: $R_{min} = 0.054$ Å^{-1} and $R_{max} = 0.13$ Å^{-1} (Fig. 3.34). Detector counts within the selected area show a gradual enhancement on increasing field, reaching its highest magnitude at B = 0.136 T. This again

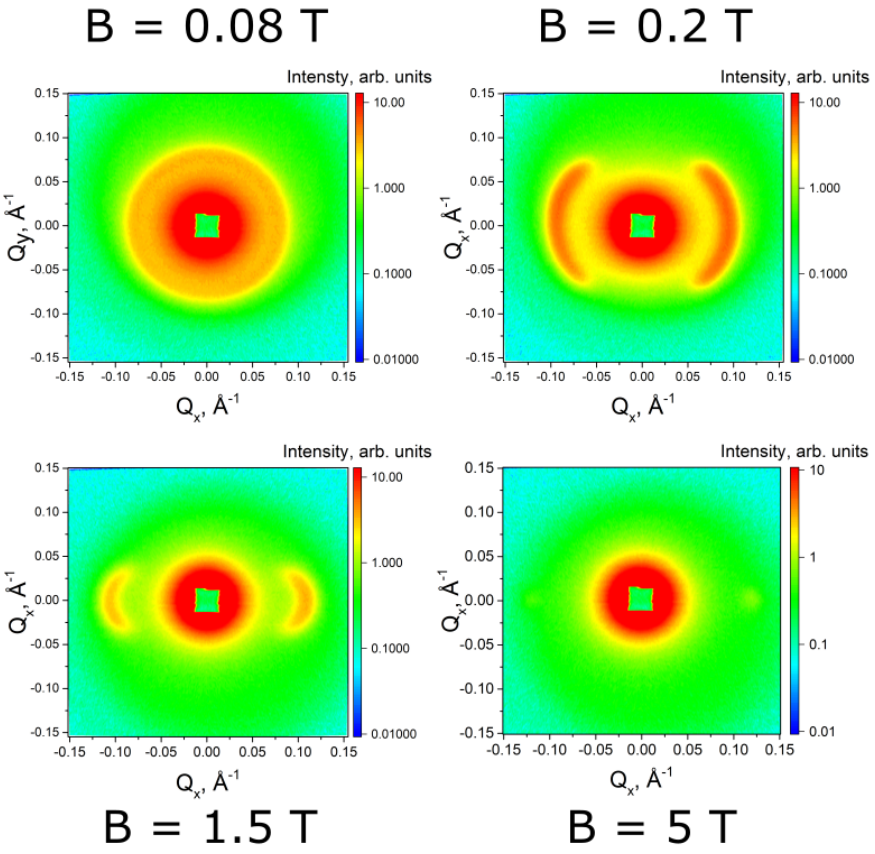

Figure 3.32: Evolution of SANS patterns for the ordered Co_5TeO_8 polymorph under applied magnetic field ($\mathbf{B} \parallel q_x$) at T = 36 K.

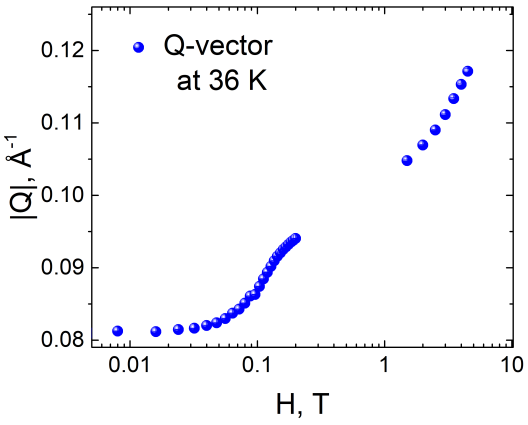

Figure 3.33: Evolution of the **Q**-vector, describing the position of the (00δ) Bragg peak for the Co_5TeO_8 polymorph under applied magnetic field ($\mathbf{B} \parallel q_x$) at 36 K.

represents the rotation of the propagation vector in some domains that were not involved in scattering events at the zero field. At the high field region (B > 1 T) the intensity of the integrated area decreases rapidly as the applied field polarises spins, bringing the system into a field-induced ferromagnetic state above $B = 5$ T.

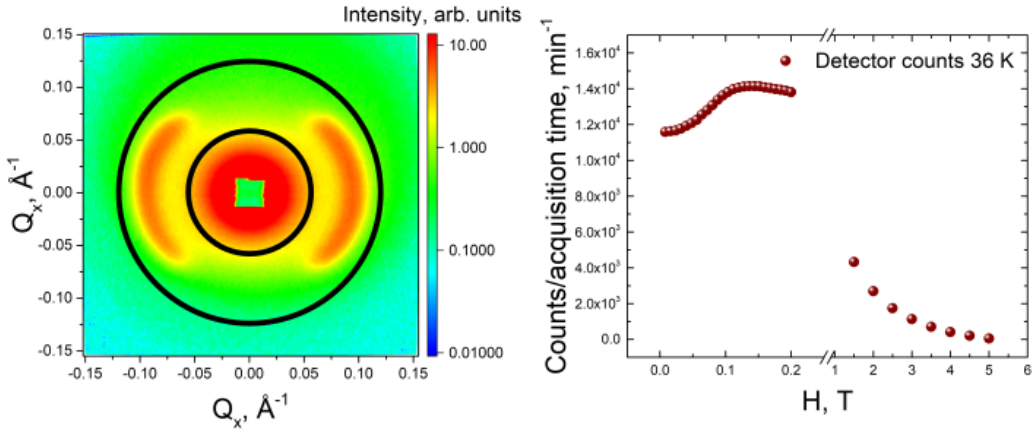

Figure 3.34: Left: SANS pattern for the ordered Co_5TeO_8 polymorph collected at 32 K and H = 0.2 T. Small and large rings represent R_{min} and R_{max} respectively. Right: the evolution of detector counts in the area of interest ($R_{min} > R > R_{max}$) as the function of the applied magnetic field (**B** || q_x) at 36 K.

3.5.3 Zero field $Co_4Zn_1TeO_8$ SANS

As discussed in the paragraph 3.4, $Co_4Zn_1TeO_8$ doesn't possess any long-range order down to T = 1.7 K and small angle neutron scattering data lies in agreement with NPD measurements. No Bragg peak is observed at 2 K for $Co_4Zn_1TeO_8$. Instead the corresponding SANS pattern, illustrated in the figure 3.35 (left), exhibits a homogeneous scattering, that looses intensity rapidly with increase of momentum transfer. SANS curves of $Co_4Zn_1TeO_8$, obtained with the same averaging procedure as those of Co_5TeO_8, reveal a slight intensity enhancement at $|Q| \approx 0.12$ Å with decreasing temperature. This behaviour is caused by the formation of short-range spin correlations (Fig. 3.35 right).

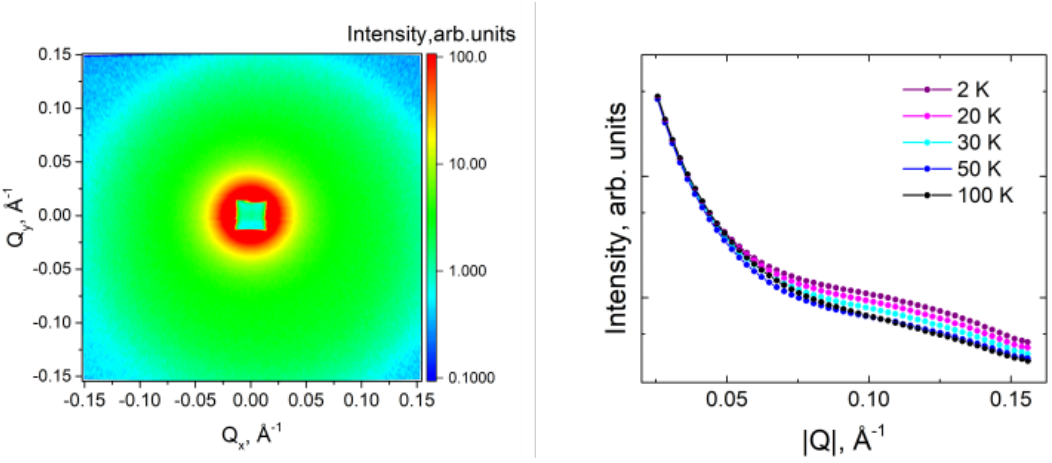

Figure 3.35: SANS pattern collected at 2 K (left) and temperature evolution of SANS curves (right) for $Co_4Zn_1TeO_8$

As for the ordered Co_5TeO_8, the scattering intensity at the high-Q region of SANS patterns of the highly-diluted $Co_4Zn_1TeO_8$ increases on cooling. But in comparison to the parent compound, the temperature evolution of the $I(Q)$ curve (Q = 0.152 Å) doesn't have a peak, instead it increases its magnitude down to lowest measured temperatures, reaching a plateau at T = 6 K (Fig. 3.36). This illustrates an increase in contribution of

dynamic spin-correlations to the scattering, which, in turn, indicates the tendency of the system to acquire a long-range ordering. However, large amount of Zn^{2+}, disrupting J_{AB} and J_{BB} exchange pathways, prevents $Co_4Zn_1TeO_8$ from ordering.

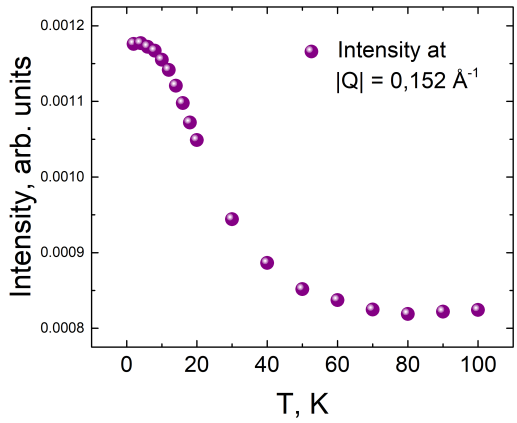

Figure 3.36: Temperature evolution of the high-Q ($|\mathbf{Q}| = 0.152$ Å^{-1}) SANS intensity for $Co_4Zn_1TeO_8$.

3.5.4 In-field $Co_4Zn_1TeO_8$ SANS

To study the response of $Co_4Zn_1TeO_8$ to the applied magnetic field, SANS patterns at 2, 10 and 20 K were collected with B = 1, 4 and 7 T (B $\perp$ beam). For each temperature, the system doesn't show any field-induced magnetic phase transition, moreover the magnetic diffuse scattering observed around $|Q| \approx 0.12$ Å is getting suppressed on increase of H (Fig. 3.37). One can assume that the in-field behaviour of $Co_4Zn_1TeO_8$ resembles the parent compound: with an increase of the applied magnetic field, Co^{2+} magnetic moments co-align with the field, so the system becomes a field-polarized ferromagnet.

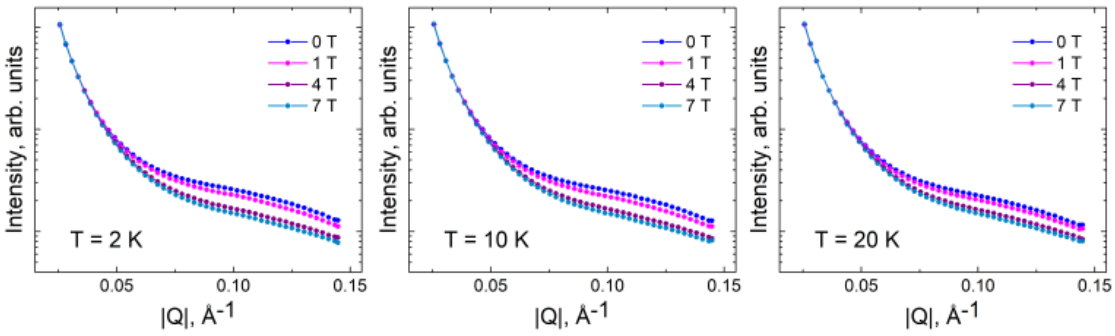

Figure 3.37: Variation of SANS patterns of $Co_4Zn_1TeO_8$ under applied magnetic field collected ($\mathbf{B} \parallel q_x$) at 2 K, 10 K and 20 K.

3.6 Short range ordering

3.6.1 Short range ordering in Co_5TeO_8

As shown by NPD and SANS experiments and summarized in the phase diagram (Fig. 3.20), the $Co_{5-x}Zn_xTeO_8$ spinel family shows the presence of short-range ordering (SRO) in a wide range of temperatures for $0 < x < 1.01$. Noticeable diffuse magnetic scattering indicates the tendency of the system to form spin correlations far above long-range order transition temperatures. Since XYZ polarization analysis is capable of distinguishing a purely magnetic scattering and reverse Monte Carlo modeling suits well as a mathematical tool to describe disordered materials, a combination of these two techniques becomes an ideal approach to study SRO in $Co_{5-x}Zn_xTeO_8$ and shed light on mechanisms of ferrimagnetic spiral long-range ordering formation. For that two samples with $x = 0$ and $x = 1.01$ were studied on the D7 diffuse scattering spectrometer.

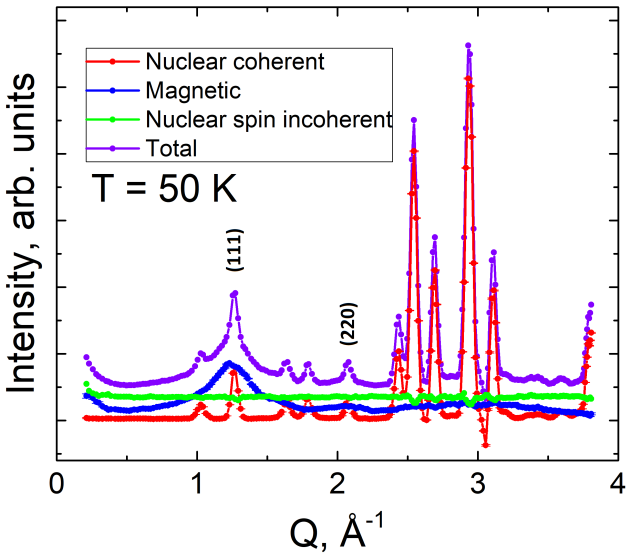

Figure 3.38: Scattering contributions discriminated with XYZ neutron polarization analysis for the ordered Co_5TeO_8 at T = 50 K

First, let us consider the behaviour of non-diluted Co_5TeO_8. Neutron XYZ polarization analysis for this compound was carried out in a range of temperatures between 50 K and 260 K. In a typical XYZ polarization analysis experiment six cross sections are measured: spin-flip (SF) and non-spin-flip (NSF) channels for primary beam polarization along x, y and z directions in the laboratory coordinate system. To improve statistics, for all conducted experiments NFS:SF ratio was set to be 1:4. Then using the approach described in section 2.2.2.7, one can distinguish nuclear spin incoherent, nuclear coherent and magnetic contributions from total scattering. Figure 3.38 illustrates a typical dataset, collected during a measurement at a single temperature. A slight intensity drop of a nuclear scattering at $Q \approx 3\text{Å}^{-1}$ present for all scattering patterns is due to data correction: quartz crystal, used for the normalization, produced a strong Bragg peak around that **Q** position. So the reduction algorithm implemented at D7 overestimates this region. However in case of magnetic scattering this may be neglected.

The temperature evolution of the diffuse magnetic scattering of the ordered Co_5TeO_8 demonstrates a couple of important characteristics (Fig. 3.39 left). First, for tempera-

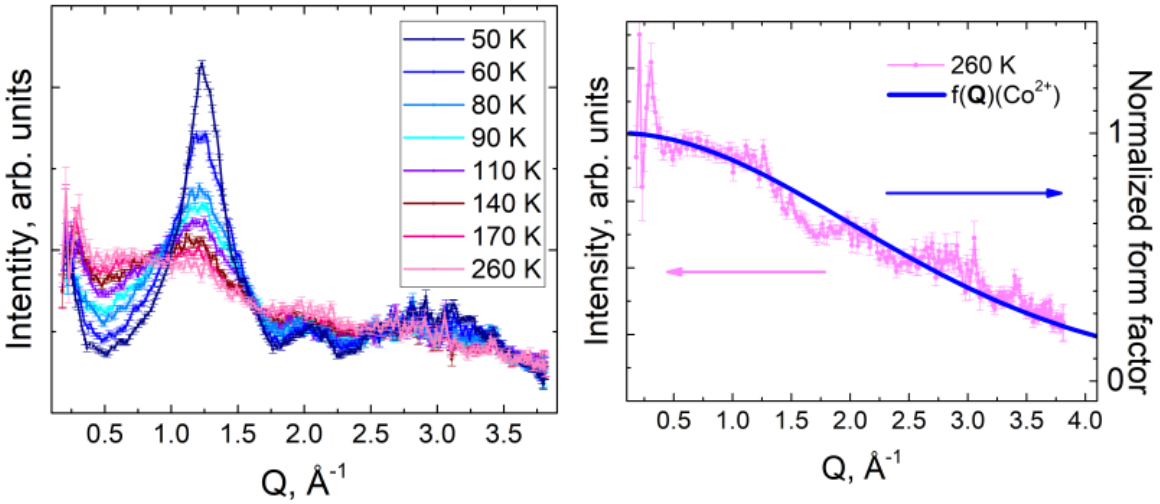

Figure 3.39: Left) Temperature evolution of the diffuse magnetic scattering obtained with XYZ neutron polarization analysis of the ordered Co_5TeO_8; right) Comparison of the diffuse magnetic scattering pattern at T = 260 K and the magnetic form factor $f(\mathbf{Q})$ of Co^{2+} ion.

tures close to T_{C1}, the diffuse magnetic scattering patterns shows the presence of distinct features, centered at around 1.25Å and 2.07Å corresponding to Bragg positions of (111) and (220) nuclear reflections, which have the strongest satellite reflections in the ordered phase. With the temperature rise these features undergo a significant intensity decrease together with an increase of width, which, in turn, indicates shortening of SRO domains. Second, in the case of neutron scattering on a purely paramagnetic system, XYZ polarization analysis will provide a magnetic scattering pattern that follows the shape of the magnetic form factor of the cation involved in scattering. Figure 3.39 (right) shows the magnetic diffuse scattering pattern at T = 260 K and the magnetic form factor $f(\mathbf{Q})$ of the Co^{2+} ion is given by:

$$f(\mathbf{Q}) =< j_0(\mathbf{Q}) > + \frac{\mathbf{L}}{(2\mathbf{S}+\mathbf{L})} < j_2(\mathbf{Q}) >, \tag{3.2}$$

where $\mathbf{L}$ is the orbital angular momentum operator, $\mathbf{S}$ is the spin operator, $< j_0(\mathbf{Q}) >$ and $< j_2(\mathbf{Q}) >$ are integrals, representing the radial distribution of unpaired electrons. An analytical approximation for the d electrons in $3d$ and $4d$ series is given by:

$$< j_n(\mathbf{Q}) >= Aexp(-a\mathbf{Q}^2) + Bexp(-b\mathbf{Q}^2) + Cexp(-c\mathbf{Q}^2) + D, \tag{3.3}$$

where A, a, B, b, C and C are numerical coefficients listed in [207]. Nevertheless diffuse magnetic scattering pattern obtained at T = 260 K follows the trend of $f(Q)$ for Co^{2+}, it still shows features at 1.25Å and 2.07Å. Thus the short-range spin correlations are present in the ordered Co_5TeO_8 polymorph up to temperatures significantly higher then the temperature of the long-range ordering.

For the RMC fit a cubic unit cell with $a = 8.553$Å with P1 symmetry, containing 20 Co^{2+} atoms corresponding to cationic arrangement of the ordered Co_5TeO_8, described in the table 3.1, was selected. A box with $7\times7\times7$ dimensions, having in total 6860 spins was used for the RMC fit in order to contain at least one modulation with the $\mathbf{k} = 0.126(1)$ corresponding to the T_{C1}. RMC fit was performed for the Q region between $Q = 0.21$Å

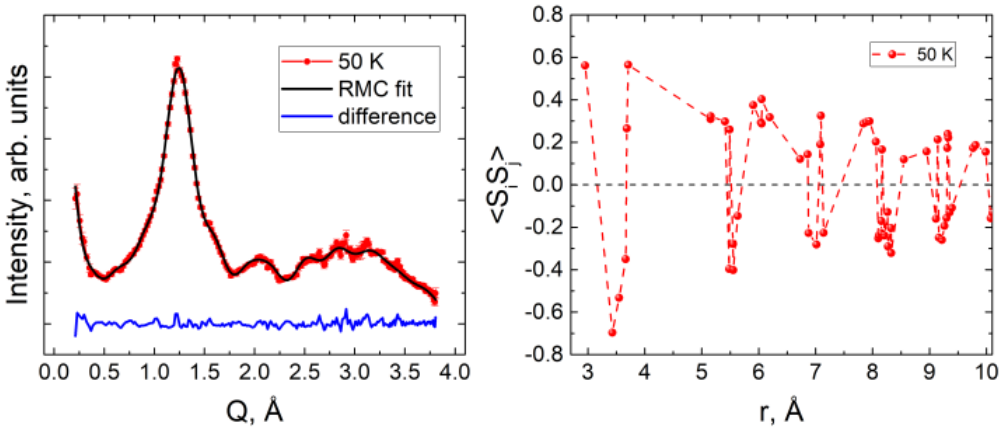

Figure 3.40: Left: RMC fit of the diffuse magnetic scattering pattern of the ordered Co_5TeO_8 polymorph at T = 50 K. Red dots - experimental data, black line - RMC fit, blue line - difference curve. Right: Radial spin-spin correlation function calculated with the results of RMC fit for T = 50 K.

and $Q = 3.80$Å. During the refinement a maximum of 3000 moves per spin was proposed. In order to check the stability, for each temperature five independent refinements were done and a radial spin-spin correlation function $< \mathbf{S}_i\mathbf{S}_j >$ was calculated as an average between the results of these independent runs. Figure 3.40 (left) shows an example of RMC fit for T = 50 K. R-factors of each fit are listed in tables A.17 - A.19 in the appendix A.

Table 3.3: The sign of a radial spin-spin correlation function at T = 50 K for the first ten pairs of Co_2^+ cations of Co_5TeO_8

r, Å	$< \mathbf{S}_i\mathbf{S}_j >$ sign	Co_2^+ pair
2.957(6)	positive	$Co_2 - Co_2$
3.427(7)	negative	$Co_1 - Co_2$
3.549(7)	negative	$Co_1 - Co_2$
3.666(7)	negative	$Co_1 - Co_2$
3.684(8)	positive	$Co_1 - Co_1$
3.707(5)	positive	$Co_1 - Co_1$
5.158(4)	positive	$Co_2 - Co_2$
5.161(6)	positive	$Co_2 - Co_2$
5.404(5)	positive	$Co_2 - Co_2$
5.481(7)	negative	$Co_1 - Co_1$
$Co_1 = A-$site (tetrahedral)		
$Co_2 = B-$site (octahedral)		

Radial spin-spin correlation may shed light on an average spin arrangement in paramagnetic state. Each point on the x-axis represents a distance at which one can find a spin

j remote from spin i, and a sign of $< \mathbf{S}_i\mathbf{S}_j >$ indicates at a relative orientation of a given spin pair: positive values indicate predominantly parallel correlation, negative - antiparallel. At T = 50 K all spin pairs, corresponding to the positive magnitudes of $< \mathbf{S}_i\mathbf{S}_j >$ are of Co^{2+} cations sharing the same oxygen environment (two octahedra or two tetrahedra) whereas the negative values of $< \mathbf{S}_i\mathbf{S}_j >$ are provided by Co^{2+} spins of different sites: octahedra and tetrahedra. Those spin correlations correspond to those observed in the inverse spinels magnetic structures. (Fig. 3.40 right). The table 3.3 summarizes spin orientations for 10 pairs of spins with the lowest distances between them. The r-distance of 2.957 Å between two Co_2 atoms is in accord with the Co-Co distance between two $[CoO_6]$ octahedra; the r-distance of 3.666 Å between two Co_1 atoms is also in agreement with distances between two Co^{2+} cations in tetrahedral environments. Thus, the antiferromagnetic coupling between Co_1 and Co_2 spins, deduced from NPD is conserved in a state slightly above T_{C1}, lacking long range ordering.

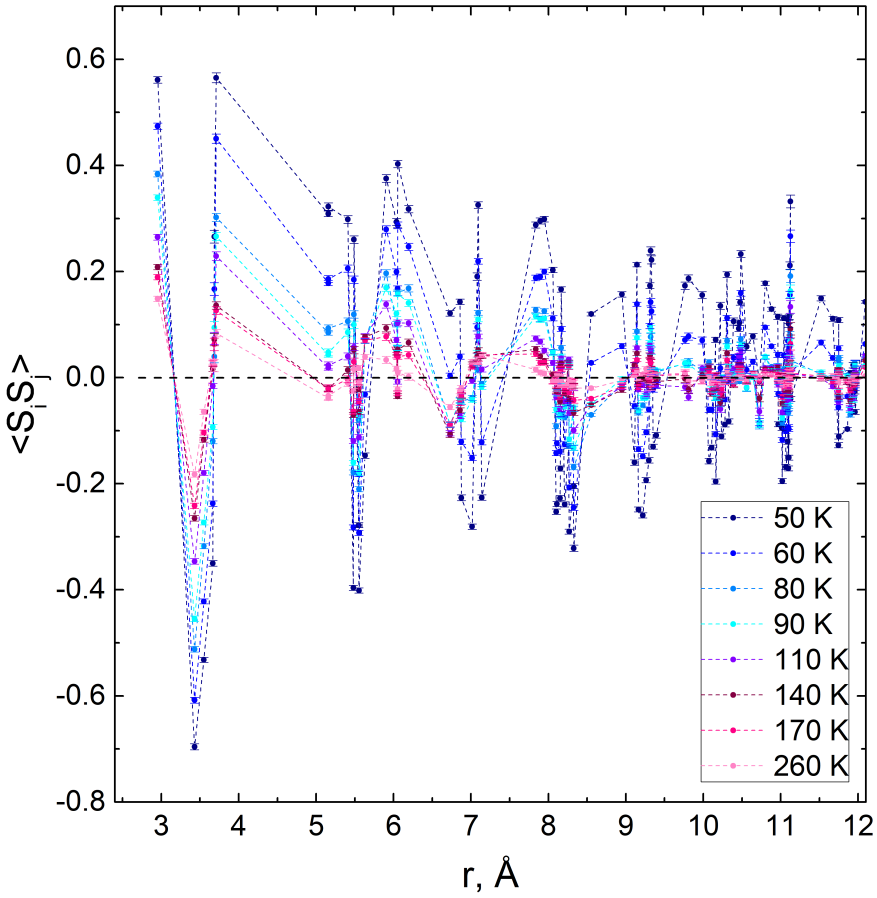

Figure 3.41: Temperature evolution of the radial spin-spin correlation function $< \mathbf{S}_i\mathbf{S}_j >$ of the ordered Co_5TeO_8.

Temperature evolution of the $< \mathbf{S}_i\mathbf{S}_j >$ function (Fig. 3.40) shows that relative spin orientation is conserved at T = 60 K. First noticeable changes take place at T = 80 K: $< \mathbf{S}_i\mathbf{S}_j >$ for r = 6.732(1)Å and r = 6.862(2)Å, corresponding to Co_1-Co_1 pairs, is changing sign from positive to negative; radial spin-spin correlation function for Co^{2+} pairs at larger r takes values close to zero, so thermal fluctuations are significant enough to break correlations in the next nearest unit cells. The more the temperature increases the more the short-range spin correlations are suppressed. However, even at T = 260 K

within $r < 3.707(5)$Å Co^{2+} cations maintain correlations and the relative orientations of their magnetic moments observed at lower temperatures.

For further analysis of the magnetic diffuse scattering of Co_5TeO_8, single crystal neutron diffraction patterns were calculated with the using the SPINDIFF program distributed with SPINVERT. The calculation was performed for (hhl) reciprocal lattice plane with h and l indices in between -5 and 5; figure 3.45 shows calculated neutron scattering intensity for all measured temperatures. First, at high temperatures, no distinct distribution of the diffuse scattering is observed, all the intensity is distributed almost homogeneously across the pattern. At T = 200 K, points arise from the magnetic diffuse scattering, that correspond to the **k** and **k** satellite reflections, typical for incommensurate spiral structures, observed for the ordered Co_5TeO_8 by NPD. The most intense satellites form four-fold patterns around (hhh) ((111) and (222)) and $(hh0)$ ((220) and (440)) positions, which is consistent with NPD observation for the ordered state. First Diffuse scattering surrounds all those (hhh) and $(hh0)$ satellite positions, indicating a lack of coherence in the magnetic scattering. On further cooling all the magnetic diffuse scattering getting more and more located on satellite positions and coincides with the decrease of background scattering between reciprocal space points, corresponding to magnetic Bragg peak positions in the ordered phase. Approaching T_{C1}, the main features shrink into well-defined Bragg peaks and eventually, at T = 60 K all the remaining neutron intensity is left at (111), (222) and (440) peaks and their satellites. It has to be pointed out, taht there are two types of short-range magnetic domains by which these four-fold patterns may be produced: $\mathbf{k}_i1 = (00\delta)$ and $\mathbf{k}_i2 = (\delta\delta\delta)$. While both are providing exactly the same scattering patterns, the latter one is more likely to take place. First of all, the magnetic structure in the ordered state is described with $\mathbf{k}_i = (00\delta)$, which naturally makes $\mathbf{k}_i1$ more probable. Second, in the D7 experiment the raw data was obtained as the powder average of all possible orientations of ordered Co_5TeO_8 crystallites, thus these four-folded patterns may arise as the result of a combination of misoriented $\mathbf{k}_i1$ domains, that effectively provide patterns similar to those of $\mathbf{k}_i2$. Finally, bringing together the results of RMC fit in the direct and reciprocal space, one can conclude that the short-range ordering in the ordered Co_5TeO_8 polymorph possess the same ferrimagnetic spiral nature as the spin arrangement in the ordered phase.

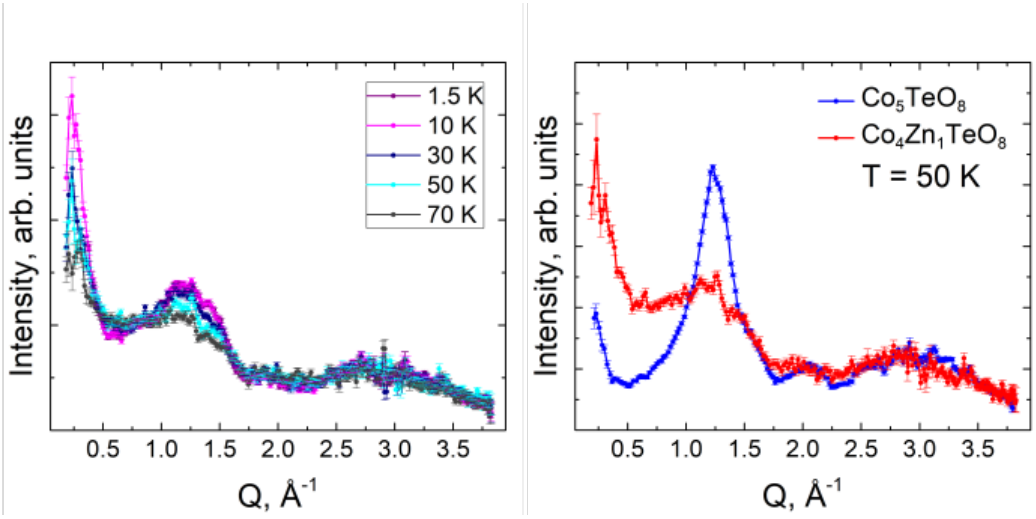

Figure 3.42: Left) Temperature evolution of the diffuse magnetic scattering obtained with XYZ neutron polarization analysis of the $Co_{3.99}Zn_{1.01}TeO_8$; right) Comparison of the diffuse magnetic scattering patterns of the ordered Co_5TeO_8 and $Co_{3.99}Zn_{1.01}TeO_8$ at T = 50 K.

3.6.2 Short range ordering in $Co_{3.99}Zn_{1.01}TeO_8$

As it was discussed earlier, the large amount of magneto-diluting agent introduced into Co_5TeO_8 suppresses the long-range magnetic ordering in the system. However, NPD and SANS data taken for $Co_{3.99}Zn_{1.01}TeO_8$ shows the presence of a strong magnetic diffuse scattering at low temperatures. This behaviour was studied with the XYZ polarization analysis in the temperature range between 1.5 K and 70 K (Fig. 3.42 left). All collected diffuse magnetic scattering patterns show a broad feature centered at $Q \approx 1.2$Å and some additional intensity in the low-Q part, which loose intensity on temperature increase. However, at T = 70 K the diffuse scattering peak is still well-pronounced, indicating relative stability of short-range spin correlations at a given temperature. Comparing the pattern of $Co_{3.99}Zn_{1.01}TeO_8$ to that of parent compound one can see that, regardless to the obvious intensity loss and broadening, diffuse scattering features of these compounds overlap. So one can expect the diluted sample to have a rather similar behaviour (Fig. 3.42 right).

Reverse Monte Carlo fit was performed using a cubic cell with a lattice parameter $a = 8.551$Å; 20 Co^{2+} atoms in the cell with P1 symmetry were set with respect to the cationic arrangement in $P4_332$ group, obtained with the Rietveld refinement (table A.9). RMC fit was performed for the Q region between $Q = 0.37$Å and $Q = 3.82$Å; a $7 \times 7 \times 7$ box was used; maximum 3000 moves per spin was proposed; five independent refinements were carried out to check the stability for each temperature point. Agreement factors for each RMC fit performed for $Co_{3.99}Zn_{1.01}TeO_8$ are listed in tables A.20 and A.21 in the appendix A. Figure 3.43 displays the results of a single RMC fit of data, taken at T = 1.5 K. Radial spin-spin correlation function at T = 1.5 K gives the same relative orientation for spin pairs as that, obtained for the parent compound at T = 50 K. However $< \mathbf{S}_i\mathbf{S}_j >$ of the diluted sample damp faster with increasing distance, indicating a shrinking of SRO domains driven by Zn^{2+} substitution (Fig. 3.43).

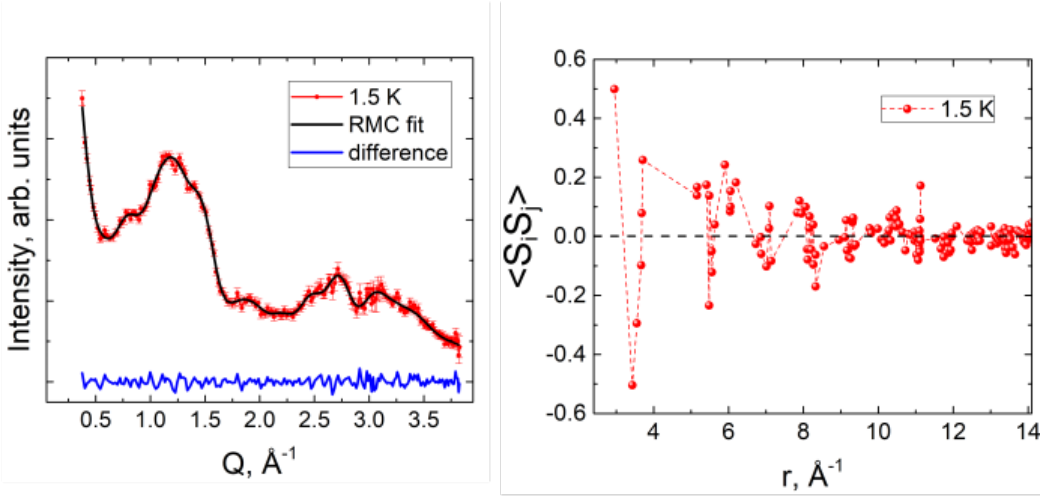

Figure 3.43: Left: RMC fit of the diffuse magnetic scattering pattern of the ordered $Co_{3.99}Zn_{1.01}TeO_8$ polymorph at T = 1.5 K. Red dots - experimental data, black line - RMC fit, blue line - difference curve. Right: Radial spin-spin correlation function calculated with the results of RMC fit for T = 1.5 K

On heating, short-range correlations first display a certain stability, as radial spin-spin correlation functions for T = 1.5 K and T = 10 K show close magnitudes for equidistant spin pairs. Nevertheless with further temperature increase $< \mathbf{S}_i\mathbf{S}_j >$ collapses to zero at

distances $r > 5.4$Å, indicating short-range correlations present on a scale within the next nearest unit cell.

To conclude on the magnetic behaviour of $Co_{3.99}Zn_{1.01}TeO_8$, neutron scattering maps for (hhl) reciprocal lattice plane, the same as for the parent compound, were calculated (Fig. 3.46). At T = 70 K the scattering intensity is concentrated in the ring-shaped features around (hhl) and (hhh) points, indicating magnetic diffusion as a result of lacking long-range ordering. These features are surrounded by satellites forming four-fold patterns, nevertheless some intensity is distributed across the pattern in the form of a background scattering. On cooling, incoherent background intensity is getting suppressed while the main features together with their satellites are getting more intense. In comparison to the ordered Co_5TeO_8, main features at (hhl) and (hhh) preserve their shape down to 1.5 K. Indeed this is another sign of the dilution with Zn^{2+} in $Co_{5-x}Zn_xTeO_8$ to break the magnetic coherence in the system. However, as in the non-diluted compound, satellite features together with the behaviour of $< \mathbf{S}_i\mathbf{S}_j >$ function point out the ferrimagnetic spiral nature of short-range spin correlation of $Co_{3.99}Zn_{1.01}TeO_8$ 3.44.

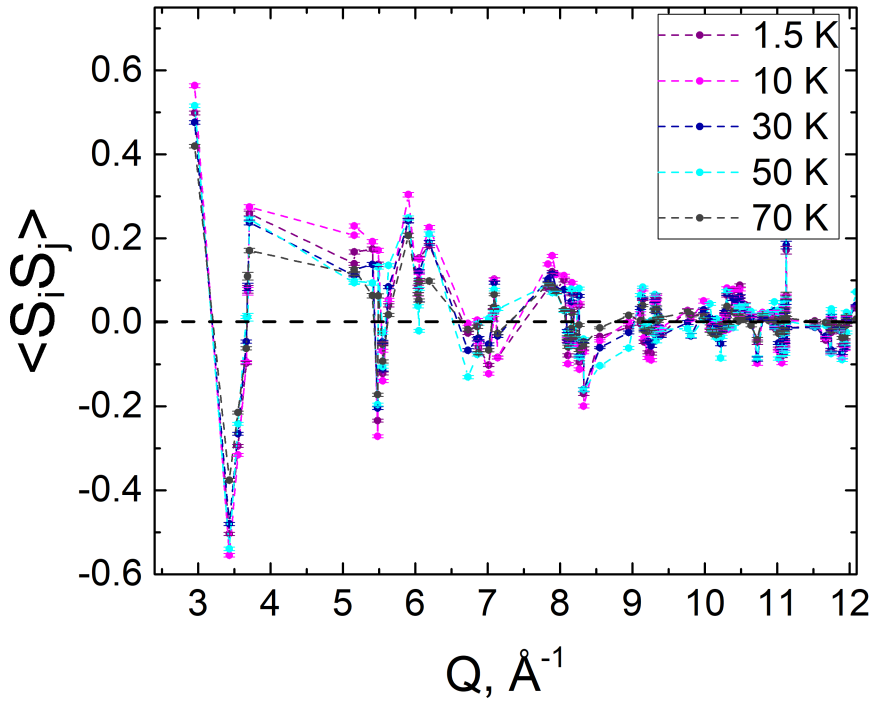

Figure 3.44: Temperature evolution of the radial spin-spin correlation function $< \mathbf{S}_i\mathbf{S}_j >$ of $Co_{3.99}Zn_{1.01}TeO_8$.

Results of the XYZ polarization analysis allow us to conclude that the formation of a SRO domains with ferrimagnetic spiral-like spin correlations is an inherent feature of the $Co_{5-x}Zn_xTeO_8$ family with x $\in [0, 1.01]$. Still for $x = 1$, the half of $A-$site cations in $(Co_{1-x/2}Zn_{x/2})[Co_{1.5}Te_{0.5}]O_4$ is occupied by the non-magnetic agent, thus magnetic dilution of A-site, within the given range of Zn^{2+} concentrations, is not enough to modify J_{AB} for suppressing this behaviour.

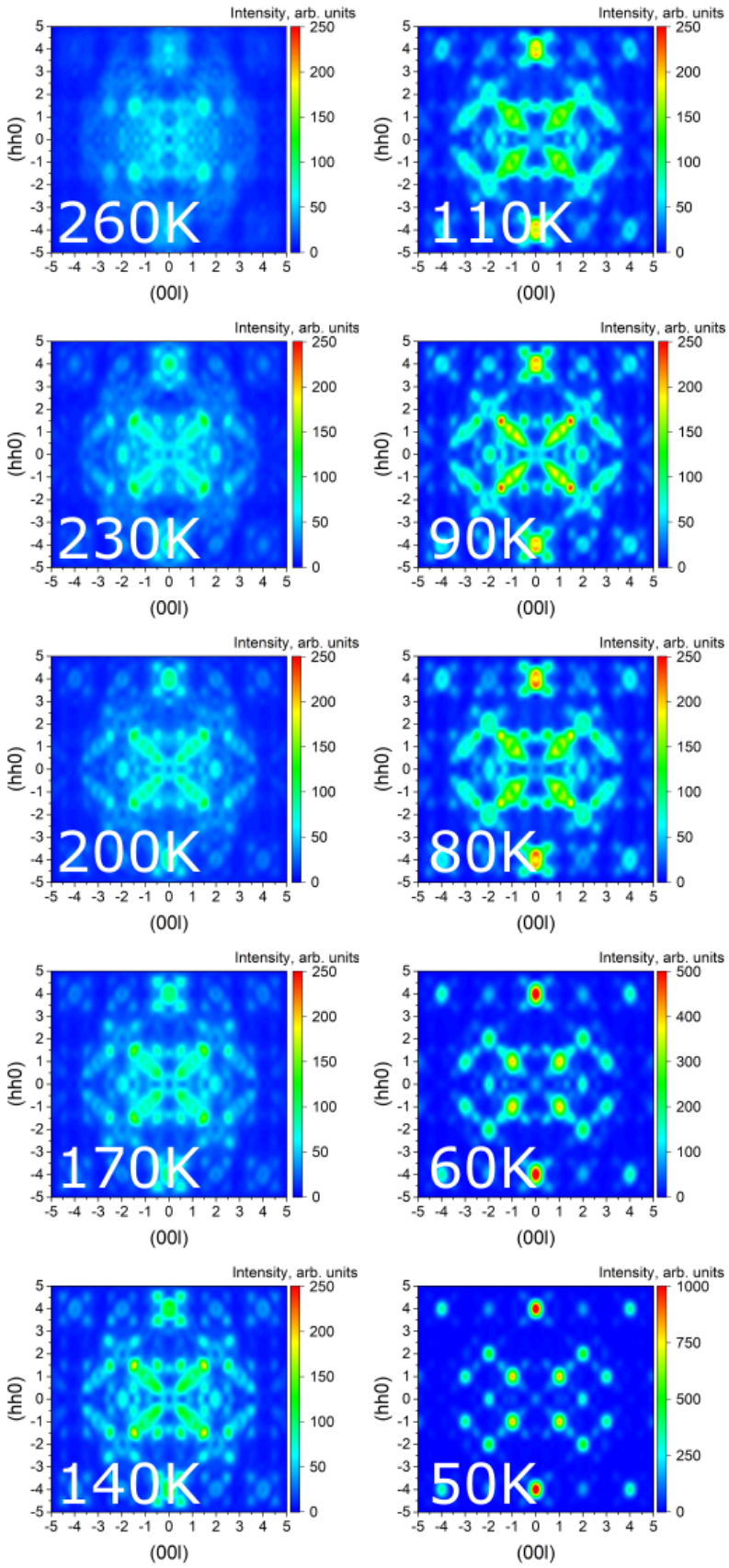

Figure 3.45: Single-crystal magnetic diffuse scattering patterns calculated from RMC refimenent in the (hhl) plane for the ordered Co_5TeO_8 polymorph at all studied temperatures

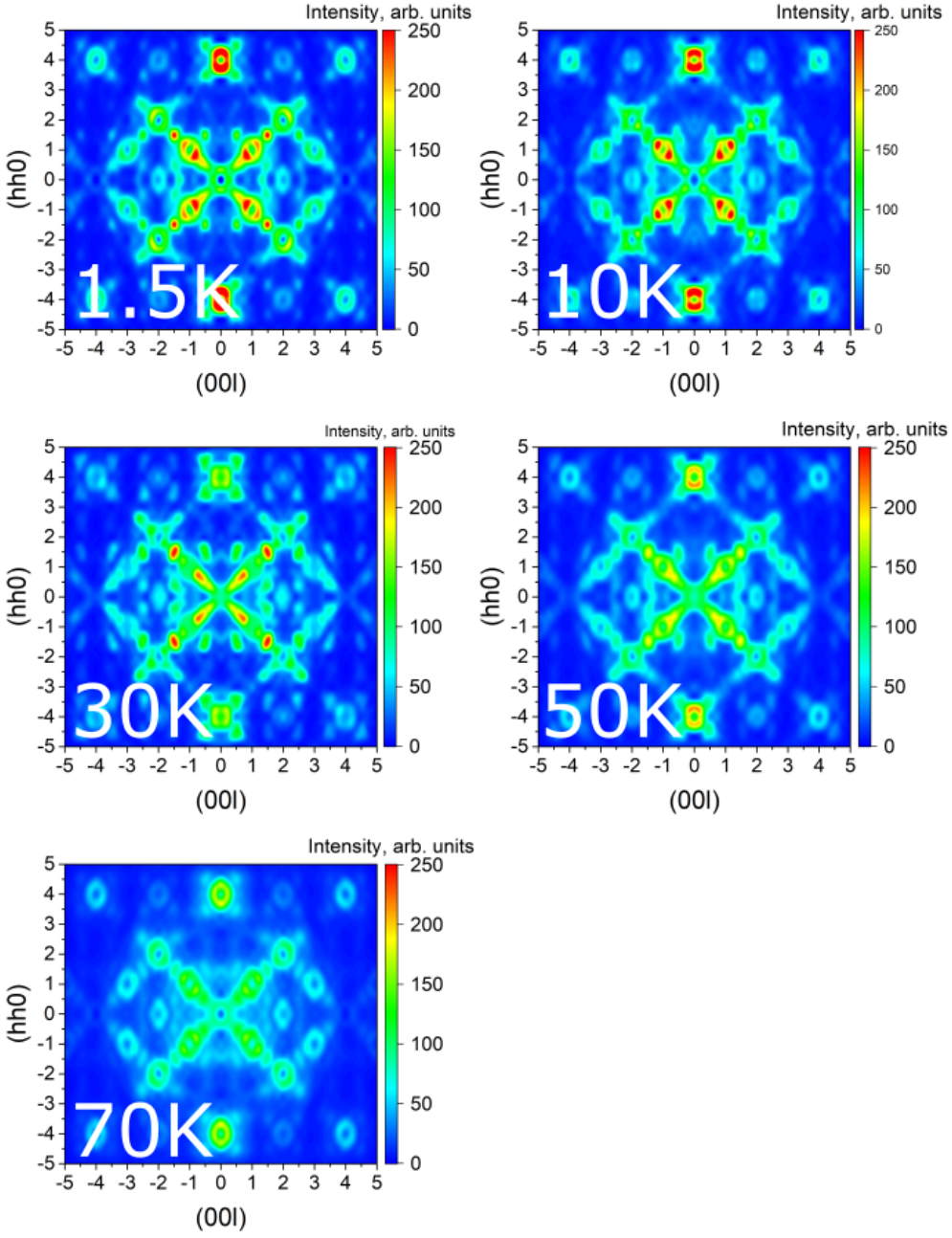

Figure 3.46: Single-crystal magnetic diffuse scattering patterns calculated from RMC refimenent in the (hhl) plane for $Co_{3.99}Zn_{1.01}TeO_8$ at all studied temperatures

3.7 Electric behaviour and magnetoelectric coupling

First, the results of dielectric spectroscopy for the disordered Co_5TeO_8 polymorph are going to be highlighted. In order to shed light on the charge subsystem of the compound, the method was used to measure the temperature evolution of capacitance at fixed applied magnetic field.

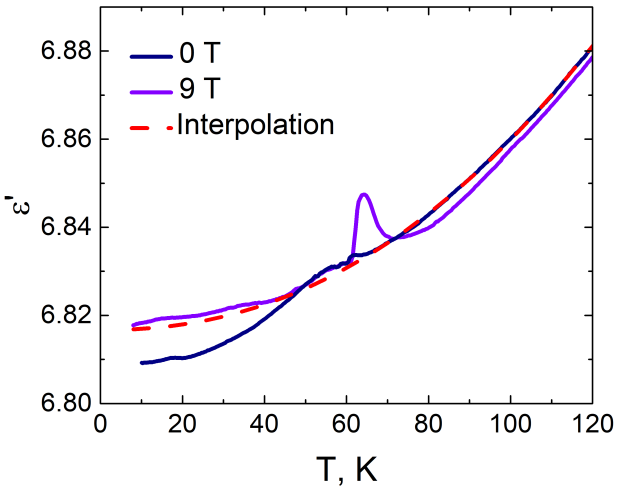

Figure 3.47: Temperature evolution of the zero-field permittivity (dark blue) and permittivity at B = 9 T (violet curve) of the disordered Co_5TeO_8 polymorph and an interpolation of the high-temperature region (red dashed curve).

For the disordered polymorph two $\epsilon(T)$ curves were obtained for B = 0 T and B = 9 T in temperature regions between 10 K and 125 K and 8 K and 125 K respectively (fig. 3.47). On cooling, a zero-field curve decreases smoothly at a temperature region far above the transition temperature $T_N = 40$ K. First noticeable changes appear at $T \approx 60$ K. So, for better distinguishing of features of $\epsilon(T)$ curves, the high temperature part of the temperature evolution of the zero-field dielectric constant ($T > 60K$) was interpolated to low temperatures with the following expression:

$$C(T) = A + BT^V, \tag{3.4}$$

where A, B and V are refinable parameters. The equation 3.4 is only used as a guide for the eyes. It is seen that at $T \approx 60$ K the zero-field $\epsilon(T)$ curve shows a hump, and on further cooling the curve deviates from the high-temperature interpolation, and then undergoes a decrease at the temperature close to T_N. This slight increase below 60 K overlaps with the maximum intensity of the diffuse scattering observed with NPD (3.9 right). Thus both short-range and long-range magnetic orderings affect the charge subsystem of the disordered polymorph.

Applying a 9 T magnetic field leads to substantial changes in the behaviour of the $\epsilon(T)$ curve. While a bump below 60 K, related to the emergence of SRO domains, overlaps with the one observed for B = 0 T, the low-temperature part is significantly increased. More important, there is a sharp peak growing at $T_C = 70$ K, indicating a clear magneto-electric coupling in the system.

To analyse of the field-dependent electronic behaviour, one may calculate the variation of the dielectric constant between the zero-field and the finite field state. The so-called

magnetoelectric factor, which may be defined as

$$\Delta\epsilon = \frac{\epsilon(B) - \epsilon(0)}{\epsilon(0)} = \frac{C(B) - C(0)}{C(0)}, \tag{3.5}$$

where C is capacitance. For the disordered polymorph $\Delta\epsilon(T)$ curve at B = 9 T reaches the maximum value of 0.2% at T_C (Fig. 3.48), however the larger deviation of $\Delta\epsilon$ occurs at low temperatures, for $T < T_N$. From the Ginzboug-Landau approximation of the thermodynamic potential (equation 1.1) of a multiferroic material follows that [208]:

$$\delta\epsilon \propto \gamma M^2. \tag{3.6}$$

Thus, the change of the dielectric constant of a magnetoelectric material is expected to be proportional to the square of its magnetization.

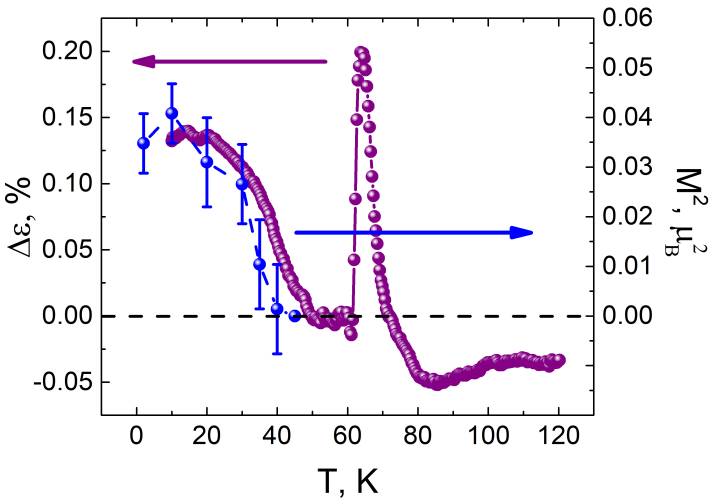

Figure 3.48: Temperature evolution of the magnetoelectric factor at B = 9 T (violet curve) and the square of magnetization obtained with the Rietveld refinement of the low temperature NPD data (blue curve) of the disordered Co_5TeO_8 polymorph.

The figure 3.48 clearly shows that the expression 3.6 is fulfilled since two curves, $M^2(T)$ and $\Delta\epsilon(T)$ overlap, the presence of magnetoelectric coupling in the disordered Co_5TeO_8 is ascertained. However, considering the magnetoelectric behaviour of a certain material, its magnetic symmetry, namely the actions of operations of its magnetic point group, should be taken into account. It allows to calculate symmetry-adapted tensors describing various properties of this material [209]. The form of these tensors may be calculated using MTENSOR program hosted at Bilbao Crystallographic Server [210]. Unfortunately, the magnetic symmetry of the disordered polymorph forbids the effect of electric polarization in the system, thus the compound is magnetoelectric but not multiferroic.

To study the electrical properties of the ordered Co_5TeO_8 polymorph, two independent approaches were used, the first one is the thermal variation of the capacitance at a fixed magnetic field, the second one is the isothermal capacitance measurement as a function of the applied field.

Let us first consider capacitance measurements as a function of temperature at a fixed applied field. All measurements in this regime were taken in the temperature region between 7 K and 145 K. On cooling a zero-field capacitance of the ordered polymorph (Fig. 3.49) shows a decrease and at the high temperature region ($T < T_{C1}$) the $C(T)$ curve

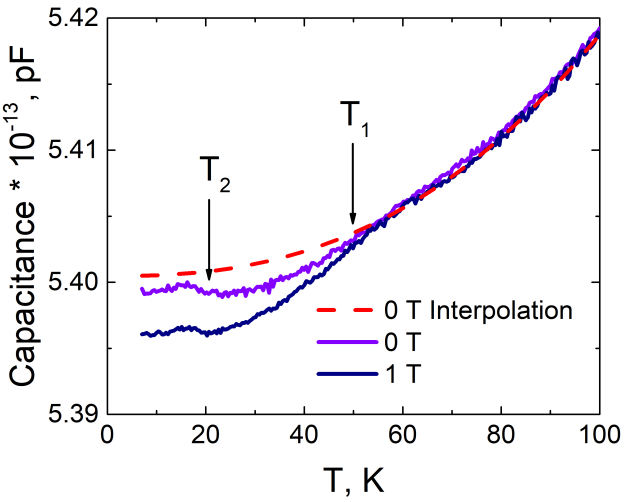

Figure 3.49: Temperature evolution of the zero-field capacitance (dark blue) and capacitance at B = 1 T (violet curve) of the ordered Co_5TeO_8 polymorph and an interpolation of the high-temperature region (red dashed curve).

clearly follows a trend that may be interpolated to low temperatures with the equation 3.4. However, approaching T_{C1}, at $T_1 \approx 50$ K, the capacitance curve decreases faster than the high-temperature interpolation. Below T_{C2}, at $T_2 \approx 15$ K, $C(T)$ exhibits a small feature. This behaviour indicates that both magnetic phase transitions in ordered Co_5TeO_8 are correlated with the behaviour of the electronic subsystem. To trace the evolution of dielectric properties under applied magnetic field, the same $C(T)$ measurement was taken at 1 T. It is seen that, regardless of an increase of capacitance magnitude at low temperatures, $C(T)$ at $B = 1$ T curve deviates from the high-temperature interpolation and shows the same features at T_1 and T_2 as the zero-field capacitance. Thus applying a magnetic field changes the dielectric properties of ordered Co_5TeO_8.

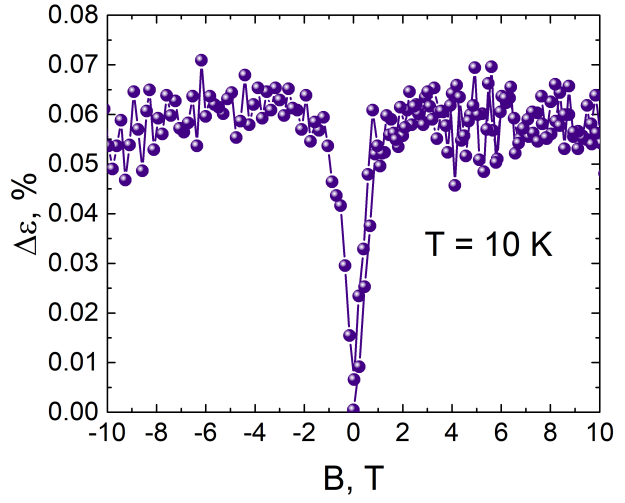

Figure 3.50: Field dependence of the magnetoelectric factor, obtained from the isothermal $C(H)$ variation for the ordered Co_5TeO_8 polymorph taken at T = 10 K.

Another way to observe the impact of the applied magnetic field over an electronic properties is measuring the capacitance field-evolution at fixed temperatures. This was done for a set of temperatures between 80 K and 10 K in the applied magnetic field region between -10 T and 10 T along the $z-$axis in the laboratory frame. Figure 3.50 illustrates $C(H)$ variation measured for the ordered Co_5TeO_8 at T = 10 K. The ordinate axis is the magnetoelectric factor which is defined by the equation 3.5. The $C(H)$ measurement for T = 10 K shows the behaviour inherent to all measured temperatures: with an increase of the applied field $\Delta\epsilon$ grows rapidly reaching its highest value at $B \approx 2$ T, then a further increase of B does not effect the magnetoelectric factor. The temperature evolution of $\Delta\epsilon$ at $B = 1$ T is plotted in figure 3.51 in red dots.

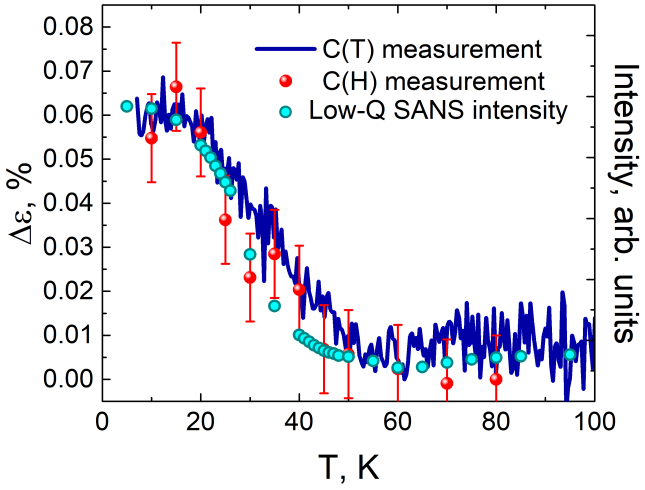

Figure 3.51: Temperature evolution the magnetoelectric factor at 1 T obtained from $C(T)$ (blue line) and $C(H)$ (red dots) measurements and low-Q SANS intensity at $|Q| = 0.027$ Å^{-1} for the ordered Co_5TeO_8 polymorph.

The same equation 3.5 can be applied to $C(T)$ measurements, shown on figure 3.49 to obtain the temperature evolution of $\Delta\epsilon$. The result is shown in figure 3.51 as a blue line. Remarkably, the results provided by two independent methods overlap, confirming that there was no spurious effect from temperature drift. Both $\Delta\epsilon$ temperature dependences exhibit a noticeable increase below T_{C1}. On further cooling $\Delta\epsilon(T)$ grows, reaching a plateau below 20 K. This indicates the onset of major changes in the charge subsystem with the emergence of the ferrimagnetic conical spin ordering. This is clearly seen by plotting the temperature evolution of the low-Q SANS intensity, discussed in details in paragraph 3.5. This small angle scattering signal is proportional to the square of magnetization, so its overlap with $\Delta\epsilon(T)$ curves demonstrates the direct interplay between charge and spin subsystems in the ordered Co_5TeO_8 polymorph. It should be also pointed out, although there is a clear magnetoelectric coupling in the ordered Co_5TeO_8, that the effect is rather subtle: both methods provide a top magnitude of $\approx 0.06\%$.

In the ordered Co_5TeO_8, the point group deduced from the magnetic superspace group is 4, the symmetry-adapted tensor for electric polarization is of the form:

$$P_i = \begin{pmatrix} 0 \\ 0 \\ P_3 \end{pmatrix}. \tag{3.7}$$

So the magnetic symmetry of the compound allows the polarization occurrence along the crystallographic c-axis. The magnetoelectric tensor α_{ij}, is a second rank tensor relating the induced magnetization $\mathbf{M}_i$ to the applied electric field $\mathbf{E}_j$

$$\mathbf{M}_i = \alpha_{ij}\mathbf{E}_j \tag{3.8}$$

that for Co_5TeO_8 is of the form:

$$\alpha_{ij} = \begin{pmatrix} \alpha_{11} & \alpha_{12} & 0 \\ -\alpha_{12} & \alpha_{22} & 0 \\ 0 & 0 & \alpha_{33} \end{pmatrix}. \tag{3.9}$$

Dielectric spectroscopy measurements were also performed on the highly diluted compound $Co_{3.99}Zn_{1.01}TeO_8$. This may allow to establish correlations between the lack of the long-range magnetic ordering and the electric behaviour of the system. Capacitance as a function of temperature for $Co_{3.99}Zn_{1.01}TeO_8$ was measured at $B = 1$ T and 5 T in the temperature region between 8 K and 120 K (Fig. 3.52 left). The high-temperature part of the zero-field $C(T)$ curve was interpolated with the same 3.4 equation. Below 50 K the zero-field capacitance increases, separating from the high-temperature trend, which is opposite for the compounds with long-range magnetic ordering, discussed previously in this paragraph. Low-temperature NPD measurements of $Co_{3.99}Zn_{1.01}TeO_8$ has revealed that around 50 K a diffuse magnetic scattering unambiguously appears on diffraction patterns, thus the short-range magnetic ordering provokes changes within the charge subsystem of the compound. A closer look at the low-temperature part of zero-field $C(T)$ dependence may be taken on the right part of the figure 3.52: after reaching its minimum, the capacitance exhibits two distinct features at $T_1 = 40$ K and $T_2 = 15$ K. These temperatures are close to the long-range ordering transition temperatures shown by $Co_{5-x}Zn_xTeO_8$ with $x \leq 0.76$. This may indicate the presence of magnetic phase transitions on a short-range scale which were not detected by other techniques. As soon as the magnetic field of 5 T is applied, all features below 50 K are suppressed, and the capacitance curve almost match with the high temperature interpolation of the zero-field data. This behavior implies a negative magnetoelectric effect.

The negative magnetoelectric effect was also confirmed by the field variation of the capacitance at a set of fixed temperatures. To obtain the field dependence of $\Delta\epsilon$ the equation 3.5 was applied to all measured $C(H)$ curves (3.53). Below 15 K no difference is observed for magnetoelectric factors: smoothly declining bell-shaped curves match, reaching a minimum magnitude of $\Delta\epsilon(H) \approx$ -0.15. Upon temperature increase $\Delta\epsilon(H)$ curves flatten up with a simultaneous increase of their magnitudes, however at the highest measured temperature of 60 K some effect is still present. As D7 results demonstrate the presence of a short-range ordering at least up to 70 K, one can expect noticeable field-driven changes in $C(H)$ up to this temperature.

It has to be said that several attempts were made to measure an electric polarization in ordered Co_5TeO_8 and $Co_{3.99}Zn_{1.01}TeO_8$ using piezoelectric current technique. Unfortunately, the signal to noise ratio was not sufficient to detect any non-negligible effect in

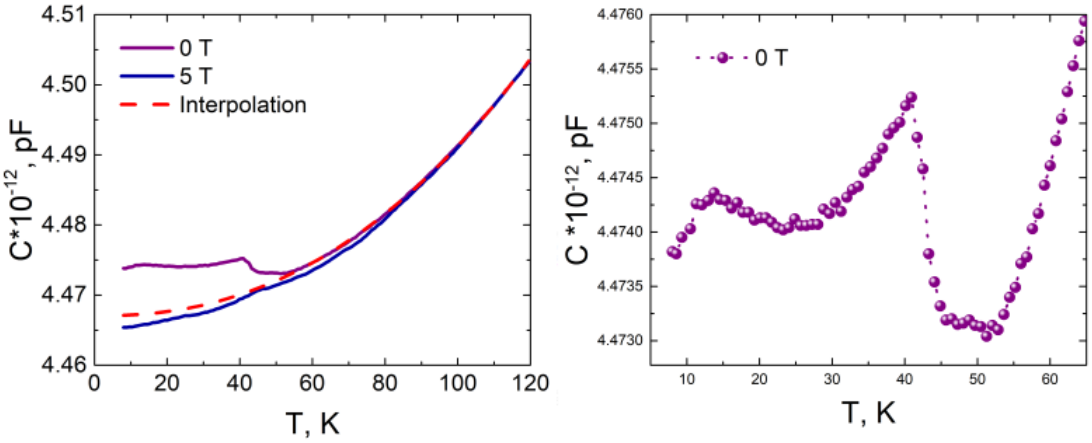

Figure 3.52: Left: Temperature evolution of the zero-field capacitance (purple curve), capacitance at $B = 5$ T (blue curve) and the high-temperature interpolation of the zero-field capacitance of $Co_{3.99}Zn_{1.01}TeO_8$; Right: Low-temperature region of the zero-field capacitance of $Co_{3.99}Zn_{1.01}TeO_8$.

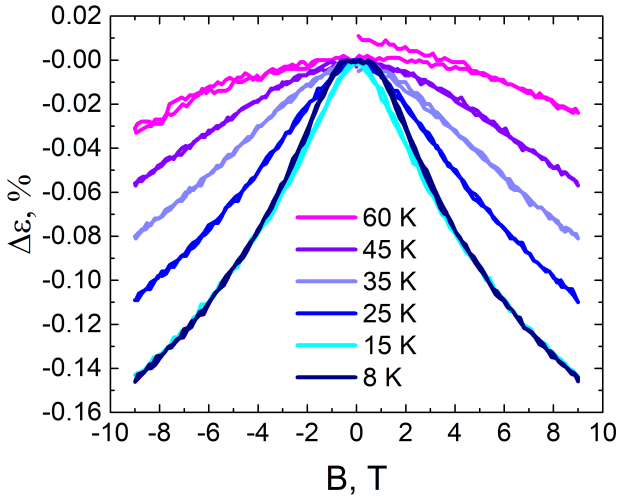

Figure 3.53: Magnetic field variation of the dielectric constant increment at constant temperatures obtained for $Co_{3.99}Zn_{1.01}TeO_8$ polymorph.

both samples. However, one can not conclude about the total absence of electric polarization for both compounds since the measurement was done on polycrystalline pellets. For precise measurements single crystals are required.

3.8 Discussion

The case of Co_5TeO_8 polymorphs provides an excellent possibility to examine the relationship between the structure and the properties of materials with identical chemical composition, yet contrasting physical behaviour. To some extend these two materials exhibit similar characteristics, however, it is remarkable how slight structural alteration such as of B-site subordering between Co^{2+} and Te^{6+} induces different scenarios for the

disordered and ordered Co_5TeO_8.

First, it has to be said that these two polymorphs have nearly identical cell parameters and relatively close magnetic phase transition temperatures.The inverse magnetic susceptibility are also similar: both polymorphs show short-range magnetic ordering for temperatures below 260 K and long-range ordering at $T_N = 40$ K for the disordered polymorph and $T_{C1} = 45$ K for the ordered one. NPD revealed a rather common magnetic behaviour in the disordered Co_5TeO_8. Indeed ferrimagnetic ground state is typical for the major part of spinel compounds with both A- and B-sites occupied by magnetic cations. In the long-range magnetic ordering state, the ordered polymorph shows a different behaviour with an incommensurate ferrimagnetic spiral spin ordering. Thus, in the case of the Co_5TeO_8 polymorphs, the transformation from B-sites with disordered Co^{2+}/Te^{6+} occupancy ($Fd\bar{3}m$ structure) to B-sites with an ordered occupancy ($P4_332$ structure) has large incidence on the long-range magnetic state. To our knowledge, the presence of these two distinct magnetic behaviour for these two Co_5TeO_8 polymorphs is unique in spinels. One other spinel compound $LiFe_5O_8$ can also crystallise in both disordered ($Fd\bar{3}m$) and ordered polymorph ($P4_332$) with exactly the same cationic order on the B-sites than ordered Co_5TeO_8. Nevertheless, there are no differences in their magnetic properties, i.e. ferrimagnetic with high T_N value above 900K [211]. So one can wonder why such distinct behaviours are observed for Co_5TeO_8 polymorphs, and mostly why an incommensurate ferrimagnetic spiral spin ordering arises in the ordered polymorph. As already mentioned in the introduction part, with the u parameter introduced in LKDM theory:

$$u = \frac{4\, J_{BB}\, |\mu_B|}{3\, J_{AB}\, |\mu_A|}, \tag{3.10}$$

one can quantify the magnitude of the Magnetic Geometrical Frustration (MGF) by comparing J_{AB} and J_{BB} interactions. Maximal MGF correspond to $u = \infty$ when $J_{AB} = 0$ and $\mu_A = 0$ while weak MGF occurs up to $u = 1.298$. Thus, for $u \geq 1.298$, at the ground state, the ferrimagnetic spiral long-range configuration is not stable. Weak MGF are preserved and ferrimagnetic spiral short-range order arises below the re-entrant spin glass transition T_F. This is the case for both spinel compounds $CoCr_2O_4$ and $MnCr_2O_4$ with respective u parameters of 2 and 1.5. In these compounds, re-entrant spin glass like behaviour is observed with the presence of ferrimagnetic spiral short-range orders that coexist with ferrimagnetic spiral long-range order below T_F (≈ 13 K for $CoCr_2O_4$ and ≈ 14 K for $MnCr_2O_4$). For $8/9 \leq u < 1.298$ the ferrimagnetic spiral long-range order is stable at the ground state, then for $u < 8/9$ the spinel magnetic behaviour corresponds to the Néel long-range configuration with a classic ferrimagnetic state. In Co_5TeO_8, the magnetic dilution of the B-sites must lower the J_{AB} interaction. Since the observed ground state is colliear ferrimagnetic for the disordered Co_5TeO_8 polymorph and a ferrimagnetic spiral long-range order for the ordered polymorph, one can suppose that for both polymorphs, the u parameter should be close to 8/9, but the structural differences are sufficient to affect slightly the J_{BB}/J_{AB} ratio. Moreover, comparing ratio μ_B/μ_A for the two polymorphs, one can see they are relatively close: 1.22 for the disordered Co_5TeO_8 and 1.25 for the ordered one. Thus, one can suppose u slightly lower than 8/9 for the disordered polymorph and u slightly bigger than 8/9 for the ordered polymorph. Another way of estimating the degree of frustration is the ratio between Θ and T_N ($f = |\Theta/T_N|$) that is commonly used in quantum and frustrated magnetism. In the ordered Co_5TeO_8 polymorph $f = 2.88$ which is not weak, one can conclude the combination of magnetic frustration and the DM interaction are responsible for stabilization of the long-range spin modulation in the system. Indeed, the magnetic structure of the ordered Co_5TeO_8 can be considered as a

distorted ferrimagnet. While the disordered Co_5TeO_8 with a random distribution of Co^{2+} and Te^{6+} may be taken as a common representative of spinel magnetic spinel compounds, the $B-$site subordering of the $P4_332$ structure, moderates the magnetic structure with a long periodic conical spin modulation.

A combination of the NPD and the zero-field SANS measurements have helped to shed light on the nature of the phase transition at $T_{N2} = 27$ K for the ordered Co_5TeO_8 compound. As observed by the NPD, short-range correlations set in far above the long-range ordering transition temperature $T_{N1} = 45$ K, which appears as a magnetic diffuse scattering on NPD patterns. Below T_{N1}, NPD patterns shows the presence of both: magnetic reflections ($\mathbf{k}_0$ and $\mathbf{k}_i = (00\delta)$ and the diffuse magnetic halo, indicating the co-existence of long- and short-range magnetic ordering. Upon cooling below T_{N2} the intensity of the magnetic diffuse scattering decreases, until it is entirely suppressed at T_{N2}. At the same time the temperature evolution of the n-index, defining the slope of the low-$\mathbf{Q}$ part of the SANS intensity ($\propto Q^{-n}$), shows a rapid growth below T_{N1}, coinciding with the development of the magnetic order; whereas below T_{N2} it reaches a plateau with $n \approx 3.78$, being close to Porod scattering regime. The latter points out a well-defined domain structure below T_{N2}. Summarising, one can conclude that magnetic ordering is reaching a stable configuration with a transition at T_{N2}. This lies in agreement with $u < 1.298$ for the ordered polymorph as supposed previously. The ferrimagnetic spiral long-range order corresponds to the stable ground state.

The SANS under applied magnetic field has extended the magnetic phase diagram of the ordered Co_5TeO_8, obtained with the magnetic susceptibility measurements. The bulk characterization technique remained insensitive to an in-field domain reorientation at 32 K. One can expect a field-induced magnetic phase transition at $H_{C1} = 0.06$ T, however SANS performed on a polycrystalline sample is cannot ascertain of defining a magnetic structure at the atomic level.

As for the magnetic dilution, let us first mention the $B-$site dilution as it is inherently present in the Co_5TeO_8 as the quarter of octahedral sites are occupied with the non-magnetic Te^{6+}. For clarity, the chemical formula of a studied system may be written in the generalized spinel notation as $(Co_{1-x/2}Zn_{x/2})[Co_{1.5}Te_{0.5}]O_4$. Here the studied system can be compared to a couple of series based on the $CoCr_2O_4$ compound. The first one is $Co(Cr_{1-x}Al_x)_2O_4$ series [212]. Upon the increase of an Al^{3+} content the magnetic behaviour of the system is similar to the parent compound up to $x = 0.2$: first a ferrimagnetic order appears at T_C which is then followed by a ferrimagnetic spin-spiral transition at T_S. For the $0.2 < x \leq 0.5$ the long-range ferrimagnetic spiral state is suppressed in favour of the re-entrant spin glass behaviour. Regardless to the stability of the long-range ferrimagnetic ordering in the $Co(Cr_{1-x}Al_x)O_4$, it turns out that the ordered Co_5TeO_8 polymorph sustains the incommensurate spin modulation under a greater $B-$site dilution. The second series is the $Co(Cr_{1-x}Co_x)_2O_4$ for which it was shown that the substitution of Cr^{3+} with Co^{3+} enhances both saturated electric polarization and magnetization. However, in the studied case, the magnetic dilution on the $B-$site does not boost up ferroelectric performance, since the magnetoelectric effect is very weak in the case of both Co_5TeO_8 polymorphs. Unfortunately, ordered phases of either $Co_2Cr_3AlO_8$ and $Co_2Cr_3CoO_8$ with a $P4_332$ crystal structure do not exist, so it is hard to prove if the cations ordering on the B-sites is indeed the driving force to recover a ferrimagnetic spiral configuration. Let us discuss the introduction of Zn^{2+} in the system, which happens exclusively at tetrahedral $A-$sites for the studied series. Remarkably, it leaves no chance to obtain a disordered polymorph, and the crystal structure adopts only the $P4_332$ space group. Another surprising feature exhibited by the $(Co_{1-x/2}Zn_{x/2})[Co_{1.5}Te_{0.5}]O_4$ family is the stability of the

long-range magnetic ordering. While the second magnetic phase transition appearing at T_{N2} in the parent compound endures only a small dilution with $x = 0.04$ and it is is completely suppressed at a higher Zn^{2+} content, the long-range magnetic ordering itself is preserved up to a rather high $x = 0.76$. Known literature does not provide a wide number of studies on the influence of the $A-$site dilution over magnetic behaviour in spinels where both $A-$ and $B-$ sites are occupied with magnetic ions. The studied case may be only compared to $Ni_{1-x}Zn_xFe_2O_4$ [213] or $M_{1-x}Zn_xFeCrO_4$ family, where M is Cu^{2+} [197], Ni^{2+} [214] or Co^{2+} [215]. The most stable magnetic behaviour is shown by $Ni_{1-x}Zn_xFe_2O_4$ ($0 \leq x \leq 0.5$), where the long-range ordering transition temperature is reduced from $T_C \approx$ 860 K for $x = 0$ to $T_C \approx 620$ K for $x = 1$. For the $Co_{1-x}Zn_xFeCrO_4$ a transition from the uniaxial to canted ferromagnetic structure was observed using NPD technique, however the Mössbauer spectroscopy confirms the presence of a spin-glass component at low temperatures for $0 \leq x \leq 1$. Large amount of Zn^{2+} breaks the ferrimagnetic ordering in $Ni_{1-x}Zn_xFeCrO_4$ in favour of a semi-spin-glass transition appearing for $x \leq 0.6$. Another series from the same family with Cu^{2+} is also ferrimagnetic for $x \leq 0.6$. Compounds with higher values of x display cluster spin-glass like behaviour. However, most importantly, discussing the $A-$site dilution, the studied series should be compared to another $CoCr_2O_4$ series with the Zn^{2+} substitution at the tetrahedral positions [150]. It was shown that $Zn_{1-x}Co_xCr_2O_4$ with $1 \leq x \leq 0.6$ adopts the behaviour of the $CoCr_2O_4$ while for a larger amount of diluting agent ($0.6 < x \leq 1$), the system has a spin-glass ground state preceded by a frustrated long-range antiferromagnetic ordering. Hereby $Zn_{1-x}Co_xCr_2O_4$ and $(Co_{1-x/2}Zn_{x/2})[Co_{1.5}Te_{0.5}]O_4$ are showing similar behaviour: long-range ferrimagnetic spin-spiral ordering is suppressed when more than 40% of the tetrahedral positions are occupied with a non-magnetic cation. With above said, it is clear that for such systems the cationic composition at both sites is of a high importance for the stability of the long-range magnetic ordering against the magnetic dilution. It is also clear that with $x = 0.76$ the system endures a massive magnetic dilution on both tetrahedral and octahedral positions. Remarkably, on the entire range of Zn^{2+} content, the spin structure remains conical, nevertheless in the high dilution region ($x = 0.58$, 0.76) the antiferromagnetic coupling between $A-$ and $B-$sites is sufficiently weakened. This indirectly indicates the presence of an additional contribution, which stabilizes the spin modulation, which may be the Dzyaloshinskii-Moriya interaction in this case. Upon further increase of the non-magnetic cation in the $A-$site, the system reaches a percolation threshold and the long-range magnetic ordering is suppressed entirely in favour of a short-range ordering similar to those described above for some other spinel compounds.

As for the short-range ordering, the neutron XYZ polarization analysis demonstrates the stability of magnetism in $Co_{5-x}Zn_xTeO_8$ from another point of view. Observations made with the NPD exhibited a magnetic diffuse halo around the fundamental (111) reflection up to $T \approx 125$ K for the parent compound. However, the XYZ polarization analysis was sensitive enough to discover non-negligible spin correlations up to 260 K, which is being closer to room temperature rather than to T_{C1}. Noitice that, short-range spin correlations in the ordered Co_5TeO_8 are of the same ferrimagnetic conical nature as the spin configuration at the ordered state. Moreover, the highly diluted $Co_{3.99}Zn_{1.01}TeO_8$ shows the same type of behaviour. These pinpoint the fact that magnetism in the ordered $Co_{5-x}Zn_xTeO_8$ spinel series is robust and dictated by the cationic arrangement within $P4_332$ structure. Unfortunately, there was no possibility to carry out the XYZ polarization analysis on the disordered Co_5TeO_8 polymorph, nevertheless the NPD can provide some important insights on a short-range ordering in this compound. Similar to the ordered polymorph the disordered one shows the presence of a strong magnetic diffuse scattering

at relatively high temperatures: at 100 K it already reaches ≈ 44% of its maximum value. Thus, one can assume the temperature region of short-range ordering existence in the disordered polymorph extends far above the ferrimagnetic transition temperature. However there is also a noticeable dissimilarity between two polymorphs: in the case of the disordered polymorph the magnetic halo is preserved down to 1.7 K, so the spin-glass component is present even at the ground state of the compound. This arise as follows: for the disordered $Fd\bar{3}m$ structure Te^{6+} acts as a magneto-diluting agent, perturbing the ferrimagnetic order.

Having a complete neutron diffraction study of the $Co_{5-x}Zn_xTeO_8$ series, one may provide first rough estimations of J_{AB} and J_{BB} exchanges in the system. Those are superexchange interactions since next nearest Co^{2+} cations are coupled via intermediary non-magnetic O^{2-}, thus according to Goodenough-Kanamori rules, Co^{2+}-O^{2-}-Co^{2+} bonds forming angles close to straight should favour an antiferromagnetic interaction [216, 217, 79]. And this is the case of the intersite J_{AB} interaction. Right angle bonds, in turn, should host a coupling of a ferromagnetic nature, which takes place for Co^{2+} cations at the $B-$site. However, the LKDM model implies that both interactions to be of the same nature, thus J_{AB} and J_{BB} should be both antiferromagnetic. This consideration is indirectly prooved by a deeply negative Weiss temperature (Θ = -130 K). Placing an exact value of μ_B/μ_A ratio in the equation B.4, one may see that $J_{BB}/J_{AB} > 0.54$ for the ordered Co_5TeO_8, thus J_{BB} is twice smaller then J_{AB}, however the $A-$site magnetic dilution weakens the latter significantly since for large x values in $Co_{5-x}Zn_xTeO_8$ the long-range magnetic ordering is suppressed. At this point the system acquires a similar behaviour to $ZnFe_2O_4$ for which $u = \infty$[139]. The real difficulty behind building up a magnetic ground state model of the Co_5TeO_8 is a large number of magnetic cations in the unit cell: both polymorphs contain 20 atoms the magnetic unit cell. Moreover, the local environment of $B-$site Co^{2+} cations in the case of the ordered polymorph implies a complex scheme of exchange pathways, in a way that requires introduction of additional superexchange $J_{AB'}$, $J_{BB'}$, etc. This of course is a subject of a future work. It should be also said, that the LKDM model requires only next-nearest exchange interactions between $A-$ and $B-$site spins, one should consider a possible contribution of Dzyaloshinskii-Moriya interaction to the ground state of the ordered Co_5TeO_8 as the $P4_332$ space group is lacking a centre of inversion.

Dielectric properties were studied for three compounds: both disordered and ordered Co_5TeO_8 and $Co_{3.99}Zn_{1.01}TeO_8$. All three compound exhibit features corresponding to magnetoelectric coupling, however each of them in a different manner. Without application of a magnetic field, the disordered polymorph shows a significant drop in capacitance at T_N. So, changes on the charge subsystem are clearly related to the magnetic ordering. At a high magnetic field this change in the capacitance is wiped out; however, another sharp feature is observed at $T \approx 60$ K. This may be due to field-induced magnetic phase transition. Unfortunately the magnetic spacegroup $I4_1/am'd'$ is non-polar, so the compound is not multiferroic. The ordered polymorph, in turn, displays two features coinciding with the magnetic phase transitions at T_{C1} and T_{C2}. Both of them are tuneable with the magnetic field. Moreover, contrary to the disordered polymorph, the superspace magnetic group $P4_3(00\gamma)0$ allows an electric polarization $\mathbf{P}$ along the c-axis, yet one should not expect a high value of $\mathbf{P}$ because the capacitance variation if lower than 0.1%. An attempt to quantify electric polarization on the ordered Co5TeO8 was made. The measurements were always perturbed by too high leakage currents and we didn't succeed in measuring any polarisation current, which must be very weak or even null. The most remarkable results are achieved for the highly-diluted $Co_{3.99}Zn_{1.01}TeO_8$ compound, which, as it was discussed above, does not possess long-range magnetic order. Nevertheless, zero-field

dielectric spectroscopy provides two distinct features at $T_1 = 40$ K and $T_2 = 13$ K. The first temperature corresponds to the clear emergence of the magnetic diffuse scattering halo on NPD patterns, so it may be concluded that the conical short-range spin ordering, found with XYZ polarization analysis somehow triggers the changes in the electronic subsystem. Although the short-range ordering in $Co_{3.99}Zn_{1.01}TeO_8$ exists at least up to 70 K, the critical concentration of short-range ordered domains, enough to provoke the electronic subsystem response, is reached only at 40 K. The second temperature may indicate some kind of short-range ordering transition, analogous to the transitions occurring at T_{C2} for samples with $x \leq 0.76$. So one can expect a spin reorientation within short-range ordered domains. For both ordered Co_5TeO_8 and $Co_{3.99}Zn_{1.01}TeO_8$ electric polarization measurements have not revealed any significant effect, however to prove or disprove a possible multiferroic behaviour measurements should be carried out on single crystals.

As it was already mentioned, there are only few spinel oxides of formula M_5AO_8 that present a $P4_332$ cubic structure with a cationic ordering A/M on the B-sites. Ordered Fe_5LiO_8 exist but without any ferrimagnetic spiral spin ordering. We can thus wonder if the ordered Co_5TeO_8 is a unique case or if other ordered spinel may present the same long-range and short-range ferrimagnetic spiral spin structures. We also know that among $3d$ magnetic cations, Co^{2+} is known for its peculiar behavior. Indeed, the magnetic moment of Co^{2+} reveals a high orbital contribution. Thus we can wonder if the other cobalt-based oxide spinels with an ordered $P4_332$ structure could also favor the emergence of ferrimagnetic spiral spin structures. For these reasons, a few syntheses of ordered spinels for different chemical system were tried, with both methods: solid-state synthesis and hydrothermal synthesis. First, there was an attempt to substitute Te^{6+} by another chalcogen cation Se^{6+} or other cations with a valence of VI (Mo^{6+}, W^{6+}), that has never succeeded to obtain a spinel phase. There was also an attempt to use non-magnetic cation of valence V, IV and III: Sb^{5+}, Sn_4^+ or Ga^{3+}. These cations have the abilities in the first hand, to form spinel phases with cobalt and on the other hand to preferentially occupy octahedral environments in oxides. In all cases, despite the long ramps of cooling, only $Fd\bar{3}m$ disordered spinel phases were obtained. All these phases present ferrimagnetic behavior at low temperature. It should be also said that numerous attempts were made to obtain single crystals of Co_5TeO_8 phases. The synthesis was done by vapour transport technique in different conditions such as temperature regime in both "hot" and "cold" zones and with different transport agents ($PtCl_2$, I_2). However, single crystals were not available: Te is volatile at high temperatures which prevents Co_5TeO_8 from nucleation.

Conclusions

Within the current research a comprehensive study of Co_5TeO_8 spinel was carried out. First of all, it has to be said that there is no other spinel system so widely studied with neutron scattering techniques. The long-range and the short range magnetic ordering is exhaustively described with the help of neutrons in addition to the classical bulk characterization techniques. Such a complex approach made it possible to unambiguously relate the structure of studied compounds to exhibited properties and unveil microscopic mechanisms of magnetism in Co_5TeO_8.

It was found that the compound could be obtained in two structural forms: a centrosymmetric disordered $Fd\bar{3}m$ and non-centrosymmetric ordered $P4_332$ structures. The main difference between two polymorphs is a octahedral $B-$site subordering. In the disordered polymorph, Co^{2+} and Te^{6+} are randomly distributed within the octahedral positions whereas in the ordered one there is a particular positioning of $B-$site cations in the crystal structure. Such an arrangement is possible due to the charge and the size difference between Co^{2+} and Te^{6+} cations.

The combination of bulk magnetic measurements and the neutron powder diffraction has revealed that the disordered polymorph orders in ferrimagnetic structure at $T_N = 40$ K described with the $I4_1/am'd'$ space group. The ordered Co_5TeO_8 polymorph undergoes an incommensurate ferrimagnetic spiral spin ordering below $T_{C1} = 45$ K followed by a second magnetic phase transition at $T_{C2} = 27$ K. This last transition is associated with the emergence of an additional ferrimagnetic component and an abrupt change in the magnitude of the magnetic propagation vector $\mathbf{k} = (00\gamma)$ from $\gamma = 0.086$ at T = 30 K to $\gamma \approx 0.14$ on the range between 27 K and 1.7 K. The magnetic symmetry of the ordered polymorph is described with $P4_3(00\gamma)0$ magnetic superspace group. The incommensurate spin modulation in the ordered polymorph is stabilized via the combination of magnetic frustration and Dzyaloshinskii-Moriya interaction, which takes place due to the lack of inversion centre in the crystal structure.

The influence of the magnetic dilution was studied for the $Co_{5-x}Zn_xTeO_8$ family. It was found that with the introduction of Zn^{2+} the crystal structure adopts only the $P4_332$ space group. For the studied range of $0 \leq x \leq 1.01$, Zn^{2+} occupies tetrahedral $A-$sites exclusively, so preserving the Co^{2+}-Te^{6+} ordering in the octahedral sites. For the entire studied range a strong magnetic diffuse scattering was observed on neutron diffraction patterns. A small magnetic dilution, $x = 0.04$, does not affect the magnetic structure significantly, while for $0.21 \leq x \leq 0.76$ the second magnetic phase transition is suppressed. In the range of Zn^{2+} content of $0.04 \leq x \leq 0.76$, the long-range spin ordering is described with the same magnetic symmetry as the parent compound. Between $x = 0.76$ and $x = 1.01$ a percolation threshold is reached and for $Co_{3.99}Zn_{1.01}TeO_8$ only a diffuse magnetic scattering is observed.

With the small-angle neutron scattering technique under applied magnetic field, it was observed that in the field region 0.06 T $\leq x \leq$ 0.09 T the ordered Co_5TeO_8 enters into a

multi-domain state.

NPD measurements pointed out the presence of magnetic diffuse scattering for all studied samples, so it was decided to use the XYZ neutron polarization analysis for characterization of the short-range ordering in the ordered Co_5TeO_8 and $Co_{3.99}Zn_{1.01}TeO_8$ compounds. It was found that the short-range ordering in both samples has the same ferrimagnetic conical nature as the long-range magnetic ordering in the studied family. Surprisingly, the short-range ordering exists up to relatively high temperatures.

The dielectric spectroscopy demonstrated that both ordered and disordered Co_5TeO_8 polymorphs and $Co_{3.99}Zn_{1.01}TeO_8$ are magnetoelectric, however the electric polarisation is allowed only for the $P4_3(00\gamma)0$ magnetic structure. Surprisingly, the highly-diluted $Co_{3.99}Zn_{1.01}TeO_8$, which does not possess the long-range ordering, exhibits two features in the temperature variation of capacitance: the first on at $T_1 = 40$ K is related to the critical concentration of short-range conical domains, whereas the second one at $T_2 \approx 13$ K may be due to spin reorientation within short-range domains.

As for perspectives and future work we have to emphasize that all samples were available only in the powder form, thus it may be interesting to obtain single crystals of the ordered Co_5TeO_8 compound. That will allow to precise the description of the complex magnetic ordering as well as to examine the magnetic dynamics of the compound with the neutron triple-axis technique. The latter may shed light on the microscopic nature of magnetism in the studied system and build up a complete model describing exchange interactions beyond the Lyons, Kaplan, Dwight, Menyuk approach. The discussion on magnetic structure of Co_5TeO_8 was held in terms on LKDM theory, however, the u parameter and exchange constants J_{AA} and J_{BB} remain unknown. Using inelastic neutron scattering one could elaborate a precise model of magnetic interactions in the system. Besides that, availability of single crystals will also open a window of possibilities to extend the variety of neutron scattering experiments with application of magnetic field. It may be interesting to study the evolution of magnetism under applied electric field, for this purposes small-angle neutron scattering may be beneficial as one could follow the evolution of the (00δ) diffraction peak as a fucntion of $\mathbf{E}$. The nature of the magnetic transition at T_{C2} in the ordered Co_5TeO_8 remains unknown. Thus, various spectroscopic techniques may be useful to shed light on it. Also the dynamics of the $Co_{3.99}Zn_{1.01}TeO_8$ may be of a particular interest. Multiferroic behaviour of the $Co_{5-x}Zn_xTeO_8$ remains uncertain and again single crystals are needed for careful characterization of electric properties of the family. Seemingly, $B-$site ordered spinel compounds with the non-centrosymmetric $P4_332$ structure could host diverse unconventional magnetic behaviour. So search and study of novel spinel materials with a such structure should be also considered as a future activity.

Appendix A

Complementary materials for the chapter 3

A.1 Tables

Table A.1: Details of the XRPD and NPD data acquisition and Rietveld refinement for both Co5TeO8 polymorphs at room temperature

Compound	Disordered	Ordered	
Diffractometer	3T2	PANalytical X'Pert-Pro	D2b
Radiation, Å	Neutron λ =1.225	X-ray Co-$K\alpha$ λ = 1.78	Neutron λ = 1.59476
2θ range/step, °	10 - 122/0.05	10 - 150/0.016	2 - 160/0.05
Temperature, $C°$	20	20	
Space group	$Fd\bar{3}m$	$P4_332$	
a, Å	8.5541(1)	8.5531(1)	
V, Å^3	625.94(1)	625.43(1)	
Rietveld refinement:		Combined X-ray and Neutron data	
Peak shape function	Pseudo-Voigt	Pseudo-Voigt	
Background Chebychev Polynomial number	13	9	
Asymmetry	Finger, Cox & Jephcoat	Finger, Cox, Jephcoat	
Anisotropic reflection broadening condition	-	h + k = 2n + 1; k + l = 2n + 1	
Phases/mass concentration, %	Co_5TeO_8 / 82.21(0.81) Co_3TeO_6 / 10.33(0.71) Co_3O_4 / 7.45(0.24)	Co_5TeO_8 / 100	
Agreement factors			
R_p	2.42	2.93	2.71
R_{wp}	2.99	3.10	3.37
R_{exp}	2.29	2.98	4.57
χ^2	1.71	10.0	11.0

Table A.2: Selected interatomic distances for both Co_5TeO_8 polymorphs.

Disordered Co_5TeO_8			Ordered Co_5TeO_8		
Atom 1	Atom 2	Distance (Å)	Atom 1	Atom 2	Distance (Å)
Co_1/Te_1	O_1	2.0577(5) (×6)	Co_1	O_1	1.9270(36)
	Co_1	3.0254(1)		O_2	2.0190(32) (×3)
Co_2	O_1	2.0000(4) (×4)	Co_2	O_1	2.0030(31) (×2)
				O_2	2.1445(17)
				O_2	2.1450(17)
				O_2	2.1735(31) (×2)
				Co_2	2.9532(18)
				Co_2	2.9532(24) (×2)
			Te	O_1	1.9421(26) (×3)
				O_2	1.9425(15) (×3)

Table A.3: Individual bond valence sums for ordered Co_5TeO_8.

Atom	BVS(v.u.)	Coordination number	Polyhedra distortion ($x10^{-4}$)
Co_1	1.769(8)	4	3.98
Co_2	1.996(6)	6	12.552
Te	5.603(12)	6	0.002
O_1	1.824(8)		
O_2	1.913(6)		

Bond valence parameters: Te−O: R_0 = 1.917 Å, B = 0.37 Å,

Co−O: R_0 = 1.692 Å, B = 0.37 Å.

Bond Valence = $exp((R_0 - R)/B)$

Table A.4: Atomic positions and U_{iso} for $Co_{5-x}Zn_xTeO_8$ x = 0.04

Space group $P4_332$; $a = 8.5543(2)$Å						
Atom	Wykoff pos.	Occ.	x	y	z	U_{iso}(Å)
Co_1	8c	0.98(8)	0.4995(6)	0.5005(6)	0.0005(6)	0.0071(8)
Zn_1	8c	0.20(8)	0.4995(6)	0.5005(6)	0.0005(6)	0.0071(8)
Co_2	12d	1	0.6120(4)	0.3620(4)	0.37500	0.0061(8)
Te_1	4b	1	0.87500	0.37500	0.12500	0.0035(8)
O_1	8c	1	0.6298(2)	0.1298(2)	0.3702(2)	0.0076(6)
O_2	24e	1	0.64852(15)	0.36623(19)	0.12648(15)	0.0060(3)
Reliability factors						
NPD: $R_p = 2.86$, $R_wp = 3.82$, $R_exp = 1.87$ $\chi^2 = 4.18$						

Table A.5: Atomic positions and U_{iso} for $Co_{5-x}Zn_xTeO_8$ x = 0.21 at room temperature

Space group $P4_332$; $a = 8.5533(1)$Å						
Atom	Wykoff pos.	Occ.	x	y	z	U_{iso}(Å)
Co_1	8c	0.894(7)	0.5003(3)	0.4997(3)	-0.0003(3)	0.0047(5)
Zn_1	8c	0.106(7)	0.5003(3)	0.4997(3)	-0.0003(3)	0.0047(5)
Co_2	12d	1	0.6120(4)	0.3620(4)	0.37500	0.0061(8)
Te_1	4b	1	0.87500	0.37500	0.12500	0.0034(6)
O_1	8c	1	0.62897(19)	0.12896(19)	0.37103(19)	0.0035(5)
O_2	24e	1	0.64906(13)	0.36594(17)	0.12692(15)	0.0034(3)
Reliability factors						
NPD: $R_p = 2.77$, $R_{wp} = 3.73$, $R_{exp} = 1.87$ $\chi^2 = 3.97$						
XRPD: $R_p = 2.27$, $R_{wp} = 3.45$, $R_{exp} = 2.29$ $\chi^2 = 2.27$						
Global user-weighted $\chi^2 = 3.48$						

Table A.6: Atomic positions and U_{iso} for $Co_{5-x}Zn_xTeO_8$ x = 0.38 at room temperature

Space group $P4_332$; $a = 8.5527(2)$Å						
Atom	Wykoff pos.	Occ.	x	y	z	U_{iso}(Å)
Co_1	8c	0.813(9)	0.4993(6)	0.5007(6)	0.0007(6)	0.0053(7)
Zn_1	8c	0.187(9)	0.4993(6)	0.5007(6)	0.0007(6)	0.0053(7)
Co_2	12d	1	0.6124(4)	0.3624(4)	0.37500	0.0035(8)
Te_1	4b	1	0.87500	0.37500	0.12500	0.0005(3)
O_1	8c	1	0.6297(3)	0.1296(3)	0.3703(3)	0.0068(6)
O_2	24e	1	0.64830(18)	0.3663(2)	0.12637(16)	0.0050(3)
Reliability factors						
NPD: $R_p = 2.90$, $R_{wp} = 3.91$, $R_{exp} = 1.89$ $\chi^2 = 4.24$						
XRPD: $R_p = 2.14$, $R_{wp} = 2.85$, $R_{exp} = 2.31$ $\chi^2 = 1.53$						
Global user-weighted $\chi^2 = 3.45$						

Table A.7: Atomic positions and U_{iso} for $Co_{5-x}Zn_xTeO_8$ x = 0.58 at room temperature

Space group $P4_332$; $a = 8.5524(2)$Å						
Atom	Wykoff pos.	Occ.	x	y	z	U_{iso}(Å)
Co_1	8c	0.876(7)	0.5002(3)	0.4998(3)	-0.0002(3)	0.0042(4)
Zn_1	8c	0.124(7)	0.5002(3)	0.4998(3)	-0.0002(3)	0.0042(4)
Co_2	12d	1	0.6125(2)	0.3625(2)	0.37500	0.0030(5)
Te_1	4b	1	0.87500	0.37500	0.12500	0.0005(3)
O_1	8c	1	0.62926(17)	0.12925(17)	0.37074(17)	0.0037(4)
O_2	24e	1	0.64877(11)	0.36602(16)	0.12701(14)	0.0037(2)
Reliability factors						
NPD: $R_p = 3.26$, $R_{wp} = 4.40$, $R_{exp} = 1.91$ $\chi^2 = 5.34$						

Table A.8: Atomic positions and U_{iso} for $Co_{5-x}Zn_xTeO_8$ x = 0.89 at room temperature

Space group $P4_332$; $a = 8.5512(2)$Å						
Atom	Wykoff pos.	Occ.	x	y	z	U_{iso}(Å)
Co_1	8c	0.565(8)	0.5011(3)	0.4989(3)	-0.0011(3)	0.0059(4)
Zn_1	8c	0.435(8)	0.5011(3)	0.4989(3)	-0.0011(3)	0.0059(4)
Co_2	12d	1	0.6121(2)	0.3621(2)	0.37500	0.0034(5)
Te_1	4b	1	0.87500	0.37500	0.12500	0.0023(6)
O_1	8c	1	0.6292(2)	0.1292(2)	0.3708(2)	0.0080(6)
O_2	24e	1	0.64804(15)	0.3667(2)	0.12654(16)	0.0078(3)
Reliability factors						
NPD: $R_p = 3.31$, $R_{wp} = 4.32$, $R_{exp} = 1.90$ $\chi^2 = 5.19$						
XRPD: $R_p = 2.79$, $R_{wp} = 4.03$, $R_{exp} = 2.28$ $\chi^2 = 3.12$						
Global user-weighted $\chi^2 = 4.58$						

Table A.9: Atomic positions and U_{iso} for $Co_{5-x}Zn_xTeO_8$ x = 1.01 at room temperature

Space group $P4_332$; $a = 8.5514(2)$Å						
Atom	Wykoff pos.	Occ.	x	y	z	U_{iso}(Å)
Co_1	8c	0.493(8)	0.5004(2)	0.4996(2)	-0.0004(2)	0.0042(4)
Zn_1	8c	0.507(8)	0.5004(2)	0.4996(2)	-0.0004(2)	0.0042(4)
Co_2	12d	1	0.6124(2)	0.3624(2)	0.37500	0.0030(5)
Te_1	4b	1	0.87500	0.37500	0.12500	0.0014(4)
O_1	8c	1	0.62910(19)	0.12909(19)	0.37090(19)	0.0032(5)
O_2	24e	1	0.64870(11)	0.36618(18)	0.12689(15)	0.0047(3)
Reliability factors						
NPD: $R_p = 3.13$, $R_{wp} = 4.20$, $R_{exp} = 1.95$ $\chi^2 = 4.65$						
XRPD: $R_p = 2.58$, $R_{wp} = 3.57$, $R_{exp} = 2.27$ $\chi^2 = 2.46$						
Global user-weighted $\chi^2 = 4.02$						

Table A.10: Parameters of magnetic structure of the disordered Co_5TeO_8 polymorph at T = 1.7 K

G4-1, $\lambda = 2.42$Å, 2θ range/step: $0^o - 82^o/0.1^o$	
Magnetic space group $I4_1/am'd'$	
Atom	$M_x(\mu_B)$
Co1	-1.94(6)
Co2	2.39(7)
Reliability factors: $R_p = 1.99$; $R_{wp} = 2.66$; $R_{exp} = 1.32$; $\chi^2 = 4.08$	

Table A.11: Parameters of magnetic structure of the ordered Co_5TeO_8 polymorph at 30 K and 1.7 K

G4-1, $\lambda = 2.42$Å, 2θ range/step: $0^o - 82^o/0.1^o$								
Atom	$M(\mu_B)$	$\Theta(^o)$	$M_{cos}(\mu_B)$	$\phi_{cos}(^o)$	$\Theta_{cos}(^o)$	$M_{sin}(\mu_B)$	$\phi_{sin}(^o)$	$\Theta_{sin}(^o)$
T = 30 K								
Co_{1-1}	1.2481	180	-2.32(7)	0	90	-2.32(7)	90	90
Co_{1-2}	1.2481	180	-2.32(7)	0	90	-2.32(7)	90	90
Co_{2-1}	1.5601	0	2.57(7)	35.52(4.07)	90	2.57(7)	125.52(4.07)	90
Co_{2-2}	1.5601	0	2.57(7)	35.52(4.07)	90	2.57(7)	125.52(4.07)	90
Co_{2-3}	1.5601	0	2.57(7)	35.52(4.07)	90	2.57(7)	125.52(4.07)	90
Resulting magnetic moments: $\mu_{Co1} = 1.71(9)\mu_B$, $\mu_{Co2} = 2.02(9)\mu_B$								
Reliability factors: $R_p = 3.54$; $R_{wp} = 5.03$; $R_{exp} = 1.52$; $\chi^2 = 11.0$								
T = 1.7 K								
Co_{1-1}	2.5894	180	-1.37(12)	0	90	-1.37(12)	90	90
Co_{1-2}	2.5894	180	-1.37(12)	0	90	-1.37(12)	90	90
Co_{2-1}	3.2764	0	1.46(9)	67.34(5.76)	90	1.46(9)	157.34(5.76)	90
Co_{2-2}	3.2764	0	1.46(9)	67.34(5.76)	90	1.46(9)	157.34(5.76)	90
Co_{2-3}	3.2764	0	1.46(9)	67.34(5.76)	90	1.46(9)	157.43(5.76)	90
Resulting magnetic moments: $\mu_{Co1} = 2.68(7)\mu_B$, $\mu_{Co2} = 3.36(7)\mu_B$								
Reliability factors: $R_p = 3.39$; $R_{wp} = 4.69$; $R_{exp} = 1.52$; $\chi^2 = 9.48$								

Table A.12: Parameters of magnetic structure of the ordered $Co_{4.96}Zn_{0.04}TeO_8$ at 1.7 K

G4-1, $\lambda = 2.42$Å, 2θ range/step: $0^o - 82^o/0.1^o$								
Atom	$M(\mu_B)$	$\Theta(^o)$	$M_{cos}(\mu_B)$	$\phi_{cos}(^o)$	$\Theta_{cos}(^o)$	$M_{sin}(\mu_B)$	$\phi_{sin}(^o)$	$\Theta_{sin}(^o)$
Co_{1-1}	1.9316	180	-0.85(12)	0	90	-0.85(12)	90	90
Co_{1-2}	1.9316	180	-0.85(12)	0	90	-0.85(12)	90	90
Co_{2-1}	2.3134	0	0.78(11)	48.15(6.78)	90	0.78(11)	138(6.78)	90
Co_{2-2}	2.3134	0	0.78(11)	48.15(6.78)	90	0.78(11)	138(6.78)	90
Co_{2-3}	2.3134	0	0.78(11)	48.15(6.78)	90	0.78(11)	138(6.78)	90
Resulting magnetic moments: $\mu_{Co1} = 1.98(7)\mu_B$, $\mu_{Co2} = 2.34(8)\mu_B$								
Reliability factors: $R_p = 3.70$; $R_{wp} = 5.05$; $R_{exp} = 1.58$; $\chi^2 = 10.3$								

Table A.13: Parameters of magnetic structure of the ordered $Co_{4.79}Zn_{0.21}TeO_8$ at 1.7 K

D1b, $\lambda = 2.42$Å, 2θ range/step: $0^o - 128^o/0.1^o$								
Atom	$M(\mu_B)$	$\Theta(^o)$	$M_{cos}(\mu_B)$	$\phi_{cos}(^o)$	$\Theta_{cos}(^o)$	$M_{sin}(\mu_B)$	$\phi_{sin}(^o)$	$\Theta_{sin}(^o)$
Co_{1-1}	1.4925	180	-1.95(06)	0	90	-1.95(06)	90	90
Co_{1-2}	1.4925	180	-1.95(06)	0	90	-1.95(06)	90	90
Co_{2-1}	1.4413	0	2.58(0.04)	23.87(4.46)	90	2.58(0.04)	133.87(4.46)	90
Co_{2-2}	1.4413	0	2.58(0.04)	23.87(4.46)	90	2.58(0.04)	133.87(4.46)	90
Co_{2-3}	1.4413	0	2.58(0.04)	23.87(4.46)	90	2.58(0.04)	133.87(4.46)	90
Resulting magnetic moments: $\mu_{Co1} = 1.78(7)\mu_B$, $\mu_{Co2} = 1.94(7)\mu_B$								
Reliability factors: $R_p = 3.72$; $R_{wp} = 5.12$; $R_{exp} = 1.58$; $\chi^2 = 11.1$								

Table A.14: Parameters of magnetic structure of the ordered $Co_{4.62}Zn_{0.38}TeO_8$ at 1.7 K

D1b, $\lambda = 2.42$Å, 2θ range/step: $0^o - 128^o/0.1^o$								
Atom	$M(\mu_B)$	$\Theta(^o)$	$M_{cos}(\mu_B)$	$\phi_{cos}(^o)$	$\Theta_{cos}(^o)$	$M_{sin}(\mu_B)$	$\phi_{sin}(^o)$	$\Theta_{sin}(^o)$
Co_{1-1}	1.5030	180	-1.53(09)	0	90	-1.53(09)	90	90
Co_{1-2}	1.5030	180	-1.53(09)	0	90	-1.53(09)	90	90
Co_{2-1}	0.9422	0	2.66(0.04)	27.90(5.51)	90	2.66(0.04)	117.90(5.51)	90
Co_{2-2}	0.9422	0	2.66(0.04)	27.90(5.51)	90	2.66(0.04)	117.90(5.51)	90
Co_{2-3}	0.9422	0	2.66(0.04)	27.90(5.51)	90	2.66(0.04)	117.90(5.51)	90
Resulting magnetic moments: $\mu_{Co1} = 1.69(9)\mu_B$, $\mu_{Co2} = 1.63(8)\mu_B$								
Reliability factors: $R_p = 4.88$; $R_{wp} = 6.09$; $R_{exp} = 2.69$; $\chi^2 = 5.14$								

Table A.15: Parameters of magnetic structure of the ordered $Co_{4.42}Zn_{0.58}TeO_8$ at 1.7 K

D1b, $\lambda = 2.42$Å, 2θ range/step: $0^o - 128^o/0.1^o$								
Atom	$M(\mu_B)$	$\Theta(^o)$	$M_{cos}(\mu_B)$	$\phi_{cos}(^o)$	$\Theta_{cos}(^o)$	$M_{sin}(\mu_B)$	$\phi_{sin}(^o)$	$\Theta_{sin}(^o)$
Co_{1-1}	1.3034	180	1.25(15)	0	90	1.25(15)	90	90
Co_{1-2}	1.3034	180	1.25(15)	0	90	1.25(15)	90	90
Co_{2-1}	-0.9194	0	-2.70(0.08)	46.00(6.97)	90	-2.70(0.08)	136.00(6.97)	90
Co_{2-2}	-0.9194	0	-2.70(0.08)	46.00(6.97)	90	-2.70(0.08)	136.00(6.97)	90
Co_{2-3}	-0.9194	0	-2.70(0.08)	46.00(6.97)	90	-2.70(0.08)	136.00(6.97)	90
Resulting magnetic moments: $\mu_{Co1} = 1.45(11)\mu_B$, $\mu_{Co2} = 1.63(17)\mu_B$								
Reliability factors: $R_p = 6.36$; $R_{wp} = 8.69$; $R_{exp} = 2.72$; $\chi^2 = 10.2$								

Table A.16: Parameters of magnetic structure of the ordered $Co_{4.24}Zn_{0.76}TeO_8$ at 1.7 K

D1b, $\lambda = 2.42$Å, 2θ range/step: $0^o - 128^o/0.1^o$								
Atom	$M(\mu_B)$	$\Theta(^o)$	$M_{cos}(\mu_B)$	$\phi_{cos}(^o)$	$\Theta_{cos}(^o)$	$M_{sin}(\mu_B)$	$\phi_{sin}(^o)$	$\Theta_{sin}(^o)$
Co_{1-1}	1.4444	180	1.26(15)	0	90	1.26(15)	90	90
Co_{1-2}	1.4444	180	1.26(15)	0	90	1.26(15)	90	90
Co_{2-1}	-0.4614	0	-2.77(0.04)	37.60(9.01)	90	-2.77(0.04)	127.60(9.01)	90
Co_{2-2}	-0.4614	0	-2.77(0.04)	37.60(9.01)	90	-2.77(0.04)	127.60(9.01)	90
Co_{2-3}	-0.4614	0	-2.77(0.04)	37.60(9.01)	90	-2.77(0.04)	127.60(9.01)	90
Resulting magnetic moments: $\mu_{Co1} = 1.58(14)\mu_B$, $\mu_{Co2} = 1.46(13)\mu_B$								
Reliability factors: $R_p = 5.41$; $R_{wp} = 6.86$; $R_{exp} = 2.91$; $\chi^2 = 5.55$								

Table A.17: Agreement factors of the RMC fit of the ordered Co_5TeO_8 polymorph diffuse magnetic scattering at 50, 60 and 80 K

T, K	Run	R-factor	T, K	Run	R-factor	T, K	Run	R-factor
50	1	3.21	60	1	3.31	80	1	3.38
	2	3.20		2	3.31		2	3.38
	2	3.21		3	3.31		3	3.39
	4	3.21		4	3.31		4	3.38
	5	3.21		5	3.31		5	3.38

Table A.18: Agreement factors of the RMC fit of the ordered Co_5TeO_8 polymorph diffuse magnetic scattering at 90, 110 and 140 K

T, K	Run	R-factor	T, K	Run	R-factor	T, K	Run	R-factor
90	1	3.10	110	1	3.49	140	1	3.26
	2	3.11		2	3.48		2	3.26
	2	3.10		3	3.48		3	3.24
	4	3.10		4	3.49		4	3.25
	5	3.11		5	3.49		5	3.25

Table A.19: Agreement factors of the RMC fit of the ordered Co_5TeO_8 polymorph diffuse magnetic scattering at 170, 200, 230 and 260 K

T, K	Run	R-factor	T, K	Run	R-factor	T, K	Run	R-factor	T, K	Run	R-factor
170	1	3.13	200	1	3.10	230	1	3.10	260	1	3.95
	2	3.12		2	3.09		2	3.09		2	3.95
	2	3.12		3	3.09		3	3.10		3	3.95
	4	3.12		4	3.09		4	3.10		4	3.95
	5	3.12		5	3.09		5	3.09		5	3.95

Table A.20: Agreement factors of the RMC fit of the $Co_{3.99}Zn_{1.01}TeO_8$ diffuse magnetic scattering at 1.5, 10 and 30 K

T, K	Run	R-factor	T, K	Run	R-factor	T, K	Run	R-factor
1.5	1	3.12	10	1	3.67	30	1	4.46
	2	3.12		2	3.67		2	4.46
	2	3.12		3	3.67		3	4.46
	4	3.12		4	3.67		4	4.46
	5	3.12		5	3.67		5	4.46

Table A.21: Agreement factors of the RMC fit of the $Co_{3.99}Zn_{1.01}TeO_8$ diffuse magnetic scattering at 50 and 70 K

T, K	Run	R-factor	T, K	Run	R-factor
1.5	1	5.29	10	1	5.27
	2	5.29		2	5.27
	2	5.29		3	5.26
	4	5.29		4	5.26
	5	5.29		5	5.26

A.2 .mcif files

Below .mcif files of disordered Co_5TeO_8 polymorph at 1.7K, ordered Co_5TeO_8 polymorph at 1.7K and ordered Co_5TeO_8 polymorph at 30K are given. All .mcif files were generated automatically with FullProf.

Disordered Co_5TeO_8 T = 1.7 K

```
##############################################################################
###     FullProf-generated mCIF output file   (version: May 2019)        ###
##############################################################################

# Please notify any error or suggestion to:
#          Juan Rodriguez-Carvajal (jrc@ill.eu)
# Improvements will be progressively added as needed.

#      Date: 07/09/2020  Time: 12:27:57.559

#==============================================================================
 data_global
#==============================================================================

data_
_audit_creation_date  07/09/2020
_audit_creation_method  "FullProf Suite"

_citation_journal_abbrev ?
_citation_journal_volume ?
_citation_page_first     ?
_citation_page_last      ?
_citation_article_id     ?
_citation_year           ?
loop_
_citation_author_name
?

_atomic_positions_source_database_code_ICSD  ?
_atomic_positions_source_other    .

_Neel_temperature  ?
_magn_diffrn_temperature  ?
_exptl_crystal_magnetic_properties_details
;
;
_active_magnetic_irreps_details
;
;

_magnetic_space_group_standard_setting  'no'
_parent_space_group.name_H-M  ""
_parent_space_group.IT_number  227

_space_group_magn.number_BNS 141.557
_space_group_magn.name_BNS   I4_1/am'd'
_parent_space_group.transform_Pp_abc  ''
```

```
_parent_space_group.child_transform_Pp_abc  ''
_magnetic_space_group.transform_BNS_Pp_abc  ''
_space_group_magn.number_OG  ?
_space_group_magn.name_OG    ?


_cell_length_a     8.5857(4)
_cell_length_b     8.5857(4)
_cell_length_c     8.5857(4)
_cell_angle_alpha  90.0000
_cell_angle_beta   90.0000
_cell_angle_gamma  90.0000


loop_
   _space_group_symop_magn_operation.id
   _space_group_symop_magn_operation.xyz
  1  x,y,z,+1
  2  x,z,y,-1
  3  -x+1/4,z,-y+1/4,+1
  4  -x+1/4,y,-z+1/4,-1
  5  x+1/4,z+1/4,-y,+1
  6  -x+1/4,-y+1/4,z,-1
  7  -x,z+1/4,y+1/4,-1
  8  -x,y+1/4,z+1/4,+1
  9  -x,-y,-z,+1
 10  -x,-z,-y,-1
 11  x+3/4,-z,y+3/4,+1
 12  x+3/4,-y,z+3/4,-1
 13  -x+3/4,-z+3/4,y,+1
 14  x+3/4,y+3/4,-z,-1
 15  x,-z+3/4,-y+3/4,-1
 16  x,-y+3/4,-z+3/4,+1

loop_
   _space_group_symop_magn_centering.id
   _space_group_symop_magn_centering.xyz
  1  x,y,z,+1
  2  x+1/2,y+1/2,z,+1
  3  x+1/2,y,z+1/2,+1
  4  x,y+1/2,z+1/2,+1

loop_
   _atom_site_label
   _atom_site_type_symbol
   _atom_site_fract_x
   _atom_site_fract_y
   _atom_site_fract_z
```

```
   _atom_site_U_iso_or_equiv
   _atom_site_occupancy
   _atom_site_adp_type
 Co1 Co  0.50000  0.50000  0.50000  0.00555  1.00000 Uiso
 Co2 Co  0.12500  0.12500  0.12500  0.00630  1.00000 Uiso


loop_
   _atom_site_moment.label
   _atom_site_moment.crystalaxis_x
   _atom_site_moment.crystalaxis_y
   _atom_site_moment.crystalaxis_z
 Co1 -1.94(6)  0.00000  0.00000
 Co2  2.39(7)  0.00000  0.00000
```

Ordered Co_5TeO_8 T = 1.7 K

```
##############################################################################
###     FullProf-generated mCIF output file   (version: September 2019)   ###
##############################################################################

# Please notify any error or suggestion to:
#          Juan Rodriguez-Carvajal (jrc@ill.eu)
# Improvements will be progressively added as needed.

#     Date: 28/10/2020  Time: 19:52:39.366

#==============================================================================
 data_global
#==============================================================================

data_
_audit_creation_date  28/10/2020
_audit_creation_method  "FullProf Suite"
_chemical_name_systematic
;
;
_chemical_formula_sum  '?'

_citation_journal_abbrev ?
_citation_journal_volume ?
_citation_page_first     ?
_citation_page_last      ?
_citation_article_id     ?
_citation_year           ?
_citation_DOI            ?
loop_
_citation_author_name
?

#     Name                        Explanation                              Standard?
#    ------                     -----------                              ---------
 '_pd_proc_ls_prof_chi2'     'Chi-square for all considered points in LSQ'                 no
 '_pd_proc_R-Bragg'          'Rietveld R-factor based on integrated intensities'           no
 '_pd_proc_Magn_R-factor'    'As the previous item but only for magnetic reflections'      no


_atomic_positions_source_database_code_ICSD  .
_atomic_positions_source_other               .

_Neel_temperature  ?
_magn_diffrn_temperature  ?
_exptl_crystal_magnetic_properties_details
;
;
_active_magnetic_irreps_details
;
```

;

Reliability factors for the current refinement
_pd_proc_ls_prof_chi2 9.4814
_pd_proc_Magn_R-factor 4.2991

_space_group_magn.ssg_number "78.1.19.1.m19.1"
_space_group_magn.ssg_name "P4_3(0,0,g)0"
_space_group_magn.point_group_name "4"
_parent_space_group.IT_number 0

_cell_length_a 8.54979(7)
_cell_length_b 8.54979(7)
_cell_length_c 8.54979(7)
_cell_angle_alpha 90.0000
_cell_angle_beta 90.0000
_cell_angle_gamma 90.0000

_cell_modulation_dimension 1

loop_
_cell_wave_vector_seq_id
_cell_wave_vector_x
_cell_wave_vector_y
_cell_wave_vector_z
1 0.00000 0.00000 0.1345(12)

loop_
_space_group_symop_magn_ssg_operation.id
_space_group_symop_magn_ssg_operation.algebraic
1 x1,x2,x3,x4,1
2 -x1,-x2+1/2,x3+1/2,x4+1/2,1
3 x2+3/4,-x1+1/4,x3+1/4,x4+3/4,1
4 -x2+1/4,x1+1/4,x3+3/4,x4+1/4,1

loop_
_atom_site_label
_atom_site_type_symbol
_atom_site_fract_x
_atom_site_fract_y
_atom_site_fract_z
_atom_site_U_iso_or_equiv
_atom_site_occupancy
_atom_site_adp_type
Co1_1 Co 0.00062 -0.00062 0.00062 0.00000 1.00000 Uiso
Co1_2 Co 0.50062 0.00062 0.49938 0.00000 1.00000 Uiso

```
 Co2_1 Co  0.12500  0.13702  0.38702  0.00000  1.00000 Uiso
 Co2_2 Co  0.62500  0.86298  0.11298  0.00000  1.00000 Uiso
 Co2_3 Co  0.86298  0.61298  0.12500  0.00000  1.00000 Uiso


loop_
   _atom_site_moment.label
   _atom_site_moment.spherical_modulus
   _atom_site_moment.spherical_azimuthal
   _atom_site_moment.spherical_polar
 Co1_1  2.59(4)  0.00000  180.000
 Co1_2  2.59(4)  0.00000  180.000
 Co2_1  3.28(5)  0.00000  0.00000
 Co2_2  3.28(5)  0.00000  0.00000
 Co2_3  3.28(5)  0.00000  0.00000

loop_
   _atom_site_Fourier_wave_vector.seq_id
   _atom_site_Fourier_wave_vector.q1_coeff
  1   1

loop_
   _atom_site_moment_Fourier.atom_site_label
   _atom_site_moment_Fourier.axis
   _atom_site_moment_Fourier.wave_vector_seq_id
   _atom_site_moment_Fourier_param.cos
   _atom_site_moment_Fourier_param.sin
 Co1_1  mod  1 -1.37(12) -1.37(12)
 Co1_1  azi  1  0.00000  90.0000
 Co1_1  pol  1  90.0000  90.0000
 Co1_2  mod  1 -1.37(12) -1.37(12)
 Co1_2  azi  1  0.00000  90.0000
 Co1_2  pol  1  90.0000  90.0000
 Co2_1  mod  1  1.46(10)  1.46(10)
 Co2_1  azi  1  67(6)  157(6)
 Co2_1  pol  1  90.0000  90.0000
 Co2_2  mod  1  1.46(10)  1.46(10)
 Co2_2  azi  1  67(6)  157(6)
 Co2_2  pol  1  90.0000  90.0000
 Co2_3  mod  1  1.46(10)  1.46(10)
 Co2_3  azi  1  67(6)  157(6)
 Co2_3  pol  1  90.0000  90.0000


#  The refinement has been performed using spherical components for moments and amplitudes.
#  Here we give the components transformed to the crystallographic unitary frame (moments in
Bohr magnetons)
#  for compatibility with external programs. The standard deviations have been calculated  using the
#  propagation error formula without taking into account the correlations between parameters.
```

```
loop_
   _atom_site_moment.label
   _atom_site_moment.crystalaxis_x
   _atom_site_moment.crystalaxis_y
   _atom_site_moment.crystalaxis_z
 Co1_1  0.00000  0.00000 -2.59(4)
 Co1_2  0.00000  0.00000 -2.59(4)
 Co2_1  0.00000  0.00000  3.28(5)
 Co2_2  0.00000  0.00000  3.28(5)
 Co2_3  0.00000  0.00000  3.28(5)


loop_
   _atom_site_moment_Fourier.atom_site_label
   _atom_site_moment_Fourier.axis
   _atom_site_moment_Fourier.wave_vector_seq_id
   _atom_site_moment_Fourier_param.cos
   _atom_site_moment_Fourier_param.sin
 Co1_1  x   1 -1.37(12)  0.00000
 Co1_1  y   1  0.00000 -1.37(12)
 Co1_1  z   1  0.00000  0.00000
 Co1_2  x   1 -1.37(12)  0.00000
 Co1_2  y   1  0.00000 -1.37(12)
 Co1_2  z   1  0.00000  0.00000
 Co2_1  x   1  0.56(4) -1.35(9)
 Co2_1  y   1  1.35(9)  0.56(4)
 Co2_1  z   1  0.00000  0.00000
 Co2_2  x   1  0.56(4) -1.35(9)
 Co2_2  y   1  1.35(9)  0.56(4)
 Co2_2  z   1  0.00000  0.00000
 Co2_3  x   1  0.56(4) -1.35(9)
 Co2_3  y   1  1.35(9)  0.56(4)
 Co2_3  z   1  0.00000  0.00000
```

Ordered Co_5TeO_8 T = 30 K

```
##############################################################################
###     FullProf-generated mCIF output file   (version: September 2019)   ###
##############################################################################

# Please notify any error or suggestion to:
#          Juan Rodriguez-Carvajal (jrc@ill.eu)
# Improvements will be progressively added as needed.

#     Date: 14/07/2020  Time: 14:00:02.480

#==============================================================================
 data_global
#==============================================================================

data_
_audit_creation_date  14/07/2020
_audit_creation_method  "FullProf Suite"
_chemical_name_systematic
;
;
_chemical_formula_sum  '?'

_citation_journal_abbrev ?
_citation_journal_volume ?
_citation_page_first     ?
_citation_page_last      ?
_citation_article_id     ?
_citation_year           ?
_citation_DOI            ?
loop_
_citation_author_name
?

#     Name                        Explanation                              Standard?
#    ------                     -----------                             ---------
 '_pd_proc_ls_prof_chi2'     'Chi-square for all considered points in LSQ'                 no
 '_pd_proc_R-Bragg'          'Rietveld R-factor based on integrated intensities'           no
 '_pd_proc_Magn_R-factor'    'As the previous item but only for magnetic reflections'      no


_atomic_positions_source_database_code_ICSD  .
_atomic_positions_source_other               .

_Neel_temperature  ?
_magn_diffrn_temperature  ?
_exptl_crystal_magnetic_properties_details
;
;
_active_magnetic_irreps_details
;
```

;

Reliability factors for the current refinement
_pd_proc_ls_prof_chi2 11.0096
_pd_proc_Magn_R-factor 7.2785

_space_group_magn.ssg_number "78.1.19.1.m19.1"
_space_group_magn.ssg_name "P4_3(0,0,g)0"
_space_group_magn.point_group_name "4"
_parent_space_group.IT_number 0

_cell_length_a 8.54975(8)
_cell_length_b 8.54975(8)
_cell_length_c 8.54975(8)
_cell_angle_alpha 90.0000
_cell_angle_beta 90.0000
_cell_angle_gamma 90.0000

_cell_modulation_dimension 1

loop_
_cell_wave_vector_seq_id
_cell_wave_vector_x
_cell_wave_vector_y
_cell_wave_vector_z
1 0.00000 0.00000 0.0859(3)

loop_
_space_group_symop_magn_ssg_operation.id
_space_group_symop_magn_ssg_operation.algebraic
1 x1,x2,x3,x4,1
2 -x1,-x2+1/2,x3+1/2,x4+1/2,1
3 x2+3/4,-x1+1/4,x3+1/4,x4+3/4,1
4 -x2+1/4,x1+1/4,x3+3/4,x4+1/4,1

loop_
_atom_site_label
_atom_site_type_symbol
_atom_site_fract_x
_atom_site_fract_y
_atom_site_fract_z
_atom_site_U_iso_or_equiv
_atom_site_occupancy
_atom_site_adp_type
Co1_1 Co 0.00062 -0.00062 0.00062 0.00000 1.00000 Uiso
Co1_2 Co 0.50062 0.00062 0.49938 0.00000 1.00000 Uiso

```
 Co2_1 Co  0.12500  0.13702  0.38702  0.00000  1.00000 Uiso
 Co2_2 Co  0.62500  0.86298  0.11298  0.00000  1.00000 Uiso
 Co2_3 Co  0.86298  0.61298  0.12500  0.00000  1.00000 Uiso


loop_
   _atom_site_moment.label
   _atom_site_moment.spherical_modulus
   _atom_site_moment.spherical_azimuthal
   _atom_site_moment.spherical_polar
 Co1_1  1.25(8)  0.00000  180.000
 Co1_2  1.25(8)  0.00000  180.000
 Co2_1  1.56(8)  0.00000  0.00000
 Co2_2  1.56(8)  0.00000  0.00000
 Co2_3  1.56(8)  0.00000  0.00000

loop_
   _atom_site_Fourier_wave_vector.seq_id
   _atom_site_Fourier_wave_vector.q1_coeff
  1   1

loop_
   _atom_site_moment_Fourier.atom_site_label
   _atom_site_moment_Fourier.axis
   _atom_site_moment_Fourier.wave_vector_seq_id
   _atom_site_moment_Fourier_param.cos
   _atom_site_moment_Fourier_param.sin
 Co1_1  mod  1 -2.32(7) -2.32(7)
 Co1_1  azi  1  0.00000  90.0000
 Co1_1  pol  1  90.0000  90.0000
 Co1_2  mod  1 -2.32(7) -2.32(7)
 Co1_2  azi  1  0.00000  90.0000
 Co1_2  pol  1  90.0000  90.0000
 Co2_1  mod  1  2.57(7)  2.57(7)
 Co2_1  azi  1  36(4)  126(4)
 Co2_1  pol  1  90.0000  90.0000
 Co2_2  mod  1  2.57(7)  2.57(7)
 Co2_2  azi  1  36(4)  126(4)
 Co2_2  pol  1  90.0000  90.0000
 Co2_3  mod  1  2.57(7)  2.57(7)
 Co2_3  azi  1  36(4)  126(4)
 Co2_3  pol  1  90.0000  90.0000


#  The refinement has been performed using spherical components for moments and amplitudes.
#  Here we give the components transformed to the crystallographic unitary frame (moments in
Bohr magnetons)
#  for compatibility with external programs. The standard deviations have been calculated  using the
#  propagation error formula without taking into account the correlations between parameters.
```

```
loop_
   _atom_site_moment.label
   _atom_site_moment.crystalaxis_x
   _atom_site_moment.crystalaxis_y
   _atom_site_moment.crystalaxis_z
 Co1_1  0.00000  0.00000 -1.25(8)
 Co1_2  0.00000  0.00000 -1.25(8)
 Co2_1  0.00000  0.00000  1.56(8)
 Co2_2  0.00000  0.00000  1.56(8)
 Co2_3  0.00000  0.00000  1.56(8)


loop_
   _atom_site_moment_Fourier.atom_site_label
   _atom_site_moment_Fourier.axis
   _atom_site_moment_Fourier.wave_vector_seq_id
   _atom_site_moment_Fourier_param.cos
   _atom_site_moment_Fourier_param.sin
 Co1_1  x   1 -2.32(7)  0.00000
 Co1_1  y   1  0.00000 -2.32(7)
 Co1_1  z   1  0.00000  0.00000
 Co1_2  x   1 -2.32(7)  0.00000
 Co1_2  y   1  0.00000 -2.32(7)
 Co1_2  z   1  0.00000  0.00000
 Co2_1  x   1  2.09(5) -1.49(4)
 Co2_1  y   1  1.49(4)  2.09(5)
 Co2_1  z   1  0.00000  0.00000
 Co2_2  x   1  2.09(5) -1.49(4)
 Co2_2  y   1  1.49(4)  2.09(5)
 Co2_2  z   1  0.00000  0.00000
 Co2_3  x   1  2.09(5) -1.49(4)
 Co2_3  y   1  1.49(4)  2.09(5)
 Co2_3  z   1  0.00000  0.00000
```

Bibliography

[1] Georg Busch. Early history of the physics and chemistry of semiconductors-from doubts to fact in a hundred years. *European Journal of Physics*, 10(4):254, 1989. 1

[2] Michael Riordan and Lillian Hoddeson. The origins of the pn junction. *IEEE spectrum*, 34(6):46–51, 1997. 1

[3] Ian M Ross. The invention of the transistor. *Proceedings of the IEEE*, 86(1):7–28, 1998. 1

[4] Robert W Keyes. Physical limits of silicon transistors and circuits. *Reports on Progress in Physics*, 68(12):2701, 2005. 1

[5] Daniel Khomskii. Trend: Classifying multiferroics: Mechanisms and effects. *Physics*, 2:20, 2009. 1, 2, 8, 9, 143, 145

[6] James Clerk Maxwell. Viii. a dynamical theory of the electromagnetic field. *Philosophical transactions of the Royal Society of London*, (155):459–512, 1865. 1, 143

[7] Pierre Curie. Sur la symétrie dans les phénomenes physiques, symétrie d'un champ électrique et d'un champ magnétique. *Ann Fond Louis Broglie*, 19:137, 1994. 1, 143

[8] DN Astrov. Magnetoelectric effect in chromium oxide. *Sov. Phys. JETP*, 13(4):729–733, 1961. 1, 143

[9] Ie E Dzyaloshinskii. On the magneto-electrical effects in antiferromagnets. *Soviet Physics JETP*, 10:628–629, 1960. 1, 143

[10] Edgar Ascher, Harry Rieder, Hans Schmid, and H Stössel. Some properties of ferromagnetoelectric nickel-iodine boracite, $Ni_3B_7O_{13}I$. *Journal of Applied Physics*, 37(3):1404–1405, 1966. 1, 143

[11] Smolenskiĭ. Ferroelectromagnets. 1, 8

[12] Elbio Dagotto. Correlated electrons in high-temperature superconductors. *Reviews of Modern Physics*, 66(3):763, 1994. 1

[13] Yoshinori Tokura. *Colossal magnetoresistive oxides*. CRC Press, 2000. 1

[14] Raffaele Resta. Macroscopic polarization in crystalline dielectrics: the geometric phase approach. *Reviews of modern physics*, 66(3):899, 1994. 1

[15] RD King-Smith and David Vanderbilt. Theory of polarization of crystalline solids. *Physical Review B*, 47(3):1651, 1993. 1

[16] GA Smolenskii, VA Isupov, NN Krainik, and AL Agranovskaya. Concerning the coexistence of the ferroelectric and ferrimagnetic states. *Izvestiya Rossijskoj Akademii Nauk. Seriya Fizika Atmosfery i Okeana*, 25:1333, 1961. 1, 143

[17] Nicola A Hill. Why are there so few magnetic ferroelectrics? journal of physical chemistry, 104, 6694-6709, 2000. 1, 8, 143

[18] JBNJ Wang, JB Neaton, H Zheng, V Nagarajan, SB Ogale, B Liu, D Viehland, V Vaithyanathan, DG Schlom, UV Waghmare, et al. Epitaxial bifeo3 multiferroic thin film heterostructures. *science*, 299(5613):1719–1722, 2003. 2, 7, 8, 143

[19] T Kimura, T Goto, H Shintani, K Ishizaka, T-h Arima, and Y Tokura. Magnetic control of ferroelectric polarization. *nature*, 426(6962):55, 2003. 2, 13, 143

[20] Thomas Lottermoser, Thomas Lonkai, Uwe Amann, Dietmar Hohlwein, Jörg Ihringer, and Manfred Fiebig. Magnetic phase control by an electric field. *Nature*, 430(6999):541, 2004. 2

[21] N Hur, S Park, PA Sharma, JS Ahn, S Guha, and SW Cheong. Electric polarization reversal and memory in a multiferroic material induced by magnetic fields. *Nature*, 429(6990):392, 2004. 2, 22

[22] Yaojin Wang, Jiefang Li, and D Viehland. Magnetoelectrics for magnetic sensor applications: status, challenges and perspectives. *Materials Today*, 17(6):269–275, 2014. 2, 143

[23] Evgeny Y Tsymbal, Alexei Gruverman, Vincent Garcia, Manuel Bibes, and A Barthélémy. Ferroelectric and multiferroic tunnel junctions. *MRS bulletin*, 37(2):138–143, 2012. 2, 143

[24] JF Scott. Data storage: Multiferroic memories. *Nature materials*, 6(4):256, 2007. 2, 143

[25] Manfred Fiebig, Th Lottermoser, Dietmar Fröhlich, Andriy V Goltsev, and Roman V Pisarev. Observation of coupled magnetic and electric domains. *Nature*, 419(6909):818, 2002. 3

[26] T Zhao, A Scholl, F Zavaliche, K Lee, M Barry, A Doran, MP Cruz, YH Chu, C Ederer, NA Spaldin, et al. Electrical control of antiferromagnetic domains in multiferroic $BiFeO_3$ films at room temperature. *Nature materials*, 5(10):823, 2006. 3

[27] HC Walker, F Fabrizi, L Paolasini, F de Bergevin, J Herrero-Martin, AT Boothroyd, D Prabhakaran, and DF McMorrow. Femtoscale magnetically induced lattice distortions in multiferroic $TbMnO_3$. *Science*, 333(6047):1273–1276, 2011. 3

[28] Andrei Pimenov, AA Mukhin, V Yu Ivanov, VD Travkin, AM Balbashov, and Alois Loidl. Possible evidence for electromagnons in multiferroic manganites. *Nature physics*, 2(2):97, 2006. 3

[29] KZ Rushchanskii, S Kamba, V Goian, P Vaněk, M Savinov, J Prokleška, D Nuzhnyy, K Knížek, F Laufek, S Eckel, et al. A multiferroic material to search for the permanent electric dipole moment of the electron. *Nature materials*, 9(8):649, 2010. 3

[30] Sinéad M Griffin, Martin Lilienblum, Kris T Delaney, Yu Kumagai, Manfred Fiebig, and Nicola A Spaldin. Scaling behavior and beyond equilibrium in the hexagonal manganites. *Physical Review X*, 2(4):041022, 2012. 3, 144

[31] Shi-Zeng Lin, Xueyun Wang, Yoshitomo Kamiya, Gia-Wei Chern, Fei Fan, David Fan, Brian Casas, Yue Liu, Valery Kiryukhin, Wojciech H Zurek, et al. Topological defects as relics of emergent continuous symmetry and higgs condensation of disorder in ferroelectrics. *Nature Physics*, 10(12):970, 2014. 3, 144

[32] Hans Schmid. Multi-ferroic magnetoelectrics. *Ferroelectrics*, 162(1):317–338, 1994. 5, 7, 144

[33] Bas B Van Aken, Jean-Pierre Rivera, Hans Schmid, and Manfred Fiebig. Observation of ferrotoroidic domains. *Nature*, 449(7163):702, 2007. 5, 6

[34] Nicola A Spaldin and Manfred Fiebig. The renaissance of magnetoelectric multiferroics. *Science*, 309(5733):391–392, 2005. 5

[35] Shuai Dong, Jun-Ming Liu, Sang-Wook Cheong, and Zhifeng Ren. Multiferroic materials and magnetoelectric physics: symmetry, entanglement, excitation, and topology. *Advances in Physics*, 64(5-6):519–626, 2015. 6, 11, 16, 144

[36] Nicola A Spaldin, Manfred Fiebig, and Maxim Mostovoy. The toroidal moment in condensed-matter physics and its relation to the magnetoelectric effect. *Journal of Physics: Condensed Matter*, 20(43):434203, 2008. 6

[37] Ekhard KH Salje. Ferroelastic materials. *Annual Review of Materials Research*, 42:265–283, 2012. 6

[38] Wilma Eerenstein, ND Mathur, and James F Scott. Multiferroic and magnetoelectric materials. *nature*, 442(7104):759, 2006. 7

[39] WF Brown Jr, RM Hornreich, and S Shtrikman. Upper bound on the magnetoelectric susceptibility. *Physical Review*, 168(2):574, 1968. 7

[40] Shou-Ling Hou and N Bloembergen. Paramagnetoelectric effects in $NiSO_4 \cdot {}_6H_2O$. *Physical Review*, 138(4A):A1218, 1965. 7

[41] JF Scott. Mechanisms of dielectric anomalies in $BaMnF_4$. *Physical Review B*, 16(5):2329, 1977. 7

[42] MJ Cardwell. Measurements of the magnetic field dependent electric susceptibility of yttrium iron garnet. *Philosophical Magazine*, 20(167):1087–1089, 1969. 7

[43] Hans Grimmer. The piezomagnetoelectric effect. *Acta Crystallographica Section A: Foundations of Crystallography*, 48(3):266–271, 1992. 7

[44] Darrell G Schlom, Long-Qing Chen, Chang-Beom Eom, Karin M Rabe, Stephen K Streiffer, and Jean-Marc Triscone. Strain tuning of ferroelectric thin films. *Annu. Rev. Mater. Res.*, 37:589–626, 2007. 7

[45] Haimei Zheng, J Wang, SE Lofland, Z Ma, Ly Mohaddes-Ardabili, T Zhao, L Salamanca-Riba, SR Shinde, SB Ogale, Feiming Bai, et al. Multiferroic $BaTiO_3$-$CoFe_2O_4$ nanostructures. *Science*, 303(5658):661–663, 2004. 7

[46] J-P Rivera. On definitions, units, measurements, tensor forms of the linear magnetoelectric effect and on a new dynamic method applied to Cr-Cl boracite. *Ferroelectrics*, 161(1):165–180, 1994. 7

[47] Hans Schmid. Some symmetry aspects of ferroics and single phase multiferroics. *Journal of Physics: Condensed Matter*, 20(43):434201, 2008. 7

[48] Sang-Wook Cheong and Maxim Mostovoy. Multiferroics: a magnetic twist for ferroelectricity. *Nature materials*, 6(1):13, 2007. 8, 9

[49] Silvia Picozzi and Claude Ederer. First principles studies of multiferroic materials. *Journal of Physics: Condensed Matter*, 21(30):303201, 2009. 8

[50] SA Fedulov. Determining the curie point of $BiFeO_3$ ferroelectric. In *Soviet Physics Doklady*, volume 6, page 729, 1962. 8

[51] SV Kiselev. Detection of magnetic order in ferroelectric $BiFeO_3$ by neutron diffraction. *Sov. Phys.*, 7:742, 1963. 8

[52] Bas B Van Aken, Thomas TM Palstra, Alessio Filippetti, and Nicola A Spaldin. The origin of ferroelectricity in magnetoelectric $YMnO_3$. *Nature materials*, 3(3):164, 2004. 9

[53] Craig J Fennie and Karin M Rabe. Ferroelectric transition in $YMnO_3$ from first principles. *Physical Review B*, 72(10):100103, 2005. 9

[54] Martin Lilienblum, Thomas Lottermoser, Sebastian Manz, Sverre M Selbach, Andres Cano, and Manfred Fiebig. Ferroelectricity in the multiferroic hexagonal manganites. *Nature Physics*, 11(12):1070, 2015. 9

[55] Philippe Coeuré, Philippe Guinet, Jean C Peuzin, Georges Buisson, and E Felix Bertaut. Ferroelectric properties of hexagonal orthomanganites of yttrium and rare earths. In *Proceedings of the International Meeting on Ferroelectricity*, volume 1, page 332. Institute of Physics of the Czechoslovak Academy of Sciences, Prague, 1966. 9

[56] M Eibschütz, HJ Guggenheim, SH Wemple, I Camlibel, and M DiDomenico Jr. Ferroelectricity in $BaM^{2+}F_4$. *Physics Letters A*, 29(7):409–410, 1969. 9

[57] Claude Ederer and Nicola A Spaldin. Electric-field-switchable magnets: the case of $BaNiF_4$. *Physical Review B*, 74(2):020401, 2006. 9

[58] Naoshi Ikeda, Hiroyuki Ohsumi, Kenji Ohwada, Kenji Ishii, Toshiya Inami, Kazuhisa Kakurai, Youichi Murakami, Kenji Yoshii, Shigeo Mori, Yoichi Horibe, et al. Ferroelectricity from iron valence ordering in the charge-frustrated system $LuFe_2O_4$. *Nature*, 436(7054):1136, 2005. 9

[59] DV Efremov, J Van den Brink, and DI Khomskii. Nature mater. 3, 853 (2004). *arXiv preprint cond-mat/0306651*, 2003. 9

[60] Jeroen Van Den Brink and Daniel I Khomskii. Multiferroicity due to charge ordering. *Journal of Physics: Condensed Matter*, 20(43):434217, 2008. 9

[61] Yoshinori Tokura, Shinichiro Seki, and Naoto Nagaosa. Multiferroics of spin origin. *Reports on Progress in Physics*, 77(7):076501, 2014. 9, 14, 17, 146, 147

[62] YJ Choi, HT Yi, S Lee, Q Huang, Valery Kiryukhin, and S-W Cheong. Ferroelectricity in an ising chain magnet. *Physical review letters*, 100(4):047601, 2008. 10, 60, 146

[63] Hua Wu, T Burnus, Z Hu, C Martin, A Maignan, JC Cezar, A Tanaka, NB Brookes, DI Khomskii, and LH Tjeng. Ising magnetism and ferroelectricity in Ca_3CoMnO_6. *Physical review letters*, 102(2):026404, 2009. 10, 146

[64] Y Noda, H Kimura, M Fukunaga, S Kobayashi, I Kagomiya, and K Kohn. Magnetic and ferroelectric properties of multiferroic RMn_2O_5. *Journal of Physics: Condensed Matter*, 20(43):434206, 2008. 10

[65] Shintaro Ishiwata, Yoshio Kaneko, Yusuke Tokunaga, Yasujiro Taguchi, Taka-hisa Arima, and Yoshinori Tokura. Perovskite manganites hosting versatile multiferroic phases with symmetric and antisymmetric exchange strictions. *Physical Review B*, 81(10):100411, 2010. 11

[66] A Munoz, JA Alonso, MT Casais, MJ Martínez-Lope, JL Martínez, and MT Fernández-Díaz. The magnetic structure of $YMnO_3$ perovskite revisited. *Journal of Physics: Condensed Matter*, 14(12):3285, 2002. 11

[67] V Yu Pomjakushin, Michel Kenzelmann, Andreas Dönni, A Brooks Harris, Taro Nakajima, Setsuo Mitsuda, Makoto Tachibana, Lukas Keller, Joël Mesot, Hideaki Kitazawa, et al. Evidence for large electric polarization from collinear magnetism in $TmMnO_3$. *New Journal of Physics*, 11(4):043019, 2009. 11

[68] Igor Dzyaloshinsky. A thermodynamic theory of "weak" ferromagnetism of antiferromagnetics. *Journal of Physics and Chemistry of Solids*, 4(4):241–255, 1958. 11, 146

[69] Tôru Moriya. Anisotropic superexchange interaction and weak ferromagnetism. *Physical review*, 120(1):91, 1960. 11, 146

[70] Tôru Moriya. New mechanism of anisotropic superexchange interaction. *Physical Review Letters*, 4(5):228, 1960. 11, 146

[71] L Shekhtman, O Entin-Wohlman, and Amnon Aharony. Moriya's anisotropic superexchange interaction, frustration, and dzyaloshinsky's weak ferromagnetism. *Physical review letters*, 69(5):836, 1992. 11, 146

[72] Ivan A Sergienko and E Dagotto. Role of the dzyaloshinskii-moriya interaction in multiferroic perovskites. *Physical Review B*, 73(9):094434, 2006. 11, 146

[73] Hosho Katsura, Naoto Nagaosa, and Alexander V Balatsky. Spin current and magnetoelectric effect in noncollinear magnets. *Physical review letters*, 95(5):057205, 2005. 12, 13, 146

[74] Maxim Mostovoy. Ferroelectricity in spiral magnets. *Physical Review Letters*, 96(6):067601, 2006. 12

[75] G Lawes, A Brooks Harris, Tsuyoshi Kimura, N Rogado, Robert J Cava, Amnon Aharony, Ora Entin-Wohlman, Taner Yildirim, Michel Kenzelmann, C Broholm, et al. Magnetically driven ferroelectric order in $Ni_3V_2O_8$. *Physical review letters*, 95(8):087205, 2005. 13, 15, 147

[76] T Goto, T Kimura, G Lawes, AP Ramirez, and Y Tokura. Ferroelectricity and giant magnetocapacitance in perovskite rare-earth manganites. *Physical review letters*, 92(25):257201, 2004. 14

[77] T Kimura, G Lawes, T Goto, Y Tokura, and AP Ramirez. Magnetoelectric phase diagrams of orthorhombic $RMnO_3$ (R= Gd, Tb, and Dy). *Physical Review B*, 71(22):224425, 2005. 14, 22

[78] Y Yamasaki, S Miyasaka, T Goto, H Sagayama, T Arima, and Y Tokura. Ferroelectric phase transitions of 3 d-spin origin in $Eu_{1-x}Y_xMnO_3$. *Physical Review B*, 76(18):184418, 2007. 14

[79] Junjiro Kanamori. Superexchange interaction and symmetry properties of electron orbitals. *Journal of Physics and Chemistry of Solids*, 10(2-3):87–98, 1959. 14, 100

[80] T Kimura, S Ishihara, H Shintani, T Arima, KT Takahashi, K Ishizaka, and Y Tokura. Distorted perovskite with e g 1 configuration as a frustrated spin system. *Physical Review B*, 68(6):060403, 2003. 14

[81] Michel Kenzelmann, A Brooks Harris, S Jonas, C Broholm, Jürg Schefer, SB Kim, CL Zhang, S-W Cheong, Owen P Vajk, and Jeffrey W Lynn. Magnetic inversion symmetry breaking and ferroelectricity in $TbMnO_3$. *Physical review letters*, 95(8):087206, 2005. 14

[82] Y Yamasaki, H Sagayama, T Goto, M Matsuura, K Hirota, T Arima, and Y Tokura. Electric control of spin helicity in a magnetic ferroelectric. *Physical review letters*, 98(14):147204, 2007. 15

[83] G Lawes, Michel Kenzelmann, N Rogado, KH Kim, Guillermo A Jorge, Robert J Cava, Amnon Aharony, Ora Entin-Wohlman, A Brooks Harris, Taner Yildirim, et al. Competing magnetic phases on a kagomé staircase. *Physical review letters*, 93(24):247201, 2004. 15, 147

[84] Koji Taniguchi, N Abe, T Takenobu, Y Iwasa, and T Arima. Ferroelectric polarization flop in a frustrated magnet $MnWO_4$ induced by a magnetic field. *Physical review letters*, 97(9):097203, 2006. 15, 147

[85] AH Arkenbout, TTM Palstra, T Siegrist, and T Kimura. Ferroelectricity in the cycloidal spiral magnetic phase of $MnWO_4$. *Physical Review B*, 74(18):184431, 2006. 15, 147

[86] S Park, YJ Choi, CL Zhang, and Sang-Wook Cheong. Ferroelectricity in an s= 1/2 chain cuprate. *Physical review letters*, 98(5):057601, 2007. 15

[87] S Seki, Y Yamasaki, M Soda, M Matsuura, K Hirota, and Y Tokura. Correlation between spin helicity and an electric polarization vector in quantum-spin chain magnet $LiCu_2O_2$. *Physical review letters*, 100(12):127201, 2008. 15

[88] Yutaka Naito, Kenji Sato, Yukio Yasui, Yusuke Kobayashi, Yoshiaki Kobayashi, and Masatoshi Sato. Ferroelectric transition induced by the incommensurate magnetic ordering in $LiCuVO_4$. *Journal of the Physical Society of Japan*, 76(2):023708–023708, 2007. 15

[89] Florian Schrettle, Stephan Krohns, Peter Lunkenheimer, Joachim Hemberger, Norbert Büttgen, H-A Krug Von Nidda, AV Prokofiev, and Alois Loidl. Switching the ferroelectric polarization in the s= 1/ 2 chain cuprate $LiCuVO_4$ by external magnetic fields. *Physical Review B*, 77(14):144101, 2008. 15

[90] MG Banks, RK Kremer, C Hoch, A Simon, B Ouladdiaf, J-M Broto, H Rakoto, C Lee, and M-H Whangbo. Magnetic ordering in the frustrated heisenberg chain system cupric chloride $CuCl_2$. *Physical Review B*, 80(2):024404, 2009. 15

[91] S Seki, T Kurumaji, S Ishiwata, H Matsui, H Murakawa, Y Tokunaga, Y Kaneko, T Hasegawa, and Y Tokura. Cupric chloride $CuCl_2$ as an s= 1 2 chain multiferroic. *Physical Review B*, 82(6):064424, 2010. 15

[92] T Kimura, Y Sekio, H Nakamura, T Siegrist, and AP Ramirez. Cupric oxide as an induced-multiferroic with high-t_c. $Naturematerials, 7(4) : 291 - -294, 2008.$ 15

[93] Shintaro Ishiwata, Yasujiro Taguchi, Hiroshi Murakawa, Yoshinori Onose, and Yoshinori Tokura. Low-magnetic-field control of electric polarization vector in a helimagnet. *Science*, 319(5870):1643–1646, 2008. 15

[94] Chenglong Jia, Shigeki Onoda, Naoto Nagaosa, and Jung Hoon Han. Bond electronic polarization induced by spin. *Physical Review B*, 74(22):224444, 2006. 16

[95] Chenglong Jia, Shigeki Onoda, Naoto Nagaosa, and Jung Hoon Han. Microscopic theory of spin-polarization coupling in multiferroic transition metal oxides. *Physical Review B*, 76(14):144424, 2007. 16

[96] Taka-hisa Arima. Ferroelectricity induced by proper-screw type magnetic order. *Journal of the Physical Society of Japan*, 76(7):073702–073702, 2007. 16, 147

[97] Setsuo Mitsuda, Motoshi Mase, K Prokes, Hideaki Kitazawa, and H Aruga Katori. Field-induced magnetic phase transitions in a triangular lattice antiferromagnet $CuFeO_2$ up to 14.5 t. *Journal of the Physical Society of Japan*, 69(11):3513–3516, 2000. 16, 147

[98] S Seki, Y Yamasaki, Y Shiomi, S Iguchi, Y Onose, and Y Tokura. Impurity-doping-induced ferroelectricity in the frustrated antiferromagnet $CuFeO_2$. *Physical Review B*, 75(10):100403, 2007. 17

[99] N Terada, T Nakajima, Setsuo Mitsuda, H Kitazawa, K Kaneko, and N Metoki. Ga-substitution-induced single ferroelectric phase in multiferroic $CuFeO_2$. *Physical Review B*, 78(1):014101, 2008. 17

[100] T Nakajima, Setsuo Mitsuda, S Kanetsuki, K Tanaka, K Fujii, N Terada, M Soda, M Matsuura, and K Hirota. Electric polarization induced by a proper helical magnetic ordering in a delafossite multiferroic $CuFe_{1-x}Al_xO_2$. *Physical Review B*, 77(5):052401, 2008. 17

[101] JW Cable, MK Wilkinson, EO Wollan, and WC Koehler. Neutron diffraction investigation of the magnetic order in MnI_2. *Physical Review*, 125(6):1860, 1962. 17, 147

[102] T Sato, H Kadowaki, and K Iio. Successive phase transitions in the hexagonal-layered heisenberg antiferromagnets MnX_2 (X= Br, I). *Physica B: Condensed Matter*, 213:224–226, 1995. 17, 147

[103] T Kurumaji, S Seki, S Ishiwata, H Murakawa, Y Tokunaga, Y Kaneko, and Y Tokura. Magnetic-field induced competition of two multiferroic orders in a triangular-lattice helimagnet MnI_2. *Physical review letters*, 106(16):167206, 2011. 17

[104] T Kurumaji, S Seki, S Ishiwata, H Murakawa, Y Kaneko, and Y Tokura. Magnetoelectric responses induced by domain rearrangement and spin structural change in triangular-lattice helimagnets NiI_2 and CoI_2. *Physical Review B*, 87(1):014429, 2013. 17

[105] A Zheludev, T Sato, Takatsugu Masuda, K Uchinokura, G Shirane, and B Roessli. Spin waves and the origin of commensurate magnetism in $Ba_2CoGe_2O_7$. *Physical Review B*, 68(2):024428, 2003. 17

[106] HT Yi, YJ Choi, S Lee, and S-W Cheong. Multiferroicity in the square-lattice antiferromagnet of $Ba_2CoGe_2O_7$. *Applied Physics Letters*, 92(21):212904, 2008. 17

[107] H Murakawa, Yoshinori Onose, S Miyahara, N Furukawa, and Y Tokura. Ferroelectricity induced by spin-dependent metal-ligand hybridization in $Ba_2CoGe_2O_7$. *Physical review letters*, 105(13):137202, 2010. 17

[108] H Murakawa, Y Onose, S Miyahara, N Furukawa, and Y Tokura. Comprehensive study of the ferroelectricity induced by the spin-dependent d-p hybridization mechanism in $Ba_2XGe_2O_7$ (X= Mn, Co, and Cu). *Physical Review B*, 85(17):174106, 2012. 18

[109] ND Khanh, N Abe, K Kubo, M Akaki, M Tokunaga, T Sasaki, and T Arima. Magnetic control of electric polarization in the noncentrosymmetric compound $(Cu,Ni)B_2O_4$. *Physical Review B*, 87(18):184416, 2013. 18

[110] Karol Marty, Virginie Simonet, Eric Ressouche, Rafik Ballou, Pascal Lejay, and Pierre Bordet. Single domain magnetic helicity and triangular chirality in structurally enantiopure $Ba_3NbFe_3Si_2O_{14}$. *Physical review letters*, 101(24):247201, 2008. 18

[111] M Janoschek, P Fischer, J Schefer, B Roessli, V Pomjakushin, M Meven, V Petricek, G Petrakovskii, and L Bezmaternikh. Single magnetic chirality in the magnetoelectric $NdFe_3(B_{11}O_3)_4$. *Physical Review B*, 81(9):094429, 2010. 18

[112] Sebastian Mühlbauer, Benedikt Binz, F Jonietz, Christian Pfleiderer, Achim Rosch, Anja Neubauer, Robert Georgii, and Peter Böni. Skyrmion lattice in a chiral magnet. *Science*, 323(5916):915–919, 2009. 18

[113] Tony Hilton Royle Skyrme. A unified field theory of mesons and baryons. *Nuclear Physics*, 31:556–569, 1962. 18

[114] S Seki, S Ishiwata, and Y Tokura. Magnetoelectric nature of skyrmions in a chiral magnetic insulator Cu_2OSeO_3. *Physical Review B*, 86(6):060403, 2012. 18

[115] Shinichiro Seki, XZ Yu, S Ishiwata, and Yoshinori Tokura. Observation of skyrmions in a multiferroic material. *Science*, 336(6078):198–201, 2012. 18

[116] V Ovidiu Garlea and Bryan C Chakoumakos. Magnetic structures. In *Experimental Methods in the Physical Sciences*, volume 48, pages 203–290. Elsevier, 2015. 19, 21, 148

[117] S Krupička and P Novak. Oxide spinels. *Handbook of ferromagnetic materials*, 3:189–304, 1982. 19

[118] Yoshihiko Okamoto, Gøran J Nilsen, J Paul Attfield, and Zenji Hiroi. Breathing pyrochlore lattice realized in a-site ordered spinel oxides $LiGaCr_4O_8$ and $LiInCr_4O_8$. *Physical review letters*, 110(9):097203, 2013. 19

[119] Ya A Kesler, EG Zhukov, DS Filimonov, ES Polulyak, TK Menshchikova, and VA Fedorov. $CuCr_2S_4$-based quaternary cation-substituted magnetic phases. *Inorganic materials*, 41(9):914–919, 2005. 19

[120] H áM Palmer et al. Structural, magnetic and electronic properties of $Fe_{0.5}Cu_{0.5}Cr_2S_4$. *Journal of Materials Chemistry*, 9(3):637–640, 1999. 19

[121] TG Aminov, DI Kirdyankin, GG Shabunina, and VM Novotortsev. Magnetic properties of $Cu_{0.5}Fe_{0.5-x}Ga_xCr_2S_4$ solid solutions. *Russian Journal of Inorganic Chemistry*, 57(7):991–997, 2012. 19

[122] NV Ter-Oganessian. Cation-ordered $(A)_{1/2}(A)_{1/2}B_2X_4$ magnetic spinels as magnetoelectrics. *Journal of magnetism and magnetic materials*, 364:47–54, 2014. 19

[123] PB Braun. A superstructure in spinels. *Nature*, 170(4339):1123–1123, 1952. 19

[124] María Ángeles Arillo, María Luisa López, Carlos Pico, María Luisa Veiga, Javier Campo, José Luis Martínez, and Alejandro Santrich-Badal. Order- disorder transitions and magnetic behaviour in lithium ferrites $Li_{0.5+0.5x}Fe_{2.5-1.5x}Ti_xO_4$ (x= 1.28 and 1.50). *European Journal of Inorganic Chemistry*, 2003(13):2397–2405, 2003. 19

[125] M Ferriol and S Lecocq. Structural characterization of $ZnLiNbO_4$. *European Journal of Solid State and Inorganic Chemistry*, 35(10-11):707–714, 1998. 19

[126] Kazuhiko Mukai, Yuichi Kato, and Hideyuki Nakano. Determination of cation distribution in the $Fe[Li_{1/2}Fe_{3/2}]O_4$- $LiFeTiO_4$ - $Li[Li_{1/3}Ti_{5/3}]O_4$ system: Mixed nature of solid solution and superlattice. *Journal of Solid State Chemistry*, 247:67–76, 2017. 19

[127] Louis Néel. Magnetic properties of ferrites: ferrimagnetism and antiferromagnetism. *Ann. Phys*, 3:137–198, 1948. 19, 59

[128] J Samuel Smart. The néel theory of ferrimagnetism. *American Journal of Physics*, 23(6):356–370, 1955. 19

[129] J-H Chung, M Matsuda, S-H Lee, K Kakurai, H Ueda, TJ Sato, H Takagi, K-P Hong, and S Park. Statics and dynamics of incommensurate spin order in a geometrically frustrated antiferromagnet cdcr 2 o 4. *Physical review letters*, 95(24):247204, 2005. 20

[130] S Ji, S-H Lee, C Broholm, TY Koo, W Ratcliff, S-W Cheong, and P Zschack. Spin-lattice order in frustrated $ZnCr_2O_4$. *Physical review letters*, 103(3):037201, 2009. 20

[131] M Matsuda, H Ueda, A Kikkawa, Y Tanaka, K Katsumata, Y Narumi, T Inami, Y Ueda, and S-H Lee. Spin–lattice instability to a fractional magnetization state in the spinel $HgCr_2O_4$. *Nature Physics*, 3(6):397–400, 2007. 20

[132] Yutaka Ueda, Naoki Fujiwara, and Hiroshi Yasuoka. Magnetic and structural transitions in $(Li_xZn_{1-x})V_2O_4$ with the spinel structure. *Journal of the Physical Society of Japan*, 66(3):778–783, 1997. 20

[133] Z Zhang, Despina Louca, A Visinoiu, S-H Lee, JD Thompson, T Proffen, A Llobet, Y Qiu, S Park, and Y Ueda. Local order and frustration in the geometrically frustrated spinels $Cd_{1-x}Zn_xV_2O_4$. *Physical Review B*, 74(1):014108, 2006. 20

[134] Elisa M Wheeler, Bella Lake, ATM Nazmul Islam, Manfred Reehuis, Paul Steffens, Tatiana Guidi, and Adrian H Hill. Spin and orbital order in the vanadium spinel MgV_2O_4. *Physical Review B*, 82(14):140406, 2010. 20

[135] F Yokaichiya, Alexander Krimmel, Vladimir Tsurkan, I Margiolaki, P Thompson, HN Bordallo, A Buchsteiner, N Stüßer, DN Argyriou, and Alois Loidl. Spin-driven phase transitions in $ZnCr_2Se_4$ and $ZnCr_2S_4$ probed by high-resolution synchrotron x-ray and neutron powder diffraction. *Physical Review B*, 79(6):064423, 2009. 20

[136] YV Tymoshenko, YA Onykiienko, T Müller, Ronny Thomale, Stephan Rachel, Alistair S Cameron, PY Portnichenko, Dmitry V Efremov, V Tsurkan, Douglas L Abernathy, et al. Pseudo-goldstone magnons in the frustrated s= 3/2 heisenberg helimagnet $ZnCr_2Se_4$ with a pyrochlore magnetic sublattice. *Physical Review X*, 7(4):041049, 2017. 20

[137] Gregory J Macdougall, Vasile O Garlea, Adam A Aczel, HD Zhou, and Stephen E Nagler. Magnetic order and ice rules in the multiferroic spinel FeV_2O_4. *Physical Review B*, 86(6):060414, 2012. 20

[138] Vasile O Garlea, Rongying Jin, David Mandrus, Bertrand Roessli, Q Huang, M Miller, Arthur J Schultz, and Stephen E Nagler. Magnetic and orbital ordering in the spinel MnV_2O_4. *Physical review letters*, 100(6):066404, 2008. 20

[139] Keisuke Tomiyasu and Isao Kagomiya. Magnetic structure of $NiCr_2O_4$ studied by neutron scattering and magnetization measurements. *Journal of the Physical Society of Japan*, 73(9):2539–2542, 2004. 20, 22, 100, 149

[140] TA Kaplan. Classical theory of spin configurations in the cubic spinel. *Physical Review*, 119(5):1460, 1960. 21, 148

[141] DH Lyons and TA Kaplan. Method for determining ground-state spin configurations. *Physical Review*, 120(5):1580, 1960. 21, 148

[142] DH Lyons, TA Kaplan, K Dwight, and N Menyuk. Classical theory of the ground spin-state in cubic spinels. *Physical Review*, 126(2):540, 1962. 21, 148

[143] JM Hastings and LM Corliss. Magnetic structure of manganese chromite. *Physical Review*, 126(2):556, 1962. 21, 149

[144] Y Yamasaki, S Miyasaka, Y Kaneko, J-P He, T Arima, and Y Tokura. Magnetic reversal of the ferroelectric polarization in a multiferroic spinel oxide. *Physical review letters*, 96(20):207204, 2006. 21, 22, 60, 149, 150

[145] G Lawes, B Melot, K Page, C Ederer, MA Hayward, Th Proffen, and R Seshadri. Dielectric anomalies and spiral magnetic order in $CoCr_2O_4$. *Physical Review B*, 74(2):024413, 2006. 21

[146] N Menyuk, A Wold, D Rogers, and K Dwight. Magnetic transitions in cubic spinels. In *Proceedings of the Seventh Conference on Magnetism and Magnetic Materials*, pages 1144–1145. Springer, 1962. 21, 149

[147] N Menyuk, K Dwight, and A Wold. Ferrimagnetic spiral configurations in cobalt chromite. *Journal de physique*, 25(5):528–536, 1964. 21, 149

[148] Young Jai Choi, J Okamoto, DJ Huang, KS Chao, HJ Lin, CT Chen, M Van Veenendaal, TA Kaplan, and Sang-Wook Cheong. Thermally or magnetically induced polarization reversal in the multiferroic $CoCr_2O_4$. *Physical review letters*, 102(6):067601, 2009. 22, 150

[149] Ingyu Kim, Yoon Seok Oh, Yong Liu, Sae Hwan Chun, Jun-Sik Lee, Kyung-Tae Ko, Jae-Hoon Park, Jae-Ho Chung, and Kee Hoon Kim. Electric polarization enhancement in multiferroic $CoCr_2O_4$ crystals with cr-site mixing. *Applied Physics Letters*, 94(4):042505, 2009. 22, 23, 150

[150] Brent C Melot, Jennifer E Drewes, Ram Seshadri, EM Stoudenmire, and Arthur P Ramirez. Magnetic phase evolution in the spinel compounds $Zn_{1-x}Co_xCr_2O_4$. *Journal of Physics: Condensed Matter*, 21(21):216007, 2009. 22, 23, 99, 150

[151] H Kasper. Die lichtabsorption von Ni^{2+} und Co^{2+} in 2,6-spinellen. *Zeitschrift fur anorganische und allgemeine Chemie*, 354(1-2):78–84, 1967. 22, 151

[152] Juan Rodríguez-Carvajal. Recent advances in magnetic structure determination by neutron powder diffraction. *physica B*, 192(1-2):55–69, 1993. 23, 50, 151

[153] Harald Schäfer, Herbert Jacob, and Karl Etzel. Chemische transportreaktionen. i. über den transport des bodenkörpers im temperaturgefälle mit hilfe heterogener gleichgewichte. *Zeitschrift für anorganische und allgemeine Chemie*, 286(1-2):27–41, 1956. 25

[154] Michael Binnewies, Robert Glaum, Marcus Schmidt, and Peer Schmidt. Chemical vapor transport reactions–a historical review. *Zeitschrift für anorganische und allgemeine Chemie*, 639(2):219–229, 2013. 26

[155] John Clarke. Squids. *Scientific American*, 271(2):46–53, 1994. 26, 27

[156] RL Fagaly. Superconducting quantum interference device instruments and applications. *Review of scientific instruments*, 77(10):101101, 2006. 27

[157] M Buchner, K Höfler, B Henne, V Ney, and A Ney. Tutorial: Basic principles, limits of detection, and pitfalls of highly sensitive squid magnetometry for nanomagnetism and spintronics. *Journal of Applied Physics*, 124(16):161101, 2018. 28

[158] Kalim Deshmukh, Sowmya Sankaran, Basheer Ahamed, Kishor K Sadasivuni, Khadheer SK Pasha, Deepalekshmi Ponnamma, PS Rama Sreekanth, and Kuppanna Chidambaram. Dielectric spectroscopy. In *Spectroscopic Methods for Nanomaterials Characterization*, pages 237–299. Elsevier, 2017. 29

[159] Gordon Leslie Squires. *Introduction to the theory of thermal neutron scattering*. Courier Corporation, 1996. 31, 45

[160] Particle Data Group et al. Review of particle physics. *Journal of Physics G: Nuclear and particle physics*, 33(1):001, 2006. 31

[161] Paul scherrer institute website. spallation target. https://www.psi.ch/en/bsq/spallation-target. 33

[162] Gen Shirane, Stephen M Shapiro, and John M Tranquada. *Neutron scattering with a triple-axis spectrometer: basic techniques*. Cambridge University Press, 2002. 36, 38

[163] Albert Furrer, Thierry StrÃ, et al. *Neutron scattering in condensed matter physics*. World Scientific Publishing Company, 2009. 37

[164] GJ Long. Neutron diffraction. 2003. 39

[165] AL Patterson. The scherrer formula for x-ray particle size determination. *Physical review*, 56(10):978, 1939. 41

[166] AR Stokes and AJC Wilson. The diffraction of x rays by distorted crystal aggregates-i. *Proceedings of the Physical Society*, 56(3):174, 1944. 42

[167] Peter W Stephens. Phenomenological model of anisotropic peak broadening in powder diffraction. *Journal of Applied Crystallography*, 32(2):281–289, 1999. 42

[168] José Baruchel, Jean-Louis Hodeau, Mogens S Lehmann, Jean-René Regnard, and Claire Schlenker. *Neutron and synchrotron radiation for condensed matter studies*. Springer, 1993. 42, 43

[169] D1b, crg - high intensity two-axis powder diffractometer. https://www.ill.eu/users/instruments/instruments-list/d1b/description/instrument-layout/. 44

[170] LA Feigin, Dimitrij I Svergun, et al. *Structure analysis by small-angle X-ray and neutron scattering*, volume 1. Springer, 1987. 43

[171] T Reimann, S Mühlbauer, M Schulz, B Betz, A Kaestner, V Pipich, P Böni, and C Grünzweig. Visualizing the morphology of vortex lattice domains in a bulk type-ii superconductor. *Nature communications*, 6(1):1–8, 2015. 43

[172] K Karube, JS White, N Reynolds, JL Gavilano, H Oike, A Kikkawa, F Kagawa, Y Tokunaga, Henrik M Rønnow, Y Tokura, et al. Robust metastable skyrmions and their triangular–square lattice structural transition in a high-temperature chiral magnet. *Nature materials*, 15(12):1237–1242, 2016. 43, 75

[173] D33 - massive dynamic q-range small-angle diffractometer. https://www.ill.eu/users/instruments/instruments-list/d33/description/instrument-layout/. 45

[174] O Schärpf and H Capellmann. The xyz-difference method with polarized neutrons and the separation of coherent, spin incoherent, and magnetic scattering cross sections in a multidetector. *physica status solidi (a)*, 135(2):359–379, 1993. 45

[175] RM Moon, T Riste, and WC Koehler. Polarization analysis of thermal-neutron scattering. *Physical Review*, 181(2):920, 1969. 46

[176] JR Stewart, PP Deen, KH Andersen, H Schober, J-F Barthélémy, JM Hillier, AP Murani, T Hayes, and B Lindenau. Disordered materials studied using neutron polarization analysis on the multi-detector spectrometer, d7. *Journal of Applied Crystallography*, 42(1):69–84, 2009. 47

[177] D7 -diffuse scattering spectrometer. https://www.ill.eu/users/instruments/instruments-list/d7/description/instrument-layout/. 48

[178] Ferenc Mezei. Neutron spin echo: A new concept in polarized thermal neutron techniques. *Zeitschrift für Physik A Hadrons and nuclei*, 255(2):146–160, 1972. 48

[179] HaM Rietveld. A profile refinement method for nuclear and magnetic structures. *Journal of applied Crystallography*, 2(2):65–71, 1969. 49

[180] Newton-raphson method. https://www.sciencedirect.com/topics/engineering/newton-raphson-method. 49

[181] Newton-raphson method. https://www.sciencedirect.com/topics/mathematics/gauss-newton-method. 49

[182] RL McGreevy and L Pusztai. Reverse monte carlo simulation: a new technique for the determination of disordered structures. *Molecular simulation*, 1(6):359–367, 1988. 50

[183] Matthew G Tucker, David A Keen, Martin T Dove, Andrew L Goodwin, and Qun Hui. Rmcprofile: reverse monte carlo for polycrystalline materials. *Journal of Physics: Condensed Matter*, 19(33):335218, 2007. 50

[184] Andrew L Goodwin, Matthew G Tucker, Martin T Dove, and David A Keen. Magnetic structure of mno at 10 k from total neutron scattering data. *Physical review letters*, 96(4):047209, 2006. 50

[185] M Laver, EM Forgan, Asger Bech Abrahamsen, C Bowell, Th Geue, and R Cubitt. Uncovering flux line correlations in superconductors by reverse monte carlo refinement of neutron scattering data. *Physical review letters*, 100(10):107001, 2008. 50

[186] Joseph AM Paddison and Andrew L Goodwin. Empirical magnetic structure solution of frustrated spin systems. *Physical review letters*, 108(1):017204, 2012. 50

[187] Nicholas Metropolis and Stanislaw Ulam. The monte carlo method. *Journal of the American statistical association*, 44(247):335–341, 1949. 51

[188] Joseph AM Paddison, J Ross Stewart, and Andrew L Goodwin. Spinvert: a program for refinement of paramagnetic diffuse scattering data. *Journal of Physics: Condensed Matter*, 25(45):454220, 2013. 51

[189] Ilan Asriel Blech and BL Averbach. Spin correlations in mno. *Physics Physique Fizika*, 1(1):31, 1964. 52

[190] N Jovic, B Antic, A Kremenovic, Anne Spasojevic-de Bire, and V Spasojevic. Cation ordering and order–disorder phase transitionin Co-substituted $Li_4Ti_5O_{12}$ spinels. *physica status solidi (a)*, 198(1):18–28, 2003. 56, 152

[191] RW Cheary and NW Grimes. Investigation of antiphase domains in lithium ferrite by analysis of the broadened x-ray lines. *Acta Crystallographica Section A: Crystal Physics, Diffraction, Theoretical and General Crystallography*, 34(1):74–84, 1978. 56

[192] NE Brese and M O'keeffe. Bond-valence parameters for solids. *Acta Crystallographica Section B: Structural Science*, 47(2):192–197, 1991. 57

[193] Robert D Shannon. Revised effective ionic radii and systematic studies of interatomic distances in halides and chalcogenides. *Acta crystallographica section A: crystal physics, diffraction, theoretical and general crystallography*, 32(5):751–767, 1976. 58

[194] Maud Giot, Alain Pautrat, Gilles André, Damien Saurel, Maryvonne Hervieu, and Juan Rodriguez-Carvajal. Magnetic states and spin-glass properties in bi 0.67 ca 0.33 mn o 3: Macroscopic ac measurements and neutron scattering. *Physical Review B*, 77(13):134445, 2008. 59

[195] Y Yafet and Ch Kittel. Antiferromagnetic arrangements in ferrites. *Physical Review*, 87(2):290, 1952. 60

[196] W Schiessl, W Potzel, H Karzel, M Steiner, GM Kalvius, A Martin, MK Krause, I Halevy, J Gal, W Schäfer, et al. Magnetic properties of the $ZnFe_2O_4$ spinel. *Physical Review B*, 53(14):9143, 1996. 62

[197] SM Yunus, H-S Shim, C-H Lee, MA Asgar, FU Ahmed, and AKM Zakaria. Investigation of the magnetic structure of the spinel compound $Zn_xCu_{1-x}FeCrO_4$ by neutron diffraction. *Journal of magnetism and magnetic materials*, 241(1):40–50, 2002. 62, 99

[198] SM Yunus, JA Fernandez-Baca, MA Asgar, and FU Ahmed. Neutron diffraction study of magnetic ordering in the spinel oxide $Co_xMn_{1-x}Al_{2x}Fe_{2-2x}O_4$. *Journal of alloys and compounds*, 298(1-2):9–17, 2000. 62

[199] JM Perez-Mato, SV Gallego, ES Tasci, LUİS Elcoro, Gemma de la Flor, and MI Aroyo. Symmetry-based computational tools for magnetic crystallography. *Annual Review of Materials Research*, 45:217–248, 2015. 63

[200] H. t. stokes, d. m. hatch, and b. j. campbell, isodistort, isotropy software suite. iso.byu.edu. https://stokes.byu.edu/iso/isodistort.php. Accessed: 2020-08-06. 65, 154

[201] Harold T Stokes, Dorian M Hatch, Branton J Campbell, and David E Tanner. Isodisplace: a web-based tool for exploring structural distortions. *Journal of Applied Crystallography*, 39(4):607–614, 2006. 65, 154

[202] Grasp - the script application designed for the graphical inspection, analysis and reduction of multi-detector data produced by the small-angle neutron scattering (sans) instruments. https://www.ill.eu/users/support-labs-infrastructure/software-scientific-tools/grasp/. Accessed: 2020-11-10. 72

[203] G Porod, O Glatter, and O Kratky. Small angle x-ray scattering. *by O. Glatter and O. Kratky, Academic Press, London*, page 17, 1982. 73

[204] BG Ueland, Jeffrey W Lynn, Mark Laver, Young Jai Choi, and S-W Cheong. Origin of electric-field-induced magnetization in multiferroic $HoMnO_3$. *Physical review letters*, 104(14):147204, 2010. 73, 157

[205] M Hennion and I Mirebeau. Diffusion de neutrons aux petits angles (dnpa) et magnétisme: concepts et applications. *Le Journal de Physique IV*, 9(PR1):Pr1–51, 1999. 73

[206] JW Lynn, L Vasiliu-Doloc, and MA Subramanian. Spin dynamics of the magnetoresistive pyrochlore $Tl_2Mn_2O_7$. *Physical review letters*, 80(20):4582, 1998. 74

[207] PJ Brown. International tables for crystallography vol c, ed ajc wilson, 1995. 83

[208] GA Smolenskiĭ, VoMn Yudin, ES Sher, and Yu E Stolypin. Antiferromagnetic properties of some perovskites. *JETP*, 16:622, 1963. 92

[209] RR Birss. Symmetry and magnetism 36p, 1964. 92

[210] Samuel V Gallego, Jesus Etxebarria, Luis Elcoro, Emre S Tasci, and J Manuel Perez-Mato. Automatic calculation of symmetry-adapted tensors in magnetic and non-magnetic materials: a new tool of the bilbao crystallographic server. *Acta Crystallographica Section A: Foundations and Advances*, 75(3):438–447, 2019. 92

[211] Sung Yong An, In-Bo Shim, and Chul Sung Kim. Synthesis and magnetic properties of $LiFe_5O_8$ powders by a sol–gel process. *Journal of magnetism and magnetic materials*, 290:1551–1554, 2005. 97

[212] R Padam, Tapati Sarkar, Roland Mathieu, S Thota, and D Pal. Magnetic phase diagram of $Co(Cr_{1-x}Al_x)_2O_4$ (x= 0.0–1.0). *Journal of Applied Physics*, 122(7):073908, 2017. 98

[213] MA Ahmed, Nagwa Okasha, and L Salah. Influence of yttrium ions on the magnetic properties of Ni–Zn ferrites. *Journal of magnetism and magnetic materials*, 264(2-3):241–250, 2003. 99

[214] AKM Zakaria, MA Asgar, S-G Eriksson, FU Ahmed, SM Yunus, and H Rundlöf. The study of magnetic ordering in the spinel system $Zn_xNi_{1-x}FeCrO_4$ by neutron diffraction. *Journal of magnetism and magnetic materials*, 265(3):311–320, 2003. 99

[215] R Chakravarthy, L Madhav Rao, SK Paranjpe, SK Kulshreshtha, and SB Roy. Perturbed magnetic ordering in the disordered spinel $Zn_xCo_{1-x}FeCrO_4$. *Physical Review B*, 43(7):6031, 1991. 99

[216] John B Goodenough. Theory of the role of covalence in the perovskite-type manganites [la, m (ii)] mn o 3. *Physical Review*, 100(2):564, 1955. 100

[217] John B Goodenough. An interpretation of the magnetic properties of the perovskite-type mixed crystals la1- xsrxcoo3- λ. *Journal of Physics and Chemistry of Solids*, 6(2-3):287–297, 1958. 100

Appendix B

Résumé en français

L'une des classes de matériaux les plus prometteuses pour stimuler la technologie en général et la puissance de calcul en particulier sont les multiferroïques magnétiques - des matériaux présentant un couplage mutuel entre les sous-systèmes magnétiques intrinsèques et électroniques [5]. L'histoire de la magnétoélectricité est riche et s'étend désormais sur trois siècles. Tout a commencé en 1865 avec les équations de Maxwell qui ont montré que les interactions magnétiques et les mouvements de charges électriques sont de même nature [6]. A la toute fin du XIXe siècle en 1894, Pierre Curie, utilisant des considérations de symétrie, prédit la possibilité d'un couplage entre degrés de liberté électroniques et magnétiques dans les cristaux isolants [7]. Pourtant, la première véritable observation de l'effet magnétoélectrique n'a eu lieu qu'en 1960 avec la découverte de Cr_2O_3 [8] basée sur la prédiction faite un an plus tôt par Dzyaloshinskii [9] suivie d'une enquête approfondie sur les boracites dans lesquelles $Ni_3B_7O_{13}I$ était le plus célèbre pour manifester le plus fort propriétés multiferroïques [10]. Repenser l'idée originale des solutions solides de pérovskites ferroélectriques contenant des ions magnétiques Nicola Spaldin [16] a fourni une prévision peu prometteuse sur les possibilités de coexistence du ferromagnétisme et de la ferroélectricité [17]. Mais un travail intense a finalement abouti à deux œuvres influentes, chacune devenant un point de pivot pour tout un champ de matériaux magnétoélectriques. La première a été la découverte de la multiferroicité à température ambiante dans les films minces $BiFeO_3$ qui a inspiré des recherches intensives sur ce composé avec des applications potentielles [18]. La seconde était l'observation du nouveau type de multiferroicité dans $TbMnO_3$ [19]. Par rapport à tous les composés précédemment connus où la ferroélectricité et le magnétisme étaient liés indirectement, dans le cas du $TbMnO_3$, l'ordre magnétique était la force motrice de la polarisation électrique, donc le couplage entre deux sous-systèmes essentiels est intrinsèquement fort.

Certes, la préoccupation majeure des multiferroïques magnétiques est motivée par un intérêt fondamental pour le domaine. D'une part, même les modèles théoriques les plus développés sont incapables de fournir une explication exhaustive de toutes les observations expérimentales, d'autre part les propriétés démontrées par des matériaux connus sont incompatibles avec les performances effectives du dispositif: températures de transition basses ou magnétoélectrique hebdomadaire l'accouplement rend la production et l'exploitation technologiquement défavorables. Cependant, certains matériaux composites trouvent leurs applications dans des dispositifs prototypes tels que des capteurs et des actionneurs [22]. Les hétérostructures en films minces de couches ferroélectriques et ferromagnétiques alternées peuvent également être utilisées comme transistors, jonctions tunnel ou capteurs magnétiques [23]. De plus, deux commandes co-dépendantes rendent ces matériaux intéressants pour le stockage de données [24]. En plus de cela, la recherche

multiferroïque a un impact énorme sur les domaines de connaissances qui sont indirectement liés ou même pas pertinents aux matériaux multiferroïques eux-mêmes à première vue. Il a été prouvé que la transition ferroélectrique dans les composés h-RMnO3 et les transitions de phase dans l'univers primitif obéissaient aux mêmes règles, ce qui en fait un terrain de jeu idéal pour tester des modèles cosmologiques. [30, 31]

Par conséquent, la recherche et l'étude de nouveaux composés multiferroïques sont d'une grande importance soit pour élargir la compréhension fondamentale de la nature et des applications techniques possibles. Ainsi, au cours de ce travail de recherche, des oxydes de tellure (VI) à base de cobalt à structures magnétiques complexes ont été étudiés.

Parmi ces composés, une attention particulière a été portée à la série des spinelles $Co_{5-x}Zn_xTeO_8$ pour leurs propriétés magnétiques multiferroïques potentielles. Au cours de ces 3 années, des travaux approfondis ont été menés sur les synthèses, le raffinement des structures cristallines, et la caractérisation de leurs propriétés magnétiques et diélectriques, combinant plusieurs techniques: caractérisation magnétique classique (SUID, PPMS) et diverses expériences de diffusion neutronique. Ce manuscrit fournit des informations générales sur l'effet magnétoélectrique et les matériaux multiferroïques, les différentes techniques expérimentales qui ont été utilisées pour l'étude de la série spinelle de $Co_{5-x}Zn_xTeO_8$ et tous les résultats expérimentaux et leur discussion.

Comme cela avait été initialement proposé par Schmid en 1994, les multiferroïques sont une classe de matériaux combinant au moins deux ordres ferroïques primaires [32]. La liste des ferroïques contient quatre types d'ordre: ferroélectrique, ferromagnétique, ferroélastique et ferrotoroïque. Tous sont décrits par l'émergence spontanée d'une propriété correspondante appelée un paramètre d'ordre qui est uniforme à travers les domaines, des régions de supports géométriquement restreintes, qui peuvent être commutées hystérétiquement par un champ externe approprié. Dans le cas d'un contrôle ferroélectrique, le paramètre d'ordre est la polarisation commutable électriquement sous champ électrique, pour les ferromagnétiques il s'agit de la magnétisation et du champ magnétique, et les matériaux ferroélastiques sont caractérisés par une déformation spontanée sous contrainte appliquée. L'ordre ferrotoroïque est représenté par le moment toroïdal généré par les tourbillons de moments magnétiques. Il convient également de mentionner que cette classification comprend également les ordres anti-ferroïques comme l'anti-ferroélectricité et l'anti-ferromagnétisme dans lesquels les moments associés s'annulent dans un état ordonné.

La symétrie spatio-temporelle est un point clé pour la caractérisation des ordres ferroïques primaires. Les quatre états possèdent des propriétés de transformation différentes sous les opérateurs de parité d'inversion temporelle et d'inversion spatiale. Par exemple, la ferroélectricité associée à la polarisation spontanée $\mathbf{P}$, qui est donnée par $\sum_i Q_i \mathbf{r}_i$ où Q_i représente la charge à la position r_i. Evidemment, avec l'émergence d'un dipôle électrique, l'inversion spatiale est violée tandis que la symétrie d'inversion temporelle est préservée. Le moment magnétique $\mathbf{M}$, à son tour, montre une caractéristique opposée. Étant un vecteur axial, cette quantité peut être représentée comme une boucle de courant, donc est proportionnelle à $(dQ\mathbf{r}/dt) \times \mathbf{r}$ où t est le temps. Donc le moment magnétique $\mathbf{M}$ rompt la symétrie d'inversion du temps mais reste invariant sous l'inversion spatiale [35]. Puisque la polarisation $\mathbf{P}$ et le moment magnétique $\mathbf{M}$ ont des propriétés de symétrie différentes, les ordres ferroélectrique et ferromagnétique sont généralement indépendants. Cependant, ces deux paramètres d'ordre pourraient être combinés par couplage magnétoélectrique: une co-dépendance mutuelle des sous-systèmes électroniques et magnétiques d'un matériau. Ainsi, dans ce cas, les multiferroïques combinant l'ordre de spin et de charge sont asymétriques spatio-temporelles.

Aucune compréhension approfondie de ce phénomène ne pourrait être obtenue sans un

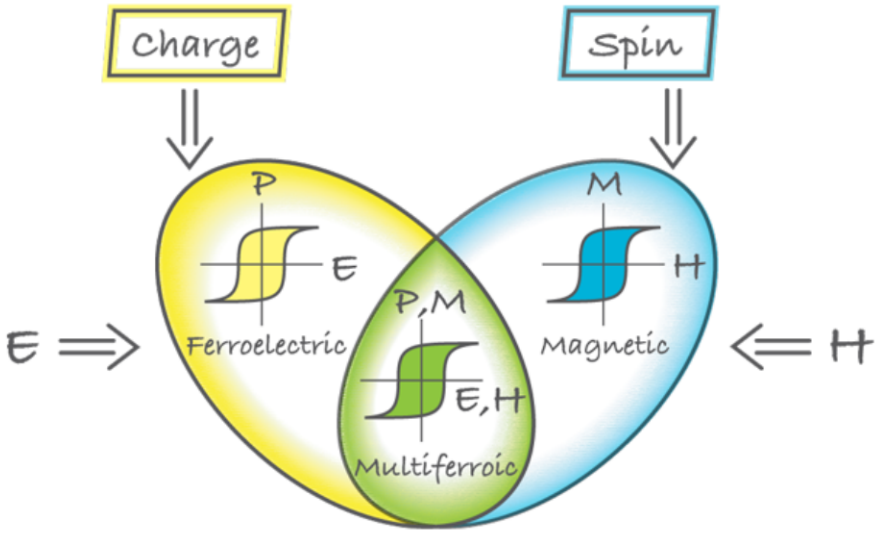

Figure B.1: Les multiferroïques magnétiques combinent à la fois l'ordre de rotation et de charge. Les matériaux ferroélectriques et ferromagnétiques présentent respectivement une polarisation hystérétique et une réponse de magnétisation à un champ électrique et magnétique. Dans le cas idéal, une interaction entre les degrés de liberté électroniques et magnétiques en multiferroïques permet d'avoir une réponse magnétique à un champ électrique et une réponse électronique à un champ magnétique [5].

examen attentif des mécanismes microscopiques de la multiferroicité. Dans la plupart des matériaux ferroélectriques, la polarisation en masse provient des déplacements atomiques de cations chargés positivement et de leur environnement anionique. En termes de liaison covalente, de tels décalages sont énergétiquement favorables lorsque la coque d du cation est vide. En revanche, les ordres magnétiques à longue portée proviennent d'interactions d'échange entre des électrons non appariés dans la coque d partiellement remplie dans le cas des ions de métaux de transition. Et voici le problème que ces deux exigences, lors du remplissage de la coque d, rendent le magnétisme et la ferroélectricité mutuellement exclusifs. Néanmoins, il existe d'autres mécanismes de polarisation qui permettent d'éviter cette limitation de d^0 par rapport à d^n. Essentiellement, il n'y a pas de mécanisme microscopique unique de ferroélectricité et de polarisation; il résulte d'une interaction entre la charge, l'ordre orbitale ou de spin et les distorsions structurelles.

Pour classer les multiferroïques magnétiques, il peut être pratique d'utiliser la classification proposée par Khomskii, qui consiste à diviser les matériaux multiferroïques en deux groupes: multiferroïques de type-I et de type-II [5]. Les multiferroïques de type-II sont constitués de ceux dans lesquels la ferroélectricité est induite par certains types particuliers d'arrangements de spin à longue portée, tandis que les types-I sont tous les autres. Les matériaux de type I présentent généralement de grandes valeurs de polarisation $\mathbf{P}$ et des températures de transition élevées, pour les transitions ferroélectriques et magnétiques, qui se situent souvent au-dessus de la température ambiante. Cependant les multiferroïques de type I possèdent un couplage magnétoélectrique plutôt hebdomadaire. Parmi les mécanismes multiferroïques de type I supportant la ferroélectricité, on peut trouver des phases mixtes de pérovskite, des aimants hébergeant des paires isolées, de la ferroélectricité géométrique et de l'ordre de charge.

Les multiferroïques du deuxième type sont souvent appelés multiferroïques d'origine

de spin en raison du fait que pour ces composés, l'ordre magnétique lui-même est une force motrice pour qu'une polarisation électrique se produise [61]. Ainsi, il est évident que les composés représentant ce type de multiferroicité possèdent un fort couplage entre les sous-systèmes magnétiques et électroniques, qui, à son tour, permettent une haute accordabilité de l'aimantation sous champ électrique appliqué ainsi qu'une stimulation magnétique provoquera un changement drastique de polarisation. Cependant, la polarisation montrée par les multiferroïques de type II est généralement faible par rapport aux valeurs indiquées par les composés du premier type. Une autre caractéristique des multiferroïques de type-II est les températures d'entraînement magnétique relativement basses. En effet, tous les matériaux de ce groupe sont des aimants frustrés: des arrangements de spin complexes, nécessaires à l'émergence de la polarisation, sont le résultat d'interactions magnétiques concurrentes, qui empêchent l'établissement d'un ordre à longue portée. à des températures élevées.

Pour ce qui concerne des mécanismes microscopiques de la ferroélectricité à commande magnétique, les multiferroques d'origine de spin peuvent être divisés en trois grands groupes. Le premier est caractérisé par des ordres magnétiques proportionnels les transportant pour provoquer un rétrécissement d'échange le long de directions cristallographiques particulières, le second est représenté par des aimants avec un type spécial de structures de spin incommensurables, tandis que le troisième utilise la géométrie de la configuration électronique des ions magnétiques et de leurs ligands . Quelle que soit la manière dont la polarisation électrique est générée, les trois groupes d'ordonnances magnétiques rompent la symétrie d'inversion spatiale.

Le mécanisme de striction d'échange exploite exclusivement l'interaction de Heisenberg et se déroule dans des aimants colinéaires ou presque colinéaires. Le point crucial pour la striction d'échange est la présence de cations magnétiques voisins de différentes valences qui pourraient subir une dimérisation à basse température. Le premier exemple pour illustrer ce phénomène est un aimant Ising quasi-unidimensionnel Ca_3CoMnO_6 [62, 63]. Un tel comportement pourrait également être trouvé dans les manganites orthorhombiques RMn_2O_5.

L'interaction Dzyaloshinskii-Moriya (DM) ou échange antisymétrique [68, 69, 70, 71] est un élément clé dans la compréhension de la ferroélectricité dans les aimants en spirale. Cette interaction apparaît comme la correction relativiste des interactions d'échange en présence d'un couplage spin-orbite. L'interaction DM, entraînée par les déplacements d'oxygène, s'est avérée jouer un rôle essentiel dans la stabilisation de l'ordre de spin incommensurable dans le multiferroïque $TbMnO_3$ pérovskite [72]. Ceci est souvent appelé un mécanisme DM inverse. Cependant, dans le cas de spins inclinés, une polarisation électrique peut survenir suite à une polarisation électronique. Ce mécanisme est souvent appelé modèle de courant de spin [73]. Et dans les deux cas, la polarisation électrique $\mathbf{P}$ est:

$$\mathbf{P} \propto \mathbf{e}_{ij} \times (\mathbf{S}_i \times \mathbf{S}_j) \tag{B.1}$$

où $\mathbf{e}_{ij}$ est le vecteur unitaire reliant le site i et le site j et $\mathbf{S}$ est l'opérateur de spin correspondant. On voit donc que quel que soit le mécanisme microscopique de la ferroélectricité, la direction de la polarisation électrique définie par les équations B.1 est universelle et inhérente à toute structure de spin modulée sans commune mesure. Pour résumer les scénarios possibles dans les modèles de DM inversé et de courant de spin, la figure B.2 illustre divers types de structures de spin incommensurables avec la polarisation électrique qu'elles génèrent. Evidemment, si le vecteur $\mathbf{e}_{ij}$ est parallèle au produit croisé des opérateurs de spin aux sites i-iem et j-iem, la polarisation résultante induite par ces

mécanismes est nulle.

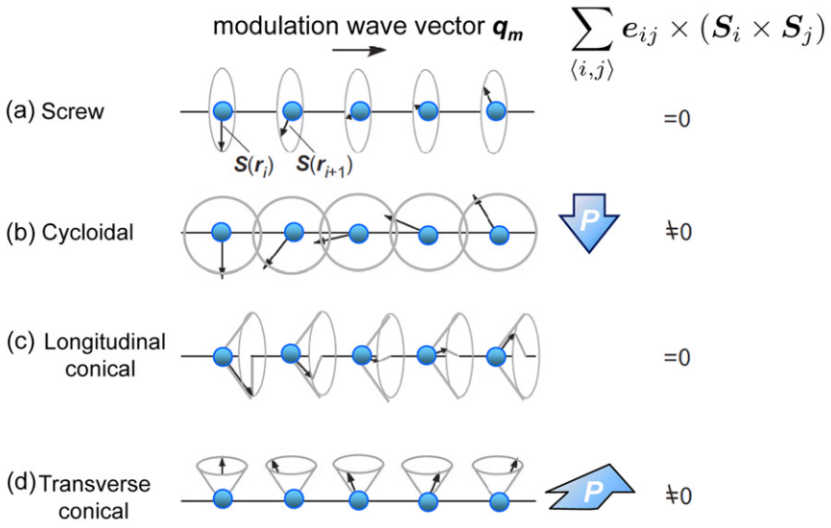

Figure B.2: Plusieurs types de structures magnétiques modulées avec la polarisation électrique correspondante qu'elles génèrent via des mécanismes inverses de Dzyaloshinskii-Moriya ou de courant de spin [61].

Concernant les exemples d'aimants spiralés présentant des propriétés multiferroïques, on peut prendre comme exemple les manganites de type pérovskite $RMnO_3$ (R = Tb, Dy, $Eu_{1-x}Y_x$) comme exemple: état de base magnétique de cette famille est souvent décrite avec un ordre de spin cycloïdal. Ces dernières années, des études approfondies ont conduit à la découverte de nombreux composés différents possédant des structures hélimagnétiques incommensurables induisant une polarisation électrique où la frustration magnétique est la principale cause de stabilisation de ces structures de spin. Parmi les exemples, il peut y avoir des composés avec des structures nucléaires centrosymétriques comme $Ni_3V_2O_8$ ($Cmca$) [75, 83] et $MnWO_4$ ($P2/c$) [84, 85]. Il convient également de souligner le fait que même si certaines structures magnétiques modulées ne produisent pas naturellement de polarisation électrique dans le courant de spin ou les modèles DM inverses, elles peuvent être manipulées de manière externe avec le champ magnétique pour le faire comme il a été trouvé dans $Ba_2Mg_2Fe_{12}O_{22}$.

L'interaction spin-orbite peut également produire un dipôle électrique entre les orbitales d d'un ion de métal de transition et les orbitales p d'un ligand. Considérant l'environnement local, pour chaque ion de métal de transition P^{orb} peut être exprimé sous la forme de [96]:

$$\mathbf{P} = \sum_i (\mathbf{S} \cdot \mathbf{e}_i)^2 \mathbf{e}_i, \tag{B.2}$$

où la somme est prise sur toutes les liaisons et le $\mathbf{e}$ est le vecteur du cation du métal de transition et des anions ligand. Le mécanisme décrit avec l'équation B.2 est appelé hybridation p-d dépendante du spin. La principale différence entre l'hybridation p-d et le mécanisme de striction d'échange ou de courant de spin / DM inverse décrit précédemment est que pour les deux derniers sites magnétiques sont nécessaires alors que le mécanisme d'hybridation p-d produit une polarisation électrique avec un seul site magnétique. Ce modèle décrit bien le comportement multiferroïque de composés avec un réseau triangulaire et des structures de rotation de vis appropriées. Cela peut être trouvé dans deux types de structures triangulaires typiques: delafossite [97] et CdI_2 [101, 102].

Dans tous les systèmes de modèles magnétiques, les composés spinelles $(A)[B_2]X_4$ sont l'une des familles les plus polyvalentes possédant une pléthore extraordinaire de phénomènes magnétiques, y compris le multiferroisme [116]. Une large multitude d'états fondamentaux magnétiques apparaît avec une variabilité chimique de ces systèmes: les sites A et B sont occupés par des cations de métaux de transition de valences différentes et X est l'oxygène ou les chalcogènes (soufre, sélénium, tellure). Le spinelle minéral $MgAl_2O_4$ a une structure $Fd\bar{3}m$ cubique de paramètre $a = 8.0625(7)$Å. Les atomes d'oxygène forment un réseau compact où les cations bivalents Mg^{2+} occupent les sites A (positions *8a*) correspondant aux sites tétraédriques $[MgO_4]$ et les cations trivalents Al^{3+}, occupent les sites B (positions cristallographiques *16d*) correspondant aux sites octaédriques $[AlO_6]$. Tous les octaèdres $[AlO_6]$ sont reliés par les arêtes et forment des couches de Kagome (Fig. **??**) qui sont normales à la direction <111> et où résident des cavités d'une section hexagonale appelée fenêtre de Kagome . Chaque fenêtre de Kagome est entourée de part et d'autre de deux tétraèdres $[MgO_4]$.

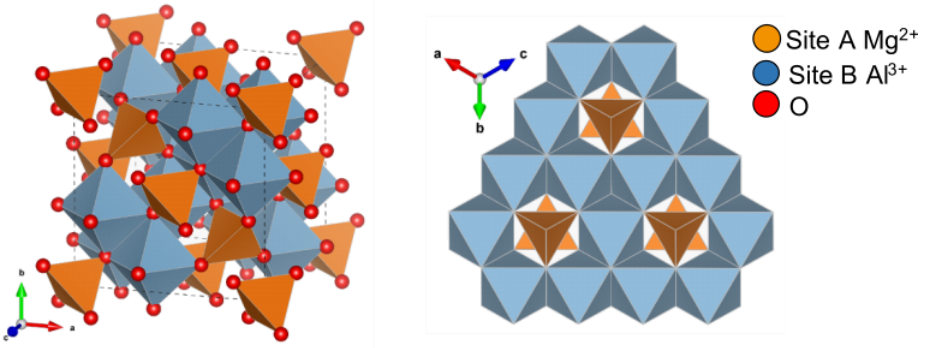

Figure B.3: À gauche: La structure cristalline du minéral spinelle d'origine, ce MgAl2O4. Les cations de magnésium mis en cage dans un environnement oxygène octaédrique tandis que les cations aluminium sont entourés de huit atomes d'oxygène qui forment un environnement octaédrique. A droite: la projection de la structure selon la direction [111] représentant l'arrangement polyèdre. Remarquablement, les octaèdres à partage de bord forment une couche Kagome.

Puisque les composés spinelles sont constitués de deux sous-structures, A et B, le hamiltonien magnétique le plus simple peut être écrit comme:

$$\hat{H} = \sum_{x,y=A,B} J_{x,y} \sum_{i,j} (\hat{S}_i \cdot \hat{S}_j), \tag{B.3}$$

où la première somme se réfère à la nature de l'interaction d'échange: inter- ou intra-sous-structure et la seconde est prise sur les paires de spins voisines dans la voie d'échange donnée. Ainsi, dans la plupart des cas concernant les composés spinelles, l'état fondamental magnétique est défini par l'interaction entre les interactions d'échange intra-sous-structure J_{AA} et J_{BB} et inter-sous-réseau J_{AB}.

Pour les interactions non négligeables J_{AA} et J_{BB}, des états fondamentaux exotiques peuvent être trouvés. La théorie LKDM (Lyon, Kaplan, Dwight, Menyuk) [140, 141, 142] qui considère les interactions d'échange de Heisenberg entre les cations voisins les plus proches que l'état fondamental des phases du spinelle cubique est entièrement décrit par un seul paramètre:

$$u = \frac{4\, J_{BB}\, |\mu_B|}{3\, J_{AB}\, |\mu_A|}, \tag{B.4}$$

où μ_A et μ_B sont des moments magnétiques de cations occupant respectivement les sites A - et B. Pour $u \leqslant 8/9$ la structure spin adopte la configuration Néel. Pour des valeurs plus grandes de u, il a été montré que la configuration de spin d'énergie la plus basse est ce que l'on appelle l'état de spirale de spin ferrimagnétique trouvé dans ce MnCr2O4 ($u = 1{,}5$). Il a deux transitions de phase magnétiques: à $43K$, les intensités de réflexion fondamentale montrent une forte amélioration indiquant une transition vers un état ferrimagnétique, et à T = 18K un ensemble de réflexions satellites apparaît, qui peut être décrit avec une conique ferrimagnétique. structure avec un accord satisfaisant [143].

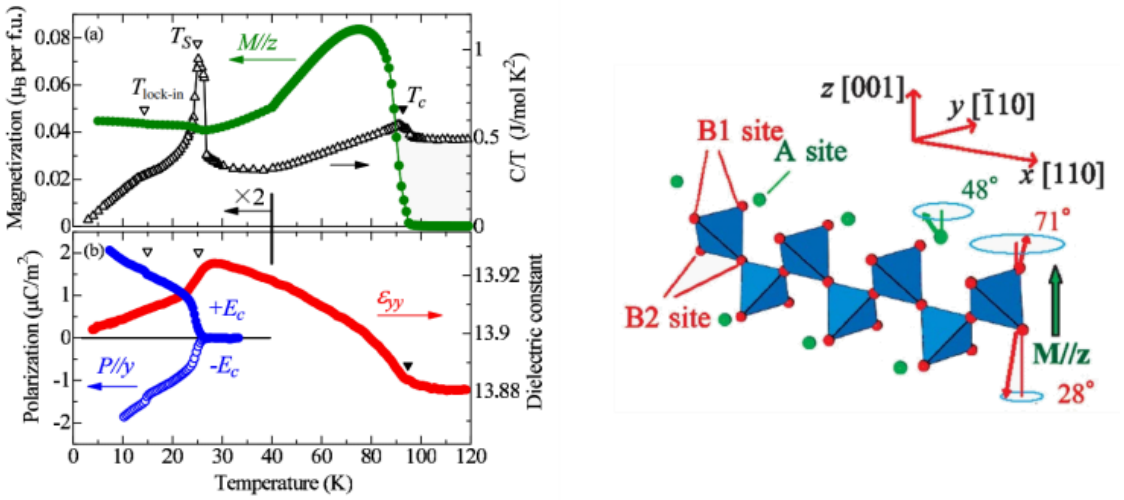

Figure B.4: À gauche: caractéristiques macroscopiques de $CoCr_2O_4$. Evolution de la température a) de l'aimantation **M** et de la chaleur spécifique divisée par la température (C / T), et b) de la constante diélectrique mesurée selon la direction y à une fréquence de 10 kHz et la polarisation électriquement induite selon l'axe $textity$ (|| [$Bar110$]). À droite: structure magnétique de $CoCr_2O_4$ [144].

Il existe un autre $CoCr_2O_4$ ($u = 2$), qui a des caractéristiques similaires. La variation de température de l'aimantation associée à la chaleur spécifique montre trois transitions distinctes à 93 K, 27 K et 13 K [144, 146]. Ces résultats sont en accord avec les mesures de diffraction sur poudre de neutrons [147]. qui révèlent un net gain d'intensité des réflexions nucléaires fondamentales en dessous de $T_C = 93K$ qui se produisent à la suite d'une transition de phase paramagnétique-ferrimagnétique (Fig. B.4). A $T_S = 27K$, le diagramme NPD montre l'émergence d'un ensemble de réflexions satellites résultant d'une phase magnétique incommensurable. La structure en spirale ferrimagnétique avec modulation de spin se propageant le long de la direction [110] et de l'axe du cône le long de la direction [001] prédite par la théorie LKDM a fourni un bon accord avec les observations expérimentales. Plus tard, ce résultat a été prouvé par une expérience de diffraction neutronique monocristalline qui a confirmé la présence du vecteur de propagation $\mathbf{k} = (\delta, \delta, 0)$ avec $\delta = 0{,}626 \pm 0.009$ à 8K [139]. La théorie LKDM prédit également que pour $u \geqslant 1.298$, les configurations en spirale ferrimagnétique à longue portée sont localement instables. Dans le cas de $CoCr_2O_4$ avec $u = 2$, cette instabilité provient d'une faible frustration magnétique géométrique (MGF) due à une magnitude égale des moments magnétiques aux sites tétraédrique et octaédrique provoque un ordre en spirale à courte portée qui se traduit par un comportement de type réentrant-spin-glass en dessous de $T_{lock-in} = 13K$.

Concernant le sous-système électronique $CoCr_2O_4$ montre également une image assez riche. Au refroidissement, la constante diélectrique atteint son maximum à T_S ce qui

coïncide avec une émergence de polarisation électrique. Remarquablement, il n'y a pas de transition de phase structurelle vers les températures plus basses et la structure nucléaire reste $Fd\bar{3}m$ de sorte que la centrosymétrie est localement rompue par l'ordre de spirale ferrimagnétique qui se traduit par la polarisation électrique le long de $[\bar{1}10]$ direction, qui est en accord avec le modèle de courant de spin. Par conséquent, $CoCr_2O_4$ est un composé multiferroïque de type-II. La polarisation électrique est hebdomadaire, cependant, la polarisation elle-même montre un comportement curieux sous des stimuli externes. Il a été montré que la grandeur et la direction de **P** dépendent fortement de la grandeur et du signe du champ magnétique appliqué le long de la direction [001]. De plus, **P** présente une inversion induite par champ complet signifiant un couplage magnétoélectrique robuste dans le système [144]. De plus, le signe de polarisation dans $CoCr_2O_4$ peut être modifié thermiquement: **P** flops brusquement de $2\mu C/m^2$ à $-2\mu C/m^2$ à $T_{lock-in}$ sans le changement de handness ou le **k** vector [148].

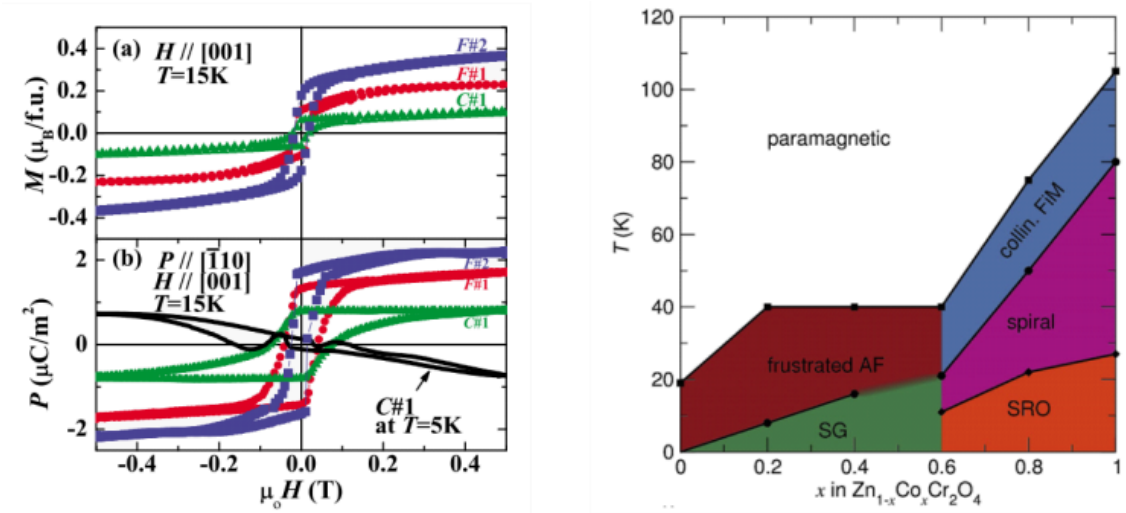

Figure B.5: À gauche: dépendance du champ magnétique de a) Magnétisation selon la direction [001] b) Polarisation selon la direction $[\bar{1}10]$ mesurée à T = 15 K pour $Co(Cr2-xCo_x)O_4$. C#1, F#1 et F#2 désignent respectivement x = 0,0, 0,14 et 0,18 [149]. A droite: diagramme de phase magnétique d'une famille $Zn_{1-x}Co_xCr_2O_4$. Les acronymes suivants signifient AF - antiferromagnétisme, FiM - ferrimagnétisme, SG - spin-glass, SRO - commande à courte portée [150]. .

En même temps, la polarisation dans $CoCr_2O_4$ peut être manipulée en interne, en faisant varier la composition chimique. Il a été démontré que le mélange de cations non magnétiques d^{10} dans le système A-sites conduit à une suppression de l'ordre de spin en spirale. L'introduction de Zn^{2+} modifie le magnétisme dans le système pour adopter un comportement antiferromagnétique frustré qui ne donne pas lieu à une polarisation électrique (B.5) [150]. Au contraire, une dilution magnétique sur le site B peut conduire à l'effet inverse. Les cations Co^{3+} magnétiquement inactifs au sous-réseau Cr^{3+} sont susceptibles de réduire la polarisation négative et la contribution de magnétisation des cations au site B. Cela améliore à la fois la polarisation électrique saturée et la magnétisation de champ appliquée avec une augmentation de la quantité d'agent magnéto-diluant [149].

On peut ainsi formuler une recette potentielle pour un composé multiferroïque de type II qui peut posséder des propriétés ferroélectriques intrigantes. Premièrement, il faudrait un spinelle cubique contenant des cations magnétiques de mêmes magnitudes ou proches de moments magnétiques aux sites A - et B - pour stabiliser une structure

spirale ferrimagnétique à longue portée. Deuxièmement, il doit y avoir de la place pour une dilution magnétique du site B qui peut potentiellement augmenter les performances ferroélectriques du système.

Parmi les composés spinelles, Kasper a rapporté en 1967 la synthèse de phases Co_5TeO_8, $CoZn_4TeO_8$ et $NiZn_4TeO_8$ avec superstructure cubique primitive [151]. Aucune des structures nucléaires n'a été publiée mais on a supposé que les cations Te^{6+} ne pouvaient occuper que des sites octaédriques avec la formule suivante $[(Co_2)[Co_3Te]O_8$. Puisque Co^{2+} et Te^{6+} ont des valences et des tailles différentes, il est possible d'obtenir des couches de Kagome ordonnées (Fig. B.3) avec Te^{6+} et Co^{2+} tous deux dans un environnement octaédrique mais occupant deux sites cristallographiques différents. Plus tard, Rodriguez-Carvajal a publié une première étude sur la diffraction neuronale de Co_5TeO_8 [152]. Il rapporte la présence d'une première transition en dessous de 60 K avec une forte diffusion diffuse qui se développe autour de la réflexion (111). Puis à plus basse température, la diffusion diffuse se condense en réflexions satellites correspondant à une structure magnétique incommensurable avec un vecteur de propagation $\mathbf{k} = (0, 0, \delta)$ avec $\delta = 0,08$ à 30 K Lors du refroidissement, δ devient plus petit et la longueur de corrélation augmente (accentuation de la réflexion). En dessous de 4,2 K, l'état fondamental magnétique se rapproche d'un état ferrimagnétique conventionnel. Ainsi, il apparaît que le comportement magnétique de Co_5TeO_8 ressemble à celui de la phase spinelle $CoCr_2O_4$. Comme aucune mesure magnétique et aucune structure nucléaire ou magnétique de Co_5TeO_8 n'ont été publiées, nous avons décidé de réexaminer ce composé et la série $Co_{5-x}Zn_xTeO_8$, qui sont de sérieux candidats. aux matériaux multiferroïques de type-II.

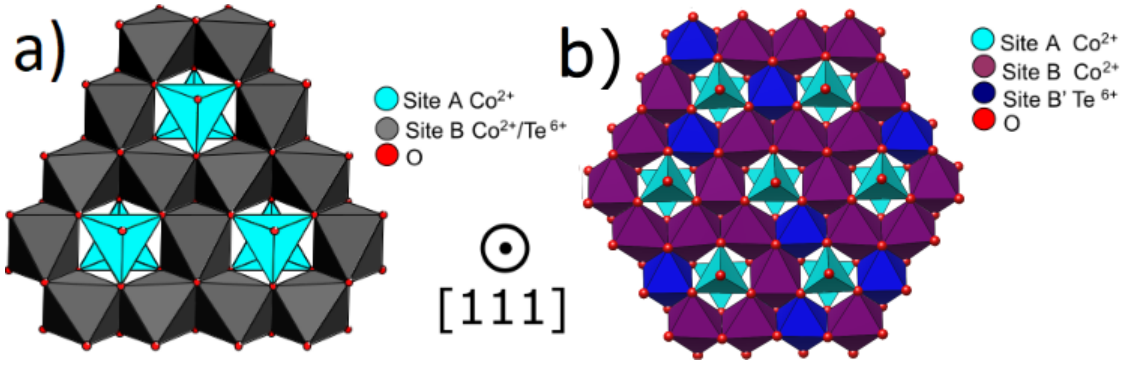

Figure B.6: Kagome couches de a) le polymorphe ordonné et b) désordonné de Co_5TeO_8

Tous les échantillons étudiés de la famille des Co_5TeO_8 et $Co_{5-x}Zn_xTeO_8$ purs sont disponibles uniquement sous forme de poudre et ont été préparés par la méthode des réactions à l'état solide. Il existe deux routines de synthèse pour préparer le composé Co_5TeO_8 pur. La première consiste à préparer un mélange stoechiométrique de $Co(OH)_2$ et de TeO_3 avec un rapport de 5 à 1 chauffé à 750^o. Une autre façon est de mélanger $Co(OH)_2$ avec $Te(OH)_6$ avec un rapport de 5:1:1. Un léger excès de $Te(OH)_6$ est nécessaire pour éviter une oxydation inutile de Co due à une tendance de Te à se volatiliser à des températures élevées. Ces précurseurs sont chauffés à 940^oC pendant 20 heures sous flux d'azote après que l'échantillon est lentement refroidi à la température en 24 heures. Pour étudier le comportement magnétique du système lors de la dilution magnétique, une série d'échantillons de poudre ce $Co_{5-x}Zn_xTeO8avec\ 0 \leqslant x \leqslant 1$ ont été synthétisés. Pour cela, $Co(OH)_2$, ZnO, $Te(OH)_6$ avec le rapport respectif de 5-x:1:1,1. Les précurseurs ont été chauffés à 740^oC pendant 20 heures sous un flux constant d'azote gazeux.

Le raffinement par Rietveld des données NPD enregistrées avec le diffractomètre 3T2

(LLB, Saclay) sur l'échantillon préparé avec la première routine a révélé que la structure nucléaire était $Fd\bar{3}m$ (#227) groupe d'espaces avec le paramètre de cellule unitaire $a = 8.5572(2)$Å. Le modèle utilisé pour le raffinement suppose une occupation mixte de Co^{2+} et de Te^{6+} au site octaédrique ($16d$) avec un rapport de 0,75/0,25 respectivement. Aucun écart significatif par rapport au nominal de 0,75/0,25 pour le rapport Co/Te n'a été observé. Puisque la distribution cationique au site B est aléatoire, plus tard dans le texte, ce polymorphe sera appelé le désordonné Co_5TeO_8.

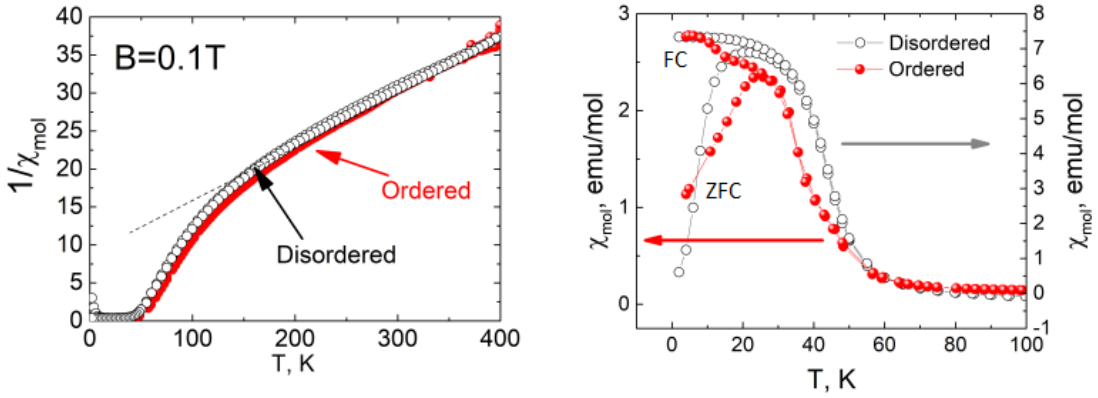

Figure B.7: Évolution de la température de la susceptibilité DC magnétique inverse (à gauche) et de la susceptibilité DC magnétique (à droite) mesurée à B = 0,01 T.

Des études combinées de diffraction des rayons X (XRPD) et de diffraction de poudre de neutrons (NPD) à température ambiante ont révélé que l'échantillon préparé avec la deuxième routine est exempt d'impuretés. En plus des principaux pics spinelles, les modèles XRPD et NPD montrent l'existence de réflexions supplémentaires à des angles de 2 θ bas typiques des phases spinelles ordonnées [190]. Ces motifs ont été indexés et affinés avec le groupe d'espace non centrosymétrique $P4_332$ (#212) avec le paramètre de cellule unitaire $a = 8.5531(1)$Å. Dans cette structure, le site B correspond à deux sites cristallographiques avec des positions Wyckoff 4 milliards et $12d$. Pour le modèle initial, nous avons supposé que les positions $4b$ et $12d$ étaient entièrement occupées par Te^{6+} et Co^{2+} respectivement. Le raffinement de Rietveld ne montre aucun désordre entre les sites $4b$ et $12d$, donc cet arrangement cationique particulier ainsi que le polymorphe adoptant cette structure sera appelé le Co_5TeO_8 ordonné plus tard. La comparaison entre les couches de Kagome des polymorphes désordonnés et ordonnés est donnée dans la figure B.6. Dans la structure ordonnée Co_5TeO_8, deux types de sites octaédriques sont identifiés: B et B '. Les cavités hexagonales trouvées dans les couches de Kagome sont alternativement entourées de trois octaèdres B et de trois octaèdres B ', puis de cinq octaèdres B et d'un octaèdre B'. De même, la structure spinelle originale, deux tétraèdres hors du plan de Kagome correspondant au site A sont adjacents aux cavités hexagonales.

Le comportement magnétique des deux polymorphes a d'abord été caractérisé par des mesures de susceptibilité magnétique à basse température. En comparant les deux courbes $1/\chi$ en fonction de la température et malgré les différences structurelles, les deux échantillons semblent présenter un comportement assez similaire: parties paramagnétiques haute température de $\chi(T)$ pour la correspondance ordonnée et Désordonné Co_5TeO_8 et bien suivant un comportement de Curie-Weiss et un ajustement linéaire d'une susceptibilité inverse dans les deux cas donne les mêmes résultats: $\mu_{eff} = 10,6\mu_B$ par unité de formule, soit 4,7 μ_B per Co^{2+}, et une température de Weiss fortement négative $\Theta = -130K$ révélant

la prédominance des interactions antiferromagnétiques (Fig. B.7).

Pour une caractérisation plus précise des transitions magnétiques apparues sur les courbes de susceptibilité DC, les susceptibilités magnétiques AC ont été mesurées sur le polymorphe ordonné. La courbe $\chi'(T)$ montre deux maxima distincts à 40 K et 27 K indiquant la présence possible de deux transitions de phase magnétiques dans le composé. La composante imaginaire de la susceptibilité magnétique $\chi(T)$, représentant les processus dissipatifs, est assez petite, cependant elle coïncide avec la forme du $\chi'(T)$, ce qui est cohérent avec la présence de deux magnétiques transitions consécutives à 40 et 27 K à B = 0,01 T pour le Co_5TeO_8 ordonné. Enfin, les mesures de susceptibilité AC dépendant du champ ont permis de fournir des informations initiales sur le diagramme de phase magnétique $B(T)$ des deux polymorphes. Le Co_5TeO_8 désordonné présente une seule transition de phase magnétique jusqu'à B = 0,2 T. Le polymorphe ordonné, à son tour, montre deux domaines magnétiques ordonnés différents nommés FM/FI-1 et FM/FI-2. Le premier domaine n'existe qu'entre 38 et 27 K et est éliminé en appliquant un champ magnétique B = 0,08 T (Fig. B.8).

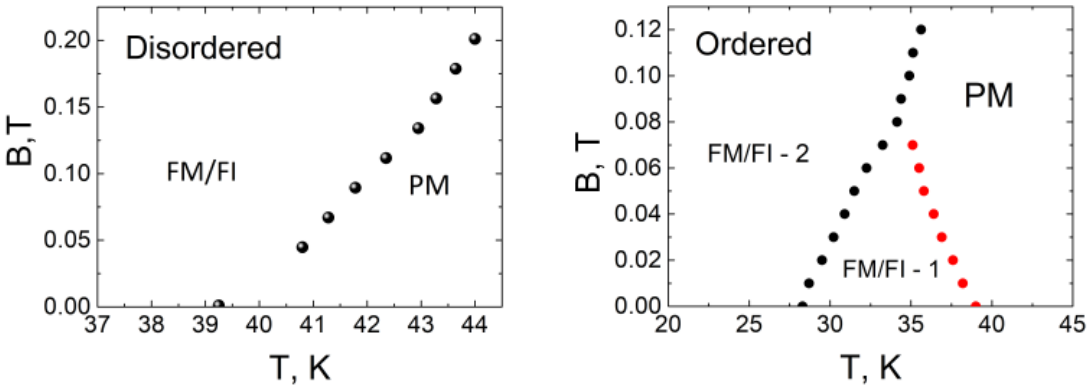

Figure B.8: Diagrammes de phase magnétiques pour les polymorphes désordonnés (à gauche) et ordonnés (à droite) Co_5TeO_8. PM signifie paramagnétique, FM - ferromagnétique, FI - ferrimagnétique.

Considérons d'abord la structure magnétique du désordonné Co_5TeO_8. L'évolution de la température des diagrammes NPD, obtenue avec un diffractomètre G4-1, montre deux caractéristiques importantes: d'une part, une amélioration significative du fond aux faibles angles de diffraction apparaissant en dessous de 195 K, suivie d'une forte augmentation de (111) et (220) intensité des pics de diffraction inférieurs à 40 K. Le développement de la diffusion diffuse à haute température correspond à l'émergence d'amas magnétiques ordonnés à courte distance comme précédemment observé dans divers spinelles magnétiques. Diffraction sur poudre neutronique (NPD) ne montrant aucune réflexion de Bragg supplémentaire en dessous de $T_N = 40K$, mais seulement l'augmentation de l'intensité de certains pics nucléaires, la cellule unitaire magnétique correspond à la cellule nucléaire et la propagation vectorielle de la structure magnétique est donc $\mathbf{k} = 0$. Le raffinement de Rietveld a révélé qu'un seul groupe d'espace magnétique, tétragonal $I4_1/am'd'$ (#144.557), fournit un modèle qui correspond aux modèles NPD avec un accord acceptable. La structure magnétique des désordres Co_5TeO_8 à T = 1,7 K s'est avérée être ferrimagnétique colinéaire avec des magnitudes de moments magnétiques pour les cations $Co\uparrow_2^+$ aux sites tétraédriques et octaédriques de $\mu_{Co1} = -1,96(6)\mu_B$ et $\mu_{Co2} = 2,39(7)\mu_B$ respectivement. La structure magnétique et l'évolution des moments magnétiques en fonction de la température sont présentées dans la figure **??**. Valeur réduite des moments magnétiques

(moment magnétique de spin seul $\mu = 3.88\mu_B$ pour Co^{2+} à un état de spin élevé) sur les deux sites ainsi que la présence de la diffusion diffuse magnétique à faible La température indique que le sous-système magnétique n'est pas parfaitement ordonné même à basse température. Les explications d'un tel comportement pourraient être les suivantes: la distribution aléatoire des cations non magnétiques Te^{6+} sur les sites B rompt la régularité dans les voies d'échange J_{AB} et J_{BB} , ce qui, à son tour, empêche le système de terminer la commande. Les clusters ordonnés à courte portée, responsables de la diffusion diffuse magnétique, devraient cependant avoir des corrélations magnétiques ressemblant à celles de la structure ferrimagnétique de l'état ordonné à longue portée, puisque le halo magnétique diffus est centré autour du pic de Bragg (111) .

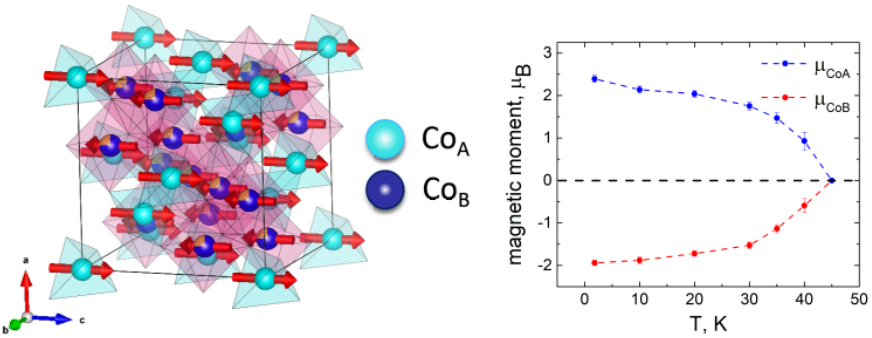

Figure B.9: La structure magnétique à T = 1,7 K (à gauche) et l'évolution de la grandeur des moments magnétiques en fonction de la température du polymorphe désordonné Co_5TeO_8.

Le comportement du Co_5TeO_8 ordonné est assez complexe. Comme observé pour le polymorphe désordonné, la diffusion magnétique diffuse est centrée autour du pic de Bragg fondamental (111), elle émerge en dessous de 200 K et son intensité augmente jusqu'à 50 K. Cette caractéristique souligne une apparition de courtes corrélations magnétiques. portée. A $T_{C1} = 45$ K, les réflexions satellites apparaissent sur les modèles NPD. Les plus nettes sont situées de chaque côté des réflexions fondamentales (hhh) et $(hh0)$. Ces réflexions satellites sont indexées avec un vecteur de propagation $\mathbf{k} = (0, 0, \gamma)$ avec $\gamma = 0.126$ à T_{C1}. Par conséquent, l'ordre magnétique à longue portée qui s'installe correspond à une structure magnétique incommensurable. À $T_{C2} = 27$ K, des changements substantiels ont lieu dans les modèles NPD. Les satellites magnétiques s'éloignent brusquement des réflexions fondamentales, acquérant la position correspondant à $\mathbf{k}_z \approx 0,14$ qui restent stables jusqu'à 1,7 K. Un changement de la valeur du vecteur de propagation se produit. produit simultanément avec l'augmentation de l'intensité de la réflexion principale de (111) et la diminution de l'intensité des réflexions du satellite. Ce comportement ressemble au cas du spinelle $CoCr_2O_4$, ce qui implique qu'en dessous de T_{C2} deux composantes magnétiques, une coexistence incommensurablement modulée et ferrimagnétique. De plus, en dessous de T_{C2}, aucune diffusion diffuse n'est plus observée, ce qui signifie que les domaines magnétiques à longue portée sont complètement ordonnés (Fig. B.10).

La structure magnétique incommensurable du Co_5TeO_8 ordonné a été résolue, en utilisant le modèle NPD collecté à 30 K, car les réflexions des satellites sont plus prononcées à ces températures. Des contraintes de symétrie possibles ont été déduites de la recherche de recuit simulé qui a abouti à une structure de spin en spirale ferrimagnétique avec des moments magnétiques de Co_1 et Co_2 couplés antiferromagnétiquement le long de l'axe c. Des groupes d'espace magnétique possibles ont été recherchés à l'aide de l'outil ISODISTORT [200, 201] qui a fourni 72 modèles de groupes de superespaces magnétiques possibles. Tous ces modèles obtenus avec ISODISTORT ont ensuite été testés avec une recherche de recuit

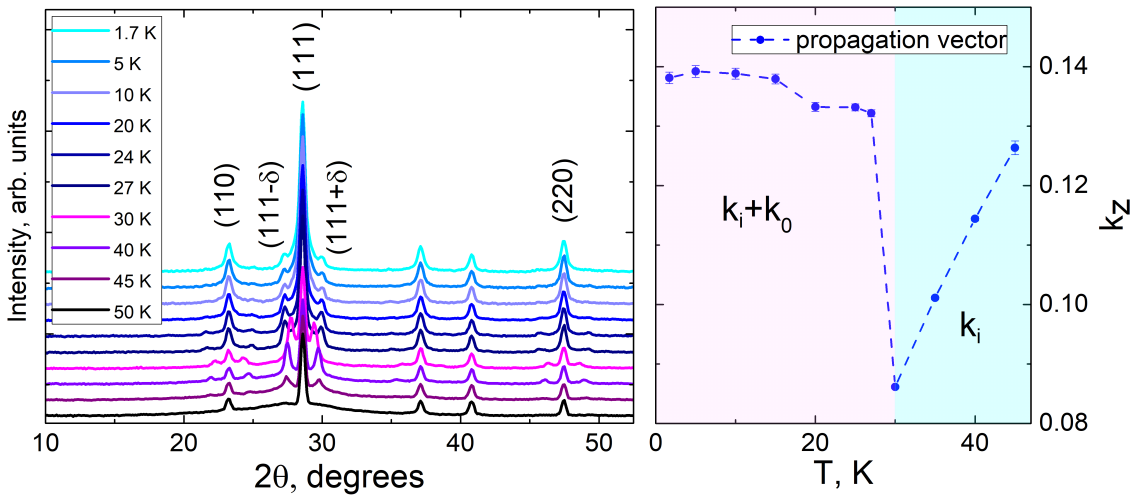

Figure B.10: Evolution en fonction de la température de la partie bas-angle des profils NPD (gauche) et de la composante $\mathbf{k}_z$ du vecteur de propagation (droite) du polymorphe ordonné Co_5TeO_8.

simulée utilisant le formalisme du superspace en coordonnées sphériques implémenté en FullPfor (jbt = -7). Les meilleurs facteurs d'accord ont été trouvés pour le groupe de superspace magnétique $P4_3(00\gamma)0$ (#78.1.19.1.m19.1). Le raffinement de Rietveld utilisant le modèle obtenu a révélé que la structure magnétique du ch Co5TeO8 ordonné est décrite avec $P4_3(00\ gamma)0$ groupe de superespaces magnétiques dans les deux ($T_{C1} < T < T_{C2}$) et régions de températures basses ($T_{C2} < T < 1,7K$).

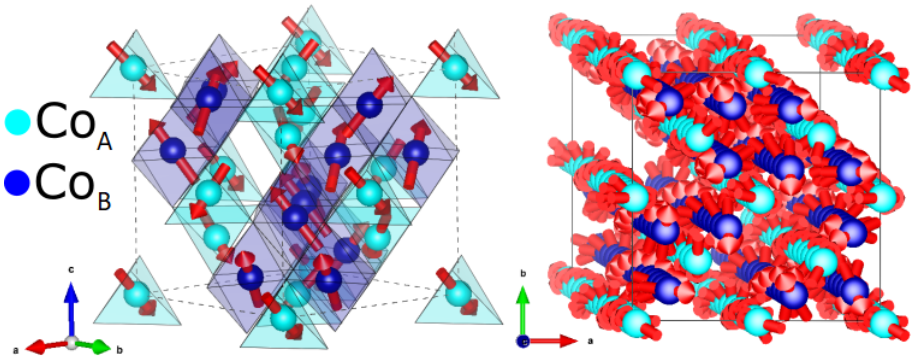

Figure B.11: Variation de température du moment magnétique (à gauche) et de l'angle du cône (à droite) du polymorphe ordonné Co_5TeO_8.

La structure magnétique elle-même est représentée par l'arrangement de spin conique avec des moments magnétiques Co^{2+} aux sites tétraédriques et octaédriques couplés de manière antiferromagnétique le long de l'axe cristallographique c sur toute la plage de températures où l'ordre à longue distance existe. Les moments magnétiques des spins de site A et B atteignent également une saturation inférieure à T_{C2} avec $\mu_{Co1} = 2,68(7)\mu_B$ et $\mu_{Co2} = 3,36(7)\mu_B$ à 1,7 K. De grandes valeurs non nulles des moments magnétiques aux sites tétraédriques et octaédriques à T_{C1} indiquent qu'au-dessus de 45 K, le système n'est pas purement paramagnétique mais contient des domaines ordonnés à courte portée. Finalement, on peut penser à la structure magnétique du polymorphe ordonné comme le

ferrimagnet avec une distorsion modulée perpendiculaire à l'axe c (Fig. B.11).

L'influence de la dilution magnétique du site A a d'abord été étudiée par la technique de magnétométrie SQUID. L'évolution de la température de la susceptibilité magnétique a révélé que lors de l'augmentation du contenu de Zn^{2+} dans $Co_{5-x}Zn_xTeO_8$, le système présente une diminution de la réponse magnétique associée à un déplacement des maxima $\chi(T)$ vers des températures plus basses. Cependant, même une grande dilution magnétique dans le cas de x = 1, où le site $8c$ est occupé par le cation non magnétique, n'élimine pas entièrement le signal magnétique. Les profils NPD de la famille $Co_{5-x}Zn_xTeO_8$ confirment le comportement correspondant (Fig. B.12). Tout d'abord, il faut dire qu'en plus du composé d'origine, Co_5TeO_8, les échantillons dilués avec Zn^{2+} montrent une nette émergence d'une diffusion magnétique diffuse centrée sur la réflexion (111) à relativement hautes températures. Lors du refroidissement, tous les échantillons étudiés à l'exception de celui avec x = 1.01, subissent une transition de contrôle longue portée qui n'est pas en commun avec le vecteur de propagation $\mathbf{k} = (0, 0, \gamma)$. Nous avons trouvé que la structure magnétique de la famille $Co_{5-x}Zn_xTeO_8$ est décrite avec le même groupe de superspace $P4_3(00\gamma)$ (#78.1.19.1.m19.1) sur toute la plage x où la commande longue distance est observée. On a trouvé que la dilution magnétique du site A conduit à un affaiblissement du couplage antiferromagnétique le long de l'axe c.

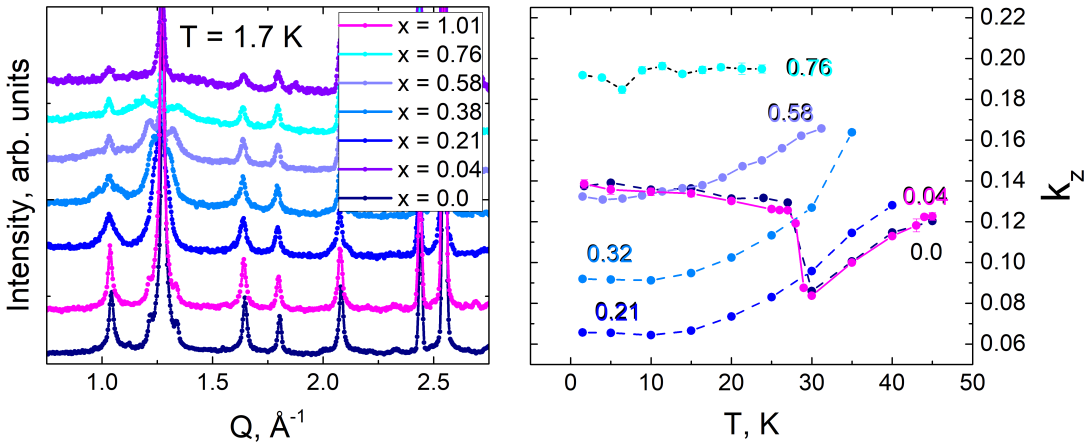

Figure B.12: Profils NPD à T = 1,7 K (à gauche) et l'évolution de la température de la composante $\mathbf{k}_z$ du vecteur de propagation (à droite) de la famille $Co_{5-x}Zn_xTeO_8$ ($0 \leq x \leq 1.01$).

Finalement, le diagramme de phase magnétique de la famille $Co_{5-x}Zn_xTeO_8$ avec $0 \leq x \leq 1.01$ est illustré sur la figure B.13. D'après les données NPD, il s'ensuit qu'il existe une région étroite de concentration de Zn^{2+} où la transition de phase ayant lieu à T_{C2} est préservée, de sorte que la phase modulée presque colinéaire dans le système nécessite un haut niveau de régularité de l'arrangement cationique.

Pour une analyse plus approfondie de l'ordre magnétique dans la famille $Co_{5-x}Zn_xTeO_8$, des expériences de diffusion de neutrons aux petits angles (SANS) ont été réalisées pour le polymorphe ordonné de Co_5TeO_8 et $Co_4Zn_1TeO_8$ avec l'utilisation du diffractomètre petit angle D33. Considérons d'abord le SANS de champ nul du composé ordonné Co_5TeO_8. Au-dessus de T_{C1} SANS, les profils montrent un signal lisse et sans relief, cependant dès que la température descend à T_{C1} un anneau homogène correspondant à (00δ) pic de Bragg de la structure en spirale ferrimagnétique est observé (Fig. B.14). L'évolution de la température du vecteur $\mathbf{Q}$ - de la réflexion magnétique observée suit la même tendance que la composante $\mathbf{k}_z$ du vecteur de propagation observé en NPD.

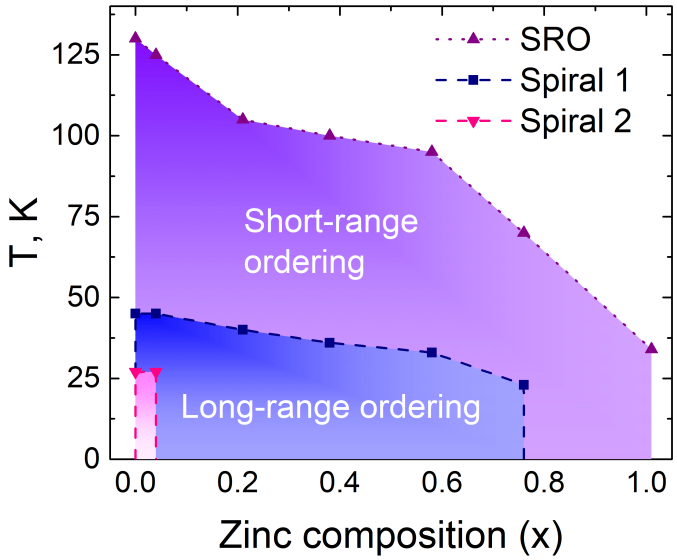

Figure B.13: Diagramme de phase magnétique de la famille $Co_{5-x}Zn_xTeO_8$.

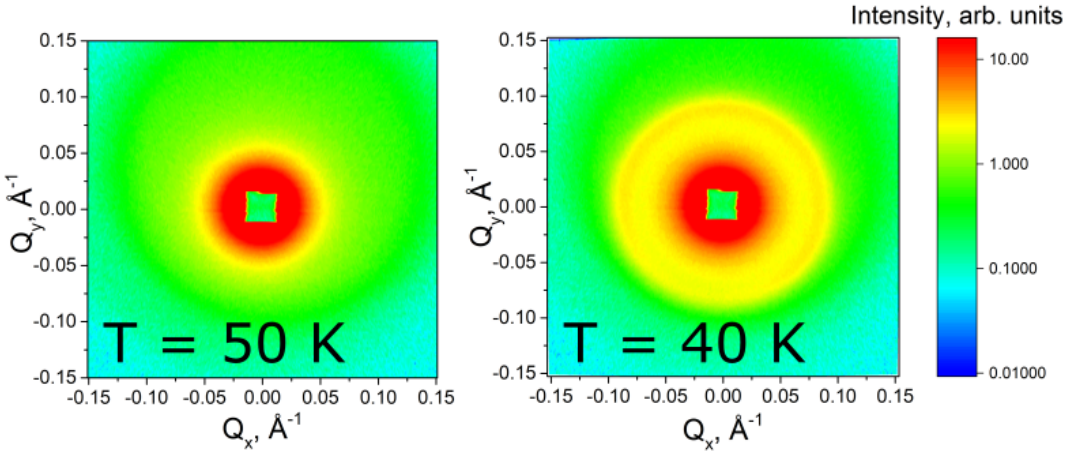

Figure B.14: La comparaison du profil SANS pour le Co_5TeO_8 ordonné à 50 K et 40 K.

Une caractéristique importante de tout motif SANS est la pente de sa partie basse - **Q**. qui est définie par la morphologie de l'échantillon. Si l'intensité de la diffusion aux petits angles est proportionnelle à Q^{-4}, un système présente un comportement dit de Porod. Image de diffusion typique causée par des systèmes non homogènes résultant de la diffusion sur les interfaces et, dans le cas des systèmes magnétiques, représente la diffusion sur les parois du domaine [204]. Comme le montre le graphique de droite de la figure **??**, lors du refroidissement, n diminue de $n \approx 3,59$ à T = 95 K à $n \approx 3,55$ à T = 46 K. En dessous de T_{C1} $n(T)$ subit une augmentation rapide, atteignant $n \approx 3,78$ à T = 5 K. Ainsi, en dessous de la température du contrôle longue portée, le Co_5TeO_8 ordonné commence à se développer une structure de domaine bien définie à basses températures, cependant la différence avec le comportement idéal de Porod indique la présence d'un léger degré de désordre magnétique dans le système.

Dans le cas d'un SANS magnétique, l'intensité varie avec le paramètre d'ordre et,

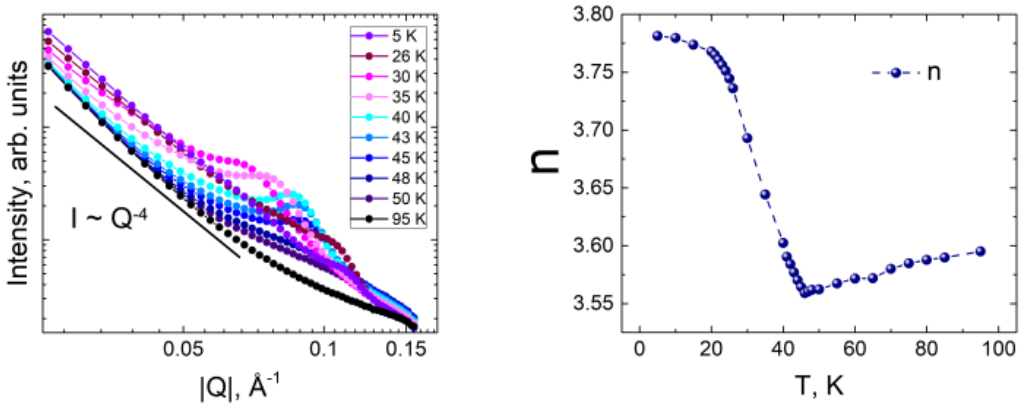

Figure B.15: Temperature evolution of the SANS intensity (left) and n from the equation 3.1 for the ordered Co_5TeO_8.

en fait, est proportionnelle au carré d'aimantation M^2 et la partie faible Q des motifs SANS contient des informations sur les corrélations magnétiques statiques. Il y a une augmentation du signal de dispersion en dessous de T_{C1} lorsque l'ordre magnétique à longue portée prend effet. Intensité à $|\mathbf{Q}| = 0.027\text{Å}^{-1}$ augmente progressivement et atteint sa saturation à basse température sans aucune particularité remarquable à $T_{C2} = 27K$. La partie Q élevée, à son tour, contient des contributions dues à des corrélations dynamiques. Dans le cas du Co_5TeO_8 ordonné, la dépendance à la température de la partie Q élevée du signal SANS démontre un comportement de diffusion critique associé à la transition d'ordre paramagnétique à longue portée vers le second ordre. L'intensité de diffusion supplémentaire à $T > T_{C1}$ se produit avec des corrélations de spin et atteint son maximum à la température de transition. Pour $T < T_{C1}$ l'intensité à $|\mathbf{Q}| = 0,125\text{Å}^{-1}$ est dû à la diffusion quasi-élastique des ondes de spin (Fig. B.16).

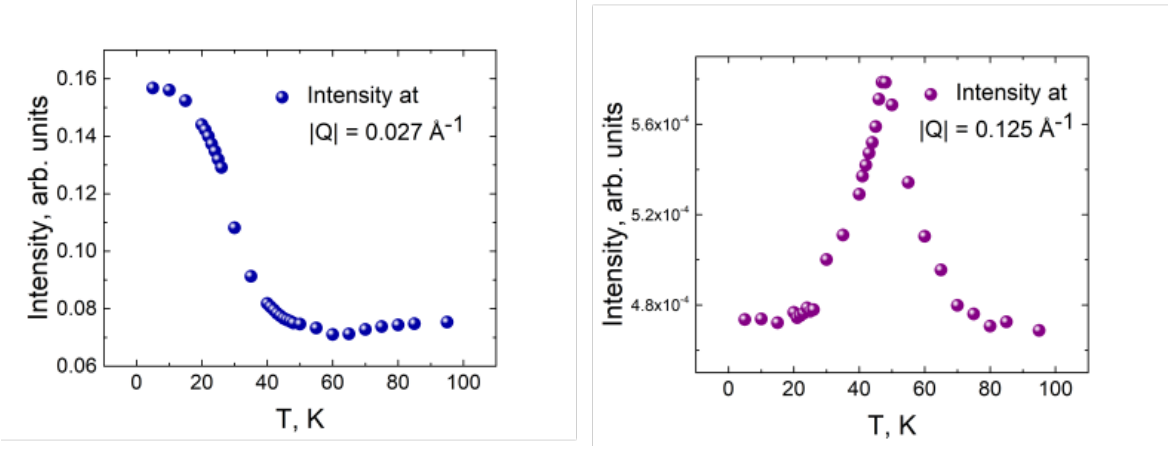

Figure B.16: Évolution de la température du Q bas ($|\mathbf{Q}| = 0,027\text{Å}^{-1}$) et du Q haut ($|\mathbf{Q}| = 0,125\text{Å}^{-1}$) Intensité SANS du Co_5TeO_8 ordonné.

L'application d'un champ magnétique au polymorphe ordonné ch Co5TeO8 révèle une structure multi-domaine à 32 K dans la région de champ entre B_{C1} = 0,06 T et B_{C2} = 0,09 T. Initialement, le $\mathbf{Q}$ -vector augmente progressivement jusqu'à $|\mathbf{Q}_1| \approx 0,072\text{Å}^{-1}$ à à H = 0,05 T. B_{C1} = 0,06 T deux pics en forme d'arc avec $|\mathbf{Q}_2| \approx 0.097\text{Å}^{-1}$ apparaissent sur les côtés gauche et droit par rapport au faisceau direct tandis que $\mathbf{Q}_1$ ring est encore

partiellement observé. Au-dessus de B_{C2} = 0,09 T auquel la fonction $\mathbf{Q}_1$ est entièrement supprimée (Fig. B.17). En dessous de B_{C1}, le polymorphe ordonné de Co_5TeO_8 est dans un état de domaine unique qui est stable aux champs bas. À B_{C1}, le système entre dans un état multidomaine induit par le champ qui est représenté par deux ensembles séparés de pics de diffraction sur les modèles SANS. Le champ critique B_{C1} fait subir à une partie des domaines magnétiques, co-alignés avec la direction du champ magnétique appliqué, une transition de phase magnétique caractérisée par une forte diminution de la périodicité de la modulation de spin. Dans le même temps, la partie des domaines magnétiques, suffisamment proche pour fournir la diffraction mais désalignée par rapport à la direction du champ, reste dans l'état Q_1, car elle nécessite un champ magnétique plus important pour induire la transition dans ce fraction de domaines. Enfin, à B_{C2}, la fonction low-Q Q_1 fusionne dans la fonction Q_2, ainsi le système entre dans un état de domaine unique induit par un champ.

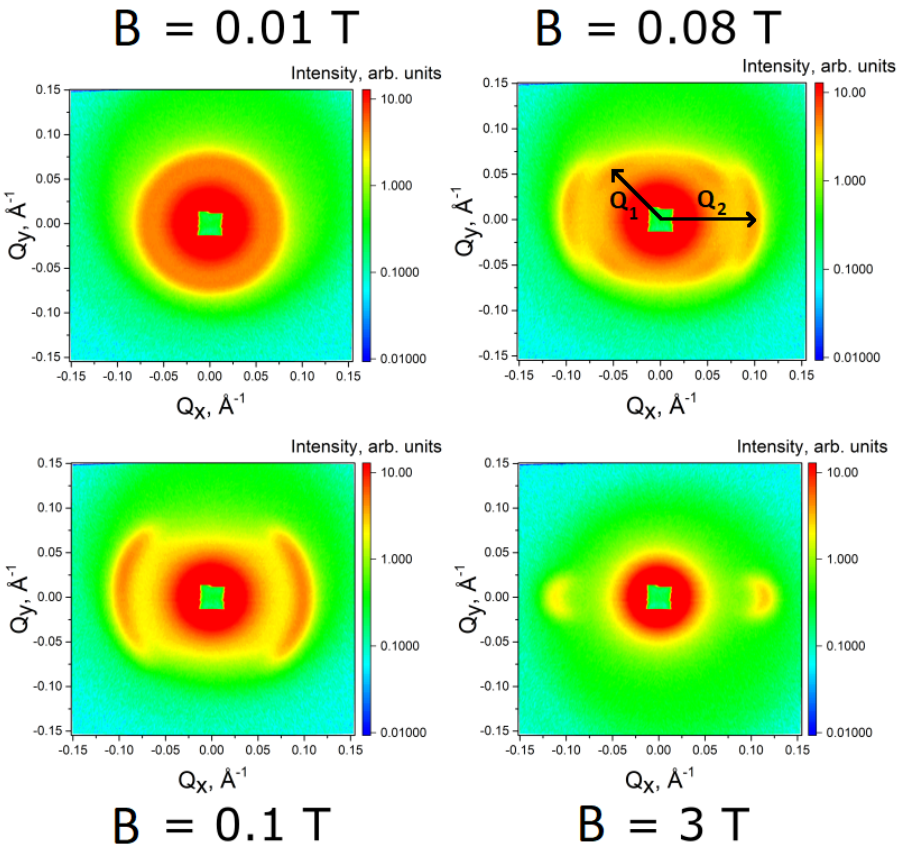

Figure B.17: Evolution des profils SANS pour le polymorphe ordonné Co_5TeO_8 sous champ magnétique appliqué à T = 32 K.

L'application d'un champ magnétique à 20 K et 36 K au Co_5TeO_8 ordonné ne supprime que l'état de spirale ferrimagnétique incommensurable en faveur d'un ferromagnet polarisé par champ.

Comme cela a été discuté ci-dessus, $Co_4Zn_1TeO_8$ ne possède aucun ordre à longue portée jusqu'à T = 1,7 K et les données de diffusion des neutrons aux petits angles sont en accord avec les mesures de NPD. Aucun pic de Bragg n'est observé à 2 K pour $Co_4Zn_1TeO_8$, à la place le motif SANS correspondant, illustré sur la figure B.18 (à gauche), présente une diffusion homogène, qui perd rapidement de l'intensité avec l'augmentation du transfert d'impulsion . Les courbes SANS de $Co_4Zn_1TeO_8$, obtenues avec la même procé-

dure de moyennage que celles de Co_5TeO_8, révèlent une légère amélioration d'intensité à $|Q| \approx 0,12$ Å avec une température décroissante. Ce comportement est provoqué par la formation de corrélations de spin à courte portée (Fig. B.18 droite). Pour étudier la réponse de $Co_4Zn_1TeO_8$ au champ magnétique appliqué, des motifs SANS à 2, 10 et 20 K ont été collectés avec H = 1, 4 et 7 T.Pour chaque température, le système ne montre aucun champ- transition de phase magnétique induite, de plus la diffusion diffuse magnétique observée autour de $|Q| \approx 0.12$ Å est supprimé lors de l'augmentation de H.

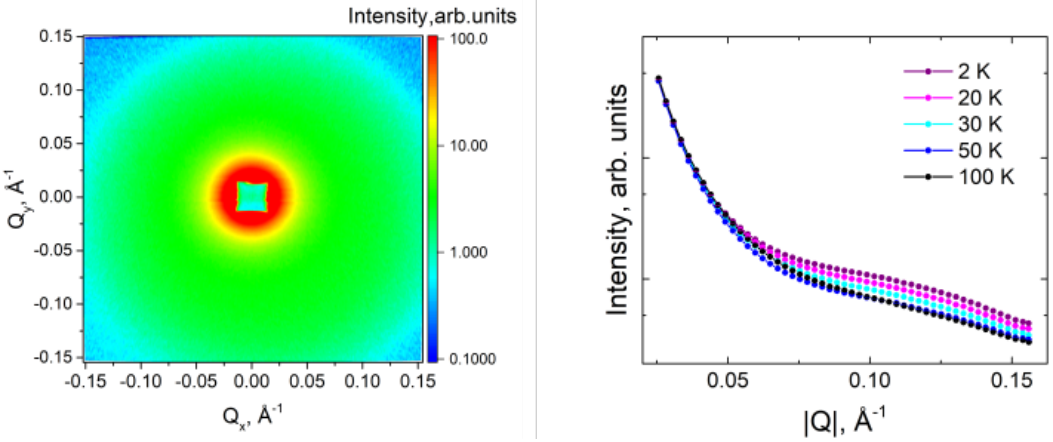

Figure B.18: Profil SANS collecté à 2 K (à gauche) et évolution de la température des courbes SANS (à droite) pour $Co_4Zn_1TeO_8$

Comme cela a été démontré par les expériences NPD et SANS et résumé dans le diagramme de phase (Fig. B.13), la famille spinelle $Co_{5-x}Zn_xTeO_8$ montre le contrôle de présence (SRO) dans une large plage de température pour 0 < x < 1,01. Une diffusion magnétique diffuse notable indique la tendance du système à former des corrélations de spin bien au-dessus des températures de transition d'ordre à longue distance.

Considérons d'abord le comportement de Co_5TeO_8 non dilué. L'analyse de polarisation Neutron XYZ pour ce composé a été réalisée dans une gamme de températures entre 50 K et 260 K. Pour des températures proches de T_{C1}, les diagrammes de diffusion magnétique diffuse montrent la présence de lignes distinctes correspondant aux positions de Bragg des réflexions nucléaires (111) et (220). Avec l'augmentation de la température, ces caractéristiques subissent une diminution significative de l'intensité avec une augmentation de la largeur, ce qui, à son tour, indique un raccourcissement des domaines ORS. La corrélation spin-spin radiale obtenue avec l'ajustement de Monte Carlo inverse (RMC) peut éclairer un arrangement de spin moyen dans un état paramagnétique. A T = 50 K, toutes les paires de spin, correspondant aux magnitudes positives de $< \mathbf{S}_i\mathbf{S}_j >$ sont des cations Co^{2+} partageant le même environnement oxygène (deux octaèdres ou deux tétraèdres) tandis que les valeurs négatives de $< \mathbf{S}_i\mathbf{S}_j >$ sont fournies par spins Co^{2+} à partir de différents sites: octaèdres et tétraèdres. Ainsi, le couplage antiferromagnétique entre les spins Co_1 et Co_2, observé par NPD est maintenu dans un état légèrement supérieur à T_{C1}, sans ordre longue distance. (Fig. B.19).

L'évolution de la température de la fonction $< \mathbf{S}_i\mathbf{S}_j >$ (Fig. B.19) montre que l'orientation relative du spin est conservée à T = 60 K. à T = 80 K: $< \mathbf{S}_i\mathbf{S}_j >$ pour $r = 6,732(1)$Å et $r = 6,862(2)$Å , correspondant aux paires Co_1 - Co_1, change le signe du positif au négatif; La fonction de corrélation spin-spin radiale pour les paires Co^{2+} à r plus grande prend des valeurs proches de zéro, donc les fluctuations thermiques sont suffisamment importantes pour briser les corrélations dans les cellules unitaires les plus

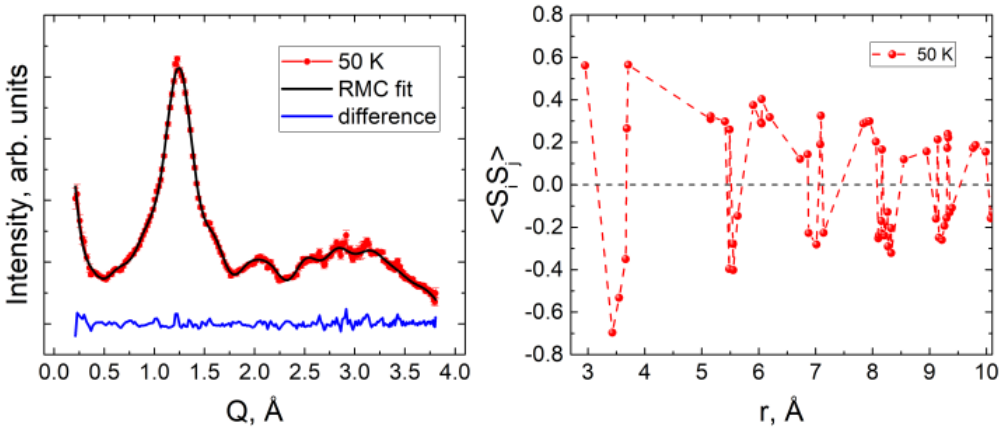

Figure B.19: Gauche: ajustement RMC du profil de diffusion magnétique diffuse du polymorphe ordonné ch Co5TeO8 à T = 50 K. Points rouges - données expérimentales, ligne noire - ajustement RMC, ligne bleue - courbe de différence. Droite: Fonction de corrélation spin-spin radiale calculée avec les résultats de l'ajustement RMC pour T = 50 K.

proches. Plus la température augmente, plus les corrélations de spin à courte portée sont supprimées. Cependant, même à T = 260 K dans les cations $r < 3.707(5)$Å Co2 + maintiennent les corrélations et les orientations relatives de leurs moments magnétiques observées à des températures plus basses. De plus, le profil de diffusion magnétique à T = 260 K montre toujours des caractéristiques distinctes, indiquant la présence de corrélations à courte portée à des températures bien supérieures à T_{C1}

Pour une analyse plus approfondie de la diffusion diffuse magnétique de ch Co5TeO8, les diagrammes de diffraction des neutrons monocristallins ont été calculés en utilisant le programme SPINDIFF distribué avec SPINVERT. Le calcul a été effectué pour un plan de réseau réciproque (hhl) avec des indices h et l compris entre -5 et 5; Premièrement, à des températures élevées, aucune distribution distincte de la diffusion diffuse n'est observée, toute l'intensité est distribuée de manière presque homogène sur le motif. A T = 200 K, des points proviennent de la diffusion diffuse magnétique, qui correspondent aux réflexions satellites **k** et **k**, typiques des structures spirales incommensurables, observées pour le Co_5TeO_8 ordonné par NPD. Les satellites les plus intenses forment des modèles quadruples autour des positions (hhh) ((111) et (222)) et $(hh0)$ ((220) et (440)), ce qui est cohérent avec l'observation NPD pour l'état ordonné. Diffuse scattering indicates a lack of coherence in the magnetic scattering. En approchant $_{C1}$, les principales caractéristiques se réduisent à des pics de Bragg bien définis et enfin, à T = 60 K, toute l'intensité neutronique restante est laissée à (111), (222) et (440) pics et leurs satellites. Enfin, en rassemblant les résultats de l'ajustement RMC dans l'espace direct et réciproque, nous pouvons conclure que l'ordre à courte portée dans le polymorphe ordonné Co_5TeO_8 a la même nature de spirale ferrimagnétique que l'arrangement du spin dans le phase ordonnée.

Comme discuté précédemment, la grande quantité d'agent magnéto-diluant introduite dans Co_5TeO_8 supprime l'ordre magnétique à longue portée dans le système. Cependant, les données NPD et SANS prises pour $Co_{3,99}Zn_{1,01}TeO_8$ montrent la présence d'une forte diffusion magnétique diffuse à basse température. Ce comportement a été étudié avec une analyse de polarisation XYZ dans la plage de température entre 1,5 K et 70 K. Tous les modèles de diffusion magnétique diffuse collectés montrent une large caractéristique centrée sur $Q \approx 1,2$Å et une intensité supplémentaire dans le -Q inférieur partie, qui

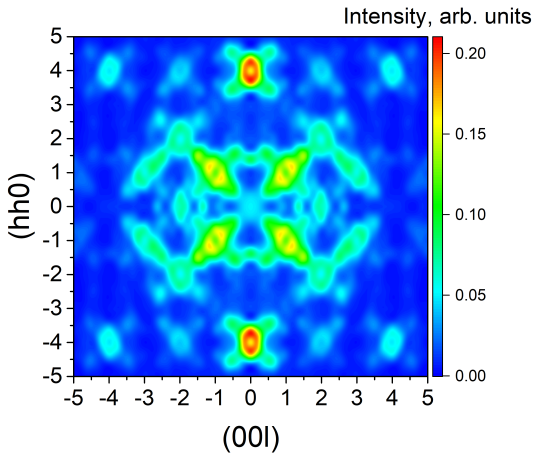

Figure B.20: Diagramme de diffusion diffuse monocristallin du Co_5TeO_8 ordonné à T = 90 K dans le plan (hhl) calculé à partir du raffinement RMC.

perd de son intensité à mesure que la température augmente. Cependant, à T = 70 K, le pic de diffusion diffuse est encore assez prononcé, indiquant une stabilité relative des corrélations de spin à courte portée à une température donnée. En comparant le modèle de $Co_{3,99}Zn_{1,01}TeO_8$ à celui du composé parent, on peut voir que, indépendamment de la perte évidente d'intensité et de l'élargissement, les caractéristiques de diffusion diffuse de ces composés se chevauchent.

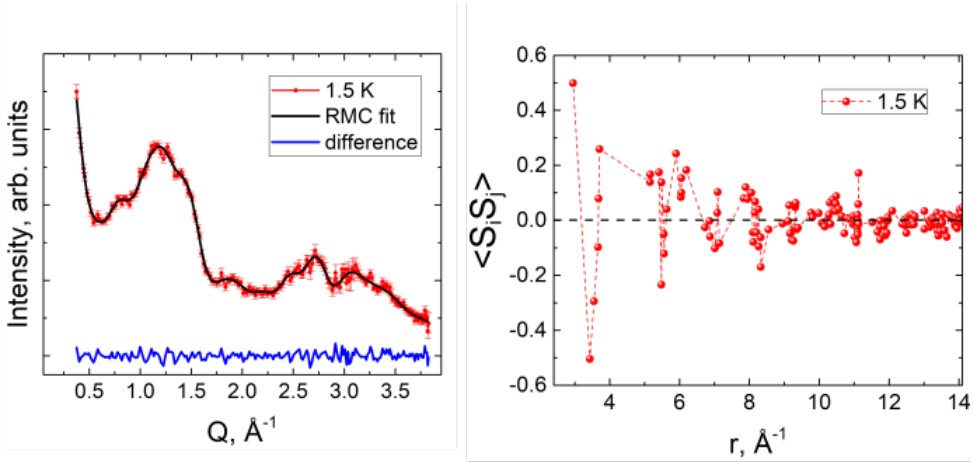

Figure B.21: Gauche: ajustement RMC du profil de diffusion magnétique diffuse du polymorphe ordonné $Co_{3,99}Zn_{1,01}TeO_8$ à T = 1.7K. Points rouges - données expérimentales, ligne noire - ajustement RMC, ligne bleue - courbe de différence. Droite: Fonction de corrélation spin-spin radiale calculée avec les résultats de l'ajustement RMC pour T = 1.5 K.

La fonction de corrélation spin-spin radiale à T = 1.5 K dans le cas de $Co_{3,99}Zn_{1,01}TeO_8$ donne la même orientation relative pour les paires de spin que celle obtenue pour le composé parent à T = 50 K. Cependant $< \mathbf{S}_i\mathbf{S}_j >$ de l'échantillon dilué mouillait plus rapidement avec l'augmentation de la distance, indiquant un rétrécissement des domaines ORS provoqué par la substitution Zn^{2+} (Fig. B.21). Lors du chauffage, les corrélations à courte portée montrent d'abord une certaine stabilité, car les fonctions de corrélation spin-spin radiale pour T = 1,5 K et T = 10 K montrent des magnitudes proches pour les paires

de spin équidistantes. Cependant, avec une nouvelle augmentation de la température, $< \mathbf{S}_i\mathbf{S}_j >$ s'effondre à zéro à des distances $r > 5,4$Å, indiquant des corrélations à courte distance présentes sur une échelle dans la cellule unitaire.

Pour conclure, le comportement magnétique des cartes de diffusion neutronique $Co_{3,99}Zn_{1,01}TeO_8$ pour le plan de réseau réciproque (hhl), le même que pour le composé parent, a été calculé. Pendant le refroidissement, l'intensité de fond incohérente est supprimée tandis que les caractéristiques principales et leurs satellites deviennent plus intenses. Par rapport au Co_5TeO_8 ordonné, les caractéristiques principales à (hhl) et (hhh) conservent leur forme jusqu'à 1,5 K. Similaire au composé non dilué, les caractéristiques du satellite ainsi que le comportement de $< \mathbf{S}_i\mathbf{S}_j >$ function pointe vers une spirale ferrimagnétique de la corrélation de spin à courte portée de $Co_{3,99}Zn_{1,01}TeO_8$ (Fig. B.22)

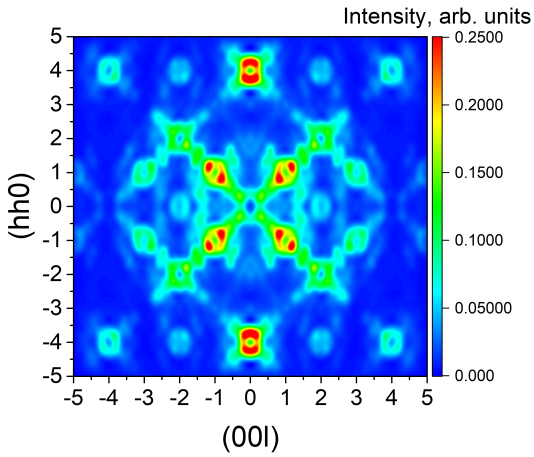

Figure B.22: Diagramme de diffusion diffuse monocristallin du $Co_{3,99}Zn_{1,01}TeO_8$ ordonné à T = 1,5 K dans le plan (hhl) calculé à partir du raffinement RMC.

Les résultats de l'analyse de polarisation XYZ nous permettent de conclure que la formation d'un domaine SRO avec des corrélations de spin spiralées ferrimagnétiques est une caractéristique inhérente à la famille $Co_{5-x}Zn_xTeO_8$ avec x $\in [0, 1.01]$ et la dilution magnétique de A-site, dans l'intervalle donné de concentrations de Zn^{2+}, n'est pas suffisante pour modifier J_{AB} pour supprimer ce comportement.

Le comportement diélectrique des polymorphes désordonnés et Co5TeO8 et Co5TeO8 a été pris en compte. Pour le polymorphe désordonné, deux courbes $\epsilon(T)$ ont été obtenues pour B = 0 T et B = 9 T. En refroidissant, une courbe de champ nul diminue doucement à une région de température bien au-dessus de la température. transition $T_N = 40$ K Les premiers changements notables apparaissent à $T \approx 60K$. Cette légère augmentation en dessous de 60 K chevauche l'intensité maximale de diffusion diffuse observée avec NPD. Ainsi, l'ordre magnétique à courte et longue portée affecte le sous-système de charge du polymorphe désordonné. L'application d'un champ magnétique de 9 T entraîne des changements substantiels dans le comportement de la courbe $\epsilon(T)$. Alors qu'une bosse en dessous de 60 K, liée à l'émergence de domaines SRO, chevauche celle observée pour B = 0 T, la partie basse température est significativement élevée. Plus important encore, il y a un pic net croissant à $T_C = 70K$, indiquant un couplage magnéto-électrique clair dans le système (Fig. B.23). Le facteur magnétoélectrique du polymorphe désordonné chevauche la courbe de magnétisation, indiquant un comportement magnétoélectrique.

Considérons d'abord les mesures de capacité en fonction de la température à un champ appliqué fixe pour le polymorphe Co5TeO8 ordonné. Lors du refroidissement, une capacité

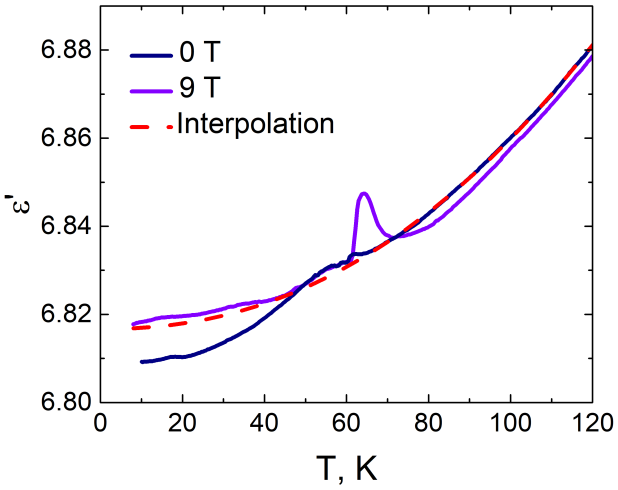

Figure B.23: Evolution de la température de la permittivité en champ nul (bleu foncé) et de la permittivité à B = 9 T (courbe violette) du polymorphe désordonné Co_5TeO_8 et une interpolation de la région haute température (courbe en pointillé rouge).

de champ nul du polymorphe ordonné (Fig. B.24) montre une diminution et à la région de haute température ($T < T_{C1}$) le $C(T)$ la courbe suit clairement une tendance. Cependant, à l'approche de T_{C1}, à $T_1 \approx 50K$, la courbe de capacité diminue plus rapidement que l'interpolation à haute température. En dessous de T_{C2}, à $T_2 \approx 20K$, $C(T)$ montre un petit pic. Ce comportement indique que les deux transitions de phase magnétiques dans Co_5TeO_8 ordonnées sont corrélées avec le comportement du sous-système électronique. Pour tracer l'évolution des propriétés diélectriques sous un champ magnétique appliqué, la même mesure $C(T)$ a été prise à 1 T.Nous voyons que, indépendamment d'une augmentation de l'amplitude de la capacité à basses températures, $C(T)$ at La courbe $B = 1$ T s'écarte de l'interpolation haute température et présente les mêmes caractéristiques à T_1 et T_2 que la capacité de champ zéro. Ainsi, l'application du champ magnétique externe modifie les propriétés diélectriques du Co_5TeO_8 ordonné. Remarquablement, la symétrie magnétique du Co5TeO8 ordonné permet une polarisation électrique

Des mesures de spectroscopie diélectrique ont également été effectuées sur un composé $Co_{3,99}Zn_{1,01}TeO_8$ hautement dilué. La capacité en fonction de la température pour $Co_{3,99}Zn_{1,01}TeO_8$ a été mesurée à $B = 1$ T et 5 T dans la zone de température entre 8 K et 120 K (Fig. B.25). Les mesures de NPD à basse température de $Co_{3,99}Zn_{1,01}TeO_8$ ont révélé qu'environ 50 K de diffusion magnétique diffuse apparaît sans ambiguïté sur les diagrammes de diffraction, ainsi l'ordre magnétique à courte portée provoque des changements dans le charge système du composé: la capacité présente deux caractéristiques distinctes à $T_1 = 40K$ et $T_2 = 13K$. Dès que le champ magnétique de 5 T est appliqué, toutes les caractéristiques inférieures à 50 K sont supprimées et la courbe de capacité correspond presque à l'interpolation à haute température des données de champ nul. Ce comportement implique un effet magnétoélectrique négatif.

Lors de la discussion des résultats, nous devons considérer le paramètre u introduit dans la théorie LKDM, on peut quantifier l'ampleur de la Frustration Géométrique Magnétique (MGF) en comparant les interactions J_{AB} et J_{BB}. MGF maximum est $u = \infty$ quand $J_{AB} = 0$ et $\mu_A = 0$ alors que le MGF faible se produit jusqu'à $u = 1.298$. Ainsi, pour $u \geq 1\ 298$, à l'état fondamental, la configuration en spirale ferrimagnétique à longue

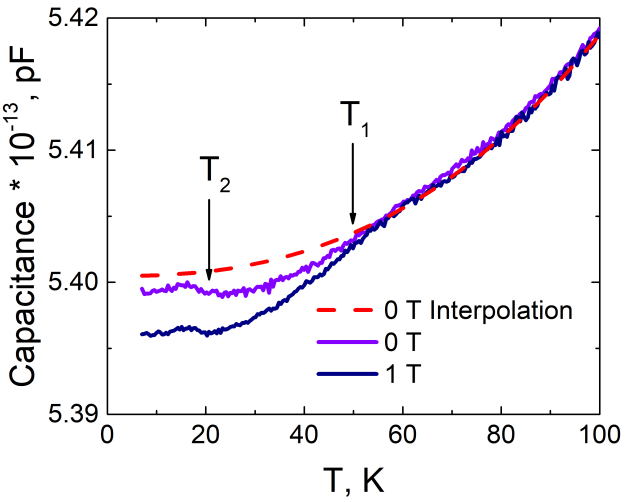

Figure B.24: Évolution de la température de la capacité de champ nul (bleu foncé) et de la capacité à B = 1 T (courbe violette) du polymorphe ordonné Co_5TeO_8 et une interpolation de la région haute température (courbe en pointillés rouges).

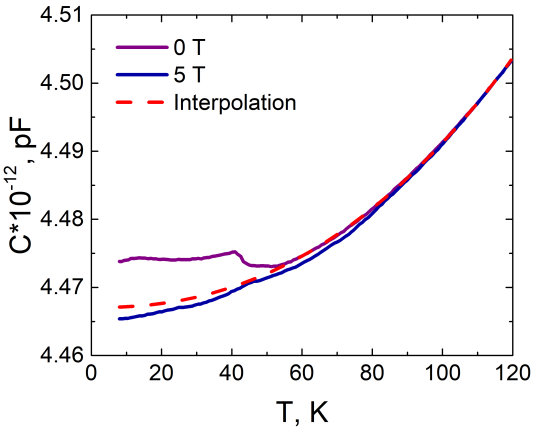

Figure B.25: Evolution de la température de la capacité de champ zéro (courbe violette), de la capacité à $B = 5$ T (courbe bleue) et de l'interpolation haute température de la capacité de champ zéro de $Co_{3,99}Zn_{1,01}TeO_8$

portée n'est pas stable. Les FGM faibles sont préservées et l'ordre en spirale ferrimagnétique à courte portée apparaît sous TF. C'est le cas des deux composés spinelles $CoCr_2O_4$ et $MnCr_2O_4$ avec des paramètres respectifs u de 2 et 1,5. Dans ces composés, un comportement de type spin-verre réentrant est observé avec la présence d'ordres de spirale ferrimagnétique à courte portée qui coexistent avec un ordre de spirale ferrimagnétique à longue portée inférieur à TF ($\approx$ 13 K pour $CoCr_2O_4$ et $\approx 14K$ pour $MnCr_2O_4$). Pour $8/9 \leq u < 1.298$ l'ordre à longue portée de la spirale ferrimagnétique est stable à l'état fondamental, alors pour $u < 8/9$ le comportement magnétique du spinelle correspond à la configuration longue portée de Néel avec un état ferrimagnétique classique. Dans Co_5TeO_8, la dilution magnétique des sites B doit abaisser l'interaction J_{AB}. Puisque l'état fondamental est un comportement ferrimagnétique pour le polymorphe désordonné Co_5TeO_8 et un ordre à longue portée en spirale ferrimagnétique pour le polymorphe ordonné, on peut

supposer que pour les deux polymorphes le demander u devrait être proche de 8/9, mais les différences structurelles sont suffisantes pour affecter légèrement le rapport J_{BB}/J_{AB}. De plus, en comparant le rapport μ_B/μ_A pour les deux polymorphes, on verra qu'ils sont relativement proches: 1,22 pour le désordonné Co_5TeO_8 et 1,25 pour celui ordonné. Ainsi, on peut supposer u légèrement inférieur à 8/9 pour le polymorphe désordonné et u légèrement supérieur à 8/9 pour le polymorphe ordonné. Une autre façon d'estimer le degré de frustration est le rapport entre Θ et T_N (f = $|\Theta\ /T_N|$) qui est couramment utilisé dans le magnétisme quantique et frustré. Dans le cas du polymorphe ordonné Co_5TeO_8 f = 2,88 qui n'est pas une semaine, on peut conclure que la combinaison de la frustration magnétique et de l'interaction DM est responsable de la stabilisation de la modulation de spin longue portée dans le système.

Appendix C

Abstract

The current thesis is dedicated to a complex neutron scattering study of magnetic behaviour $Co_{5-x}Zn_xTeO_8$ spinel series. It was found that Co_5TeO_8 may be obtained in two structural forms: disordered centrosymmetric $Fd\bar{3}m$ and ordered non-centrosymmetric $P4_332$. While the disordered polymorph is a typical Néel-type ferrimagnet with $T_N = 40$ K described with $I4_1/am'd'$ magnetic space group. The ordered polymorph possesses an incommensurate ferrimagnetic spiral spin structure with two phase transitions at $T_{C1} =$ 45 K and $T_{C1} = 27$ K described with $P4_3(00\gamma)0$ magnetic superspace. Both magnetic frustration and Dzyaloshinskii-Morya interaction stabilize the magnetic structure of the ordered Co_5TeO_8. Magnetic dilution with Zn^{2+} in $Co_{5-x}Zn_xTeO_8$ does not break the long-range magnetic ordering up to $x = 0.76$, for $x = 1.01$ only diffuse scattering is observed in neutron powder diffraction experiments. Both polymorphs demonstrate magnetic diffuse scattering far above long-range transition temperatures. Neutron XYZ polarization analysis revealed that in the case of the ordered polymorph the short-range ordering has the same ferrimagnetic spiral nature as the ordered state. Short range ordering of the highly diluted $Co_{3,99}Zn_{1,01}TeO_8$ is similar to the parent compound. Dielectric spectroscopy of the ordered and disordered Co_5TeO_8 and $Co_{3,99}Zn_{1,01}TeO_8$ revealed magnetoelectric behaviour in each case.

Stanislav Podchezertsev

Magnetoelectric coupling in cobalt-based tellurium (VI) oxides with complex spin structures

Magnetic structures | Magnetoelectric behaviour | Neutron scattering